

Machine Learning in Atomistic Simulations: Enabling the Description of Charge Transfer Effects and Sampling Multi Funnel Systems with Global Monte Carlo Moves

Inauguraldissertation

zur

Erlangung der Würde eines Doktors der Philosophie

vorgelegt der

Philosophisch-Naturwissenschaftlichen Fakultät
der Universität Basel

von

Jonas Alexander Finkler

2023

Originaldokument gespeichert auf dem Dokumentenserver der Universität Basel
edoc.unibas.ch



Dieses Werk ist lizenziert unter einer Creative Commons Namensnennung 4.0 International Lizenz (<https://creativecommons.org/licenses/by/4.0/>).

Genehmigt von der Philosophisch-Naturwissenschaftlichen Fakultät
auf Antrag von:

Prof. Dr. Stefan Goedecker
Prof. Dr. Anatole von Lilienfeld
Dr. Johannes Margraf

Basel, den 13.12.2022

Prof. Dr. Marcel Mayor
Dekan

ACKNOWLEDGEMENTS

This thesis is an assembly of results and scientific insights that I collected during the last four years. Preparing this thesis gave me a chance to reflect upon the scientific results that were collected, but it also reminded me of the numerous people that were involved in the process. Without them, none of the work presented here would have been possible. I am not only infinitely grateful for their help and support regarding scientific matters but also for the many joyful moments, enlightening coffee breaks and the friendship that was brought towards me.

First, I want to thank my supervisor Prof. Dr. Stefan Goedecker, who gave me the opportunity to join his research group and allowed me to pursue my own scientific ideas and interests while still keeping me on the right track the whole time. I am also very grateful to my dear collaborator Dr. Tsz Wai Ko. Without his dedication and inspiration, the development of the fourth generation high-dimensional neural network potential would not have been possible. No less important for the success of the project are the contributions of Prof. Dr. Jörg Behler, who also gave me the chance to spend six months with his research group in Göttingen.

I am also grateful for all contributions and suggestions shared by my other collaborators Dr. Alireza Ghasemi, Ehsan Rahmatizad Khajehpasha, Dr. Giuseppe Fisicaro and Moritz Schäfer.

I further want to thank all the people I worked with at the University of Basel that made my time working on this thesis as fun and inspiring as it was: Dr. Deb Sankar De, Dr. Miglė Graužinytė, Dr. Behnam Parsaeifard, Dr. José A. Flores-Livas, Marco Krummenacher, Moritz Jodok Gubler, Hannes Huber, Martin Sommer-Jørgensen, Clara Berger, Melania D’Aniello and Andris Gulans. I will miss all the cheerful and valuable discussions we shared during our coffee breaks. Additionally, I am incredible thankful to all the people that made my stay in Göttingen such an amazing time despite all the difficulties and uncertainties due to the Covid-19 pandemic. In particular, I want to thank Dilshana Rasheeda, Xaiza Aniban, Lukas Hasecke and Emir Kocer.

Acknowledgements

The undeniably most important people that contributed to this thesis are my parents Birgit and Stephan. I am incredibly lucky for having them at my side and supporting me throughout my whole life. Similarly, I am indebted to my sister Elena and all the friends that supported me during the last years.

I also want to thank Barbara Kammermann and Uta Winzer for helping me out with any paperwork related issues and the staff of sciCORE and CSCS for their technical support.

And last but not least, I want to thank my external expert Dr. Johannes Margraf and my second supervisor Prof. Dr. Anatole von Lilienfeld for offering their valuable time to review this thesis and being part of my doctoral committee.

ABSTRACT

In recent years, machine learned potentials (MLPs) have seen tremendous progress and rapid adoption by the materials science community. Due to their high speed and accuracy, MLPs are well suited for sampling complex potential energy surfaces (PESs) with molecular dynamics and Monte Carlo (MC) simulations. Nonetheless, many open challenges remain. Despite the outstanding performance of MLPs, it has become clear, that the builtin assumption of locality limits their applicability for systems where long-ranged effects due to charge transfer are present. But even for systems, for which local MLPs provide an adequate description, complete sampling of the PES can still be hindered by high energy barriers and advanced algorithms are needed to take full advantage of the MLPs capabilities.

In this thesis, both above-mentioned challenges are addressed. In the first part, the fourth generation high-dimensional neural network potential (4G-HDNNP) is introduced. While previous generations of MLPs rely on atomic energies and charges, that only depend on the local atomic environment, the 4G-HDNNP is also able to describe long-ranged interactions caused by charge transfer effects. A charge equilibration scheme based on environment dependent electronegativities allows for the prediction of accurate atomic charges, that depend on the global state of a system, including the total charge. These charges are then not only used to compute electrostatic energies and forces, but also fed into the neural networks describing the short ranged interactions. This allows for an accurate description of changes in local bond-lengths and reactivity due to far-away changes in the electronic structure. The method’s performance is demonstrated on multiple test systems which are incorrectly described by previous methods.

The second part of the thesis, focuses on the Funnel Hopping Monte Carlo (FHMC) method. FHMC introduces a new, global, MC move to directly circumvent high energy barriers that prevent complete sampling of the configuration space during MC simulations. Gaussian mixtures, fit to the Boltzmann distribution of low energy regions, are used to propose the FHMC moves without violating the detailed balance condition. FHMC therefore allows for direct sampling of the complete Boltzmann

Abstract

distribution without resorting to any approximate expansion of the potential energy. Anharmonic effects are therefore fully included. The method is first tested on two prototypical multi-funnel systems, namely the 38 and 75 atom Lennard-Jones clusters. We then used FHMC to study a material called methylammonium lead iodide (MaPbI_3), for which we constructed a highly accurate MLP. In a recent structure search study, two non-perovskite phases of MaPbI_3 were discovered, that, despite being lower in energy than the known perovskite phases, are absent in experiments. Our FHMC simulations, for which we extended the original algorithm to periodic boundary conditions, show, that above 200 K, the experimentally observed phases are thermodynamically preferred. This explains, the absence of the non-perovskite phases in experiments, since at room temperature the perovskite phases are readily obtained. The high energetic barriers then lead to kinetic trapping of the perovskite phases upon cooling.

CONTENTS

ACKNOWLEDGEMENTS	I
ABSTRACT	III
1 INTRODUCTION	1
2 THEORETICAL BACKGROUND	7
2.1 From Quantum Mechanics to Density Functional Theory	7
2.1.1 The Schrödinger Equation	7
2.1.2 The Born-Oppenheimer Approximation	8
2.1.3 Hartree-Fock Theory	9
2.1.4 Post Hartree-Fock Wave Function Methods	13
2.1.5 Density Functional Theory	14
2.1.6 Atomic Charges	18
2.2 Simulation Methods for the Potential Energy Landscape	20
2.2.1 Molecular Dynamics	20
2.2.2 Monte Carlo Simulations	22
2.2.3 Hamiltonian Monte Carlo	24
2.2.4 Structure Search	26
2.2.5 Force Fields	28
3 MACHINE LEARNED POTENTIALS	31
3.1 Introduction	31
3.1.1 Artificial Neural Networks	34
3.2 Previous Generations of Machine Learned Potentials	38
3.2.1 First Generation Machine Learned Potentials	38
3.2.2 Second Generation Machine Learned Potentials	39
3.2.3 Third Generation Machine Learned Potentials	42
4 FOURTH GENERATION HIGH-DIMENSIONAL NEURAL NETWORK POTENTIALS	45
4.1 Introduction	45

4.2	The 4G-HDNNP Model	48
4.2.1	Mathematical Details of the 4G-HDNNP Implementation . .	52
4.3	Test Systems Showing the 4G-HDNNPs Capability	60
4.3.1	A Benchmark for Organic Molecules	61
4.3.2	Metal Clusters: Ag ₃	63
4.3.3	NaCl Cluster Ions	66
4.3.4	Au ₂ Cluster on MgO(001)	67
4.3.5	DFT Calculations	71
4.4	Other Nonlocal MLPs	72
4.5	Summary and Outlook	73
5	LEARNING A SMOOTHED VERSION OF THE OVERLAP MATRIX FINGERPRINT	77
6	FUNNEL HOPPING MONTE CARLO	89
6.1	Broken Ergodicity	89
6.1.1	The Harmonic Superposition Approximation	91
6.2	Advanced Monte Carlo Techniques	93
6.2.1	Replica Exchange Monte Carlo	94
6.2.2	Smart Darting Monte Carlo	96
6.3	The Funnel Hopping Monte Carlo Algorithm	97
6.3.1	Identifying Equivalent Configurations Using Eckart Space and the RMSD	98
6.3.2	Using Gaussian Mixtures to Propose Monte Carlo Moves . .	102
6.4	Results	108
6.4.1	38 atom Lennard-Jones cluster	109
6.4.2	75 atom Lennard-Jones cluster	112
6.5	Summary	114
7	EXPERIMENTAL ABSENCE OF THE NON-PEROVSKITE GROUND STATE PHASES OF MAPbI ₃ EXPLAINED BY A MLP BASED FHMC STUDY	117
7.1	Introduction	117
7.2	Modification of the FHMC Method for MaPbI ₃	120
7.2.1	Extension to Periodic Boundary Conditions	121
7.2.2	Changes in Volume	123
7.2.3	Special Treatment of the Methylammonium Molecules	123
7.2.4	Replica Exchange	123
7.2.5	Other Simulation Details	125

7.3	Neural Network Potential	126
7.4	Results	130
7.4.1	FHMC Study of the Experimentally Known Phases	130
7.4.2	FHMC Study Including the Two Delta Phases	133
7.5	Summary	137
8	CONCLUSION AND OUTLOOK	139
	ACRONYMS	145
	BIBLIOGRAPHY	147
	APPENDIX	175
A.1	Details for the 4GHDNNP Test Systems	175
A.1.1	$C_{10}H_2/C_{10}H_3^+$	175
A.1.2	$Ag_3^{+/-}$ clusters	180
A.1.3	$Na_{8/9}Cl_8^+$ clusters	183
A.1.4	Au_2-MgO	187
B.2	Details for the $MaPbI_3$ FHMC Simulations	193
B.2.1	Supercells	193
B.2.2	Symmetry Functions Used for the $MaPbI_3$ HDNNP	198
B.2.3	Quasi Harmonic Approximation	206

1 INTRODUCTION

Ancient periods of human history, such as the stone, bronze or the iron age, are commonly named after the most dominant materials that were driving the technological progress at the time. While this is certainly an oversimplification and ignores many social, economic and cultural achievements, it is true that the materials that are available inspire and shape the inventions, developments and constructions achieved by humans.

While the technological progress of previous periods of human history was driven by the discovery of a few specific material, it is much harder to decide, after which material the current period should be named. A walk through a city might inspire someone to call it the concrete or glass age. A walk through nature or a dive in the ocean might lead someone to the conclusion that plastics are the most dominating material on the earth today. While these materials are abundant and in plain sight, the technological progress is driven by a huge variety of other novel materials. Superconductors are used in MRI machines, planes are build from special metal alloys and organic LEDs make up the displays of our phones, to name only a few. Our current age might therefore as well simply be called the age of materials.

Unlike the materials used by prehistoric humans, modern materials are synthesized artificially, and in many cases have been developed to fit very specific needs and purposes. This ability to design new materials by targeting desired properties is enabled by our understanding of the physics that describe the interactions of the atoms that make up any material.

While humans have been synthesizing chemical substances and materials for a long time, like extracting metals from ores, rendering fat into soap or making alloys such as bronze, these feats were the results of accidental discovery and experimentation followed by a careful improvement of the observed reactions. Only in the recent history from the 17th to the 19th century, more deliberate control over chemical reactions was gained by the development of the theories of atoms and molecules, which form the basis of modern chemistry [1]. However, the understanding of the chemical

1 Introduction

bond and the microscopic structure of matter was rudimentary and chemistry was based on empirical rules, derived from experimental observations.

This changed with the discovery of the elementary particles and the development of quantum mechanics, about a century ago. With the Schrödinger equation at its heart, the theory of quantum mechanics describes the interactions between the electrons and nuclei that make up the atoms. Despite the fact, that quantum mechanics provides an almost complete description of the mechanics involved in chemical bonding, it could only be used to provide a qualitative understanding and description of chemical processes in the beginning. The problem lies in the high complexity of the Schrödinger equation, for which analytical solutions can only be found in the most simple cases, such as the hydrogen atom.

Multiple parallel developments allowed scientists to overcome this limitation and obtain quantitative predictions from quantum mechanics, leading to what we today know as materials sciences. The first development are approximations to the Schrödinger equation, that reduce the mathematical complexity of the problem. Similarly influential were the developments of appropriate computational methods and algorithms that enabled the application of computers with their ever-increasing compute power to solve the problem. The importance of these developments is highlighted by the Nobel Prize in chemistry which was awarded to Walter Kohn and John A. Pople in 1998 for the development of density functional theory (DFT) and its implementation in the GAUSSIAN computer program respectively.

In addition to quantum mechanical methods, which usually only describe an instantaneous state of an atomistic system, atomistic simulation methods were needed, that allow to extract the macroscopic properties of materials from the underlying microscopic interactions. Nowadays, a plethora of simulation methods are available, that enable the prediction of various properties based on the interactions arising from quantum mechanical principles. These include the geometric ground state, electronic properties such as absorption spectra, mechanical properties, and thermal properties such as thermal expansion coefficients, heat capacities or phase transition temperatures. The ability to directly predict such properties in simulations without the need for costly synthesis and experimentation allows us to develop materials with targeted properties by screening large numbers of candidates. Additionally, simulation of known materials can shed light on the microscopic dynamics responsible for certain properties and helps us to understand effects that cannot be probed by experiments.

In the beginning, atomistic simulations were not based on quantum mechanics, but instead artificial systems, such as hard spheres, were simulated to study emergent properties of the atomistic dynamics, such as phase transitions. In this context, two fundamental simulation methods, namely Monte Carlo (MC) sampling [2] and molecular dynamics (MD) [3] were introduced in the 1950s. In MC simulations, statistical properties are evaluated by sampling random configurations from a target distribution such as the Boltzmann distribution of systems at a constant temperature. In MD simulations, Newton’s equations of motion are integrated to obtain the physical trajectories of the atoms. An introduction to MC, MD and a few other simulation methods, which are relevant in the context of this thesis, is given in Section 2.2. Later on, simulations for more realistic model systems, such as liquid argon [4] or water [5] started to emerge. In these simulations, the atomic interaction are modeled using what is nowadays known as classical force fields. These consist of rather simple mathematical expressions, that are derived from physical intuition and have only few free parameters that are fit to experimental values.

In parallel to the development of atomistic simulations, the computer was rapidly adopted as a tool to tackle the solutions to the electronic Schrödinger equation. However, the high computational cost of these quantum mechanics based (*ab-initio*) methods prevented their adaption in MD and MC simulations. This was changed by Car and Parrinello [7], who, in 1985, published a scheme to integrate DFT with MD. By overcoming the limitations of classical force fields, this method massively increased the predictive power of atomistic simulations. Since then, *ab-initio* methods, such as DFT are the basis for many simulations. A brief introduction into the most relevant quantum mechanical methods, including DFT, is given in Section 2.1. Although quantum mechanics based methods allowed for a more faithful description of atomistic systems, they did not render classical force fields obsolete. Due to their much lower computational complexity, force fields are still in wide use today, to study systems of large size and time scales that are inaccessible with *ab-initio* methods.

More recently, machine learning based methods have been emerging that bridge the gap between the highly efficient classical force fields and the computationally expensive but much more accurate *ab-initio* methods. The basic concept behind these machine learning based methods is that instead of a physics inspired function with few free parameters, a very general, highly parametrized, functional form is used to model the inter atomic potential. These general, flexible functions are then fit to

An in depth overview of the historical developments of atomistic simulations can be found in Reference [6].

1 Introduction

large data sets of *ab-initio* reference data. In the first attempts to employ machine learning methods to construct data driven potentials, Blank et al. [8] relied on position coordinates and rotation angles as inputs to an artificial neural network (ANN). While a highly accurate fit of the potential energy could be achieved, this approach has the disadvantage that the trained potential is highly system specific and does not allow for applications to larger and more complex systems. Furthermore, important symmetries, such as the invariance of the energy under rotation, translation or the permutation of equivalent atoms are not preserved.

This problem was overcome by the introduction of the high dimensional neural network potential (HDNNP) by Behler and Parrinello [9] in 2007. Instead of directly using atomic positions as inputs to the ANNs, the total energy of the system is expressed as a sum of atomic energies, each of which depends on a set of atomic environment descriptors called symmetry functions [10], that encode the local atomic environment in a way that preserves all important symmetries. Since only the local environment is considered, HDNNPs can be trained on reference data from smaller systems and then applied to systems of arbitrary size, with a linear scaling computational cost. Since then, many other methods relying on local environment descriptors have been proposed and many successful applications have been reported. These potentials, which can be considered the second generation of machine learned potentials (MLPs), are still in wide use today. Nevertheless, it has been realized, that in some cases, relying on local environments is insufficient, since long range interactions, such as electrostatic interactions, are necessarily neglected. This realization led to the development of a third generation of MLPs that include explicit electrostatics based on environment dependent atomic charges [11]. Only recently, it has become clear, that these third-generation potentials are still unable to describe many important effects. Since the atomic charges depend on the local environment only, long ranged charge transfer and resulting changes in reactivity and geometry cannot be described. An in-depth overview over these previous generations of MLPs and the problems that lead to the development of subsequent methods can be found in Chapter 3.

The qualitative shortcomings of previous generations of MLPs inspired us to develop the fourth generation high-dimensional neural network potential (4G-HDNNP), which is presented in Chapter 4. Through a charge equilibration scheme based on local environment dependent electronegativities accurate atomic charges are predicted, that depend on the global structure of the system. In addition to the calculation of electrostatic interactions, the atomic charges are also fed into the ANNs that

predict the short ranged atomic interactions. This way, information about the global system state is introduced into the description of the local interactions and effects caused by long range charge transfer can be accurately described. The methods capability is demonstrated on several test systems, for which second and third generation methods fail to provide a qualitatively accurate description.

Due to their low computational cost, MLPs are well suited for applications in MD and MC simulations where many energy and force calculations are needed. They can provide an accuracy comparable to *ab-initio* methods for simulations that were previously restricted to less accurate classical force fields due to the required size or timescale of the simulation. This massively increased the predictive power of MD and MC simulations and the scale of the systems to which they could be applied.

Unfortunately, standard MD and MC methods are not sufficient for the simulation of many important systems as many effects take place on vastly different time scales than the underlying atomistic dynamics. In these systems, high energetic barriers need to be crossed to transition between long-lived states. Such rare events pose a major bottleneck in many MC and MD simulations and in many cases prevent direct simulation approaches completely. While simulations of such systems pose a formidable challenge they are in many cases also particularly important since the accurate simulation of phase transitions allows us to make predictions about the stability and synthesizability of a given material.

The problem of high energy barriers has long been realized, and many approaches to overcome it have been proposed in the past. The most simple approaches are based on the harmonic approximation (HA). In the HA a second order Taylor expansion is used to construct an approximation to the potential energy that can be treated with analytical methods. Unfortunately, such approximations are usually only valid at lower temperatures and fail for systems where the potential energy around local minima behaves anharmonically. In these cases, extensions to the MC method are needed that overcome the problem of high barriers. Many methods rely on a bias to artificially lower the energetic barriers. In one of the first methods, called umbrella sampling [12–14], a static bias is added and the samples obtained from the simulation are then reweighted after the simulation to remove the effect of the bias. Later methods, such as metadynamics [15], multicanonical sampling [16, 17], Wang-Landau sampling [18, 19] or nested sampling [20–23] use dynamically adjusted biasing during the simulation.

During MC simulations, trial moves are proposed which are then either accepted or rejected. Conventionally, trial moves are generated by slightly displacing one

1 Introduction

or multiple atoms. Only rather small displacements can be used, since larger displacements would most likely result in high energy structures with a too small chance of being accepted. Smart darting MC [24] or simulations based on the harmonic superposition approximations [25] introduce a new, carefully constructed, type of move, which is non-local and directly circumvents high energetic barriers. In Chapter 6, the Funnel Hopping Monte Carlo (FHMC) method is presented, which, inspired by smart darting MC, also introduces a new, non-local MC move. Unlike smart darting, the method properly takes care of the rotational and permutational invariance present in atomic systems and a high acceptance rate of the trial moves is obtained by using Gaussian mixtures fit to the Boltzmann distribution of local minima to generate the trial moves. In Chapter 7, the method is then applied to a material called methylammonium lead iodide (MaPbI_3). For this material, a new ground state phase was predicted by a recent structure search study [26]. Despite being lower in energy than the experimentally observed perovskite phases, this new ground state phase is absent from experiments. The large structural difference and high energy barrier between the perovskite phases and the newly discovered ground state phase prevent a direct simulation of the phase transition with classical MC and MD methods. We therefore extended our FHMC method to periodic systems and developed a highly accurate HDNNP to drive the simulation. Our simulations show, that the newly discovered ground state phase is only thermodynamically preferred up to a temperature of 200 K. This low transition temperature explains the absence of the ground state phase from experiments, since at room temperature, the experimentally observed perovskite phases are readily obtained. The transition to the lower energy ground state phase is then prevented by kinetic trapping, due to the low available kinetic energy at the transition temperature.

2 THEORETICAL BACKGROUND

The Funnel Hopping Monte Carlo (FHMC) method presented in this thesis, is based on a model of chemical systems and materials, where the atoms are treated as point like objects, held together by forces arising from chemical bonds. Similarly, the fourth generation high-dimensional neural network potential (4G-HDNNP) tries to model exactly these forces. The concept of chemical bonding has been around in chemistry for a long time, but only with more recent advances in methodology and computing hardware, has a quantitative description of atomistic interactions become possible. In this chapter, a brief overview over the electronic structure methods, that allow us to compute the potential energy, forces and many other quantities of interacting atoms, is given. Later on, a few of the most important simulation methods, that make use of the energies and forces obtained from electronic structure methods, are also introduced.

2.1 FROM QUANTUM MECHANICS TO DENSITY FUNCTIONAL THEORY

2.1.1 THE SCHRÖDINGER EQUATION

All solid matter surrounding us, is made up of electrons and nuclei. The interaction of these particles can be described by quantum mechanics, which was developed about a century ago. In quantum mechanics, such a system of nuclei and electrons is described by a many-body wave function $\Psi(\{\mathbf{R}_I, \mathbf{r}_i\})$, with \mathbf{R}_I representing the positions of the nuclei and \mathbf{r}_i representing the positions of the electrons.

The ground state energy E of this system is then given by the time independent Schrödinger equation.

$$\mathcal{H}\Psi(\{\mathbf{R}_I\}, \{\mathbf{r}_i\}) = E\Psi(\{\mathbf{R}_I\}, \{\mathbf{r}_i\}) \quad (2.1)$$

The above equation is an eigenvalue problem, where the smallest eigenvalue corresponds to the ground state energy and the respective eigenvector to the ground state

2 Theoretical Background

wave function. Here \mathcal{H} is the time independent Hamiltonian, containing the kinetic energy terms for the nuclei \mathcal{T}_N and the electrons \mathcal{T}_e and electrostatic energy terms for the interactions between the electrons \mathcal{V}_{ee} , the protons \mathcal{V}_{NN} and between electrons and protons \mathcal{V}_{Ne} .

$$\mathcal{H} = - \underbrace{\sum_I \frac{1}{2m_I} \nabla_{\mathbf{R}_I}^2}_{\mathcal{T}_N} - \underbrace{\sum_i \frac{1}{2} \nabla_{\mathbf{r}_i}^2}_{\mathcal{T}_e} + \underbrace{\sum_{I < J} \frac{Z_I Z_J}{|\mathbf{R}_I - \mathbf{R}_J|}}_{\mathcal{V}_{NN}} + \underbrace{\sum_{i < j} \frac{1}{|\mathbf{r}_i - \mathbf{r}_j|}}_{\mathcal{V}_{ee}} - \underbrace{\sum_{I,i} \frac{Z_I}{|\mathbf{R}_I - \mathbf{r}_i|}}_{\mathcal{V}_{Ne}} \quad (2.2)$$

The m_I are the masses of the nuclei, Z_I the nuclear charges and $\nabla_{\mathbf{x}}$ the nabla operator with respect to the spatial coordinate \mathbf{x} ($\nabla_{\mathbf{x}} = \left(\frac{\partial}{\partial x_x}, \frac{\partial}{\partial x_y}, \frac{\partial}{\partial x_z} \right)$). The electronic masses and charges do not appear in the above equation because it is given in atomic units. Atomic units are defined such that the reduced Planck constant $\hbar = \frac{h}{2\pi}$, the elementary charge e , the electron mass m_e and the Bohr radius $a_0 = \frac{4\pi\epsilon_0\hbar^2}{m_e e^2}$ are all equal to 1. Distances are hence measured in Bohr (1 Bohr = 0.5292 Å) and energies in Hartree (1 Ha = 27.211 eV). These units are often very useful since they simplify many of the equations we will need. Furthermore, many of the results that we compute, such as energies or forces will be close to one in magnitude if atomic units are used. This does not only help with readability, but also avoids under- and overflow issues that computers face, when dealing with extremely small and large numbers. Therefore, if not stated otherwise, all equations in this thesis will be given in atomic units.

2.1.2 THE BORN-OPPENHEIMER APPROXIMATION

Even the hydrogen nuclei, which is the lightest of all nuclei, is roughly about two thousand times heavier than the electron. This large difference in mass results in a great disparity between the timescales on which electrons and atomic nuclei move. It is therefore a reasonable approximation to think of the heavy nuclei as almost stationary, while the light electrons adapt instantaneously to any change in the nuclear positions. This approximation is known as the Born-Oppenheimer or adiabatic approximation [27]. Since it decouples the electronic from the ionic motion, it allows us to write the total wave function of the system as a product of the electronic ($\psi(\{\mathbf{r}_i\})$) and ionic ($\phi(\{\mathbf{R}_I\})$) wave function.

$$\Psi(\{\mathbf{R}_I, \mathbf{r}_i\}) = \psi(\{\mathbf{r}_i\})\phi(\{\mathbf{R}_I\}) \quad (2.3)$$

2.1 From Quantum Mechanics to Density Functional Theory

The electronic wave function depends only indirectly on the ionic positions, through the electrostatic potential generated by them, and we assume that at each point in time, the electrons reach their ground state configuration instantly and adiabatically follow any change in the nuclear positions. The Hamiltonian used in the Born-Oppenheimer approximation is therefore

$$\mathcal{H} = \mathcal{T}_e + \mathcal{V}_{ee} + \mathcal{V}_{Ne} \quad (2.4)$$

According to the Heisenberg uncertainty principle, the heavy nuclei are much more localized in space than the electrons. This allows us to treat them as classical point particles, that react to the potential created by the surrounding electrons. In a molecular dynamics simulation for example, we will take the initial ionic positions and solve the Schrödinger equation (or a simplified version thereof, as we will see later) to obtain the electronic ground state wave function. The total energy of the system is then obtained by adding the electrostatic interaction of the ions and their kinetic energy to the electronic energy that we obtained by solving the Schrödinger equation. The resulting forces can be calculated using the Hellman-Feynman theorem [28]. We can then follow the time evolution of the ionic positions by integrating the forces according to Newton's law and recalculating the electronic ground state for the ionic positions at each time step.

The Born-Oppenheimer approximation was used in all calculations presented in this thesis. It should be noted however, that in some cases, such as superconductors, electron phonon couplings beyond the adiabatic approximation can be important.

Since we assume that the electrons adapt instantaneously to the ionic positions, the total potential energy of a system is only a function of the nuclear positions.

$$E = E(\{\mathbf{R}_I\}) \quad (2.5)$$

This function $E(\{\mathbf{R}_I\})$ is known as the potential energy surface (PES) and is often the main subject of study in this thesis, since many properties, such as the geometric ground state, reaction pathways or thermodynamic quantities can be derived from it (see Section 2.2).

2.1.3 HARTREE-FOCK THEORY

The electronic wave function is a function that depends on all N electronic positions. If we now imagine any computational treatment of such a function, meaning that

2 Theoretical Background

we would represent it by expanding it in any basis set, it is clear that the storage requirements would grow exponentially with the number of electrons in the system. Any such endeavour is therefore destined to fail, even on modern compute hardware for anything that contains more than a handful of electrons. We are therefore forced to simplify the electronic wave function. The most straightforward ansatz would be to write the wave function as a product of N single electron wave functions. This is known as the Hartree product.

$$\Phi(\{\mathbf{r}_i\}) = \phi_1(\mathbf{r}_1)\phi_2(\mathbf{r}_2)\dots\phi_{N-1}(\mathbf{r}_{N-1})\phi_N(\mathbf{r}_N) \quad (2.6)$$

This ansatz fails to capture two important properties of interacting electrons, namely correlation and exchange interactions. Correlation interaction comes from the fact that electrons react to the instantaneous position of each other, meaning that due to their electrostatic repulsion, it should be very unlikely to find two electrons at the same position or very close together. This is clearly not the case for the above wave function, since the positions of the electrons are completely independent of each other. Exchange interaction is a result of the Pauli exclusion principle. Since electrons are fermions, their wave function is required to change sign upon exchange of two electronic coordinates.

$$\phi_1(\mathbf{r}_1)\dots\phi_i(\mathbf{r}_i)\dots\phi_j(\mathbf{r}_j)\dots\phi_N(\mathbf{r}_N) = -\phi_1(\mathbf{r}_1)\dots\phi_i(\mathbf{r}_j)\dots\phi_j(\mathbf{r}_i)\dots\phi_N(\mathbf{r}_N) \quad (2.7)$$

This property is also clearly not enforced by the wave function given in Equation 2.6.

To enforce this antisymmetry upon the wave function, Slater proposed to write the total electron wave function as a determinant of single electron wave functions.

$$\Psi(\{\mathbf{r}_i\}) = \frac{1}{\sqrt{N!}} \begin{vmatrix} \phi_1(\mathbf{r}_1) & \phi_2(\mathbf{r}_1) & \cdots & \phi_N(\mathbf{r}_1) \\ \phi_1(\mathbf{r}_2) & \phi_2(\mathbf{r}_2) & \cdots & \phi_N(\mathbf{r}_2) \\ \vdots & \vdots & \ddots & \vdots \\ \phi_1(\mathbf{r}_N) & \phi_2(\mathbf{r}_N) & \cdots & \phi_N(\mathbf{r}_N) \end{vmatrix} \quad (2.8)$$

The total energy of such a wave function can then be computed as:

$$E_{\text{HF}} = \sum_{i=1}^N \int \phi_i^*(\mathbf{r}_i) h_i \phi_i(\mathbf{r}_i) d\mathbf{r}_i + \frac{1}{2} \sum_{i=1}^N \sum_{j=1}^N ([ij|ij] - [ij|ji]) \quad (2.9)$$

$$h_i(\mathbf{r}_i) = \frac{-\nabla_{r_i}^2}{2} - \sum_I \frac{Z_I}{|\mathbf{R}_I - \mathbf{r}_i|} \quad (2.10)$$

$$[ij|kl] = \int \phi_i^*(\mathbf{r}_1) \phi_j^*(\mathbf{r}_2) \frac{1}{|\mathbf{r}_1 - \mathbf{r}_2|} \phi_k(\mathbf{r}_1) \phi_l(\mathbf{r}_2) d\mathbf{r}_1 d\mathbf{r}_2 \quad (2.11)$$

The term $[ij|ji]$ is a result of the Slater determinant ansatz enforcing the antisymmetry of the wave function and is called the exchange term. As seen from Equation 2.11, $[ij|ij]$ is the electrostatic energy of the electron.

By minimizing this energy under the constraint, that the orbitals ϕ_i are orthonormal, it can be found, that the solution is given by taking the N lowest eigenfunctions of the so called Fock operator \hat{F} . Below, the restricted Fock operator ($\hat{F}_R[\{\phi_j\}](\phi_i)$) for a closed shell and non spin-polarized system is given. Note that only the $N/2$ lowest orbitals are used, since each orbital is occupied twice, with one spin-up and one spin-down electron.

$$\hat{F}_R[\{\phi_j\}]\phi_i(\mathbf{r}) = h_i\phi_i(\mathbf{r}) + \sum_{j=1}^{N/2} \left(2\hat{J}_j\phi_i(\mathbf{r}) - \hat{K}_j\phi_i(\mathbf{r}) \right) \quad (2.12)$$

The Coulomb operator \hat{J} and exchange operator \hat{K} are given by

$$\hat{J}_j\phi_i(\mathbf{r}) = \int \frac{\phi_j^*(\mathbf{r}')\phi_j(\mathbf{r}')}{|\mathbf{r} - \mathbf{r}'|} d\mathbf{r}' \phi_i(\mathbf{r}) \quad (2.13)$$

and

$$\hat{K}_j\phi_i(\mathbf{r}) = \int \frac{\phi_j^*(\mathbf{r}')\phi_i(\mathbf{r}')}{|\mathbf{r} - \mathbf{r}'|} d\mathbf{r}' \phi_j(\mathbf{r}) \quad (2.14)$$

The Hartree-Fock equations can also be solved for non-spin-restricted systems, which is only slightly more involved.

The numerical solution to these equations are obtained by expanding the wave functions $\phi_i(\mathbf{r})$ in a basis set $\chi_\mu(\mathbf{r})$.

$$\phi_i(\mathbf{r}) = \sum_{\mu} C_{\mu i} \chi_{\mu}(\mathbf{r}) \quad (2.15)$$

From which we can obtain the Roothaan-Hall equation, which is a generalized eigenvalue problem for the coefficient matrix C .

$$FC = SC\epsilon \quad (2.16)$$

Here F is the Fock operator expanded in the basis set $\chi_\mu(\mathbf{r})$, S is the overlap matrix ($S_{ij} = \int \chi_i(\mathbf{r})\chi_j(\mathbf{r})d\mathbf{r}$) and ϵ are the orbital energies. Since the Fock operator F itself depends on the molecular orbital coefficients C , the Roothaan-Hall equation has

2 Theoretical Background

to be solved iteratively until a self-consistent solution is found. For this, an initial guess is taken for C , for which F is constructed. The improved orbital coefficients are then obtained by solving Equation 2.16. This process is then repeated until a self-consistent solution for C is found.

This solution does not only allow us to access the PES in terms of energy and forces, but also other observables, such as the electron density $\rho(\mathbf{r})$ can be computed.

$$\rho(\mathbf{r}) = 2 \sum_i^{N/2} |\phi_i(\mathbf{r})|^2 \quad (2.17)$$

As we will see later, ρ is the central quantity in density functional theory (DFT) and it can also be used to compute atomic charges, as described in Section 2.1.6. These atomic charges will later play an important role in the 4G-HDNNP that is presented in Chapter 4.

Many flavours of basis sets exist, each with their own advantages and disadvantages. For example plane wave basis sets [29] are generally well suited for periodic systems and have the advantage that they form an orthonormal basis that can be systematically improved and that kinetic and Coulomb energies can be efficiently computed by taking advantage of the fast Fourier transform (FFT). However, to correctly describe the rapidly oscillating core electrons close to the nuclei, a large number of plane waves is needed. This problem can be avoided by the use of pseudopotentials, which take advantage of the fact that the core electrons do not participate in chemical bonding, by replacing them with artificial potentials. Wavelets [30] share many of the advantages of plane waves, in that they also form a systematic orthogonal basis set. In addition, they are also well suited for systems with free boundary conditions and allow for a varying resolution, such that more basis functions can be placed in regions where the wave function changes rapidly. The traditionally most popular basis sets are probably linear combinations of atomic orbitals (LCAO), which are constructed by placing a set of basis functions on each atom. Each such atomic basis function consists of a radial part, usually defined as a linear combination of Gaussian functions [31], but also other choices such as numerically defined functions [32] exist, and an angular part described by spherical harmonics. These basis sets have the advantage that the number of basis functions required is generally lower than in other methods. If Gaussians are used, the required integrals, such as overlap or Coulomb integrals can be computed analytically. However, systematic convergence

with respect to the basis set can not be obtained, making it difficult to estimate the basis-set error in computations using LCAOs.

The main limitation of the Hartree Fock method is, that the wave function is approximated by a single Slater determinant. Even if we would use a complete basis set, this is not sufficient to describe the exact wave function, since electronic correlation cannot be described. Because of this, the method is unable to describe dispersion interactions, will predict bonds that are too short and bond breaking energies that are too high.

Despite that, the method can still give reasonable values for energy differences in many cases. Further, the method is size-consistent, i.e. the energy of a system of two infinitely separated subsystems is equal to the energy of the sum of the two individual systems. The method is also variational which means the calculated energy forms an upper bound for the energy of the exact wave function solution. A naive implementation of the Hartree-Fock (HF) method scales as $\mathcal{O}(n^4)$ with n being the number of basis functions used, which is usually proportional to the number of electrons in the system. With more involved implementations, the computational complexity can be reduced significantly to around $\mathcal{O}(n^2)$ [33].

2.1.4 POST HARTREE-FOCK WAVE FUNCTION METHODS

Many methods have been developed to overcome the limitations of the single Slater determinant ansatz used by the Hartree-Fock method. Although no such methods have been used in this thesis a brief overview will be given in this chapter.

From the molecular orbitals obtained from HF, additional, excited Slater determinants can be constructed, by replacing one or more of the occupied orbitals with unoccupied orbitals. In the limit of all possible Slater determinants, a complete basis set for the wave function can be obtained. By optimizing the weights of the individual Slater determinants, an exact solution to the time independent Schrödinger equation in the Born-Oppenheimer approximation can be obtained. The accuracy of this method, called **full configuration interaction (CI)**, is therefore in principle only limited by the accuracy of the basis set from which the molecular orbitals are constructed. However, due to the exponential scaling of the method, it is only applicable to the smallest of systems and the number of Slater determinants that are used has to be truncated. These truncated approaches are known as CI-(S/SD/SDT/...) depending on the amount of Slater determinants included. This truncation causes the method to not be size-consistent anymore, but still variational.

2 Theoretical Background

In **Møller-Plesset perturbation theory**, perturbation theory is used to calculate second (MP2) or higher order corrections to the ground state energy of the Fock operator. The series of higher order corrections (MP3, MP4, ...) does not converge to the full CI solution. The method is size consistent but not variational.

Coupled cluster (CC) theory uses an exponential ansatz for the wave function.

$$|\Psi_{\text{CC}}\rangle = e^T |\Psi_{\text{HF}}\rangle \quad (2.18)$$

Where Ψ_{HF} is the HF wave function and T the excitation operator containing all possible excitation of the HF orbitals ($T = T_1 + T_2 + T_3 + \dots$), where each excited wave function is weighted with a coefficient that has to be optimized. This ansatz is able to describe the exact full CI wave function in the limit, where all excitations are included. However, in practice only some excitations are included. CCSD for example includes single and double excitations. In CCSD(T), which can be considered to be the gold-standard of electronic structure calculations nowadays, single and double excitations are fully included while triple excitations are included in a perturbative manner. Due to the exponential operator, higher order excitations are included implicitly, reusing the coefficients of the lower order excitations. The method is size consistent but not variational. Computationally the method is very demanding and CC-SD(T) scales as $\mathcal{O}(n^7)$.

2.1.5 DENSITY FUNCTIONAL THEORY

An alternative way to approach the solution of Schrödinger's equation can be found in density functional theory (DFT). The theory has its origins in the seminal work of Hohenberg and Kohn [34], where it is shown, that the electronic ground state density $\rho(\mathbf{r})$ uniquely determines the external potential of the nuclei $v(\mathbf{r})$ up to an additive constant. In other words, no two potentials that differ by more than an additive constant can give rise to the same electronic density. Combined with the fact, that the total energy E is a functional of the electronic wave function, which is uniquely determined by the external potential, it can be concluded, that $\rho(\mathbf{r})$ must be sufficient to uniquely determine E .

While the energy of any quantum state is in general a functional of its $3N$ dimensional wave function, this result shows that the ground state energy, which in many cases is the energy we are most interested in, is only a functional of the three-dimensional density $\rho(\mathbf{r})$.

2.1 From Quantum Mechanics to Density Functional Theory

Therefore, a universal functional $\mathcal{F}[\rho(\mathbf{r})]$ of the electron density $\rho(\mathbf{r})$ must exist, for which the energy expression in Equation 2.19 is minimized by the correct ground state density that would be obtained by solving the Schrödinger equation for the external potential $v(\mathbf{r})$.

$$E = \int v(\mathbf{r})\rho(\mathbf{r})d\mathbf{r} + \mathcal{F}[\rho(\mathbf{r})] \quad (2.19)$$

This is remarkable, since it indicates, that in order to find the ground state energy only the density $\rho(\mathbf{r})$ needs to be considered, which would save us many of the troubles associated with handling the very high dimensional wave function. Unfortunately, the theorem only proves the existence of such a functional, but it does not tell us anything about how such a functional would look like. Nevertheless, many functionals have been proposed that have been very successful in predicting various properties of many-body quantum-mechanical systems, making DFT one of the most widely used tools in material sciences and chemistry [35]. Despite its extraordinary success, one should keep in mind, that DFT only addresses the electronic ground state, but is not designed for describing electronic excitations and non-equilibrium properties. It is therefore rather accurate in describing some properties, such as equilibrium geometries, phonon spectra, binding energies or band structures of metals and semiconductors, while it fails to reliably predict electronic band gaps of semiconductors and insulators or bonding in systems, where dispersion interactions are of importance [36].

By comparing Equation 2.19 with the Hamiltonian given in Equation 2.4, we can rewrite the functional $\mathcal{F}[\rho(\mathbf{r})]$ as follows.

$$E = \int v(\mathbf{r})\rho(\mathbf{r})d\mathbf{r} + \mathcal{F}[\rho(\mathbf{r})] = \int v(\mathbf{r})\rho(\mathbf{r})d\mathbf{r} + \langle \Psi[\rho(\mathbf{r})] | \mathcal{T}_e + \mathcal{V}_{ee} | \Psi[\rho(\mathbf{r})] \rangle \quad (2.20)$$

Here the electron-nuclei interaction \mathcal{V}_{Ne} only depends on the electron density and is therefore included in $v(\mathbf{r})$. The kinetic and Coulomb terms of the electrons, however, only depend implicitly on the density $\rho(\mathbf{r})$. Therefore, Kohn and Sham proposed to expand the electron density using independent electrons ϕ_i .

$$\rho(\mathbf{r}) = \sum_i^N |\phi_i(\mathbf{r})|^2 \quad (2.21)$$

The Kohn-Sham wave function is then a single Slater determinant, like in HF theory. The total energy can then be expressed by the kinetic and Coulomb energy of the

2 Theoretical Background

electrons plus an extra term, called the exchange-correlation energy, $E_{\text{xc}}[\rho]$ accounting for the difference [37].

$$\begin{aligned} E &= \int v(\mathbf{r})\rho(\mathbf{r})d\mathbf{r} + \mathcal{F}[\rho(\mathbf{r})] \\ &= \int v(\mathbf{r})\rho(\mathbf{r})d\mathbf{r} + \sum_i^N \int \phi_i^*(\mathbf{r}) \frac{-\nabla^2}{2} \phi_i(\mathbf{r})d\mathbf{r} + \frac{1}{2} \iint \frac{\rho(\mathbf{r})\rho(\mathbf{r}')}{|\mathbf{r} - \mathbf{r}'|} d\mathbf{r}d\mathbf{r}' + E_{\text{xc}}[n] \end{aligned} \quad (2.22)$$

A Hamiltonian can then be constructed by defining an exchange-correlation potential $V_{\text{xc}}[\rho](\mathbf{r})$, which is the functional derivative of $E_{\text{xc}}[\rho]$ with respect to the density ρ . The electronic orbitals are then the minimum energy solution to the following expression, with an additional orthonormality constraint.

$$\left(\frac{-\nabla^2}{2} + v(\mathbf{r}) + \int \frac{\rho(\mathbf{r}')}{|\mathbf{r} - \mathbf{r}'|} d\mathbf{r}' + V_{\text{xc}}[\rho](\mathbf{r}) \right) \phi_i(\mathbf{r}) = \epsilon_i \phi_i(\mathbf{r}) \quad (2.23)$$

Due to the dependence of the left side of the above equation on the charge density ρ itself, a self-consistent approach must be used, similarly to the HF method.

The accuracy of DFT crucially depends on the quality of the exchange-correlation functional that groups together all the many body interactions that account for the exchange, correlation, self-interaction and the kinetic energy correction. Finding such a functional is a formidable task and many forms have been proposed, while research is still ongoing.

One of the simplest form of the exchange-correlation functional is the local density approximation (LDA), which, as the name implies, only depends on the local electronic density.

$$E_{\text{xc}}^{\text{LDA}} = \int \varepsilon_{\text{xc}}^{\text{LDA}}(\rho(\mathbf{r}))\rho(\mathbf{r})d\mathbf{r} \quad (2.24)$$

The most successful LDA functionals are based on the homogeneous electron gas (HEG) model, for which the exchange energy is known analytically. This expression is then applied to the local density at each point.

$$\varepsilon_{\text{x}}^{\text{LDA}}[\rho] = -\frac{3}{4} \left(\frac{3}{\pi} \right)^{1/3} \int \rho(\mathbf{r})^{4/3} d\mathbf{r} \quad (2.25)$$

Analytic expression for the correlation energy of the HEG are only known for the limits of infinitely high and low densities but intermediate values have been computed using the quantum Monte Carlo method [38].

While LDA functionals can provide fairly accurate geometries, they tend to overestimate binding energies. But given that LDA functionals reproduce the exact results for homogeneous densities, they form the basis for many other functionals.

In systems with a rapidly varying density, such as atomic systems and molecules, a better approximation of the exchange-correlation energy can be achieved by also including a dependence on the derivative of the density $\nabla\rho(\mathbf{r})$.

$$E_{\text{xc}}^{\text{GGA}} = \int \varepsilon_{\text{xc}}^{\text{GGA}}(\rho(\mathbf{r}), \nabla\rho(\mathbf{r}))\rho(\mathbf{r})d\mathbf{r} \quad (2.26)$$

These functionals are known as generalized gradient approximations (GGAs). One of the most popular GGAs is the functional proposed by Perdew Burke and Ernzerhof (PBE) [39]. While some GGA functionals are parameterized using experimental data, PBE is derived without empirical data and therefore applicable to a wide range of systems.

Functionals that also include the single particle kinetic energy density $\tau^s(\mathbf{r})$ are known as meta-GGAs.

$$E_{\text{xc}}^{\text{meta-GGA}} = \int \varepsilon_{\text{xc}}^{\text{meta-GGA}}(\rho(\mathbf{r}), \nabla\rho(\mathbf{r}), \tau^s(\mathbf{r}))\rho(\mathbf{r})d\mathbf{r} \quad (2.27)$$

The strongly constrained and appropriately normed (SCAN) functional [40] is a recently proposed meta-GGA, that obeys all 17 known exact constraints, that a meta-GGA can. It was shown to be remarkably accurate for many test systems.

Functionals that incorporate a fraction of exact exchange from HF theory, are known as hybrid functionals. Examples of such functionals are PBE0 [41], which replaces one quarter of the PBE exchange with exact exchange and B3LYP [42], which is an early meta-GGA that is still widely used in the chemistry community.

DFT calculations usually scale with $\mathcal{O}(n^3)$, with respect to the number of electrons due to the matrix diagonalization involved. Linear scaling methods [43], that take advantage of decay properties of the density matrix and employ sparse matrix linear algebra, have also been implemented [44]. However, since these methods only perform better for fairly large systems, they were not used for this thesis.

2.1.6 ATOMIC CHARGES

We saw in the previous sections, that the charge density ρ is a central property in electronic structure calculations. Due to its long range, the Coulomb potential created by ρ is essential for many reactions and interactions. It is therefore not surprising, that many force fields (see Section 2.2.5) include explicit Coulomb terms in addition to the short-ranged bonding interactions. As we will see in Chapter 4, redistribution of charge is also an important effect that leads to long-ranged interactions. Inside electronic structure codes, ρ is represented by a complicated basis expansion with many terms. This representation, which often differs between electronic structure codes, can be difficult and expensive to work with and simplified representations of ρ may be needed. One possibility is the concept of atomic charges (or higher order multipoles), which discretize the charge density by assigning it to the atoms. The atomic charges can then be used to calculate pairwise Coulomb interactions.

Since no unique decomposition of the continuous charge density into atomic charges exists various methods have been proposed. Mulliken [45] and Löwdin [46] population analysis use the occupation of atomic basis functions to assign electronic charge to atoms. The exact result is therefore dependent on the basis set used. Bader charges [47] do not depend on the basis set but instead partition the space around the atoms using a so-called zero flux surface, where the charge density reaches a minimum perpendicular to the surface. These surfaces can be difficult to compute and often require the representation of the charge density on a three-dimensional grid.

Other methods, such as Hirshfeld [48] and Becke [49] charges are computed with a smooth partitioning based on weighting functions $w_i(\mathbf{r})$.

$$Q_i = Z_i - \int \frac{w_i(\mathbf{r})}{\sum_j^N w_j(\mathbf{r})} \rho(\mathbf{r}) \quad (2.28)$$

In the Hirshfeld scheme, the electron density of a radially symmetric atom in vacuum is chosen for w_i . Alternatively, Gaussian functions of width σ can be used to obtain a smoothed Voronoi partitioning [50]. In the limit, where $\sigma \rightarrow 0$, a true Voronoi partitioning is obtained, that assigns each point in space to the nearest atom.

Methods that assign atomic charges by splitting up the charge density often fail to reproduce the external electrostatic potential and different partitioning schemes can lead to different numerical values for the charges [51]. Including atomic dipole

moments or higher order multipoles, in addition to atomic monopoles, can help to overcome this problem [52].

Other methods, such as Merz-Kollman charges [53] or CHELPG charges [54] therefore do not use the charge density ρ but fit atomic charges that reproduce other properties, in particular the electrostatic potential. Unfortunately these fitting procedures are often ill-conditioned, and numerical instabilities can arise [55]. Furthermore, the atomic charges may not be continuous with respect to the atomic positions, which is particularly important, when the atomic charges are used to train machine learning methods.

Similarly, some machine learning methods, such as the Affordable Charge Assignment (ACA) [51] or PhysNet [56] also determine atomic charges that reproduce molecular dipole moments. However, unlike the above-mentioned methods, the atomic charges are not fit to reproduce the potential of a single system, but instead, an atomic charge predicting machine learning model is fit to obtain the best agreement throughout a whole data set of structures. Similarly, the CENT2 [57] or the kQEq [58] methods use a charge equilibration scheme based on machine learned electronegativities to predict charges that reproduce a screened electrostatic potential or molecular dipole moments respectively. The large datasets used and the inductive bias introduced by the underlying machine learning models alleviate the conditioning problems encountered by methods that are applied to single structures. This may result in a larger error in the fitted quantities on a per-structure basis, but since atomic charges are a rather crude approximation anyway, this is not critical in many cases. Once trained, the models can then also be applied to new structures, without the need for expensive electronic structure calculations.

Overall, it is clear, that the method used to determine the atomic charges should be chosen depending on the intended use of the resulting charges.

2.2 SIMULATION METHODS FOR THE POTENTIAL ENERGY LANDSCAPE

In the last chapter, we saw several methods that can be used to find more or less approximate solutions to the electronic ground states of the Schrödinger equation. Many useful things can be derived from these solutions, such as x-ray diffraction patterns, ionization and band gap energies, and many more. However, in the work presented in this thesis, we mostly focus on the energy and forces acting on the nuclei that are obtained from electronic structure calculations. An exception to this is the electronic density, which we used in Chapter 4 to study long range electrostatic effects.

In Section 2.1.2, we already saw that in the Born-Oppenheimer approximation, the nuclei are treated as point like particles and that the function of the energy $E = E(\{\mathbf{R}_I\})$ for a specific set of atomic positions $\{\mathbf{R}_I\}$ is known as the potential energy surface (PES). The forces acting on each atom are the negative derivatives of the potential energy function with respect to the atomic coordinates.

$$F_{I\alpha} = -\frac{dE(\{\mathbf{R}_I\})}{dR_{I\alpha}} \quad | \quad \alpha = \{x, y, z\} \quad (2.29)$$

Most electronic structure codes allow for the analytical calculation of these derivatives and provide them as output. In addition to the forces, a wealth of information can be extracted from the PES, such as ground state geometries, reaction dynamics, thermodynamic properties, formation energies and many more. However, due to its high dimensionality, the PES of a system containing N_{at} atoms is a function of $3N_{\text{at}}$ coordinates, and it is not uncommon for N_{at} to be in the hundreds of even thousands. This makes the PES a highly complex function and due to the curse of dimensionality its exploration is exceedingly difficult.

To overcome these difficulties, many simulation methods and algorithms have been developed. In the next sections an overview over the most relevant methods will be given.

2.2.1 MOLECULAR DYNAMICS

Since we know the forces acting on all atoms, as well as their masses, we can apply Newtons equation of motion to calculate the time evolution of the system. The trajectories obtained from this process, called molecular dynamics (MD), can reveal insights that can not be directly observed in experiments due to the short time-

2.2 Simulation Methods for the Potential Energy Landscape

and length-scales involved. For instance, reaction pathways can be observed or thermodynamic ensemble averages can be computed.

To obtain the time evolution of the atomic positions, we integrate Newtons equation of motion.

$$m_I \frac{d^2 \mathbf{R}_I}{dt^2} = \mathbf{F}_I \quad (2.30)$$

Here m_I are the atomic masses.

To numerically integrate Newtons equation, we discretize it using a finite time step Δt . The most simple approach to propagate the atomic positions, starting from the initial conditions $\mathbf{R}(t=0)$ and $\mathbf{V}(t=0)$ would be Euler method, where a simple finite difference scheme is used.

$$\mathbf{R}_I(t + \Delta t) = \mathbf{R}_I(t) + \mathbf{V}_I(t)\Delta t \quad (2.31)$$

$$\mathbf{V}_I(t + \Delta t) = \mathbf{V}_I(t) + \mathbf{F}_I(\mathbf{R}_I(t)) \frac{\Delta t}{m_I} \quad (2.32)$$

It turns out however, that this scheme will result in a drift of the total energy, a quantity which should at least in theory be preserved during a MD simulation.

A more stable algorithm is the Verlet algorithm [59]. The increased long term stability is due to the fact that the Verlet algorithm is time reversible, meaning that, when one would apply the algorithm with negative time steps, it would exactly trace back the forward trajectory with positive time steps. Therefore, a time reversible algorithm cannot introduce systemic energy drifts. Short term fluctuations will still be observed, but they tend to oscillate around a mean value in the long term. The velocity Verlet algorithm propagates the positions as follows.

$$\mathbf{R}_I(t + \Delta t) = \mathbf{R}_I(t) + \mathbf{V}_I(t)\Delta t + \mathbf{F}_I(\mathbf{R}_I(t)) \frac{\Delta t^2}{2m_I} \quad (2.33)$$

$$\mathbf{V}_I(t + \Delta t) = \mathbf{V}_I(t) + (\mathbf{F}_I(\mathbf{R}_I(t + \Delta t)) + \mathbf{F}_I(\mathbf{R}_I(t))) \frac{\Delta t}{2m_I} \quad (2.34)$$

Since the total energy is conserved during MD simulations, it can be used to sample the microcanonical ensemble of a system. If one is interested in the canonical ensemble, where atomic configurations are visited according to their Boltzmann probability at a given temperature, additional modifications to the MD algorithm, so-called thermostats, have to be used. Popular methods include the Nosé-Hoover [60, 61], Langevin [62] and Andersen [63] thermostats.

2.2.2 MONTE CARLO SIMULATIONS

As we just saw, MD simulations can be used to sample the canonical ensemble of a system. This allows us to evaluate thermodynamic integrals, such as expectation values of a quantity X over the Boltzmann distribution, which can be written as

$$\langle X \rangle_T = \frac{1}{Z(T)} \int \exp\left(\frac{-E(\mathbf{R})}{k_B T}\right) X(\mathbf{R}) d\mathbf{R} \quad . \quad (2.35)$$

Here k_B is the Boltzmann constant, T the temperature and $Z(T)$ the partition function, which normalizes the Boltzmann distribution.

$$Z(T) = \int \exp\left(\frac{-E(\mathbf{R})}{k_B T}\right) d\mathbf{R} \quad (2.36)$$

Alternatively to MD simulations with a thermostat, Monte Carlo (MC) simulations can also be used. MC methods, referring to the famous Monte Carlo casino in Monaco, are computational methods which are based on random numbers. Due to the inherent randomness, these methods are not deterministic and give only approximate results with an error that depends on the number of iterations¹. In the context of atomistic simulations, the term usually refers to methods based on the Metropolis–Hastings algorithm [2, 64].

The MC method and in particular the Metropolis–Hastings algorithm have many applications and are not limited to the Boltzmann distribution in particular but are a very general method to numerically solve high dimensional integrals. The naive approach to numerical integration would be to divide the function into many small segments and then approximate the area under the curve as the sum of the area of small rectangles that fit under it.

$$\int_a^b f(x) dx \approx \sum_{i=0}^N f(a + i(b-a)/N) (b-a)/N \quad (2.37)$$

If the function $f(x)$ depends on more than one variable, a nested summation has to be used, such that the function is evaluated on a high dimensional grid over all variables. If our function depends on many variables however, such as the PES

¹ Even though, MD simulations should in principle be deterministic, this is in practice often not the case. MD trajectories are highly chaotic, meaning that a tiny change in the initial conditions can lead to a huge difference in the trajectory after only a small number of time steps. Although the algorithms used to compute the trajectory are often deterministic, numerical noise is often introduced, for example, when the order of operations is not deterministic during parallelization.

does, this approach becomes infeasible, since the number of grid points will increase exponentially with the number of variables. For instance, if we would consider a system with 5 atoms and would use $N = 10$, we would already end up with 10^{15} evaluations of the PES. Additionally, at most of these grid points, we would probably end up with completely unphysical structures, where atoms are very close together, resulting in a high energy and accordingly low Boltzmann probability. These configurations would therefore not even contribute significantly to the integral we are calculating.

This can be avoided using importance sampling. If we have a way of generating configurations \mathbf{R}_i that are already distributed according to the Boltzmann distribution, the integral in Equation 2.35 can be approximated as follows.

$$\langle X \rangle_T \approx \frac{1}{N} \sum_{i=1}^N X(\mathbf{R}_i) \quad (2.38)$$

Such configurations can be generated using the Metropolis–Hastings algorithm [2, 64], which performs a random walk over configuration space using a Markov chain. To sample a distribution $P(\mathbf{R})$, the algorithm is initialized with a starting configuration \mathbf{R}_0 . Then, a new configuration is proposed, according to a proposal distribution $g(\mathbf{R}'|\mathbf{R}_i)$. Here $g(\mathbf{R}'|\mathbf{R}_i)$ denotes the probability of proposing the new configuration \mathbf{R}' give the current configuration \mathbf{R}_i . The new configuration is then accepted with the following probability.

$$\alpha = \min\left(1, \frac{P(\mathbf{R}')g(\mathbf{R}_i|\mathbf{R}')}{P(\mathbf{R}_i)g(\mathbf{R}'|\mathbf{R}_i)}\right) \quad (2.39)$$

For this a uniformly distributed random uniform number u between zero and one is generated using a random number generator ² and compared to α . If $u < \alpha$, the new configuration is accepted ($\mathbf{R}_{i+1} = \mathbf{R}'$), it is added to the list of configurations and the process is repeated. Otherwise, the previous configuration is accounted for again ($\mathbf{R}_{i+1} = \mathbf{R}_i$).

The initial configuration \mathbf{R}_0 has to be provided by the user. To prevent any biasing due to the initialization of the algorithm, an equilibration phase can be used, where the algorithm runs for a certain amount of iterations without collecting samples. The

² Since computers are deterministic machines, obtaining true random numbers is only possible by using special hardware. While such hardware is generally present in most computers, it is mostly used for cryptographic purposes due to its slow speed. For MC simulations, pseudo-random number generators are used, to produce a deterministic series of numbers that approximates a true random sequence and fulfill the statistic requirements.

second ingredient that has to be provided by the user is the proposal distribution $g(\mathbf{R}'|\mathbf{R}_i)$. Here $g(\mathbf{R}'|\mathbf{R}_i)$ indicates the probability of proposing configuration \mathbf{R}' given the current configuration \mathbf{R}_i . Usually, small local displacements of all or one atom are used to propose a new configuration but in Chapter 6, we will see that also global moves can be constructed. In cases, where the proposal distribution is symmetric, i.e. $g(\mathbf{R}'|\mathbf{R}_i) = g(\mathbf{R}_i|\mathbf{R}')$, its contribution cancels out of the acceptance probability. The magnitude of the random displacements has to be chosen carefully. If the displacements are too large, the proposed configurations will be high in energy and the acceptance rate low. Too small displacements result in a high acceptance rate but also a higher correlation between subsequent samples and hence a larger number of iterations is needed until the simulation converges. The magnitude of the displacement should hence be chosen such that an acceptance rate of about 23.4% is obtained [65]. Furthermore, it should be noted that since only the fraction of the probabilities $P(\mathbf{R}_i)$ and $P(\mathbf{R}')$ enters the acceptance rate, the distribution P does not have to be normalized. This is especially convenient when the Boltzmann distribution is sampled, since the partition function is usually not known.

2.2.3 HAMILTONIAN MONTE CARLO

Hamiltonian Monte Carlo (HMC) [66–68] is a variation of the Metropolis–Hastings algorithm, where Hamiltonian (molecular) dynamics are used to propose the next configuration. This allows to propose configurations that are less correlated to the previous one compared to what can be achieved with random displacements. The Hamiltonian dynamics can be interpreted as molecular dynamics when a Boltzmann distribution is targeted.

Lets consider the Boltzmann distribution $P(\mathbf{R})$, which we want to sample. It is defined through the potential energy $E_{\text{pot}}(\mathbf{R})$ as follows.

$$P(\mathbf{R}) = \frac{1}{Z} \exp\left(\frac{-E_{\text{pot}}(\mathbf{R})}{k_{\text{B}}T}\right) \quad (2.40)$$

If we add a kinetic term $E_{\text{kin}}(\mathbf{V})$ to the Hamiltonian, we get the following probability distribution.

$$\begin{aligned}
 P(\mathbf{R}, \mathbf{V}) &= \exp\left(\frac{-(E_{\text{pot}}(\mathbf{R}) + E_{\text{kin}}(\mathbf{V}))}{k_{\text{B}}T}\right) \\
 &= \exp\left(\frac{-E_{\text{pot}}(\mathbf{R})}{k_{\text{B}}T}\right) \exp\left(\frac{-E_{\text{kin}}(\mathbf{V})}{k_{\text{B}}T}\right) \\
 &= P_{\text{pot}}(\mathbf{R})P_{\text{kin}}(\mathbf{V})
 \end{aligned} \tag{2.41}$$

Here \mathbf{V} are the atomic velocities. Since the two probabilities $P_{\text{kin}}(\mathbf{V})$ and $P_{\text{pot}}(\mathbf{R})$ are independent, $P_{\text{pot}}(\mathbf{R})$ can be sampled by sampling the joint distribution and simply ignoring the velocity components \mathbf{V} .

To propose a new configuration, we first sample $P_{\text{kin}}(\mathbf{V})$. Since $P_{\text{kin}}(\mathbf{V})$ is a normal distribution, this can be done efficiently with the Box–Müller algorithm [69, 70]. We then perform MD using these initial velocities and take the final configuration obtained after a fixed amount of iterations as our proposed configuration \mathbf{R}' . The MD simulation is completely deterministic and preserves phase space volume. The probability of proposing the configuration \mathbf{R}' is therefore the probability of picking the initial velocities \mathbf{V} and hence equal to $P_{\text{kin}}(\mathbf{V})$. The MD simulation is also reversible, given that a proper integration algorithm, such as the Verlet algorithm from Equation 2.33, is used. The probability of the inverse move, going from \mathbf{R}' to \mathbf{R} is hence the probability of picking the final velocities \mathbf{V}' from $P_{\text{kin}}(\mathbf{V})$. If we plug these probabilities into Equation 2.39, we get the following expression.

$$\begin{aligned}
 \alpha(\mathbf{R}', \mathbf{V}' | \mathbf{R}, \mathbf{V}) &= \min\left(1, \frac{P(\mathbf{R}')g(\mathbf{R}|\mathbf{R}')}{P(\mathbf{R})g(\mathbf{R}'|\mathbf{R})}\right) \\
 &= \min\left(1, \frac{P_{\text{pot}}(\mathbf{R}')P_{\text{kin}}(\mathbf{V}')}{P_{\text{pot}}(\mathbf{R})P_{\text{kin}}(\mathbf{V})}\right) \\
 &= \min\left(1, \frac{P(\mathbf{R}', \mathbf{V}')}{P(\mathbf{R}, \mathbf{V})}\right) \\
 &= 1
 \end{aligned} \tag{2.42}$$

Since the total energy $E_{\text{pot}}(\mathbf{R}) + E_{\text{kin}}(\mathbf{V})$ is conserved during the MD simulation, the probabilities $P(\mathbf{R}', \mathbf{V}')$ and $P(\mathbf{R}, \mathbf{V})$ are equal. In practice the energy is not exactly preserved due to errors in the time integration and the acceptance step should still be performed. This allows for a tradeoff between a larger step size of the time integration algorithm, resulting in less correlated samples, at the cost of a slightly reduced acceptance rate.

2.2.4 STRUCTURE SEARCH

To better understand the PES, it can be helpful to study it in terms of its local minima. By assigning each point on the PES to the local minimum where a local geometry optimization would end up, the PES can be partitioned into so-called catchment basins. Neighboring catchment basins are connected via transition states. Transition states are saddle points on the PES, i.e., structures with zero force but one negative eigenvalue in their Hessian matrix. A geometry optimization after a small perturbation along the two directions of the eigenvector corresponding to the negative eigenvalue will lead to the two minima, that are connected by the saddle point. By systematically exploring the PES and connecting local minima through

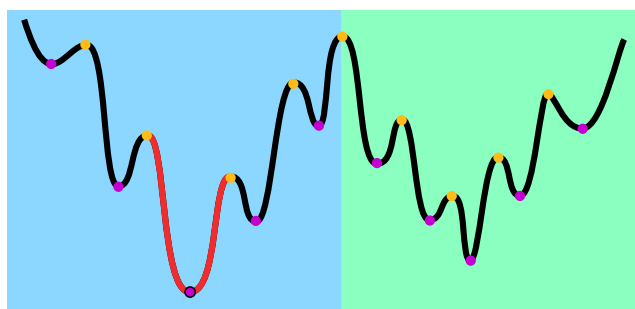


Figure 2.1: Illustration of the potential energy landscape of a two-funnel system. Local minima are marked by pink dots. The global minimum is outlined in black. Saddle points are marked by orange dots. The two funnels are indicated by the light-blue and light-green background color.

transition states, a so called disconnectivity graph can be built, that represents the structure of the PES [71]. These graphs reveal the structure of the PES and allow for a classification into structure seeking, glassy or multi funnel systems [72]. In structure seeking systems, local minima are arranged in a funnel like manner, that allow for a gradual relaxation towards the global minimum through intermediate minima that are energetically close and share a low barrier height³. Such structure seeking systems are characterized by relatively low downhill barriers compared to the uphill barriers [74]. The uphill barriers are the energetic barriers which have to be crossed to go from an energetically lower minimum to a higher lying one. The

³ One of the best examples for structure seeking systems are proteins. Levinthal argued, that even if proteins would visit only a fraction possible minima during their folding process, until the biologically active (free energy) ground state is found, more time than the age of the universe would be required [73]. But since proteins actually fold on very short timescales, this argument is known as Levinthal's paradox. Due to the strong structure seeking behaviour of proteins, only a small number of transition states is actually visited during the folding process.

downhill barriers are the ones encountered when going in the opposite direction. In multi funnel systems, several funnels exist which are separated by high barriers compared to the energetic difference of the lowest minima of each funnel. Such a system can therefore easily find its way to the lowest minimum of one funnel while a transition towards the global ground state might be hindered. In glassy systems, large numbers of local minima with similar energies and comparable up- and downhill barriers are present and the structure of the PES does not form a driving force towards the global minimum.

Since many systems in nature are structure seekers and can be found in their global ground state, finding that structure through simulations is of high interest. This can be done for example through simulated annealing [75], where the physical relaxation process is directly simulated by an MD simulation during which the temperature is gradually reduced.

Due to the limitations in the accessible time scales through MD simulations, the relaxation process that takes place in nature can often not be simulated directly. To overcome this problem, many global optimization algorithms, such as basin hopping [76], evolutionary algorithms [77–79] or metadynamics [15, 80] have been proposed that attempt to find the global minimum efficiently.

A particularly efficient global optimization method is minima hopping [81, 82]. Minima hopping systematically explores the PES by iteratively escaping the current local minimum using a short MD trajectory followed by a local geometry optimization. The MD trajectory is performed until a predefined number of minima along the trajectory have been crossed. When the local geometry optimization falls back to a previously visited local minimum, a new escape step is performed with an increased initial kinetic energy. In case that a new local minimum is found which has not been visited previously, it is either accepted or rejected according to a simple energy thresholding. The threshold is dynamically adjusted during the minima hopping run, such that half of the newly discovered minima are accepted. By automatically adjusting the kinetic energy of the escape trajectories, minima hopping takes advantage of the Bell–Evans–Polanyi principle [83], which states, that highly exothermic reactions have a low activation energy. This principle therefore suggests, that crossing low energy barriers leads to lower lying minima. Later implementations of the minima hopping method also include further improvements, such as a softening, which slightly adjusts the initial velocities of the escape trajectory towards soft vibrational modes [82]. Other variants of the method also introduce a biasing of the PES using fingerprint distances [84] or symmetry [85].

2.2.5 FORCE FIELDS

As we saw in Chapter 2, many *ab-initio* methods exist that allow us to access the PES by solving an approximate model of the underlying Schrödinger equation. We also saw, that these methods require a substantial computational effort, that in most cases scales unfavourably with the number of atoms involved. The application of these methods is therefore limited to moderately sized systems and only few calculations can be afforded. Many applications however, such as MD or MC or structure search simulations require a large number of energy and force calculations to obtain reliable results.

To enable long-time and large-scale simulations, many alternative methods to access the PES have been proposed. Most of these methods can be classified as classical force fields, where some mathematical functional form, in many cases based on physical concepts, is chosen and then parametrized using experimental measurements or *ab-initio* results. Already in their 1953 paper, Metropolis et al. [2] propose the use of a potential based on pairwise interactions, for which the total energy can be calculated by considering all pairs in the system.

$$E = \frac{1}{2} \sum_{i \neq j}^N V(r_{ij}) \quad | \quad r_{ij} = |\mathbf{r}_i - \mathbf{r}_j| \quad (2.43)$$

The computational results in the paper are limited to a hard-sphere model, where the energy of the system is infinite if any two spheres overlap and zero otherwise. One of the most widely used pairwise potentials is presumable the Lennard-Jones (LJ) potential [86, 87]. The potential consists of an attractive term of the form a/r^6 , which models Van der Waals interaction and a repulsive term of the form b/r^m . The exponent m of the repulsive term is often chosen to be 12 because it allows for an efficient computation by simply squaring the attractive term. The LJ potential is therefore well suited to model the interactions of noble gas atoms. The most commonly used form of the LJ potential is hence the 12–6 potential.

$$V_{\text{LJ}}(r) = 4\epsilon \left[\left(\frac{\sigma}{r} \right)^{12} - \left(\frac{\sigma}{r} \right)^6 \right] \quad (2.44)$$

Due to their high computational efficiency, LJ systems have been widely studied. The energy landscape of LJ clusters has been explored in detail [88] and due to their double funnel structure, the 38 [89] and 75 atom clusters are popular test systems for structure search [76, 81, 90] and MC methods [91–94].

2.2 Simulation Methods for the Potential Energy Landscape

In pairwise potentials, such as the LJ potential, the interaction between all pairs of atoms enters the final energy. A naive implementation, where all such pairs are considered results therefore in a computational cost that grows quadratically with the number of atoms in the system. Luckily, the LJ potential as well as many others that model local atomic interactions decay rapidly with increasing distance. The contributions of atom pairs with a distance larger than a predefined cutoff radius can therefore safely be ignored and only contributions from local neighbors have to be considered. For such an implementation, lists of neighboring atoms, also known as Verlet lists [59], are needed. These Verlet lists have to be constructed carefully, since simply comparing all atom pairs to determine neighbors would again result in a quadratic scaling. Instead, methods based on tree like data structures, such as k-D trees or octrees, or methods that bin atoms into a three-dimensional grid need to be used to obtain a scaling of $\mathcal{O}(N_{\text{at}} \log(N_{\text{at}}))$ or $\mathcal{O}(N_{\text{at}})$ respectively.

Unfortunately, Verlet lists cannot be used to compute the electrostatic potential, which is important in many types of systems, with a linear scaling computational cost.

$$V_{\text{elec}}(r) = \frac{q_i q_j}{r} \quad (2.45)$$

Due to the slow $1/r$ decay, the contributions from far away atom cannot be ignored and more sophisticated methods, such as the Barnes-Hut algorithm [95], fast multipole methods [96] or wavelet based methods [97, 98] have to be used to obtain a scaling of $\mathcal{O}(N_{\text{at}} \log(N_{\text{at}}))$ instead of $\mathcal{O}(N_{\text{at}}^2)$. For periodic systems, the problem becomes even more severe, as the sum for the energy does not converge when the number of neighbouring unit cells that are included is increased. This problem is solved by Ewald summation [99], which uses auxiliary Gaussian charges of opposite sign, making the effective potential short ranged. The electrostatic energy of the Gaussian charges can be efficiently calculated in reciprocal space resulting in an overall $\mathcal{O}(N_{\text{at}}^{3/2})$ scaling (see Section 4.2.1). Other methods rely on a similar approach, but use a grid based representation of the auxiliary charge distribution [100], allowing them to take advantage of the FFT to reduce the computational effort to $\mathcal{O}(N_{\text{at}} \log(N_{\text{at}}))$.

In many cases a pairwise potential alone is not sufficient to describe the complexity of the PES. Therefore, other terms, such as angular three-body terms and four body-terms describing dihedral angles have to be added. Nowadays, many implementations of force fields are available [101–106] implementing a plethora of functional forms from which the user can choose.

2 Theoretical Background

Due to the simple functional form, force fields can be evaluated very efficiently and the small number of free parameters allows for the use of few, high quality, *ab-initio* reference data points or even experimental data for fitting. A clever choice of the used functions also ensures reasonable behaviour of the potential in extreme cases, that are not present in the training data. For example, high repulsive forces when very short bond lengths are present. On the other hand, the fixed functional form and small number of free parameters also limits the accuracy that can be obtained. This limitation is tackled by machine learned potentials (MLPs), which have become increasingly popular in recent years. Instead of a predefined set of functions, MLPs use a machine learning engine, that can represent a large function space using many free parameters. Using a large amount of reference data, these methods can then be fit with a very high accuracy, such that in most cases, the accuracy of the method used for generating the training data is the limiting factor. A thorough overview over the history of MLPs and how we solved some limitations of current methods will be given in the next chapter.

3 MACHINE LEARNED POTENTIALS

3.1 INTRODUCTION

We already saw in the last section, how force fields can be used to construct an approximation to the PES, that can be evaluated orders of magnitude faster, than *ab-initio* methods and thus enables simulations of large size- and long time-scales.

Despite their success, classical force fields are inherently limited in the accuracy that they can achieve, since the predefined functional forms of the interaction potentials necessarily neglect some of the complexity present in real PESs. With the recent increase of the available computational resources, the generation of large *ab-initio* reference data sets has become possible. This, together with algorithmic improvements, has lead to the development of machine learned potentials (MLPs). Instead of a manually chosen functional form, with few free parameters, MLPs use machine-learning methods to represent the atomic interactions. These machine learning methods, such as artificial neural networks (ANNs), provide an extremely flexible functional form with many free parameters, that can be fit to a large number of reference data-points. MLPs are not constrained to a predefined set of interaction potentials that can be represented and are therefore able to very accurately reproduce energies and forces from reference data. The fitting error of MLPs is therefore often lower than the error introduced by the level of theory of the electronic structure method used to generate the training data. MLPs trained on data obtained from highly accurate reference methods, such as coupled cluster, have been constructed [110], but due to the high computational cost of these methods, DFT remains the foundation of most current MLPs. This however, does not mean that MLPs are free from any built in assumptions. As we will see later, many of

Parts of this chapter were adapted from T. W. Ko, J. A. Finkler, S. Goedecker, and J. Behler. “A fourth-generation high-dimensional neural network potential with accurate electrostatics including non-local charge transfer”. *Nature communications* 12:398, 2021 (CC BY 4.0 [108]). Parts were also adapted with permission from T. W. Ko, J. A. Finkler, S. Goedecker, and J. Behler. “General-Purpose Machine Learning Potentials Capturing Nonlocal Charge Transfer”. *Accounts of Chemical Research* 54:4, 2021, pp. 808–817 (Copyright 2021 American Chemical Society).

the currently used MLPs assume, that chemical interactions are local and hence ignore interactions beyond a certain cutoff radius. While this locality assumption allows applications to very large systems, with linearly scaling computational cost, it can be problematic for systems, where long-ranged electrostatic interactions play an important role. This lead to the development of MLPs, that include explicit Coulomb interactions through environment dependent atomic charges. In spite of countless successful applications, in recent years it has been recognized that the accuracy of MLPs relying on local atomic energies and charges is still insufficient for systems with long-ranged dependencies in the electronic structure.

These can, for instance, result from nonlocal charge transfer or ionization and are omnipresent in many important types of systems and chemical processes such as the protonation and deprotonation of organic and biomolecules, redox reactions, and defects and doping in materials. In all of these situations, small local modifications can change the system globally, resulting in different equilibrium structures, charge distributions, and reactivity. These phenomena are very common in chemistry, molecular biology and materials science, and in Figure 3.1 two typical examples from different fields are shown.

Figure 3.1a shows the Hirshfeld charges [48] of the aromatic organic molecule 2-hydroxy-anthracene obtained from DFT. If this molecule is deprotonated, the atomic charges notably change throughout the whole molecule as can be seen for instance for carbon atoms 6 and 7, whose partial charges change strongly, although they are about 8.5 Å away from the deprotonated oxygen atom. Figure 3.1b shows the optimized adsorption geometries of a gold atom on a periodic MgO(001) surface. For the ideal surface the gold atom is adsorbed on top of an oxygen atom and its Hirshfeld charge is very close to zero. If a Mg vacancy is introduced in the bottom layer of the slab outside the local environment, the preferred adsorption site does not change, but the gold atom becomes positively charged. If, on the other hand, an oxygen atom in the bottom layer is replaced by a fluorine atom, the adsorbed Au atom has a very large negative charge and the adsorption site changes to a Mg atom. Such a control of the electronic structure by doping and defects is very important for applications such as heterogeneous catalysis and in semiconductor devices. All these examples have in common that modifications in one part of the system strongly change the properties in other parts, with separations between these interacting parts being larger than typical radii of local atomic environments considered in previous generations of MLPs, which are thus unable to describe these effects. Consequently, the inclusion of nonlocal phenomena has been identified as a next key step in the

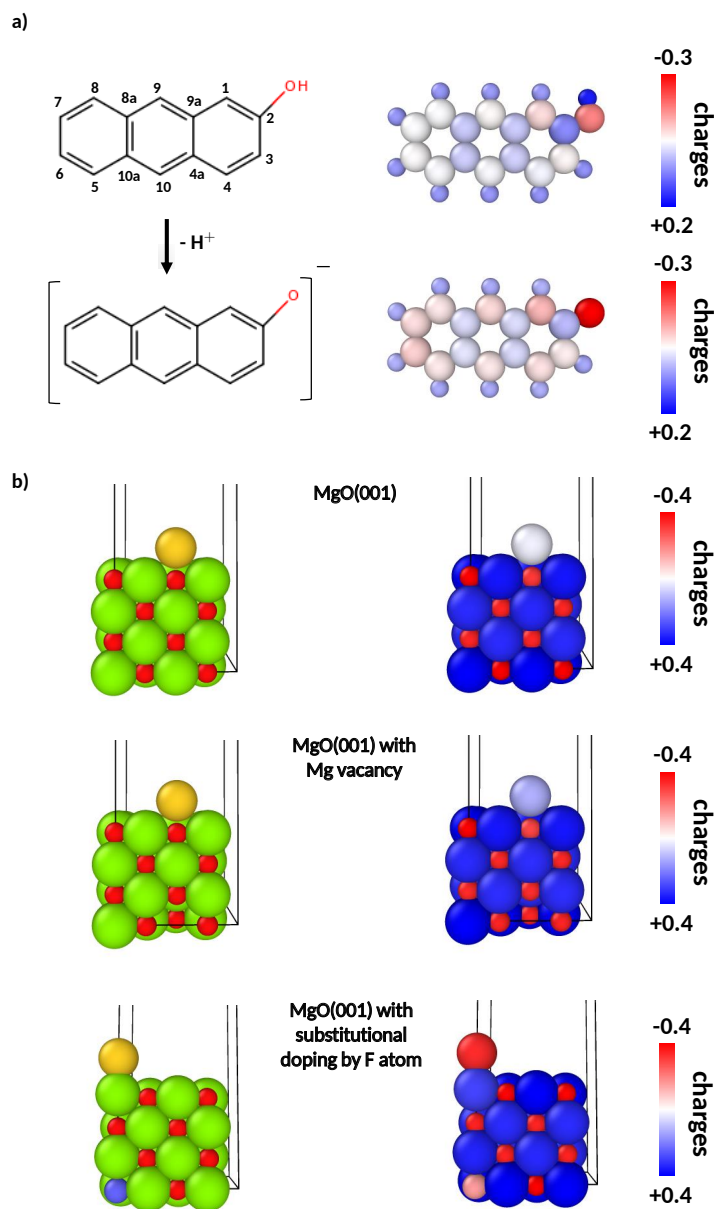


Figure 3.1: Examples for systems exhibiting long-range charge transfer. The structures and the corresponding atomic charges are displayed on the left and right hand side, respectively. Panel (a) shows the organic molecule 2-hydroxy-anthracene together with its deprotonated form. Panel (b) shows a gold atom adsorbed on the ideal MgO(001) surface, on a surface with a Mg vacancy, and on a surface with substitutional doping by a fluorine atom. Oxygen, fluorine, magnesium and gold atom are coloured in red, blue, green, and yellow, respectively. (Figure reproduced with permission from Reference [109].)

development of future MLPs and lead us to the development of the fourth generation high-dimensional neural network potential (4G-HDNNP) presented Chapter 4.

Before we can dive into the methodical details of the 4G-HDNNP, we first need to lay out some basics. This will be done in the following sections. In the next section, we will first see, how ANNs are constructed. These form the basis for many MLPs including the 4G-HDNNP. The last sections of this chapter will then outline the historical development of MLPs and the challenges that were overcome by each generation of methods.

3.1.1 ARTIFICIAL NEURAL NETWORKS

As we will see in more detail later, most modern MLPs consist of two major components. First, atomic environments are encoded using atomic environment descriptors (AEDs), that preserve important symmetries. Then a machine learning engine is used to learn the functional relationship between the environment descriptors and the energy of the system. Machine learning engines are highly parametrized general functions whose parameters are determined during the training process. Many types of MLPs have been proposed to date, like neural network potentials [8, 9, 56, 111, 112], Gaussian approximation potentials (GAPs) [113], moment tensor potentials (MTPs) [114], spectral neighbor analysis potentials (SNAPs) [115], and many others [116, 117]. Although the machine learning algorithms and the functional form of these methods are different, the basic components and challenges, such as the atomic environment description and long range interactions, remain the same. For simplicity and because the methods developed in this thesis are based on ANNs, MLPs based on ANNs will be the main focus of this thesis.

ANNs (also known as multi layer perceptrons in the machine learning community) are loosely inspired by the network formed by neurons in the brain. They consist of an input layer, several hidden layers and an output layer. Each layer contains a certain amount of nodes, that are connected to the next and the previous layers. An illustration of an ANN is shown in Figure 3.2. The shown ANN consists of three input nodes, two, fully-connected, hidden layers with four nodes each, and an output layer with a single node. The connections between the nodes are shown as black lines. Each such connection is parametrized with a weight and each node with a bias. To evaluate the ANN, input values are fed into the input nodes. The values are then propagated through the connections to each node in the first hidden layer. During the propagation, the values are multiplied with the weight of the respective connection and then summed together in the node where the bias is also added.

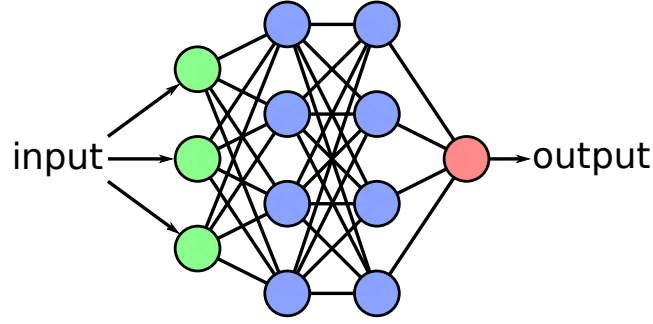


Figure 3.2: Visualization of an artificial neural network. The input nodes are shown in green, the hidden nodes in blue and the output node in red.

Before the values are propagated to the next layer, an activation function is applied. This function is important, as it introduces non-linearity into the ANN. In our cases we used the hyperbolic tangent function, however many other functions, such as the rectified linear unit (relu), sigmoid or Gaussian function are often used. In the output layer, a linear function is often used, to prevent the output from being limited to a finite range as it would be the case with the hyperbolic-tangent.

The value of each node is hence computed as

$$v_i^n = f \left(\sum_j w_{ij}^n v_j^{n-1} + b_i^n \right) . \quad (3.1)$$

Here v_i^n is the i th node in the n th layer, the w_{ij}^n are the weights, b_i^n the bias and f the activation function. The application of each layer can be conveniently written as a matrix vector multiplication, allowing for a highly efficient evaluation of the ANN on graphics processing units (GPUs). Nowadays, many other types of ANN layers, such as convolutional layers [118], pooling layers or attention based mechanisms [119] are used.

To train an ANN, its weights and biases are adjusted, such that the error between the function $f_{\text{ANN}}(x)$ represented by the ANN and the target function $y(x)$ is minimized. This error, that has to be minimized is quantified using a so-called loss function L . The total loss \mathcal{L} can then be computed as an integral over all possible inputs x .

$$\mathcal{L} = \int L(f_{\text{ANN}}(x) - y(x)) dx \quad (3.2)$$

Since this integral cannot be evaluated analytically, we have to approximate it using a set of discrete points x_i , the so-called training dataset. If we use the mean squared

error as our loss function, we get the following expression for the total training loss $\mathcal{L}_{\text{train}}$.

$$\mathcal{L}_{\text{train}} = \frac{\sum_i^N (f_{\text{ANN}}(x_i) - y(x_i))^2}{N} \quad (3.3)$$

We can now use any local optimization algorithm to minimize the training loss. For this, we need the partial derivatives of the loss with respect to the weights and biases of the ANN. These can be efficiently calculated using the backpropagation algorithm which takes advantage of the chain rule. During the forward pass (prediction) through the ANN, the values of each node are stored. To obtain the gradients, a backward pass through the ANN is performed during which the chain rule is applied to obtain the gradients with respect to the inputs as well as the weights and biases. Note, that in the case of MLPs the derivatives (forces) might also be included in the loss function. This slightly complicates the calculation of the derivatives with respect to the weights and biases. Fortunately, many modern machine learning libraries, such as TensorFlow [120] and PyTorch [121] automatically keep track of the calculations performed during the prediction of the ANN to enable automatic differentiation, without the need for any manual implementation.

In many cases, it would be too expensive, to calculate the loss \mathcal{L} over the whole training data set for each update of the ANN parameters. Therefore, optimizers, such as stochastic gradient descent or Adam [122] can be used, that rely on an approximation of the loss gradient computed from only a few samples of the training set in each iteration. Therefore, the loss during each step of the training is computed for a single sample or a batch of a few samples only. The resulting gradients do not point in the exact same direction as if the whole dataset was used, but if many updates are performed, these errors cancel out. It has been shown, that the use of an approximate loss gradient computed using only few samples from the dataset actually improves the generalization capability of ANNs [123]. This is because the additional noise drives the optimizer away from sharp minima in the loss landscape, with a high curvature and towards flat minima, which are hypothesized to provide better generalization performance [124]. For training the ANNs presented in this thesis, we used the extended Kalman filter method [125]. This method converges very rapidly and only few epochs are often required to obtain a good fit. However, the Kalman filter uses a covariance matrix of size $n \times n$, with n being the number of parameters that are to be optimized. The method therefore scales quadratically in the required memory and computation cost, which makes it only suitable for the comparably small ANNs used in MLPs.

In many cases, the number of free parameters in the ANN is larger than the number of data-points used for training. The optimization problem of minimizing the loss is therefore ill-defined, since many possible functions exist, that go through all training data-points. It is therefore important, that some data-points are excluded from the training set and used as a test set. After each epoch of training, the loss function is evaluated on the test set and the training should be stopped, once the test error starts to increase, to prevent overfitting. If the training data is noisy, this is particularly important. In that case a function that perfectly minimizes the training loss is not desirable, as it would fit to the specific noise present in the training data instead of finding the underlying function from which the training data was generated. It might hence be of advantage to impose a smoothness constraint on the learnt function. This is known as regularization. The simplest form of regularization is to choose an ANN size small enough, to prevent overwriting. If this is not sufficient, a regularization term can be added to the loss function in the form of $\alpha \sum_i p_i^2$, with α being a small number and the p_i the parameters that are optimized (for example the weights w_{ij}^n and biases b_i^n of Equation 3.1). The effect of such a regularization is illustrated in Figure 3.3.

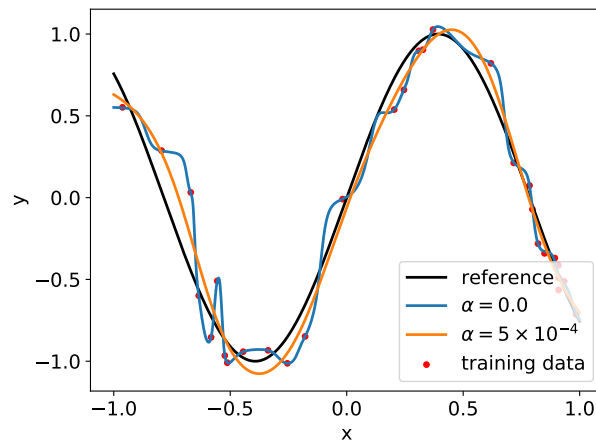


Figure 3.3: ANN fit to a part of the sine function. Random Gaussian noise was added to the training datapoints shown in red. Without regularization, the ANN overfits and fails to recreate the underlying function. A small regularization term in the loss function improves the quality of the fit.

Nowadays, many other methods to prevent overfitting exist. These include a learning-rate decay, that is adapted based on the test error of each epoch, batch normalization [126], group normalization [127], or dropout layers [128]. It should

also be noted, that the variance-bias tradeoff, that is considered in general regression tasks, does not directly apply to machine learning [129]. In short, the variance-bias tradeoff characterizes the general problem faced by many interpolation methods. When a small number of free parameters is used, the accuracy of the interpolation is necessarily limited by the small function space available, which introduces a bias towards the functions that can be represented and therefore results in underfitting. On the other hand, if the function is chosen too flexible, one can fit the training data perfectly but risks overfitting to noise in the dataset, which reduces the generalization capability. Therefore, a tradeoff has to be made between over and underfitting the training data. One would expect, that huge models with billions of free parameters, that are used nowadays, are extremely prone to overfitting. However, it turns out that the generalization performance increases when far more parameters than training samples are used [129]. It has been hypothesized, that this is due to implicit regularization applied through the use of gradient descent optimizers, that favour solutions close to the initial values of the parameters [130]. The large function space available during training allows the ANN to find more optimal solutions which extract relevant features from the input and therefore improve generalization.

3.2 PREVIOUS GENERATIONS OF MACHINE LEARNED POTENTIALS

In this section, the historical and current development of MLPs will be outlined. The key challenges that were overcome during this development lend themselves naturally to classify MLPs into four generations [107, 109, 131, 132].

3.2.1 FIRST GENERATION MACHINE LEARNED POTENTIALS

Starting with the work of Blank et al. [8] in 1995, MLPs of the first generation have been introduced. These first generation MLPs make use of ANNs and have in common that they are applicable to low-dimensional systems, by explicitly depending only on the degrees of freedom of a few atoms. For example, in their original work, Blank et al. [8] directly used the coordinates and the rotation angle of a carbon monoxide molecule as the input to an ANN. While ground-breaking contributions were made in the early years MLPs remained a niche methodology for about a decade because of the restrictions on the size of the systems. For applications to larger systems, retraining of the model is unavoidable and with the increasing number of

input parameters, the maximum system-size is limited by the size of the ANN that can be trained. First generation MLPs also do not preserve important symmetries, such as invariance of the energy under rotation, translation or the permutation of equivalent atoms.

3.2.2 SECOND GENERATION MACHINE LEARNED POTENTIALS

These problems were solved by Behler and Parrinello [9] in 2007 with the introduction of their high dimensional neural network potential (HDNNP). The key concept of the HDNNP is, that instead of using a single ANN to express the energy of the system, the total energy is expressed as a sum of atomic energies. Each atomic energy is predicted by an ANN with weights that are element specific. As input to the ANNs, atomic environment descriptors (AEDs), called atom centered symmetry functions (ACSFs) are used that express the local environment of each atom, inside a certain cutoff radius, as a vector that is invariant under the symmetry operations mentioned above. The atomic energies are hence assumed to depend on the local environment only and interactions beyond the cutoff radius of the environment descriptors are neglected. The total energy is therefore expressed as follows.

$$E = \sum_i^N E_{El(i)}(\{G_i^\mu\}) \quad (3.4)$$

With $E_{El(i)}$ being the ANN for the element $El(i)$ of atom i and $\{G_i^\mu\}$ being the set of ACSFs computed for the atom. The schematic structure of the HDNNP is illustrated in Figure 3.4.

Several types of ACSFs were proposed, the naming of which can be a bit confusing, since different numbers were chosen to differentiate them in Reference [9], Reference [10] and the input files for the software package RuNNer, in which the HDNNP was first implemented. In this thesis all ACSFs will therefore be identified with the indices used in Reference [10]. The proposed ACSFs include radial functions, which are constructed as sum of two body terms and angular functions, which are sums of three body terms. The three radial ACSFs are given as follows.

$$G_i^1 = \sum_j f_c(R_{ij}) \quad (3.5)$$

$$G_i^2 = \sum_j e^{-\eta(R_{ij}-R_s)^2} \cdot f_c(R_{ij}) \quad (3.6)$$

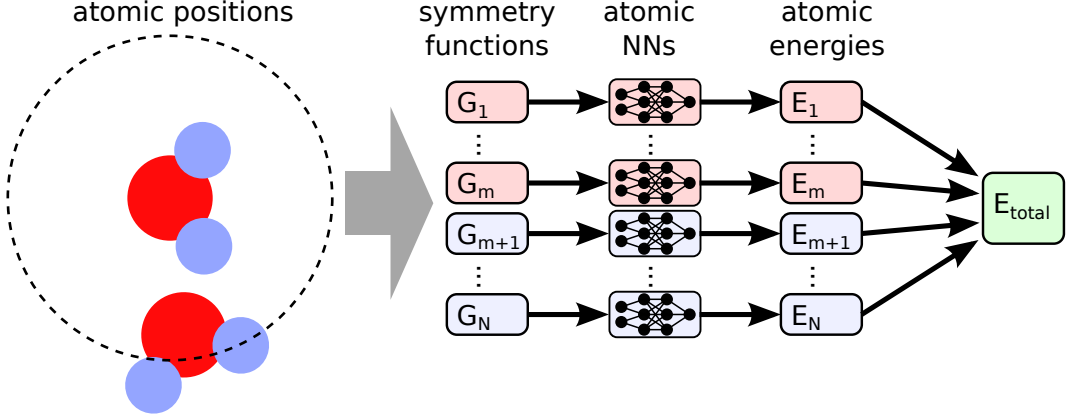


Figure 3.4: Schematic structure of a second generation high-dimensional neural network potential (2G-HDNNP). The ACSFs are computed from the atomic environment of each atom. One atoms environment is indicated by a dashed circle. The atomic neural networks are element specific as indicated by the different colours.

$$G_i^3 = \sum_j \cos(\kappa R_{ij}) \cdot f_c(R_{ij}) \quad (3.7)$$

The two angular ACSFs are the following.

$$G_i^4 = 2^{1-\zeta} \sum_{j,k \neq i} (1 + \lambda \cos \theta_{ijk})^\zeta \cdot e^{-\eta(R_{ij}^2 + R_{ik}^2 + R_{jk}^2)} \cdot f_c(R_{ij}) \cdot f_c(R_{ik}) \cdot f_c(R_{jk}) \quad (3.8)$$

$$G_i^5 = 2^{1-\zeta} \sum_{j,k \neq i} (1 + \lambda \cos \theta_{ijk})^\zeta \cdot e^{-\eta(R_{ij}^2 + R_{ik}^2)} \cdot f_c(R_{ij}) \cdot f_c(R_{ik}) \quad (3.9)$$

In these expressions the sum goes over the indices of all atoms that are inside the environment cutoff R_c . The function f_c is a cutoff function that goes to zero smoothly at R_c to prevent any discontinuities when atoms enter or leave the atomic environment. R_s , η , ζ , κ and λ are parameters that can either be chosen by hand or automatically [133]. A common choice for f_c is the following.

$$f_c(r) = \begin{cases} \tanh(1 - r/R_c)^3 & \text{if } r < R_c \\ 0 & \text{otherwise} \end{cases} \quad (3.10)$$

If multiple elements are present, separate sets of ACSFs are defined which only see atoms of one element in the case of radial ACSFs. The angular ACSFs are defined for each combination of elements, such that the sums of j and k each only include atoms of one element. This leads to a somewhat problematic growth in the number

of ACSFs with an increasing number of elements. HDNNPs have therefore only been applied to systems with a small number of elements.

Since the introduction of the ACSFs, modified versions [112, 134] as well as many alternative AEDs, like the smooth overlap of atomic positions (SOAP) [135] or overlap matrix (OM) fingerprint [136] have been proposed. In message passing neural networks (MPNNs), the AEDs are not specified manually, but instead they are learnt automatically during the training process.

Recent research has shown, that the environment representation of ACSFs and their derivatives is not complete and that certain atomic environments exist, which they cannot differentiate [137, 138]. In that sense the OM fingerprint is superior, since it is able to distinguish these pathological environments (see Chapter 5). However, experience has shown that for training MLPs, this weakness of the ACSFs is not problematic. Even if the environment of one atom is only described ambiguously, the ACSFs of the neighbouring atoms are able to distinguish the problematic structures. It is therefore expected, that no two different structures can result in the exact same ACSF values on all atoms. This allows the machine learning algorithm to compensate when global properties, such as the total energy, are trained. When local quantities, such as atomic charges or electronegativities are learned, the inability of the AEDs to distinguish structures can become problematic, since different values would have to be predicted for structures with the exact same AEDs, forcing the machine learning method to output an averaged value reducing the overall accuracy that can be obtained. Since these problems have only recently been discovered, it is still not clear how large their influence really is. Even if different environments can result in the same AEDs, such structures do not necessarily need to be present in the training data.

No matter what type of AED is used, they all share the same important properties, namely their invariance under rotation, translation and permutation of equivalent atoms. This and the fact that second generation MLPs can be trained on datasets consisting of structures with a small number of atoms but then applied to arbitrarily large systems, has lead to the success of modern MLPs. Because their ability to bridge the gap between the accuracy of first-principle methods and the scalability and speed of classical force fields second generation MLPs are widely used today with many implementations existing [113–115, 139], and many successful applications being reported [140–144].

3.2.3 THIRD GENERATION MACHINE LEARNED POTENTIALS

A major limitation of the second generation models, is the neglect of all interactions beyond the cutoff radius of the AEDs. The rate at which atomic interactions decay and hence the required cutoff radius needed to capture all relevant interactions is highly dependent on the system under study. The error introduced by a certain cutoff radius can be estimated by observing the force acting on a central atom, when atoms outside the cutoff-sphere are displaced [145] or through a locality test based on the Hessian matrix [146]. However, in many systems, long-ranged interactions are present that would require infeasibly large cutoff radii. These are, most importantly, electrostatic interactions, with their particularly slow decay of $1/r$, but also dispersion interactions are neglected. Initial attempts at including electrostatic interactions into MLPs were made by using fixed charges for each element [113, 147]. This approach however is quite limited, since the atomic charge of an atom depends on its oxidization state and therefore its local environment. In classical force field this behaviour is achieved by defining different atom types for the same element based on the direct chemical environment [148]. This approach however has disadvantages. The atomic types must either be selected in advance to the simulation, which is problematic in case reactions are simulated that drastically change the near environment of some atoms, or it must be selected dynamically during the simulation which would lead to discontinuities in the atomic charge, and therefore energies and forces, whenever atomic types change during the simulation. Third generation MLPs therefore directly determine atomic charges based on the local environment of each atom. In the third generation high-dimensional neural network potentials (3G-HDNNPs) the charges are predicted by a second set of neural networks [11, 149]. The structure of a 3G-HDNNP is illustrated in Figure 3.5. The total energy is then expressed as follows.

$$E_{\text{tot}} = E_{\text{short}} + E_{\text{elec}} = \sum_i^N E_{\text{El}(i)}(\{G_i^\mu\}) + E_{\text{elec}}(\mathbf{R}, \{Q_i(\{G_i^\mu\})\}) \quad (3.11)$$

The method is trained by first fitting the charge neural networks to reference charges obtained from DFT calculations. Since from DFT calculations only a charge density is obtained, different partitioning methods, such as the Hirschfeld [48], Becke [49] or other schemes based on smooth Voronoi partitioning [50] can be used to obtain atomic partial charges (see Section 2.1.6). Once the ANNs for the atomic charges are trained, electrostatic energies and forces are predicted for the whole dataset. The

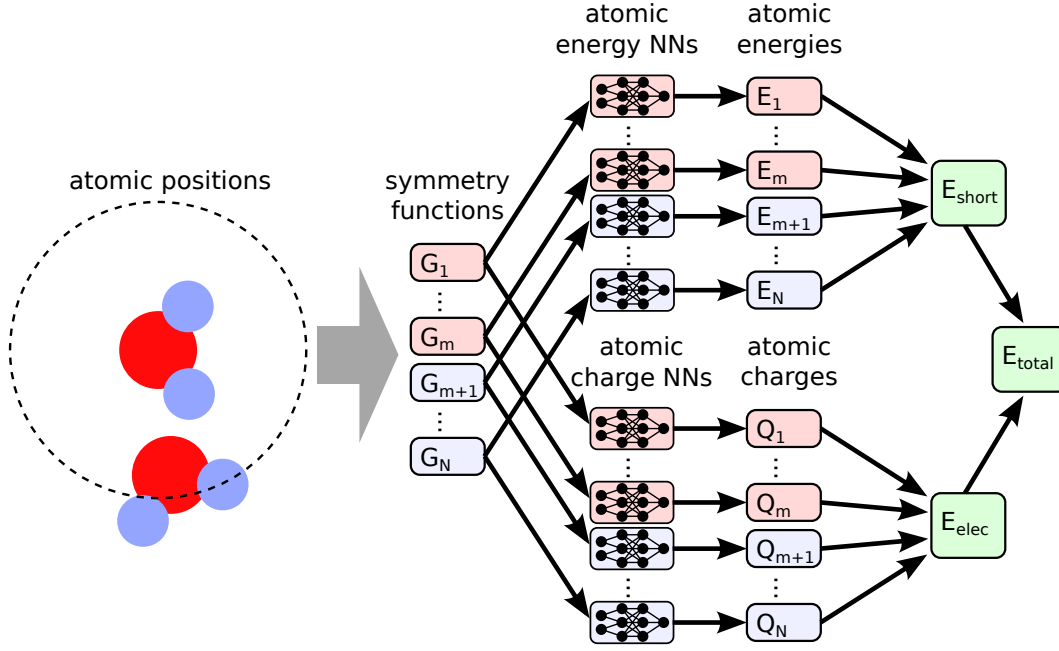


Figure 3.5: Schematic structure of a 3G-HDNNP. Symmetry functions are used to compute atomic energies as well as atomic charges. The charges are then used to compute an electrostatic energy contribution which is added to the sort range energy to obtain the total energy.

short-range neural networks are then trained to the remaining energy and forces obtained by subtracting the electrostatic contribution from the DFT reference.

$$E_{\text{short}} = E_{\text{ref}} - E_{\text{elec}} \quad (3.12)$$

As the atomic charges do now depend on the atomic environment and therefore the atomic coordinates, special care has to be taken, during the calculation of the electrostatic forces to include the partial derivative of the atomic charges with respect to the atomic positions of the neighbouring atoms.

$$F_{i\alpha} = -\frac{dE}{dr_{i\alpha}} = -\frac{\partial E}{\partial r_{i\alpha}} - \sum_j \frac{\partial E}{\partial Q_j} \frac{\partial Q_j}{\partial r_{i\alpha}} \quad | \quad \alpha = x, y \text{ or } z \quad (3.13)$$

For more details about the construction and properties of second- and third-generation HDNNPs, the interested reader is referred to several reviews [150–152]. As a final note, it should be mentioned, that recently it has been shown that long-range electrostatic effects can be also captured by introducing a nonlocal long-distance equivariant

3 *Machine Learned Potentials*

(LODE) representation [153] which is dependent on a Coulomb-type atomic density potential [154].

4 FOURTH GENERATION HIGH-DIMENSIONAL NEURAL NETWORK POTENTIALS

4.1 INTRODUCTION

With their environment dependent charges, third-generation models are able to account for Coulomb interactions beyond the atomic environment cutoff. The atomic charges themselves however, depend on the local environment only and are therefore unable to adjust to far away changes. The methods are therefore not able to account for long-range charge transfer effects or a change in the total system charge. In many systems this can result in a qualitatively incorrect description as illustrated in Figure 4.1. The figure shows an $\text{XC}_7\text{H}_7\text{O}$ molecule, where X represents different functional groups. Protonation and deprotonation reactions, which are common in organic chemistry are shown. On the right side of the figure, the atoms color indicates the Hirshfeld atomic charge of each atom. It can be seen that the charge on the oxygen atom changes significantly, depending on the functional group attached to the left side of the molecule. A cutoff indicating the atomic environment that would be used to calculate an atomic descriptor is indicated with a dashed circle. Since the atomic environment does not include the functional group that is changed, second- and third-generation MLPs are not able to describe the change in atomic charge and the resulting change in reactivity on the right most atom.

This limitation of local atomistic potentials in the description of long-range charge transfer and of systems in different charge states has been recognized already some

Parts of this chapter were adapted from T. W. Ko, J. A. Finkler, S. Goedecker, and J. Behler. "A fourth-generation high-dimensional neural network potential with accurate electrostatics including non-local charge transfer". *Nature communications* 12:398, 2021 (CC BY 4.0 [108]). Parts were also adapted with permission from T. W. Ko, J. A. Finkler, S. Goedecker, and J. Behler. "General-Purpose Machine Learning Potentials Capturing Nonlocal Charge Transfer". *Accounts of Chemical Research* 54:4, 2021, pp. 808–817 (Copyright 2021 American Chemical Society).

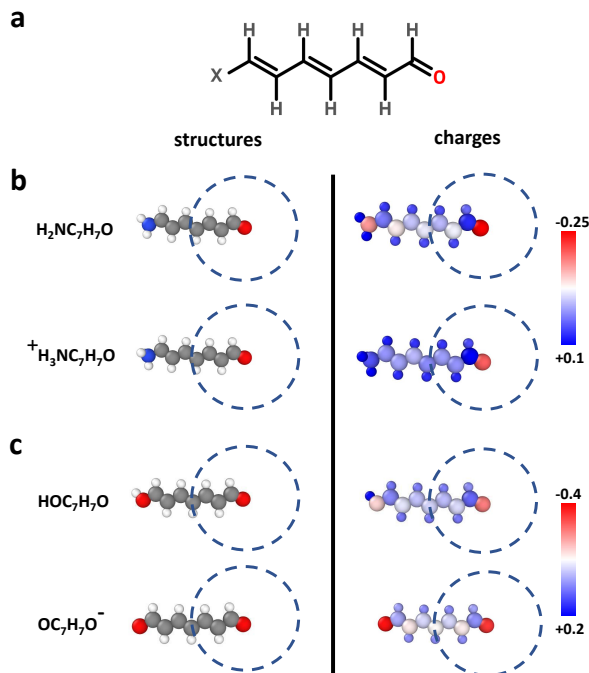


Figure 4.1: Illustration of long-range charge transfer in a molecular system. In **a** the investigated molecule $\text{XC}_7\text{H}_7\text{O}$ with X representing different functional groups is shown. In **b** it can be seen that the protonation of NH_2 group yields a positive ion and results in different charges of the oxygen atom as can be seen in the plot of the DFT atomic partial charges on the right side. In both cases, the local chemical environments of the oxygen atoms are identical within the cutoff spheres shown as dashed circles. In **c** the deprotonation of the OH group yields a negative ion and both oxygen atoms become chemically equivalent with the nearly same negative partial charge. Also in this case the chemical environment of the right oxygen atom is identical to the neutral molecule although the charge distribution differs. All these cases cannot be correctly described by local methods like second or third generation MLPs. (Figure reproduced with permission from Reference [107].)

time ago, and for simple empirical force fields different solutions have been proposed [101, 155–157]. In the context of MLPs the first method that has been proposed to address this problem is the charge equilibration via neural network technique (CENT) [158–160]. In this method, a charge equilibration [155] scheme is applied, which allows for a global redistribution of the charge over the full system to minimize a charge-dependent total energy expression. The charges are based on atomic electronegativities, which are determined as a function of the local chemical environment and expressed by atomic neural networks similar to the charges in third generation MLPs. This method has enabled the inclusion of long-range charge transfer in an MLP framework for the first time, but due to the employed energy

expression this method is primarily applicable to ionic systems [161–163], and the overall accuracy is still lower than in case of other state-of-the-art MLPs. Recently, another promising method has been proposed by Xie, Persson, and Small [164] aiming for a correct description of systems with different charge states. In this method, atomic neural networks are used, which do not only depend on the local structure but also on atomic populations, which are determined in a self-consistent process. The training data for different populations has been generated using constrained DFT calculations, and a first application for Li_nH_n clusters has been reported. Furthermore, an extension of the AIMNet method has been proposed [165], which can be used to predict energies and atomic charges for systems with non-zero total charge. Here, the interaction range between atoms is increased through iterative updates during which information is passed between nearby atoms. Although the resulting charges are not used to calculate explicit Coulomb interactions, many related quantities, such as electronegativities, ionization potentials or condensed Fukui functions can be derived.

We therefore developed a general solution for the limitations of current MLPs by introducing a 4G-HDNNP, which is applicable to long-range charge transfer and multiple charge states. It consists of highly accurate short-range atomic energies similar to those used in 2G-HDNNPs and charges determined from a charge equilibration method relying on electronegativities in the spirit of the CENT approach. Both, the short-range atomic energies and the electronegativities are expressed by atomic neural networks as a function of the chemical environments. The capabilities of the method are illustrated for a series of model systems showcasing typical scenarios in chemistry and materials science that cannot be correctly described by conventional MLPs. For all these systems we demonstrate that 4G-HDNNPs trained to DFT data are able to provide reliable energies, forces and charges in excellent agreement with electronic structure calculations. In the beginning of the following section the methodology of 4G-HDNNPs is introduced and the relation to other generations of HDNNPs and the CENT method is discussed. Subsequently, the results for a series of periodic and non-periodic benchmark systems are presented, including a detailed comparison to the performance of 2G- and 3G-HDNNPs. We show that previous generations of HDNNPs, which are unable to take distant structural changes into account, yield inaccurate energies and forces, and even distinct local minima of the PES can be missed, which are correctly resolved by the 4G-HDNNP. These results are general and equally apply to other types of previous generation MLPs.

4.2 THE 4G-HDNNP MODEL

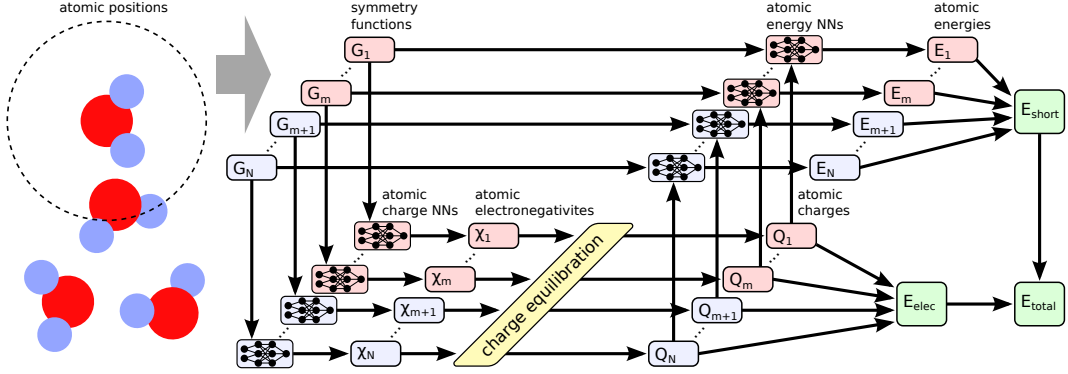


Figure 4.2: Schematic structure of the 4G-HDNNP. Atomic electronegativities are predicted by a second set of neural networks. From these atomic charges are obtained through a global charge equilibration process. In addition to the computation of the electrostatic energy the atomic charges are used as inputs to the short range neural networks.

The overall structure of the 4G-HDNNP is shown schematically in Figure 4.2. Like in 2G-HDNNPs the total energy consists of a short-range part, which, as we will see below, requires in addition non-local information, and an electrostatic long-range part, which is not truncated.

$$E_{\text{total}}(\mathbf{R}, \mathbf{Q}) = E_{\text{elec}}(\mathbf{R}, \mathbf{Q}) + E_{\text{short}}(\mathbf{R}, \mathbf{Q}) \quad (4.1)$$

The electrostatic part $E_{\text{elec}}(\mathbf{R}, \mathbf{Q})$ depends on a set of atomic charges $\mathbf{Q} = \{Q_i\}$, which are trained to reference charges obtained in DFT calculations, and the positions of the atoms $\mathbf{R} = \{\vec{r}_i\}$. An important difference to 3G-HDNNPs is, that these charges are not directly expressed by atomic neural networks as a function of the local atomic environments, but they are obtained indirectly from a charge equilibration scheme based on atomic electronegativities $\{\chi_i\}$ that are adjusted to yield charges in agreement with the DFT reference charges, which we choose to be Hirshfeld charges [48], but many other choices are in principle possible.

Like in the CENT approach the atomic electronegativities are local properties defined as a function of the atomic environments using atomic neural networks. As in 2G- and 3G-HDNNPs there is one type of atomic neural network with a fixed architecture per element in the system, making all atoms of the same type chemically equivalent. While the specific values of the electronegativities depend on the positions of all neighboring atoms inside a cutoff sphere of radius R_c . The

positions of the neighboring atoms inside this sphere are specified by a vector \mathbf{G}_i of atom-centered symmetry functions [10], which ensures the translational, rotational and permutational invariance of the electronegativities.

To predict the atomic charges, which are represented by Gaussian charge densities of width σ_i taken from the covalent radii of the respective elements, a charge equilibration scheme [155] is used. In this scheme, the charge is distributed among the atoms in an optimal way to minimize the energy expression below.

$$E_{\text{Qeq}} = E_{\text{elec}} + \sum_{i=1}^{N_{\text{at}}} (\chi_i Q_i + \frac{1}{2} J_i Q_i^2) \quad (4.2)$$

Here E_{elec} is the electrostatic energy of the Gaussian charges and J_i the element-specific hardness. The J_i do not depend on the chemical environment and are constant for each element. While they are manually chosen in the CENT method, we optimize them during training. They are hence treated as free parameters like the weights and biases of the neural networks. For the electrostatic energy we then obtain the following.

$$E_{\text{elec}} = \sum_{i=1}^{N_{\text{at}}} \sum_{j<i}^{N_{\text{at}}} \frac{\text{erf}\left(\frac{r_{ij}}{\sqrt{2}\gamma_{ij}}\right)}{r_{ij}} Q_i Q_j + \sum_{i=1}^{N_{\text{at}}} \frac{Q_i^2}{2\sigma_i\sqrt{\pi}} \quad (4.3)$$

$$\gamma_{ij} = \sqrt{\sigma_i^2 + \sigma_j^2} \quad (4.4)$$

To solve this minimization problem the derivatives of E_{Qeq} with respect to the charges Q_i are calculated and set to zero.

$$\frac{\partial E_{\text{Qeq}}}{\partial Q_i} = 0, \forall i = 1, \dots, N_{\text{at}} \implies \sum_{j=1}^{N_{\text{at}}} A_{ij} Q_j + \chi_i = 0 \quad (4.5)$$

The elements of the matrix \mathbf{A} are given by the following expression.

$$[A]_{ij} = \begin{cases} J_i + \frac{1}{\sigma_i\sqrt{\pi}}, & \text{if } i = j \\ \frac{\text{erf}\left(\frac{r_{ij}}{\sqrt{2}\gamma_{ij}}\right)}{r_{ij}}, & \text{otherwise} \end{cases} \quad (4.6)$$

Considering the constraint that the sum of all charges must be equal to the total charge Q_{tot} of the system, the following set of linear equations is solved by including this constraint via the Lagrange multiplier λ .

$$\left(\begin{array}{ccc|c} & & & 1 \\ & A & & \vdots \\ & & & 1 \\ \hline 1 & \dots & 1 & 0 \end{array} \right) \begin{pmatrix} Q_1 \\ \vdots \\ Q_{N_{\text{at}}} \\ \lambda \end{pmatrix} = \begin{pmatrix} -\chi_1 \\ \vdots \\ -\chi_{N_{\text{at}}} \\ Q_{\text{tot}} \end{pmatrix} \quad (4.7)$$

Highly optimized algorithms are available for systems of linear equations, which can be efficiently solved for small and medium-sized systems containing up to about ten thousand atoms in a few seconds on modern hardware. For larger systems the cubic scaling of the standard algorithms can pose a bottleneck. In that case one could resort to using iterative solvers for which the most expensive part of each iteration is a matrix vector multiplication involving the matrix \mathbf{A} . This corresponds to the evaluation of the electrostatic potential at each atoms position for which numerous low-complexity algorithms, such as fast multipole [96] or particle-particle-mesh methods [100], are known. In this way it is possible to reduce the effort from cubic to nearly linear scaling, providing access to very large systems. An implementation of such an iterative solver is currently under development in the n2p2 [139] code.

Overall, this process is like in the CENT, but the main difference is in the training process. In CENT only the error with respect to the DFT energies is minimized and the atomic charges obtained during the charge equilibration process serve merely as intermediate quantities, which do not have a strict physical meaning. In the 4G-HDNNP, the charges are trained directly to reproduce reference charges from DFT, which therefore are qualitatively meaningful although one should be aware that atomic partial charges are not physical observables and different partitioning schemes can yield different numerical values [51].

Once the atomic electronegativities have been learned, a functional relation between the atomic structure and the atomic partial charges is available. The intermediate global charge equilibration step ensures that these charges depend on the atomic positions, chemical composition and total charge of the entire system, and thus in contrast to 3G-HDNNPs non-local charge transfer is naturally included.

In a second step, the local atomic energy contributions yielding the short-range energy according to the following equation have to be determined.

$$E_{\text{short}} = \sum_{i=1}^{N_{\text{at}}} E_{\text{El}(i)}(\{G_i^\mu\}, Q_i) \quad (4.8)$$

Like in 2G-HDNNPs the short range atomic energies are provided by individual atomic neural networks based on information about the chemical environments. An important difference to 2G-HDNNPs is that the atomic energies in addition depend on non-local information that is provided to the short-range atomic neural networks by using not only the atom-centered symmetry function values describing the positions of the neighboring atoms inside the cutoff spheres, but also the atomic partial charges determined in the first step (see Figure 4.2). This information is required to take into account changes in the local electronic structure resulting from possible long-range charge transfer, which has an immediate effect on the local many-body interactions.

The short-range atomic neural networks are then trained to express the remaining part of the total energy E_{ref} according to the equation below, where the electrostatic energy E_{elec} is determined based on the partial charges resulting from the fitted atomic electronegativities.

$$E_{\text{short}} = E_{\text{ref}} - E_{\text{elec}} = \sum_{i=1}^{N_{\text{at}}} E_i(\{\mathbf{G}_i\}, Q_i) \quad (4.9)$$

Thus, by construction the goal of the short-range part is to represent all energy contributions that are not covered by the electrostatic energy such that double counting is avoided. In addition to the energies, also the forces are used for determining the parameters of the short range atomic neural networks. We note that since the short range energy depends on the atomic charges, which in turn are functions of all atomic coordinates, the derivatives $\partial E_{\text{short}}/\partial Q_i$ as well as $\partial Q_i/\partial \mathbf{R}$ have to be considered in the computation of the forces.

In summary, in contrast to the CENT method, the short range interactions are not described through the charges resulting from the charge equilibration process but are described by separate short-range neural networks, which enables a more accurate description of the total energy.

4.2.1 MATHEMATICAL DETAILS OF THE 4G-HDNNP IMPLEMENTATION

As only linear and quadratic terms in Q_i appear in E_{elec} and E_{Qeq} , they can be expressed using matrix notation

$$[\mathbf{E}]_{ij} = \begin{cases} \frac{1}{\sigma_i \sqrt{\pi}}, & \text{if } i = j \\ \frac{\text{erf}\left(\frac{r_{ij}}{\sqrt{2}\gamma_{ij}}\right)}{r_{ij}}, & \text{otherwise} \end{cases} \quad (4.10)$$

$$E_{\text{elec}} = \frac{1}{2} \mathbf{Q}^\top \mathbf{E} \mathbf{Q} \quad (4.11)$$

and

$$E_{\text{Qeq}} = \frac{1}{2} \mathbf{Q}^\top \mathbf{A} \mathbf{Q} + \mathbf{Q}^\top \boldsymbol{\chi} \quad , \quad (4.12)$$

with \mathbf{Q} being a column vector containing the atomic charges Q_i , $\boldsymbol{\chi}$ being a column vector of the electronegativities and \mathbf{A} being the matrix described in Equation 4.6. From Equation 4.11, it can be seen, that the vector obtained from the product $\mathbf{E} \mathbf{Q}$ corresponds to the electrostatic potential arising from the charge distribution.

It has to be noted that because the total energy of a continuous charge distribution is always positive, the matrix \mathbf{A} is positive definite, if the $J_i > 0$.

The Q_i are now chosen, such that they minimize the energy E_{Qeq} under the additional constraint of total charge conservation.

$$\sum_{i=1}^{N_{\text{at}}} Q_i = Q_{\text{tot}} \quad (4.13)$$

To solve this minimization problem, we set the derivatives with respect to the charges to zero,

$$\frac{dE_{\text{Qeq}}}{dQ_i} = 0 \quad . \quad (4.14)$$

Including the constraint of total charge conservation using a Lagrange multiplier λ we end up with a system of linear equations as shown in Equation 4.7, which we can rewrite for simplicity as

$$\mathbf{A}' \mathbf{Q}' = \boldsymbol{\chi}' \quad , \quad (4.15)$$

where \mathbf{A}' and \mathbf{Q}' represent the $(N_{\text{at}} + 1 \times N_{\text{at}} + 1)$ matrix and column vector in the left hand side respectively, while $\boldsymbol{\chi}'$ is the column vector on the right hand side. The electronegativities χ_i are predicted by neural networks, for each atom individually, depending on the local chemical environments. The hardness values of J_i are constant

for a given element, and they are also optimized during the training of the neural networks. To ensure their positiveness during optimization, the J_i are represented through intermediate parameters \tilde{J}_i , such that $J_i = \tilde{J}_i^2$.

During training and for the calculation of the forces, several derivatives are needed, the calculation of which will be explained in the text below. The force components F_{r_α} are given by the negative derivative of the energy with respect to the atomic coordinates r_α .

$$F_{r_\alpha} = -\frac{dE_{\text{total}}(\mathbf{R}, \mathbf{Q}(\mathbf{R}))}{dr_\alpha} = -\frac{\partial E_{\text{total}}}{\partial r_\alpha} - \sum_i \frac{\partial E_{\text{total}}}{\partial Q_i} \frac{\partial Q_i}{\partial r_\alpha} \quad (4.16)$$

In this equation, the partial derivative of the atomic charges with respect to the atomic positions appear. As we will see later, the calculation of these derivatives is rather expensive but explicit calculation can be avoided using a neat trick. During training however, the explicit derivatives of the charges with respect to the positions as well as the electronegativities and the hardnesses are used. This is not a problem, since the structures used for training are small compared to what could be expected during the prediction.

CALCULATION OF $\frac{\partial Q_i}{\partial r_\alpha}$

To calculate the $\frac{\partial Q_i}{\partial r_\alpha}$ we take the derivative with respect to the spatial coordinate r_α of the charge equilibration Equation 4.15. Reordering the terms yields

$$A' \frac{\partial \mathbf{Q}'}{\partial r_\alpha} = \frac{-\partial \chi'}{\partial r_\alpha} - \frac{\partial \mathbf{A}'}{\partial r_\alpha} \mathbf{Q}' \quad (4.17)$$

which includes a Lagrange multiplier that ensures $\sum_i \frac{\partial Q_i}{\partial r_\alpha} = 0$. The derivatives $\frac{\partial \mathbf{Q}}{\partial r_\alpha}$ are now obtained by solving the above system of linear equations for $\frac{\partial Q_i}{\partial r_\alpha}$. To obtain all the $3 \times N_{\text{at}}$ required derivatives we will have to solve $3 \times N_{\text{at}}$ linear equation systems of size $N_{\text{at}} + 1$. Using a neat trick, presented in Section 4.2.1, the forces can be determined without direct calculation of the $\frac{\partial \mathbf{Q}}{\partial r_\alpha}$, such that only a single linear equation system needs to be solved. Only during training, the explicit derivatives are used.

CALCULATION OF $\frac{d\mathbf{Q}}{d\chi_i}$ AND $\frac{d\mathbf{Q}}{dJ_i}$

With a similar procedure we can calculate the equation systems for the derivatives with respect to the electronegativity and hardness and obtain the following two equation.

$$A' \frac{d\mathbf{Q}'}{d\chi_i} = -\delta_i \quad (4.18)$$

$$A' \frac{d\mathbf{Q}'}{dJ_i} = -\mathbf{Q}' \quad (4.19)$$

δ_i is a vector filled with zeros except entry i , which is one. As before, a Lagrange multiplier will be necessary, to ensure that the sum of the derivatives adds up to zero. The derivatives $\frac{d\mathbf{Q}}{d\chi_i}$ and $\frac{d\mathbf{Q}}{dJ_i}$ are not needed for the prediction of the 4G-HDNNP energy and forces but are used during training, where a backpropagation through the charge equilibration step is performed to optimize the electronegativity predicting ANNs and hardness values.

EFFICIENT CALCULATION OF THE FORCES

As mentioned before, the calculation of the forces using the explicit values of $\frac{\partial Q_i}{\partial r_\alpha}$ is expensive, since $3 \times N_{\text{at}}$ linear equation systems need to be solved. This can be avoided by exploiting a method [166] that allows the calculation of the forces by solving only one linear equation system instead. The same method can be used for the calculation of the stress tensor, i.e., the derivatives of the energy with respect to the lattice vectors. In that case the partial derivatives $\frac{\partial A'_{ij}}{\partial l_{k\alpha}}$ and $\frac{\partial b_i}{\partial l_{k\alpha}}$ are used in the below equations, with $l_{k\alpha}$ being the α -th component of the k -th lattice vector.

The total energy of the 4G-HDNNP is a function of the atomic coordinates (\mathbf{R}) and the charges (\mathbf{Q}), which also depend on the atomic coordinates,

$$E_{\text{total}} = E_{\text{total}}(\mathbf{R}, \mathbf{Q}(\mathbf{R})) \quad . \quad (4.20)$$

We now define an auxiliary function L with

$$L = E_{\text{total}} + \sum_{i=1}^{N_{\text{at}}+1} \lambda_i \left(\sum_{j=1}^{N_{\text{at}}+1} A'_{ij} Q'_j - \chi'_i \right) \quad . \quad (4.21)$$

Here $\sum_{j=1}^{N_{\text{at}}+1} A'_{ij} Q'_j - \chi'_i$ are the differences of the left hand side minus the right hand sides of Equation 4.15, which were solved to determine the charges Q_i . These terms

are therefore always zero, making L equal to E_{total} . We now choose λ such that the partial derivatives $\frac{\partial L}{\partial Q'_i}$ are zero,

$$\frac{\partial L}{\partial Q'_i} = \frac{\partial E_{\text{total}}}{\partial Q'_i} + \sum_{j=1}^{N_{\text{at}}+1} A'_{ij} \lambda_j = 0 \quad . \quad (4.22)$$

For this we solve the linear equation system

$$\sum_{j=1}^{N_{\text{at}}+1} A'_{ij} \lambda_j = -\frac{\partial E_{\text{total}}}{\partial Q'_i} \quad . \quad (4.23)$$

Note that A' is a symmetric matrix. We now turn to the derivative $\frac{dL}{dr_\alpha}$, which is equal to $\frac{dE_{\text{total}}}{dr_\alpha}$.

$$\begin{aligned} \frac{dE_{\text{total}}}{dr_\alpha} &= \frac{dL}{dr_\alpha} \\ &= \frac{\partial E_{\text{total}}}{\partial r_\alpha} + \sum_{i=1}^{N_{\text{at}}+1} \frac{\partial E_{\text{total}}}{\partial Q'_i} \frac{\partial Q'_i}{\partial r_\alpha} \\ &\quad + \sum_{i=1}^{N_{\text{at}}+1} \lambda_i \left(\sum_{j=1}^{N_{\text{at}}+1} \frac{\partial A'_{ij}}{\partial r_\alpha} Q'_j + \sum_{j=1}^{N_{\text{at}}+1} A'_{ij} \frac{\partial Q'_j}{\partial r_\alpha} - \frac{\partial \chi'_i}{\partial r_\alpha} \right) \end{aligned} \quad (4.24)$$

Rearranging the equation yields the following.

$$\begin{aligned} \frac{dE_{\text{total}}}{dr_\alpha} &= \frac{dL}{dr_\alpha} \\ &= \frac{\partial E_{\text{total}}}{\partial r_\alpha} + \sum_{i=1}^{N_{\text{at}}+1} \left(\frac{\partial E_{\text{total}}}{\partial Q'_i} + \sum_{j=1}^{N_{\text{at}}+1} A'_{ij} \lambda_j \right) \frac{\partial Q'_i}{\partial r_\alpha} \\ &\quad + \sum_{i=1}^{N_{\text{at}}+1} \lambda_i \left(\sum_{j=1}^{N_{\text{at}}+1} \frac{\partial A'_{ij}}{\partial r_\alpha} Q'_j - \frac{\partial \chi'_i}{\partial r_\alpha} \right) \end{aligned} \quad (4.25)$$

The term $\frac{\partial E_{\text{total}}}{\partial Q'_i} + \sum_j A'_{ij} \lambda_j$ is zero by definition of λ according to Equation 4.23 and can therefore be omitted, which leads to the expression below.

$$\frac{dE_{\text{total}}}{dr_\alpha} = \frac{\partial E_{\text{total}}}{\partial r_\alpha} + \sum_{i=1}^{N_{\text{at}}+1} \lambda_i \left(\sum_{j=1}^{N_{\text{at}}+1} \frac{\partial A'_{ij}}{\partial r_\alpha} Q'_j - \frac{\partial b_i}{\partial r_\alpha} \right) \quad (4.26)$$

To compute the forces $\frac{dE_{\text{total}}}{dr_\alpha}$ we hence first compute $\frac{\partial E_{\text{total}}}{\partial Q_i}$, which is the derivative of the short range ANNs with respect to the input neurons containing the atomic charges together with the partial derivative of the electrostatic energy with respect to the atomic charges. We then solve Equation 4.23 to obtain the λ_i . The final forces are then computed according to Equation 4.26. There $\frac{\partial E_{\text{total}}}{\partial r_\alpha}$ includes the electrostatic Coulomb forces and the partial derivatives of the short range energy with respect to the atomic positions.

Only the sum over the derivatives $\frac{\partial A'_{ij}}{\partial r_\alpha}$ with the charges Q'_j are needed in Equation 4.26. Therefore, explicit storage of the $N_{\text{at}} \times N_{\text{at}} \times 3 \times N_{\text{at}}$ individual derivatives can be avoided and only the $N_{\text{at}} \times 3 \times N_{\text{at}}$ terms of the sum have to be stored. Furthermore, it should be noted, that this sum corresponds to the derivative of the electrostatic potential with respect to the atomic positions. This quantity could therefore also be efficiently computed using standard Poisson solvers. Since it has to be computed for the force trick anyways, it can also be used for the computation of the electrostatic forces.

$$\frac{\partial E_{\text{elec}}}{\partial r_\alpha} = \frac{1}{2} \sum_{ij}^{N_{\text{at}}} Q_i \frac{\partial A_{ij}}{\partial r_\alpha} Q_j \quad (4.27)$$

CHARGE EQUILIBRATION FOR PERIODIC SYSTEMS

The charge equilibration equations for periodic boundary conditions are essentially identical to the corresponding equations for free boundary conditions, and the main difference is the calculation of the matrix A . Because of the periodic boundary conditions we have to resort to an Ewald summation [99] to calculate the electrostatic interaction energy.

The basic idea of Ewald summation is, that by placing Gaussian charges of the opposite sign on each of the point charges, the remaining electrostatic interaction becomes short-ranged. This short-ranged energy can then be calculated in real space (E_{real}). We then subtract the interaction energy of the auxiliary Gaussian charges again to obtain the desired total energy of the point charges. This interaction energy of the Gaussians can be efficiently calculated in reciprocal space, resulting in the energies E_{recip} and E_{self} . The electrostatic energy of N_{at} point charges can be calculated as

$$E_{\text{elec}} = E_{\text{real}} + E_{\text{recip}} + E_{\text{self}} \quad . \quad (4.28)$$

The real space part is given by

$$E_{\text{real}}^{\text{pc}} = \frac{1}{2} \sum_{i=1}^{N_{\text{at}}} \sum_{j \neq i}^{N_{\text{neig}}} Q_i Q_j \frac{\text{erfc}\left(\frac{r_{ij}}{\sqrt{2}\eta}\right)}{r_{ij}} \quad (4.29)$$

Here, N_{neig} indicates, that the sum goes over all neighbouring atoms within the real space cutoff radius r_{cut} and r_{ij} is the distance between atoms i and j and η the width of the auxiliary charges.

The reciprocal space part is

$$E_{\text{recip}}^{\text{pc}} = \frac{2\pi}{V} \sum_{\mathbf{k} \neq 0} \frac{\exp\left(\frac{-\eta^2 |\mathbf{k}|^2}{2}\right)}{|\mathbf{k}|^2} |S(\mathbf{k})|^2 \quad (4.30)$$

with

$$S(\mathbf{k}) = \sum_{i=1}^{N_{\text{at}}} Q_i \exp(i\mathbf{k} \cdot \mathbf{r}_i) \quad (4.31)$$

V being the volume of the unit cell and the sum going over all reciprocal lattice points inside reciprocal space cutoff radius $r_{\text{cut}}^{\text{recip}}$. Finally, the self-interaction correction is

$$E_{\text{self}}^{\text{pc}} = - \sum_{i=1}^{N_{\text{at}}} \frac{Q_i^2}{\sqrt{2\pi}\eta} \quad (4.32)$$

Since we use Gaussian charge distributions for the charge equilibration process, the following terms have to be added that account for the different interaction in the short-range part as well as for the self interaction of the Gaussian charges [167–169].

$$E_{\text{elec}}^{\text{Gauss}} = E_{\text{elec}}^{\text{pc}} - \frac{1}{2} \sum_{i=1}^{N_{\text{at}}} \sum_{j \neq i}^{N_{\text{neig}}} Q_i Q_j \frac{\text{erfc}\left(\frac{r_{ij}}{\sqrt{2}\gamma_{ij}}\right)}{r_{ij}} + \sum_{i=1}^{N_{\text{at}}} \frac{Q_i^2}{2\sqrt{\pi}\sigma_i} \quad (4.33)$$

Since these terms are short ranged, they can be efficiently computed in real-space. Here $E_{\text{elec}}^{\text{pc}}$ is the electrostatic energy of the point charges as given above.

The important observation is that the total energy expression of the Ewald summation contains only terms of the form $\frac{1}{2}e_{ij}Q_iQ_j$. By calculating the individual coefficients e_{ij} we can therefore construct the matrix E , such that

$$E_{\text{elec}} = \frac{1}{2} \mathbf{Q}^T \mathbf{E} \mathbf{Q} \quad (4.34)$$

Including the terms for the hardness and adding the electronegativity results in a formalism equivalent to that of the charge equilibration method for free boundary conditions.

The matrix elements e_{ij}^{pc} for point charges can be computed by combining contributions from the real space terms of Equation 4.29, the reciprocal space terms of Equation 4.30 and the self interaction terms of Equation 4.32.

$$e_{ij} = e_{ij}^{\text{real}} + e_{ij}^{\text{recip}} + e_{ij}^{\text{self}} \quad (4.35)$$

The real space terms are given as

$$e_{ij}^{\text{real}} = \begin{cases} \sum_{\mathbf{L} \neq 0} \frac{\text{erfc}\left(\frac{|\mathbf{r}_i - \mathbf{r}_j + \mathbf{L}|}{\sqrt{2\eta}}\right)}{|\mathbf{r}_i - \mathbf{r}_j + \mathbf{L}|}, & \text{if } i = j \\ \sum_{\mathbf{L}} \frac{\text{erfc}\left(\frac{|\mathbf{r}_i - \mathbf{r}_j + \mathbf{L}|}{\sqrt{2\eta}}\right)}{|\mathbf{r}_i - \mathbf{r}_j + \mathbf{L}|}, & \text{otherwise,} \end{cases} \quad (4.36)$$

where \mathbf{L} is a vector that points to neighboring unit cells, i.e., a linear combination of the three lattice vectors with integer coefficients such that periodic replica of atoms are included. The sum over \mathbf{L} is truncated such that only contributions inside the real space cutoff r_{cut} are included. The reciprocal space contributions are

$$e_{ij}^{\text{recip}} = \frac{4\pi}{V} \sum_{\mathbf{k} \neq 0} \frac{\exp\left(\frac{-\eta^2 |\mathbf{k}|^2}{2}\right)}{|\mathbf{k}|^2} \cos(\mathbf{k} \cdot (\mathbf{r}_i - \mathbf{r}_j)) \quad . \quad (4.37)$$

Finally, the self interaction terms can be computed as

$$e_{ij}^{\text{self}} = \begin{cases} \frac{-2}{\sqrt{2\pi\eta}}, & \text{if } i = j \\ 0, & \text{otherwise.} \end{cases} \quad (4.38)$$

To compute the correct matrix elements e_{ij}^{Gauss} for Gaussian shaped charges, a short ranged correction which can be computed in real space has to be added according to Equation 4.33.

$$e_{ij}^{\text{Gauss}} = e_{ij}^{\text{pc}} - \begin{cases} \left(\sum_{\mathbf{L} \neq 0} \frac{\text{erfc}\left(\frac{|\mathbf{r}_i - \mathbf{r}_j + \mathbf{L}|}{\sqrt{2\gamma_{ij}}}\right)}{|\mathbf{r}_i - \mathbf{r}_j + \mathbf{L}|} - \frac{1}{\sqrt{\pi\sigma_i}} \right), & \text{if } i = j \\ \sum_{\mathbf{L}} \frac{\text{erfc}\left(\frac{|\mathbf{r}_i - \mathbf{r}_j + \mathbf{L}|}{\sqrt{2\gamma_{ij}}}\right)}{|\mathbf{r}_i - \mathbf{r}_j + \mathbf{L}|}, & \text{otherwise} \end{cases} \quad (4.39)$$

Here σ_i is the standard deviation of the Gaussian charge on atom i and γ_{ij} is computed according to Equation 4.4. Although, the matrix elements e_{ij} depend on the parameter η , this dependence is cancelled out, when the product $E\mathbf{Q}$ is computed, because the sum of the charges Q_i is zero.

A good choice of the parameter η is critical for the performance of the Ewald summation. A large value of η increases the range of the electrostatic potential that has to be calculated in real space, while also reducing the number of terms that have to be included in the reciprocal space calculations. The different scaling behaviour of the number of reciprocal and real space terms that have to be included results in an optimal choice of η , that, dependent on the system size, results in the optimal performance. Following the derivation of Jackson and Catlow [170], we use the following cutoff radii for the real and reciprocal space sums, such that terms up to a magnitude of α are included.

$$r_{\text{cut}}^{\text{real}} = \sqrt{-2 \ln(\alpha)} \eta \quad (4.40)$$

$$r_{\text{cut}}^{\text{recip}} = \sqrt{-2 \ln(\alpha)} \eta^{-1} \quad (4.41)$$

We can see from Equation 4.29, that the number of terms per atom in the real space energy scales quadratically with the number of atoms inside the cutoff radius and hence to the power of 6 with respect to $r_{\text{cut}}^{\text{real}}$. From Equation 4.30 follows, that the number of terms per atom in the reciprocal sum scales linearly with the number of reciprocal lattice points inside the cutoff and hence cubically with respect to $r_{\text{cut}}^{\text{recip}}$. Assuming equal computational effort for each real and reciprocal space term, Jackson and Catlow [170] proposed the following choice of η , which results in an $\mathcal{O}(N_{\text{at}}^{3/2})$ scaling of the total energy calculation.

$$\eta = \frac{1}{\sqrt{2\pi}} \left(\frac{V^2}{N_{\text{at}}} \right)^{1/6} \quad (4.42)$$

Unfortunately, the same efficiency cannot be obtained during the calculation of E . For the calculation of the energy, the structure factor S is computed once for each term by a sum over all atoms, as described in Equation 4.31 and then squared. To obtain the individual matrix elements of E however, the cross terms arising through the squaring of S have to be calculated individually, necessitating two nested loops

over all atoms, which results in a quadratic instead of a linear scaling. We therefore use a different Gaussian width η_E , when calculating E .

$$\eta_E = \frac{1}{\sqrt{2\pi}} V^{1/3} \quad (4.43)$$

An implementation of the Ewald summation as well as the calculation of the matrix E and its derivatives can be found in a public github repository [171] and in the open source software RuNNer [172].

4.3 TEST SYSTEMS SHOWING THE 4G-HDNNPs CAPABILITY

In the following sections we demonstrate the limitations of MLPs based on local properties only and show how they can be overcome by the 4G-HDNNP. For this purpose we use a set of non-periodic and periodic systems, which cover a wide range of typical situations in chemistry and materials science. The non-periodic systems consist of a covalent organic molecule, a small metal cluster and a cluster of an ionic material covering very different types of atomic interactions. These examples demonstrate the simultaneous applicability of a single 4G-HDNNP to systems of different total charges and the correct description of long-range charge transfer and the associated electrostatic energy. As a periodic system we have chosen a small gold cluster adsorbed on a MgO(001) slab, which is a prototypical example for heterogeneous catalysis. We show that in contrast to established MLPs, the 4G-HDNNP is able to reproduce the change in adsorption geometry of the cluster if dopant atoms are introduced in the slab far away from the cluster. In all cases, the 4G-HDNNP PES is very close to the results obtained from DFT.

While in these examples we do not explicitly investigate the transferability of the potentials to different systems, we expect that the 4G-HDNNP in general provides an improved transferability compared to second and third generation MLPs, due to the underlying physical description of the global charge distribution and the resulting electrostatic energy. This expectation is supported by the fact that even traditional charge equilibration schemes with constant electronegativities are known to work well across different systems [173]. Furthermore, for the related CENT approach a broad transferability has already been demonstrated for different atomic environments [159].

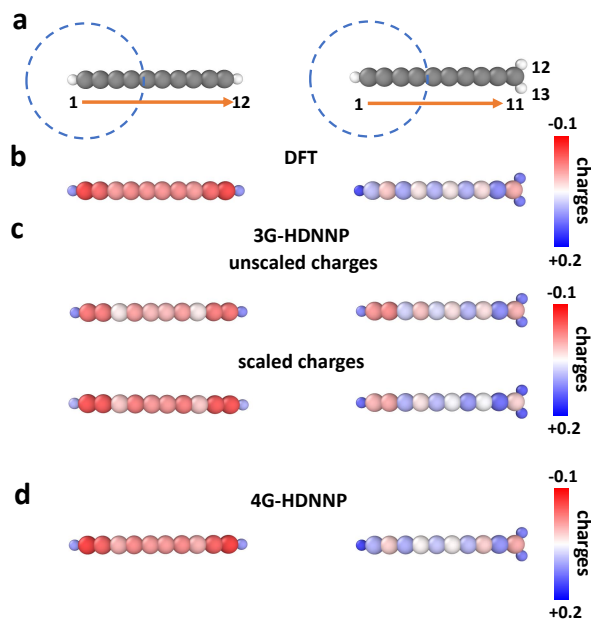


Figure 4.3: Charge redistribution in organic molecules. **a** DFT-optimized structures of C_{10}H_2 (left) and $\text{C}_{10}\text{H}_3^+$ (right) with atom IDs. Carbon and hydrogen atoms are colored in grey and white, respectively. The dashed circle shows the cutoff radius of the left carbon atom defining its chemical environment. Panel **b** shows the atomic partial charges obtained from DFT. The unscaled and scaled 3G-HDNNP charges are displayed in **c**, while the 4G-HDNNP charges are shown in **d**. (Figure reproduced with permission from Reference [107].)

4.3.1 A BENCHMARK FOR ORGANIC MOLECULES

The first model system we study is a linear organic molecule consisting of a chain of ten sp-hybridized carbon atoms terminated by two hydrogen atoms as shown in Figure 4.3a. Molecules of this type have been studied before in electronic structure calculations [174–176]. For this molecule we will now demonstrate the applicability of 4G-HDNNPs to systems with long-range charge transfer induced by protonation, which changes the total charge and the local structure in a part of the system. Since the majority of existing machine learning potentials rely on local structural information only without explicit information about the global charge distribution and total charge, they are not simultaneously applicable to both neutral and charged systems.

This is different for 4G-HDNNPs, which naturally include the correct long-range electrostatic energy for any global charge present in the training set. Because of the

protonation of the terminal carbon atom, its hybridization state changes to sp^2 and the electronic structure of the resulting $C_{10}H_3^+$ cation is modified even at very large distances along the whole molecule. This is reflected in the differences of the DFT charges of the molecules in Figure 4.3b, which have been structurally optimized by DFT.

Using a data set containing both molecules, we have constructed 2G-, 3G- and 4G-HDNNPs using a cutoff radius $R_c = 4.23\text{\AA}$ as illustrated by the circle in Figure 4.3a for the example of the left carbon atom. In Figure 4.3c we show the atomic partial charges obtained with the 3G-HDNNP in two forms: first as unscaled charges directly obtained from the atomic neural network fits without any constraint for the correct total charge of the system, and second rescaled to ensure total charges of zero or one, respectively. It can be seen that the scaling process does not significantly improve the 3G-HDNNP charges.

The atoms in the left half of the molecule are far from the added proton such that their atomic environments differ only slightly due to the DFT geometry optimization. In addition, in the training set a lot of basically identical environments but different atomic charges are present for these atoms, which results in high fitting errors due to the contradictory information. As a consequence the ANNs assign averaged charges to these atoms, which differ qualitatively from the DFT reference charges of both systems. For instance, the 3G-HDNNP partial charges on atom 2, i.e., the left carbon atom, are almost identical in both molecules, although they are very different in DFT. Note that the predicted charges of atoms 1–6 in $C_{10}H_2$ and $C_{10}H_3^+$ would be even exactly identical if the latter molecule would not have been relaxed after protonation. The charges obtained with the 4G-HDNNP shown in Figure 4.3d, on the other hand, match the DFT charges very accurately for both molecules, as they can be distinguished in this method.

The inaccurate charges obtained with the 3G-HDNNP lead to a poor quality of the PES, and the same is observed for the short-range only 2G-HDNNP. In Table 4.1 we compare the errors of the total energies as well as the mean errors of the atomic charges and forces of all HDNNP generations for the DFT optimized structures. It can be seen that the errors of all quantities obtained for the 4G-HDNNP are much lower than for the 2G- and 3G-HDNNPs. Further, we note that in several cases the energies obtained by the 3G-HDNNP are even worse than for the 2G-HDNNP, as the unphysical charge distribution to some extent prevents the accurate representation of the energy.

4.3 Test Systems Showing the 4G-HDNNPs Capability

Table 4.1: Energy and charge error obtained for the organic molecules. Energy error (meV/atom) and mean errors of the atomic charges (10^{-3} e) and forces (eV/Å) of $C_{10}H_2$ and $C_{10}H_3^+$ with respect to DFT obtained with the different HDNNP generations for the DFT optimized structures. For the 3G-HDNNP the results for scaled and unscaled charges are given.

		energy	charges	forces
$C_{10}H_2$	2G-HDNNP	0.684	—	0.095
	3G-HDNNP (unscaled)	1.255	19.72	0.430
	3G-HDNNP (scaled)	2.193	10.76	0.138
	4G-HDNNP	0.463	4.820	0.032
$C_{10}H_3^+$	2G-HDNNP	0.922	—	0.127
	3G-HDNNP (unscaled)	0.046	17.82	0.658
	3G-HDNNP (scaled)	1.425	17.72	0.259
	4G-HDNNP	0.176	5.048	0.042

To investigate the forces in more detail, we plot the individual atomic forces in both molecules using the 2G-HDNNP and the 4G-HDNNP for the DFT optimized structures as shown in Figure 4.4. For all atoms in both molecules the 4G-HDNNP yields very low force errors, with an average error of only $0.037 \text{ eV}/\text{\AA}$ underlining the quality of this PES. However, for the 2G-HDNNP the forces acting on the left half of $C_{10}H_3^+$ and on all atoms in $C_{10}H_2$ the force errors are significantly larger. The reason is again, that the 2G-HDNNP cannot distinguish both molecules for these atoms, and the force errors are only low close to the extra proton in $C_{10}H_3^+$, which can be recognized as a distinct local structural feature in the atomic environments of the right half of this molecule.

Interestingly, the relatively high errors of the 2G-HDNNP forces are not matched by high energy errors, which instead are surprisingly low and smaller than 1 meV/atom for both molecules. This suggests that the total energy predicted by 2G-HDNNPs may benefit from error compensation in the atomic energies in that the atomic energies in the right half of $C_{10}H_3^+$ are adjusted to compensate the deficiencies of the atomic energies in the left half of the molecule.

4.3.2 METAL CLUSTERS: Ag_3

In this example we investigate a small metal cluster, Ag_3 , in two different charge states. The PES of small clusters is strongly influenced by the ionization state of the cluster and the ground state can differ as a function of the total charge of the

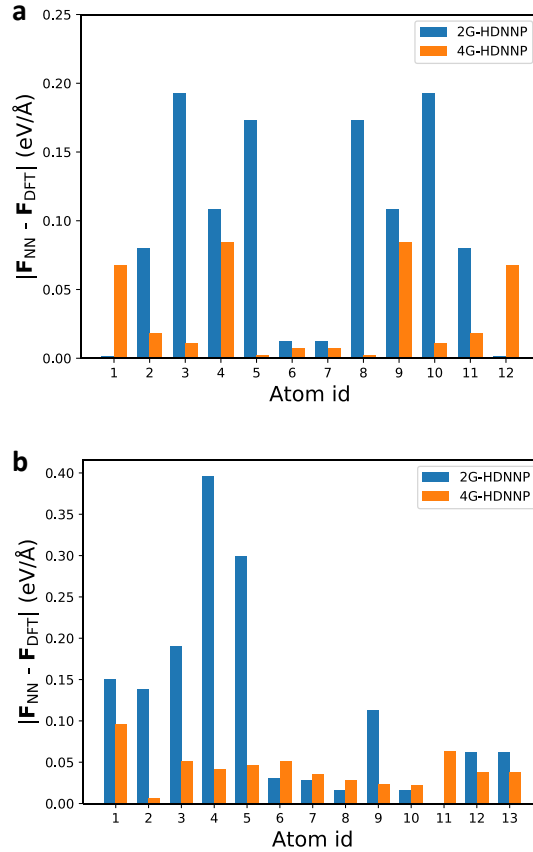


Figure 4.4: Force errors of the HDNNPs for the organic molecules. 2G- and 4G-HDNNP forces for the atoms in the DFT-optimized structures of C_{10}H_2 and $\text{C}_{10}\text{H}_3^+$ (indicated in **a** and **b** respectively). (Figure reproduced with permission from Reference [107].)

cluster [177–180]. Due to the small system size there are no long-range effects, and the full system is included in each atomic environment. Therefore, in principle, 2G-HDNNPs should be perfectly suited to describe the PES of Ag_3 , but this is only true as long as the total charge of the system does not change, since for a combination of data with different total charges, like Ag_3^+ and Ag_3^- , in the training set the unique relation between atomic positions and the energy is lost. The minimum-energy structures of both cluster ions obtained from DFT are shown in Figure 4.5a along with the atomic partial charges. After training a 2G-HDNNP and a 4G-HDNNP to data containing both types of clusters, we have reoptimized the geometries by the respective HDNNP generation. As expected, the minima obtained with the 2G-HDNNP (Figure 4.5b) are identical for both charge states, but do not agree with

4.3 Test Systems Showing the 4G-HDNNPs Capability

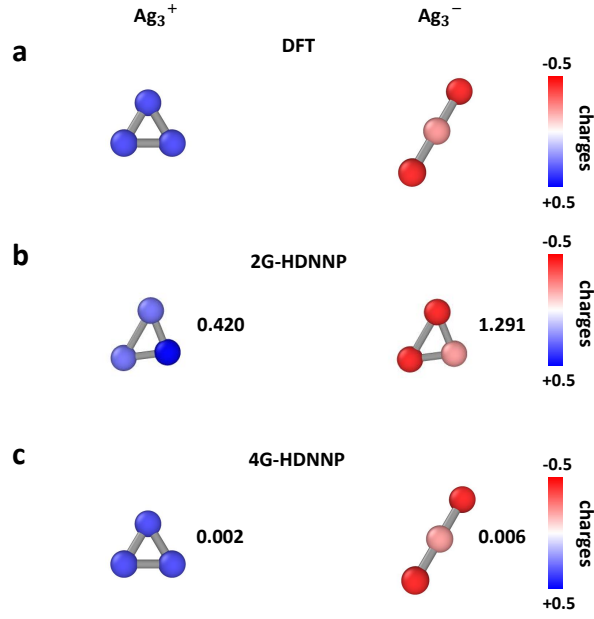


Figure 4.5: Optimized geometry and atomic charges of Ag clusters. Structures and atomic partial charges of Ag_3^+ and Ag_3^- optimized with DFT in **a**, the 2G-HDNNP in **b** and the 4G-HDNNP in **c**. The numbers give the root mean squared displacement (RMSD) in Å compared to the respective DFT minima. The partial charges in **b** are shown for illustration purposes only and have been obtained from a scaled 3G-HDNNP. (Figure reproduced with permission from Reference [107].)

any of the DFT structures. The 4G-HDNNP on the other hand, which in addition to the structural information also takes the total charge and the resulting partial charges into account, is able to predict the minima and also the atomic partial charges of both systems with very high accuracy (Figure 4.5c). In this case, the inability of the 2G-HDNNP to distinguish between clusters is also apparent from the energy errors with respect to DFT. While the energy errors for Ag_3^- and Ag_3^+ obtained from the 4G-HDNNP are only about 1.166 meV/atom and 0.320 meV/atom, respectively, the errors of the 2G-HDNNP are 0.605 and 2.017 eV/atom and thus several orders of magnitude larger. The 3G-HDNNP using scaled charges performs even worse and errors of 0.713 and 5.721 eV/atom are obtained. This is due to the non-physical electrostatic contribution calculated from the incorrectly predicted charges.

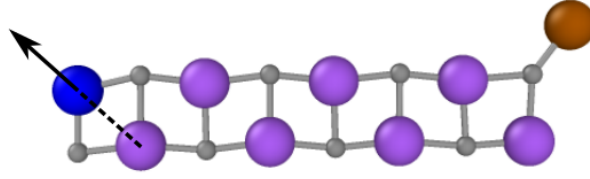


Figure 4.6: Optimized structure of the Na_9Cl_8^+ cluster. Sodium atoms are shown in purple, blue and brown, chlorine atoms in grey. The arrow indicates the direction along which the blue sodium atom is moved for the energy and force plots in Figs. 4.7a and 4.7b. The position of this atom is defined by the Na-Na distance indicated as dashed line. (Figure reproduced with permission from Reference [107].)

4.3.3 NaCl CLUSTER IONS

As the last non-periodic example, we select a system with mainly ionic bonding, which is a positively charged Na_9Cl_8^+ cluster, and we analyze the changes of the PES, if a neutral sodium atom is removed. The initial structure of the cluster ion has been obtained from a DFT geometry optimization and is shown in Figure 4.6. The sodium atoms are shown in purple, blue, and brown, while the chlorine atoms are displayed in grey. We then construct a second system by removing the brown sodium atom from the cluster while keeping the positions of the remaining atoms fixed. Since the overall positive charge of the cluster is maintained, the charge is redistributed throughout the new Na_8Cl_8^+ cluster ion.

To investigate the consequences of this change in the electronic structure on the PES, we compute and compare the energies and forces when moving the blue sodium atom along a one-dimensional path indicated by the arrow in Figure 4.6 for both cluster ions. The distance to the closest neighboring sodium atom highlighted as dashed line is used to define the structure.

Figure 4.7 shows the energies for both systems obtained with DFT and the 2G-, 3G- and 4G-HDNNPs. All energies are given as relative energies to the minimum DFT energy of the respective cluster ion and refer to the full systems. First, we note that the positions of the DFT minima differ by more than 0.1 \AA , i.e., depending on the presence of the very distant brown atom the blue atom adopts different equilibrium positions. The 2G-HDNNP, however, is unable to distinguish these minima and instead the same local minimum Na-Na distance is found for both systems, which is approximately the average value of the two DFT minima. We note that the 2G-HDNNP energy curves of the two systems are not identical but there is an energy offset, as some atomic environments in the right part of the systems differ, yielding

4.3 Test Systems Showing the 4G-HDNNPs Capability

different atomic energies. Since these environments do not change when moving the blue atom this offset is constant. For the 3G-HDNNP the same qualitative behavior is observed, and two very similar but not identical minima are found for both systems. Still, in case of the 3G-HDNNP the energy offset between both systems is not merely a constant anymore, as the long-range electrostatic interactions between the blue and the brown atom in Na_9Cl_8^+ are position-dependent. We note that in spite of these qualitative differences with respect to DFT, the 2G- and 3G-HDNNP curves show only a deviation of about 1 meV per atom from the DFT curves. This is very small and in the typical order of magnitude of state-of-the-art MLPs, and in the present case this apparently high accuracy hides the qualitatively wrong minima. Finally, the 4G-HDNNP energies for both systems are very accurate and the energy curves match the corresponding DFT curves very closely. Both distinct local minima are correctly identified and at the right positions.

Next, we turn to the forces shown in Figure 4.7b. The results are fully consistent with our discussion of the energy curves. The DFT forces acting on the displaced atom are different for both cluster ions and well reproduced by the 4G-HDNNP. The 2G-HDNNP forces of both systems are exactly identical due to the constant offset between both energy curves (Figure 4.7a), while the 3G-HDNNP forces of both systems are slightly different due to the additionally included long-range electrostatics.

4.3.4 Au_2 CLUSTER ON $\text{MgO}(001)$

As example for a periodic system we choose a diatomic gold cluster supported on a $\text{MgO}(001)$ surface. Similar systems have attracted attention because of their catalytic properties for reactions like carbon monoxide oxidation, epoxidation of propylene, water-gas-shift reactions, and the hydrogenation of unsaturated hydrocarbons [181]. Theoretical [182, 183] as well as experimental studies [184] have shown that the geometry of these clusters can be modified by the introduction of dopant atoms into the oxide substrate. This ability to control the cluster morphology is of great interest, as it can enhance the catalytic activity of the system [183]. 2G-HDNNPs have been used before to study the properties of supported metal clusters [144, 185, 186], but systems as complex as doped substrates to date have remained inaccessible, since long-range charge transfer between the dopant and the gold atoms is crucial to achieve a physically correct description of these systems.

For Au_2 at $\text{MgO}(001)$ there are two main adsorption geometries, an upright “non-wetting” orientation of the dimer attached to a surface oxygen and a “wetting” configuration, parallel to the surface, in which the two Au atoms reside on two Mg

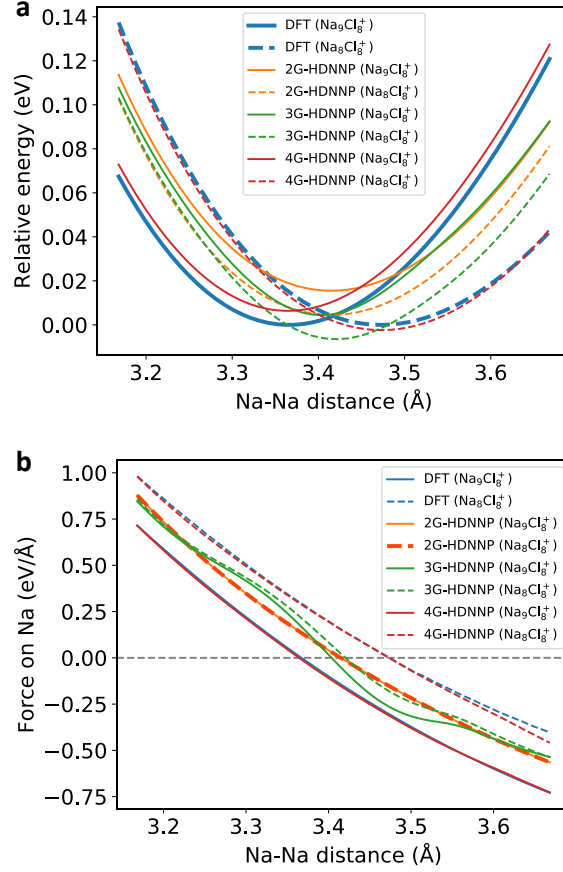


Figure 4.7: Relative energies and forces of the NaCl clusters. **a** Relative energies of all potentials with respect to the DFT minima of the Na_8Cl_8^+ and the Na_9Cl_8^+ clusters as a function of the Na-Na distance and **b** forces acting on the blue sodium atom for the the path shown in Figure 4.6. For the 3G-HDNNP unscaled charges have been used in this plot. (Figure reproduced with permission from Reference [107].)

atoms. DFT optimizations of the positions of the gold atoms with fixed substrate for the doped and undoped surfaces reveal that the presence of the dopant atoms changes the relative stability of both structures. On the pure MgO support (Figure 4.8a) the minimum energy structure is “non-wetting”, while a flat “wetting” geometry is more stable if the MgO is doped by three aluminium atoms (Figure 4.8b) corresponding to 2.86% of the slab. The Al dopant atoms were introduced into the 5th layer, resulting in a distance of more than 10 Å from the gold atoms. Despite this large separation, we found that by doping the charge on the Au_2 cluster is reduced (becomes more negative) by about 0.2 e compared to the same geometry for the undoped surface.

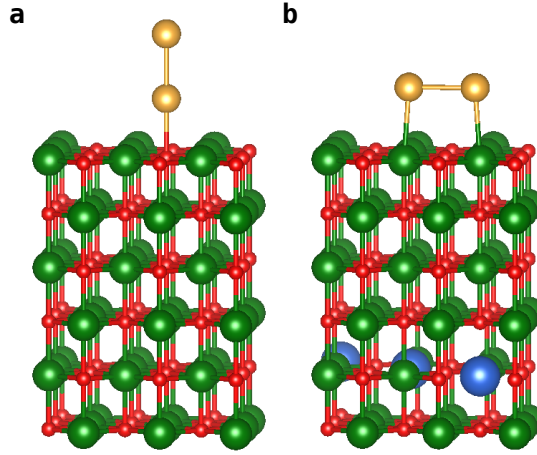


Figure 4.8: Geometry of Au_2 clusters on undoped and doped $\text{MgO}(001)$ surface. Au_2 cluster in the non-wetting geometry on the undoped **a** and the wetting geometry on Al-doped **b** $\text{MgO}(001)$ surface represented by a periodic (3×3) supercell. Au atoms are shown in yellow, O in red, Mg in green and Al in blue. The configuration of the gold cluster has been optimized by DFT for a fixed substrate. (Figure reproduced with permission from Reference [107].)

This change in the electronic structure does not only lead to a switching in the energetic order of the geometries but also to a change of the bond-length between the gold atoms and the substrate.

The energy difference ($E_{\text{wetting}} - E_{\text{non-wetting}}$) between the wetting and non-wetting configurations calculated with different methods on a doped substrate are -2.7 meV for DFT, 375 meV for the 2G-HDNNP and -41 meV for the 4G-HDNNP. On an undoped substrate we obtained 929 meV for DFT, 375 meV for the 2G-HDNNP and 975 meV for the 4G-HDNNP. These numbers were obtained after the positions of the gold atoms were optimized. In case of the 2G-HDNNP, both optimizations yield the same structure. For the 2G-HDNNP the energy differences for the doped and undoped systems are exactly the same as the dopant atoms are outside the local chemical environments of the gold atoms. Thus the 2G-HDNNP cannot take the change of the PES by doping into account. The DFT and 4G-HDNNP results agree in that there is a slight preference for the wetting configuration for the doped surface, while in the undoped case the non-wetting configuration is clearly more stable.

An analysis of the PES for the case of the non-wetting geometry for the doped and undoped slabs is given in Figure 4.9, which shows the energies relative to the minimum

DFT energies of the respective systems as a function of the distance between the bottom Au atom and its neighboring oxygen atom for DFT, the 2G-HDNNP and the 4G-HDNNP. The energy curves of the 4G-HDNNP and DFT are very similar and can resolve the different equilibrium bond lengths for the doped (4G-HDNNP: 2.342 Å; DFT: 2.332 Å) and undoped (4G-HDNNP: 2.177 Å; DFT: 2.190 Å) substrates. The 2G-HDNNP yields the same adsorption geometry with a bond length of 2.256 Å in both cases, while the energies substantially differ from the DFT values with the main effect of the dopant being a constant energy shift between both substrates, similar to what we have observed in the presence or absence of the additional sodium atom in the NaCl cluster.

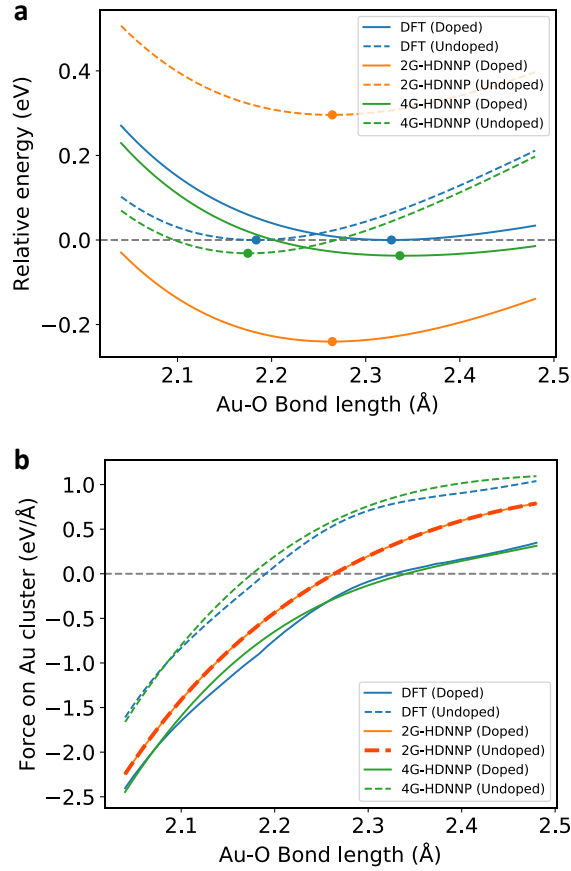


Figure 4.9: Energies and forces for the gold cluster. **a** Relative energy and **b** sum of forces acting on the Au₂ cluster for the cluster adsorbed at the MgO(001) substrate for the non-wetting geometry for the Al-doped and undoped cases. The local minima of the energy curves are marked with a dot. The Au-O bond length refers to the distance between the Au closest to the surface and its neighboring oxygen atom. (Figure reproduced with permission from Reference [107].)

4.3.5 DFT CALCULATIONS

The DFT reference data for the examples shown above has been generated using the all-electron code FHI-aims [32] employing the PBE [39] exchange-correlation functional with light settings. The total energy, sum of eigenvalues and charge density for all systems except Au₂-MgO were converged to 10^{-5} eV, 10^{-2} eV and 10^{-4} e, respectively. For the Au₂-MgO systems stricter settings have been applied by multiplying each criterion by a factor 0.1 in combination with a $3 \times 3 \times 1$ k-point grid. Spin polarized calculations have been carried out for the Au₂-MgO, NaCl and Ag₃ systems. Reference atomic charges were calculated using the Hirshfeld charge decomposition method [48]. In principle any other charge partitioning scheme could be used in the same way.

The dataset of the C₁₀H₂/C₁₀H₃⁺ molecules and the Ag₃ clusters have been constructed by performing MD simulations for each system at 300 K with 5000 steps at a time step of 0.5 fs. A Nosé-Hoover thermostat [60] was applied to run simulations in the canonical (*NVT*) ensemble, and the effective mass was set to 1700 cm^{-1} . In addition, the trajectory path during the geometry relaxations up to a numerical convergence of $0.001 \text{ eV}/\text{\AA}$ of the forces was also added to the data set to have sufficient sampling close to equilibrium structures. The geometry optimization of the Ag₃⁻ system has been terminated when reaching forces below $0.0015 \text{ eV}/\text{\AA}$.

In case of the NaCl cluster and the Au₂ cluster at the MgO surface the reference data set consists of two structurally different types of systems, and half of the data set was dedicated to each of the two cases. We performed a random sampling along the trajectories depicted in figures 4.7 and 4.9 and added further Gaussian distributed displacements to ensure sufficient sampling of the PES in the vicinity of the structures of interest. For the NaCl cluster we used Gaussian displacements with a standard deviation of 0.05 \AA . As in the Au₂-MgO system we only investigated the change in geometry of the Au₂ cluster, while the MgO substrate remained fixed during all geometry relaxations, we used a smaller magnitude of the Gaussian displacements for the substrate than for the cluster. A standard deviation of 0.02 \AA was used for the substrate and 0.1 \AA was used for the gold cluster. Half of the data set consists of structures with an undoped substrate, while the other half includes a doped substrate. Half of the samples of each substrate configuration were generated with the Au₂ cluster in its wetting configuration, and the other half with the cluster in its non-wetting configuration. The total number of reference data points for the NaCl cluster and Au₂-MgO slab is 5000, while the the Ag₃ clusters and the organic molecule it is 10019 and 11013, respectively.

The coordinates of the DFT optimized structures, lists of the symmetry functions used for building the 2G-, 3G-, and 4G-HDNNPs and training and test root mean squared errors (RMSEs) together with correlation plots for the charges, energies, and forces can be found in Appendix A.1.

4.4 OTHER NONLOCAL MLPs

The development of fourth-generation MLPs is a very active field of research, and an increasing number of methods have been published recently or are currently under development. The defining property of fourth-generation MLPs is their ability to describe long-range effects due to charge transfer as well as electrostatic interactions without truncation using an explicit Coulomb term for very large systems. Apart from CENT [158] and the 4G-HDNNP, the Becke population neural network (BpopNN) [164] method is also based on directly including information about the atomic charges, which after being redistributed over the entire system are used for the calculation of the Coulomb energy. The BpopNN method is a generalization of the energy minimization in CENT, which contains the electrostatic and local atomic energy terms. This local atomic energy depends not only on the short-range environment but also on the atomic population (i.e., the atomic charges). Unlike in CENT, where a quadratic function is used, to model the functional dependence of the atomic energy on the atomic charge, the BpopNN method uses an arbitrarily complex function, in the form of ANNs to describe the dependence of the atomic energies on the populations. The ANNs are trained on reference data obtained from a set of constrained DFT calculations [187]. This complex relationship prohibits the use of direct solver to find the populations that minimize the total energy and a self-consistent cycle called SCF-q needs to be used. The method is similar to 4G-HDNNPs in that it contains an internal representation of the electronic structure in the form of global atomic charges. Another closely related method is the charge recursive neural network (QRNN) [188] which can be considered an extension of the 4G-HDNNP method. The QRNN introduces an additional AED, that also depends on the atomic charges of the neighboring atoms. The method further uses a simplified version of the charge equilibration scheme which can be solved with a linearly scaling computational cost. This is achieved by absorbing the off diagonal terms of the linear equation systems into the electronegativities which themselves depend on neighboring atomic charges. This charge equilibration step is then applied in a recursive manner which allows for the charge information to propagate through the system. Another

class of MLPs, which has very recently gained a lot of attention are MPNNs [189]. In these methods, information is passed between neighboring atoms in multiple steps, during each of which the received information is combined and updated with information about the current local environment. Although MPNNs are still strictly speaking second generation MLPs, the effective distance at which interactions can be described can become very large through the use of many message passing steps. Examples of MPNNs include the DTNN [190] and AIMNet [191]. In recent work [165], AIMNet was extended to predict atomic charges and spins for systems with multiple charge states. This allows for the calculation of several quantities such as atomic electronegativity and hardness as well as condensed Fukui functions. MPNNs have also been used to predict atomic charges in a method called electron-passing neural networks (EPNN) [192]. Other related methods are the hierarchically interacting particle neural network (HIP-NN) [193] or SchNet [111], where information is also passed between nearby atoms.

More recently, MPNNs based on equivariant features have become popular. Examples include NequIP [194], SpookyNet [195], PaiNN [196] and Newtonnet [197]. These MLPs based on equivariant features have shown astonishing accuracy, sample-efficiency and extrapolation capabilities. Traditional methods are based on features, which are invariant, i.e., do not change, under rotation and inversion operations. In contrast, equivariant methods use features, such as vectors or higher order tensors that transform correspondingly, when the atomic geometry is transformed. To preserve the equivariance of the internal features and therefore the invariance of the total energy, the internal operations on the equivariant features have to be constructed carefully.

Due to the iterative message passing in MPNNs, the effective cutoff can become very large. This can be problematic for applications to very large systems, where parallelization across multiple compute-nodes becomes necessary. Recently, a method named Allegro [198] was proposed, that while using equivariant features, does not rely on message passing iterations. The methods performance is comparable to previously published equivariant MPNNs but can also be parallelized efficiently enabling simulations with hundreds of millions of atoms.

4.5 SUMMARY AND OUTLOOK

The development of atomistic potentials has seen rapid progress in recent years. In particular, the introduction of machine learning potentials nowadays allows us to

achieve a level of accuracy that is comparable to electronic structure calculations. This drastically extends the possible time and length scales of computer simulations of complex systems, for which reliable empirical potentials are not available. Most MLPs currently in use, still rely on a local description in the form of atomic energies. Even though long-range electrostatic interactions have been considered on the basis of fixed or local environment-dependent charges, these approaches break down quantitatively and qualitatively if the global electronic structure of a system is modified by distant parts of the system outside the local environments or by changes in the total charge. With our newly developed 4G-HDNNP, the inclusion of long-range effects due to charge transfer has become possible. Several other methods have also been proposed with very encouraging first examples illustrating their capabilities. These “non-local” MLPs close an important gap in the applicability of MLPs for many interesting systems in chemistry, biochemistry, and materials science and are expected to allow the replacement of demanding electronic structure calculations by MLPs for more and more applications in the future.

Nevertheless, development on the 4G-HDNNP is still ongoing. As already mentioned, the development of an iterative scheme to solve the charge equilibration equations is currently under development. With this new approach, the cubic scaling of the current implementation will be overcome, enabling simulation at very large scales.

Another improvement, that has already been implemented and will be published soon, is the electrostatically embedded fourth generation high-dimensional neural network potential (ee4G-HDNNP) [199]. The ee4G-HDNNP is an extension of the 4G-HDNNP, that includes two additional modifications that further improve the accuracy and transferability of the method. The first modification is the addition of a new type of descriptor of the form

$$V_i^j = \sum_{k=1}^{N_{\text{neig},j}} \frac{\text{erf}\left(\frac{R_{ik}}{\sqrt{2}\gamma_{ik}}\right) Q_k}{R_{ik}} f_{\text{cut}(R_{ik})} \quad . \quad (4.44)$$

This new descriptor captures a short-ranged, electrostatic potential arising from all $N_{\text{neig},j}$ neighboring atoms of element j . It therefore provides additional information about the neighboring charge distribution to each atom. This additional information is useful in cases, where similar atomic environments are present, for which the

charge on the central atom is the same but the charge on neighboring atoms differs. Additionally, a two-body energy of the form

$$E_{2b} = \sum_{i>j}^{N_{\text{at}}} \left(A_{ij}^{\alpha} e^{B_{ij}^{\alpha}(\mu_{ij}^{\alpha} - R_{ij})} - \frac{C_{ij}^{\alpha}}{R_{ij}^6} - \frac{D_{ij}^{\alpha}}{R_{ij}^8} \right) \cdot f_{\text{cut}}(R_{ij}) \quad (4.45)$$

is added to the potential. Like the electrostatic energy, this two-body energy is subtracted from the training data before the short-range ANNs are trained to prevent double-counting. Here, A_{ij}^{α} , B_{ij}^{α} , μ_{ij}^{α} , C_{ij}^{α} and D_{ij}^{α} are element-pair-specific parameters that are fit to pairwise binding curves. The additional two body terms increase the transferability of the model and improve the behaviour of the potential in the extrapolative regime, by, for example, ensuring a repulsive force when two atoms are close. The abilities of the ee4G-HDNNP were demonstrated on NaCl clusters of multiple charge states and sizes. The results show an improved transferability to charge states and cluster sizes, that were not present in the training data. The improved potential can even be used to perform structure search using minima hopping [81]. This is a particularly stringent test of the potential, since the minima hopping does gradually increase the kinetic energy used during MD simulations and will so explore parts of the configuration space well beyond what was sampled during the generation of the training data. The ee4G-HDNNP was also found to be able to recover the correct energetic ordering of the newly found local minima.

Future challenges in the development of the 4G-HDNNP include the improvement of the electrostatic interaction. As mentioned in Section 2.1.6, there is no unique partition of the electronic density into atomic charges, and therefore many partitioning methods exist. The Hirshfeld charges, which were used for all the above-mentioned examples, can be readily extracted from DFT charge densities, but it is known, that they are not optimal for reproducing the electrostatic potential further away from the atoms [51]. It might therefore be advantageous to adopt methods to learn the atomic charges, that improve upon this deficiency. A particularly promising method was recently described in the context of the CENT2 approach [57]. Instead of directly learning atomic charges, extracted from the DFT densities, a screened long range electrostatic potential is targeted. A modified greens functions is used to separate the electrostatic potential arising from the DFT charge density into a short-range and a screened long-range part. The electronegativity predicting ANNs are then trained, such that the predicted atomic charges recover the screened long-range potential. The remaining short-range part can then be captured by the short-range

ANNs. A similar approach was adapted by the recently published kernel charge equilibration (kQEq) method [58]. Instead of directly targeting reference atomic charges, the model is trained to reproduce accurate molecular dipole moments. The method is also based on environment dependent electronegativities but uses kernel ridge regression instead of ANNs.

Furthermore, the 4G-HDNNP currently only uses atomic monopoles and all interactions due to polarization, atomic dipole moments and higher order multipoles are captured by the short-range ANN. We hope, that an inclusion of higher order multipoles into the charge equilibration scheme of the 4G-HDNNP will further improve the accuracy of the electrostatic interactions, that can be described.

Future challenges that have to be addressed by the community in general include the description of long-ranged interactions caused by non-local effects in the electronic structure which are not caused by charge transfer. One such example, presented in a recent review [200], is a chain of carbon atoms that is terminated by two methylene groups (C_nH_4). When the two methylene groups are rotated, they experience a torsional force, due to the double bonds between the carbon atoms. The description of this effect requires a large cutoff for conventional local MLPs. Recently, a method based on a self-attention mechanism was proposed to describe such long-ranged interactions [201]. Another challenge, that becomes apparent in the same example, is that the assumption of smoothness, employed by almost all MLPs, may not always hold. While the cusp seen in the torsional energy of the cumulene molecules ($C_{2+n}H_4$) in Reference [200] is most likely an artefact of the underlying electronic structure method [202], discontinuities in the first derivative of the PES are present at conical intersections [203]. These discontinuities in the first derivatives make it challenging for MLPs to accurately learn the potential energy in the surrounding areas [204]. In cases, where the conical intersection is located at high symmetry points, an approach similar to the one shown in Section 5 for the example of a H_3 system might be possible. But in general, it is not clear yet, how discontinuities in the first derivative of the potential energy surface can be optimally handled by MLPs.

While many open challenges remain, it is clear, that the development of improved MLPs is a very active and dynamic field of research and many exciting developments can be expected in the near future.

5 LEARNING A SMOOTHED VERSION OF THE OVERLAP MATRIX FINGERPRINT

The introduction of appropriate atomic environment descriptors (AEDs), namely the atom centered symmetry functions (ACSFs) [10], is one of the key developments, that started the remarkable success of MLPs. By encoding the local atomic environment, AEDs allow for MLPs that express the total energy as a sum of atomic energies and can be applied to systems of arbitrary size. The most critical feature of the AEDs is, that they should preserve the same symmetries, i.e., rotational, translational and permutational invariance, that we naturally expect from chemical systems. In the case of ACSFs, the translational and rotational invariance is achieved by only using the distances to the central atom and angles between pairs of neighboring atoms. Permutational invariance is then obtained by summing over all neighbors and pairs of neighbors. Later on, several other types of AEDs [113, 135, 205, 206] were also developed. These AEDs are based on different mathematical expressions, but it was recently shown by Willatt, Musil, and Ceriotti [207], that most AEDs, including the ACSFs, are somewhat equivalent, since they can be expressed as n -body correlations of an atomic density.

In addition to their symmetry preserving property, AEDs should be unique. This means, that no chemically different atomic environments result in the same set of descriptors. Until recently, it was widely believed in the community [208–211], that descriptors including up to three-body features would provide an overcomplete description of the atomic environment. This assumption was first challenged by Parsaeifard and Goedecker [212], who found manifolds with almost constant AEDs. Although the AEDs on these manifolds were not exactly degenerate, it was shown that they prevent accurate machine learning of atomic properties. Then, in 2020, Pozdnyakov et al. [138], presented a strikingly simple example of two sets of atomic environments, that result in exactly the same three-body AEDs. Another counter example, included in the same paper, shows, that even the inclusion of four-body features is insufficient for a complete description. It should be noted here, that this

problem is generally not as severe as it may sound. When global properties, such as the total energy, are learned, the AEDs of neighboring atoms will be different and hence resolve the degeneracy. Furthermore, training sets constructed from chemical environments mostly only include a subset of all possible atomic environments and hence may not include any of the problematic situations. Nevertheless, relying on compensation effects is certainly not an optimal solution and may not be possible, when atomic properties, such as charges or electronegativities are learnt.

In contrast to descriptors, that are based on a truncated series of n -body terms, the OM fingerprint [136] uses a different construction. First, Gaussian type orbitals (in practice s and p orbitals are used) are placed on each atom and multiplied with a cutoff function, that decays smoothly to zero at a previously chosen cutoff distance from the central atom. The final fingerprint is then obtained by taking the sorted eigenvalue spectrum of the resulting overlap matrix. Although only two-body terms enter the overlap matrix, higher body order terms are introduced by the diagonalization step [138]. While the completeness properties of the OM fingerprint are not yet fully understood, numerical evidence [212] supports the superiority of the OM fingerprint in distinguishing atomic environments in systems that contain a single atomic species. The OM fingerprint can therefore be expected to not suffer from the above-mentioned incompleteness problems in single species systems. In systems with multiple species, however, examples of degenerate descriptors can be trivially constructed, since the atomic species is encoded through the width of the Gaussian type basis functions placed on the atoms. For an atomic neighborhood containing one atom, an equal descriptor can be obtained for a neighborhood containing an atom of a different element by simply adjusting the distance between the two atoms such that the same overlap between the two Gaussian type orbitals is obtained. This deficiency can in principle be overcome by including a few element-specific two body ACSFs in the descriptor.

To ensure a coherent fingerprint, the eigenvalues of the OM matrix have to be sorted. This is problematic when two eigenvalues cross since this can lead to discontinuities in the first derivative of the descriptor with respect to the atomic positions. In general such crossings are rare and usually not encountered during MD or MC simulations. In some rare cases, where the crossings occur at high symmetry configurations that coincide with conical intersections, this can actually be advantageous, as the kink in the AED allows the ANN to accurately recover the kink in the PES at the conical intersection, as shown in Figure 5.1.

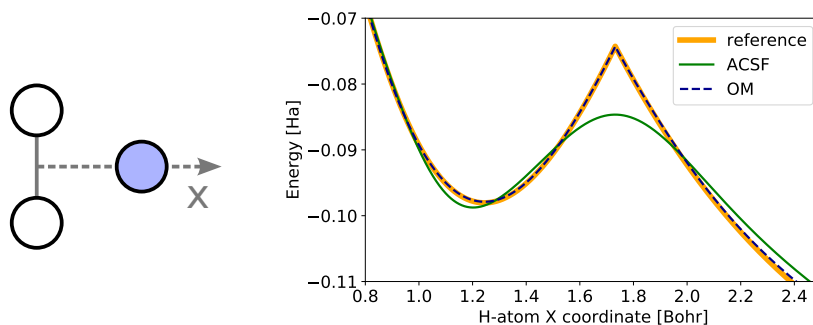


Figure 5.1: Cut through the PES of an H_3 system. The hydrogen atom shown in blue is moved along the x-axis, indicated by the dashed line in the left part of the figure. The right side shows the reference energy together with two fits obtained using ACSFs and the OM fingerprint. While the ACSFs can only learn a smooth function, the discontinuity in the first derivative of the OM fingerprint coincides with the conical intersection of the H_3 PES, where the three hydrogen atoms form an equilateral triangle, and allows for a much more accurate fit. The error introduced by the smoothness of the ACSF fit is not restricted to the kink itself but also leads to a slight offset of the local minimum in the PES.

In most cases however, the kinks are problematic, especially, in cases, where the high symmetry configurations coincide with local minima in the PES. One example for such a case is the OM fingerprint of the carbon atom in the ground state of a methane molecule. In Figure 5.2, the DFT energy together with the energy predicted by an ANN that uses the OM fingerprint of the carbon atom as inputs is shown. The discontinuity of the first derivative of the OM fingerprint at the ground state causes the same discontinuity in the energy and a global minimum of the learnt PES that is not at the high symmetry position.

One might hope, that a different ordering of the eigenvalues, that swaps eigenvalues at the crossing and therefore is continuous through them could help to resolve the issue. Unfortunately, it can easily be shown that no such ordering can exist. In Figure 5.3, OM eigenvalues are plotted along a circular path. At an angle of 0, the path goes through the ground state of methane and some eigenvalues cross. If one would now reorder the eigenvalues for the positive side of the plot, such that they are continuous, it would take two revolutions along the path to arrive back at the original descriptor for the same configuration. Furthermore, the configurations on both, sides of the plot are equivalent up to a 180 degree rotation and should hence result in the same descriptor.

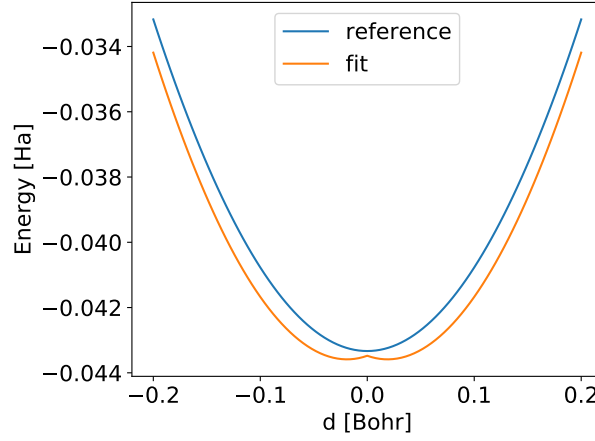


Figure 5.2: Potential energy of a methane molecule plotted on a trajectory through the ground state. The line labeled “fit” shows the energy obtained from a ANN fit that uses the OM fingerprint of the carbon atom as inputs. The discontinuity in the first derivative of the OM fingerprint causes the kink in the fit at the ground state geometry.

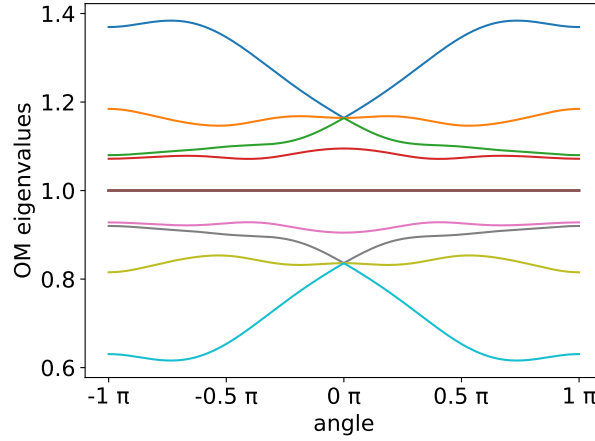


Figure 5.3: Eigenvalues of the overlap matrix along a circular path.

The problem of kinks in the OM fingerprint has been previously recognized and a post-processing scheme that transforms the eigenvalues e_i to a new descriptor \tilde{e}_i without kinks was proposed [137].

$$\tilde{e}_i = \frac{\sum_l e_l \exp\left(-\frac{1}{2}\left(\frac{e_l - e_i}{a}\right)^2\right)}{\sum_l \exp\left(-\frac{1}{2}\left(\frac{e_l - e_i}{a}\right)^2\right)} \quad (5.1)$$

When only two eigenvalues are present, this scheme is able to remove the discontinuity in the derivative. Unfortunately, the method fails, when a third eigenvalue is close in magnitude to the two crossing eigenvalues. A simple example of this failure is shown in Figure 5.4.

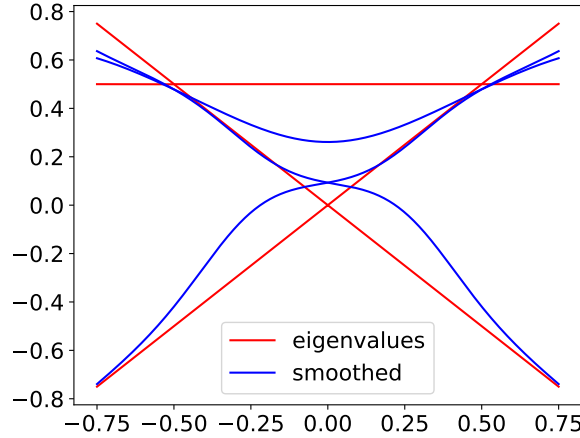


Figure 5.4: A simple example showing the failure of the smoothing scheme proposed in Reference [137]. The method is able to almost remove the kinks at ± 0.5 , where the third eigenvalue is different in magnitude compared to the crossing eigenvalues. At 0, however, the smoothing method fails and a kink is still visible.

To get rid of the discontinuities introduced by eigenvalue crossings when an arbitrary number of eigenvalues are nearby, a projection onto a set of smooth basis functions f_i can be used [213].

$$t_i = \sum_j f_i(e_j) \quad (5.2)$$

Due to the summation, the transformed descriptors t_i do not depend on the order of the e_i . Hence, this removes the difficulties that arise from the ordering, which was artificially introduced by sorting. The eigenvalues are therefore treated as a set, i.e., a collection of items that do not have any intrinsic order.

This naturally raises the question, how we can do machine learning on sets. This is not trivial, since in conventional approaches an order must always be imposed to associate one of the set elements with one of the input neurons. Due to the combinatorial explosion, summing over all permutations is also infeasible.

Luckily, it was previously shown [214], that any function f that depends on a set X with elements x , and is therefore invariant under permutation of the x can be expressed as

$$f(X) = \rho\left(\sum_{x \in X} \phi(x)\right) \quad , \quad (5.3)$$

where ρ and ϕ are suitable functions.

We can now realize, that when the projected eigenvalues t_i are used as inputs to an ANN, that for example predicts an energy, an expression that is equivalent to the one in Equation 5.3 is obtained. Then, the energy predicting ANN takes the role of ρ and the f_i represent the multivariate function ϕ . A MLP using such an appropriately projected descriptor should therefore, in principle, be perfectly able to learn the potential energy without suffering from any kinks introduced by the sorting of the OM eigenvalues and no information from the eigenvalues e_i should be lost during the projection. The question remains however, what functions should be used for the f_i . In Reference [213], a series of sine and cosine functions was proposed. Other possibilities include polynomial basis functions, such as Legendre or Tschebyschow polynomials. Unfortunately, we found these choices of basis functions unsuitable for machine learning applications. All the above-mentioned basis functions start to oscillate heavily with increasing order. This leads to very large derivatives and therefore a descriptor that changes very rapidly, even when only small displacements are applied to the atomic environment. We therefore decided to use ANNs to represent the f_i and use machine learning to obtain a set of optimal basis functions. We first attempted to train a model that includes the energy predicting ANN together with the ANN representing the f_i in one step. Unfortunately, we were not able to obtain a converged fit with this method. We therefore resorted to a two-step approach in which first the f_i are fit and then the energy predicting ANN is trained in a second step, just like with any other AED. In a first attempt, we trained the f_i to reproduce the eigenvalues e_j . For this we used the following loss function \mathcal{L}^{EV} .

$$\mathcal{L}^{\text{EV}} = \sum_i (t_{s(i)} - e_i)^2 \quad (5.4)$$

Here $s(i)$ represents the index of the i -th largest t_i . We hence first sort the t_i and then simply use the squared error with respect to the eigenvalues e_i . The resulting t_i for the circular path as shown in Figure 5.3 are shown in Figure 5.5. It can be seen, that the t_i manage to somewhat reproduce the original eigenvalues while being perfectly smooth at the crossings at the middle of the plot.

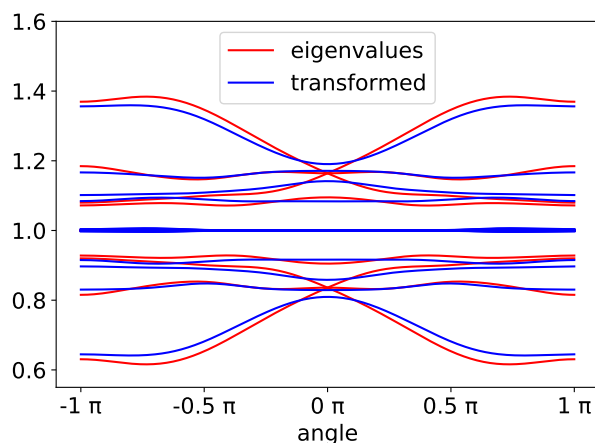


Figure 5.5: Eigenvalues of the overlap matrix along a circular path together with the transformed eigenvalues. Unlike the eigenvalues, the transformed eigenvalues are smooth.

As a second method to train the f_i , we defined a loss function \mathcal{L}^D that aims to reproduce the pairwise (euclidean) distances between pairs of structures. During the training we do not iterate over all training structures but instead pick two random structures a and b . The weights of the f_i are then optimized using the following loss function.

$$\mathcal{L}^D = \left(\sqrt{\sum_i (t_i^a - t_i^b)^2} - \sqrt{\sum_i (e_i^a - e_i^b)^2} \right)^2 + \lambda \left(\sum_i (t_i^a)^2 + (t_i^b)^2 \right) \quad (5.5)$$

Here the superscripts on the e_i and t_i indicate the configuration. The last term, including λ , serves as regularization. Since only the distances between fingerprints are used for training, adding a constant offset to all t_i would not change the loss function. The regularization term therefore ensures, that the t_i stay close to zero in magnitude. For our tests we found a value of $\lambda = 10^{-5}$ to be a good choice. A histogram of all pairwise distances in the training data, together with a plot of the learnt functions t_i are shown in Figure 5.6.

To compare the transformed versions of the OM fingerprint against the ACSFs and the untransformed OM fingerprint, we trained ANNs to predict the total energy of a methane molecule using the AEDs of the central carbon atom as inputs. We devised an energy decomposition scheme to decompose the total energy of the methane molecule into n-body terms. Fitting ANNs with ACSFs or the OM fingerprint to

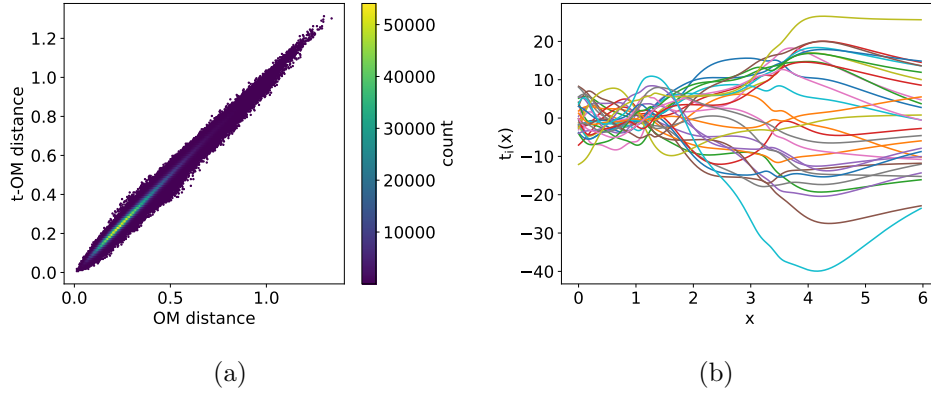


Figure 5.6: In (a), a 2D histogram of pairwise OM fingerprint distances and pairwise distances of the transformed fingerprint (t-OM) is shown. In (b), the learnt functions t_i are plotted.

each of the n-body energies individually allows us to determine whether the OM fingerprint and its transformed version really improve upon the description of higher body-order terms.

To decompose the energy of a methane molecule, we fit the energy using expressions of increasing body-order, after subtracting all the lower order contributions. The one-body energy is simply a constant energy offset. After subtracting the one-body energy, the two-body energy is fit with the following expression.

$$E_{2B} = \sum_i f_{2B}(r_i) \quad (5.6)$$

Here the sum goes over all four hydrogen atoms and r_i is the distance between each hydrogen atom and the carbon atom. The function f_{2B} , as well as the functions for the three- and four-body contributions are represented by an ANN consisting of two layers with 8 nodes each. The three body energy was then fit using the expression below.

$$E_{3B} = \sum_{i \neq j} f_{3B}(r_i, r_j, \alpha_{ij}) \quad (5.7)$$

Here α_{ij} is the angle between the hydrogen atoms i and j through the carbon atom.

In a last step, a four-body energy was fit to the remaining energy after subtracting the lower body-order contributions using the following expression.

$$E_{4B} = \sum_{i \neq j \neq k} f_{4B}(r_i, r_j, r_k, \alpha_{ij}, \alpha_{ik}, \alpha_{jk}) \quad (5.8)$$

The RMSE of the fit including the energies up to each body-order is shown in Table 5.1. One can see, that a clear convergence is obtained. The largest improvement is obtained after the inclusion of the three-body term. This might, at first, seem a bit surprising, since one would expect, that the energy is mostly dominated by the two body terms. But since the many-body expansion is only performed for the central carbon atom, two-body interactions between hydrogen atoms are only included with the three-body term.

Table 5.1: RMSE (meV) of the many-body fit including terms up to a certain body-order. The test RMSE is shown in parenthesis.

body-order	1	2	3	4
RMSD	498.6 (499.9)	376.5 (377.3)	59.01 (60.83)	9.47 (9.49)

We then benchmarked the different descriptors by fitting an ANN consisting of two layers with 15 nodes each to the energies of each body-order. We used 11 radial and 16 angular ACSFs. The OM fingerprint was constructed using three s and one p orbital. The training and test dataset consist of 5000 structures each, that were sampled from an MD trajectory at 2000 K. The results are shown in Table 5.2.

Table 5.2: RMSE (meV) obtained for energy fits using different descriptors. The test RMSE is shown in parenthesis. The body-order of the reference data is shown in the top row. The column marked with 1-4 contains results that were fit to energies from all body-orders up to four. The row marked with σ shows the standard deviation of the test and training data energies. The rows marked with ACSF and OM show results for fits that use ACSFs and the OM fingerprint as descriptors respectively. The results marked with SF+OM used the concatenated OM and SF descriptors. Results marked with OM^{EV} and OM^D are based on a transformed OM fingerprint that were trained using the \mathcal{L}^{EV} and \mathcal{L}^{D} loss functions respectively.

body-order	2	3	4	1-4
σ	326.0 (318.4)	374.3 (371.6)	59.67 (58.48)	499.2 (497.2)
ACSF	0.326 (0.991)	9.634 (15.49)	43.42 (48.09)	51.07 (61.31)
OM	24.61 (36.03)	8.340 (13.80)	4.808 (8.291)	18.05 (29.07)
ACSF+OM	0.550 (3.071)	1.904 (10.99)	2.533 (6.152)	5.568 (14.02)
OM ^{EV}	105.5 (123.9)	28.51 (33.27)	17.56 (23.09)	88.77 (96.72)
OM ^D	74.94 (85.37)	30.70 (36.62)	24.40 (28.86)	58.30 (67.79)
ACSF+OM ^D	0.359 (1.778)	5.995 (15.61)	7.745 (11.70)	10.97 (22.22)

As expected, the fit based on ACSFs performs very poorly for the four-body energy with the RMSE being almost as large as the standard deviation of the energies in the training data. The OM fingerprint on the other hand is well able to capture the four-body interactions. Both the OM fingerprint and the ACSFs perform similarly for the three-body interactions, but surprisingly, the ACSFs outperform the OM fingerprint for the two-body energies. We think, that this is due to the fact, that the ACSFs, by being sums of two body functions, provide a more direct description of the interatomic distances while in the OM fingerprint the two-body relationships are blended together with all higher-order terms by the diagonalization step. The relationship between the descriptor and the energy that has to be captured by the ANN is therefore much simpler and easier to learn when ACSFs are used. This is supported by the fact, that a simple linear ridge regression on the ACSFs already results in a training and test error of 1.99 meV and 1.80 meV respectively. A linear fit based on the OM fingerprint results in much higher training and test errors of 94.9 meV and 91.2 meV. The best fit was obtained using a descriptor that was formed by concatenating the OM fingerprint with the ACSFs. This way, the good description of two-body terms by the ACSFs and the superior description of higher body-order terms by the OM fingerprint can be combined.

The results also show, that the transformed OM fingerprint, that was trained using the loss function based on pairwise distances outperforms the one trained to reproduce the original eigenvalues. Unfortunately, the transformed versions of the OM fingerprint were not able to improve upon the original version of the fingerprint, in terms of the RMSE, even though the unphysical kink at the ground state geometry is removed. However, in combination with the ACSFs, the high accuracy for the two-body terms can be recovered. While the training error is very similar to the ACSFs alone, the test error is slightly increased, indicating slight overfitting. The RMSE of the transformed OM fingerprint combined with the ACSFs is only slightly higher than the RMSE obtained from a fit where the original OM fingerprint is combined with the ACSFs. In most cases, ensuring a smooth fit of the PES is well worth the small decrease in fitting accuracy. The results are therefore quite promising, but further research is needed to determine, how the description of two-body terms can be improved in the OM fingerprint and its transformed variants.

Future studies will also need to include test systems beyond the simple methane molecule presented in this chapter. The methane molecule proved to be a good test system, to decompose the total energy into n-body contributions, which allowed us to identify the weakness of the OM fingerprint in describing two-body interactions.

In more realistic applications however, the smoothed OM fingerprint would be used in the context of a HDNNP where the AEDs of all atoms and not only the central one would be used. In such a scenario compensation effects might occur, where the deficiencies of one AED can be accounted for in the AEDs of neighboring atoms. Future tests will therefore need to include larger test systems, where the transformed OM fingerprint is used as input to a HDNNP.

6 FUNNEL HOPPING MONTE CARLO

6.1 BROKEN ERGODICITY

In the previous Section 2.2.2 we saw how MC (or MD) simulations can be used to sample the Boltzmann distribution. Unfortunately, we often run into severe problems when we want to apply these methods. The difficulty is, that the PES can contain many local minima that are close in energy but can be separated by high energy barriers. At low enough temperatures the Boltzmann distribution of such a PES will then have sharp peaks at the energy minima while being very small at the transition states in between. Since the magnitude of the MC moves we can include in our simulation is limited, multiple subsequent MC steps across the barriers are required to pass from one minimum to another. These moves across the high energy regions are very unlikely due to the low Boltzmann probability. Hence, very long simulation times can be required until all local minima are sampled according to their correct probability. In many cases convergence cannot be achieved within the available computation time.

The situation is illustrated in the one dimensional potential energy function shown in Figure 6.1a. The potential energy function shown in the figure features two local minima separated by a barrier. The left minimum is slightly lower in energy, making it the preferred configuration at low temperatures. At higher temperatures the right minima is preferred due to it being wider and thus having a higher entropy.

When we run a MC simulation on this example energy, we would expect the individual samples to be distributed according to the Boltzmann distribution shown in Figure 6.1b. The histogram of such a simulation over 10^6 iterations at $T = 0.25$ is shown in Figure 6.2a. It can be seen that despite the large number of MC iterations, the simulation failed to predict the correct probabilities for each of the two local minima. From Figure 6.2b, it is clear that only few transitions between the two local minima happened.

Parts of this chapter were adapted from J. A. Finkler and S. Goedecker. “Funnel hopping Monte Carlo: An efficient method to overcome broken ergodicity”. *The Journal of chemical physics* 152:16, 2020, p. 164106, with the permission of AIP Publishing.

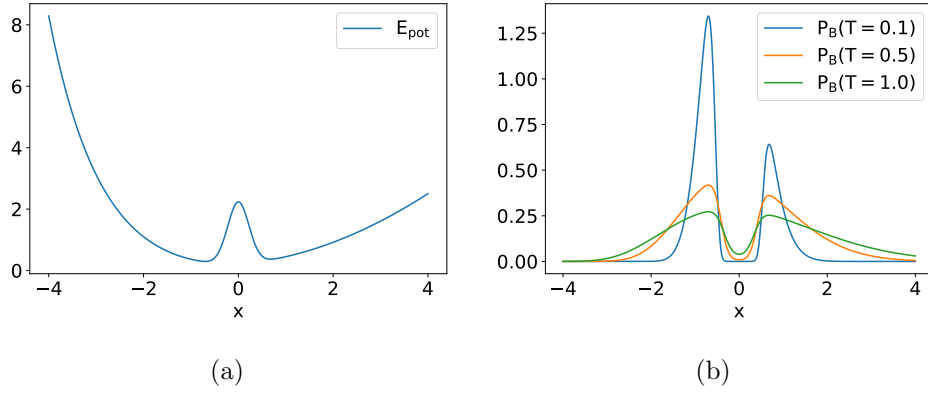


Figure 6.1: Example potential energy function (a), featuring two local minima separated by a barrier. The Boltzmann distribution is shown in (b) for different temperatures.

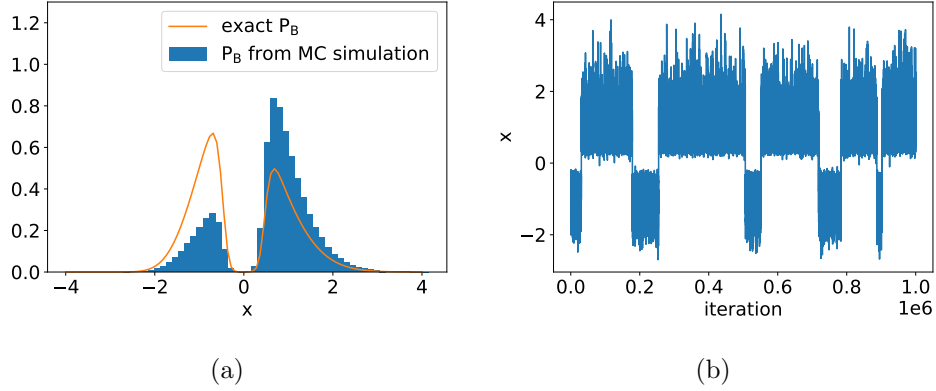


Figure 6.2: Histogram of a MC simulation of the example potential at $T = 0.25$ (a) and the position of the MC walker during each iteration (b).

Due to the higher dimensionality and the higher number of local minima which was suggested to increase exponentially with respect to the number of atoms in the system [88, 215] the problem is even more severe in real atomic systems.

The problem of energy barriers preventing complete sampling of the PES is known as broken ergodicity. In theory MC sampling is ergodic, meaning that every region on the PES will be visited according to its probability given a long enough simulation. Since the Boltzmann probability is always strictly greater than zero, even high barriers should be passed eventually. In practice however, the amount of iterations for which we can run our MC simulation is limited by the speed and capability of our computers. Therefore, if high barriers are present in the system, it can seem as if our MC simulations were not ergodic.

6.1.1 THE HARMONIC SUPERPOSITION APPROXIMATION

One way to completely avoid broken ergodicity and also the need for a MC simulation is the harmonic superposition approximation (HSA) [216, 217]. In this section the method will be explained using the previously introduced one-dimensional example potential energy function. The generalization of the method to higher dimensional systems is straightforward and can be done by using multivariate Gaussian functions instead of the one dimensional ones used here.

To apply the HSA to our example system, we approximate the energy around each local minimum using a Taylor expansion.

$$E_{\text{h.a.}}(x) = E(x_0) + \frac{1}{2}(x - x_0)^2 E''(x_0) \quad \left| \quad E''(x_0) = \frac{d^2 E(x)}{dx^2} \right|_{x_0} \quad (6.1)$$

A plot of the two approximated energies is shown in Figure 6.3 (a).

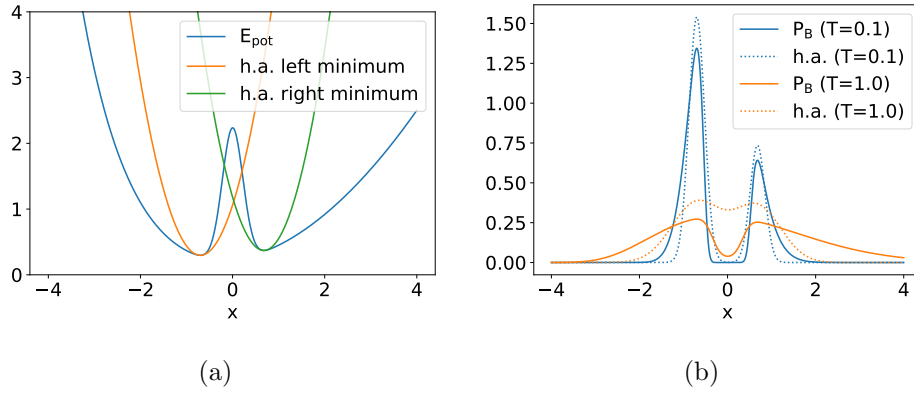


Figure 6.3: Energy derived from the harmonic approximation for both minima (a) and the corresponding Boltzmann distribution computed in the harmonic superposition approximation (b).

We can now calculate the Boltzmann probabilities for such an energy function.

$$\begin{aligned} P_{\text{B.h.a.}}(x, T) &= \frac{1}{Z_{\text{h.a.}}(T)} \exp\left(\frac{-E_{\text{h.a.}}(x)}{k_B T}\right) \\ &= \frac{1}{Z_{\text{h.a.}}(T)} \exp\left(\frac{-E(x_0)}{k_B T}\right) \exp\left(\frac{-(x - x_0)^2 E''(x_0)}{2k_B T}\right) \end{aligned} \quad (6.2)$$

The partition function $Z_{\text{h.a.}}(T)$ is given as follows.

$$Z_{\text{h.a.}}(T) = \exp\left(\frac{-E(x_0)}{k_B T}\right) \sqrt{\frac{2\pi k_B T}{E''(x_0)}} \quad (6.3)$$

We can now approximate the global Boltzmann probability $P_{\text{B.h.a.}}^{\text{global}}$ by weighting the $P_{\text{B.h.a.}}$ of each minimum by their partition function.

$$P_{\text{B.h.a.}}^{\text{global}}(x, T) = \frac{1}{\sum_j Z_{\text{h.a.}}^j(T)} \sum_i Z_{\text{h.a.}}^i(T) P_{\text{B.h.a.}}^i(x, T) \quad (6.4)$$

To obtain a good approximation, all minima that contribute significantly to $P_{\text{B.h.a.}}^{\text{global}}$ (i.e., $Z_{\text{h.a.}}^i(T)/\sum_j Z_{\text{h.a.}}^j(T) \gg 0$) have to be included in the sum in Equation 6.4. This can be challenging for systems that have many local minima with a low energy, such as atomic clusters. The global Boltzmann probability calculated in the HSA is shown in Figure 6.3 (b). It can clearly be seen, that at lower temperatures the HSA holds quite well but fails at higher temperature, since it cannot take the anharmonicity of the potential wells into account.

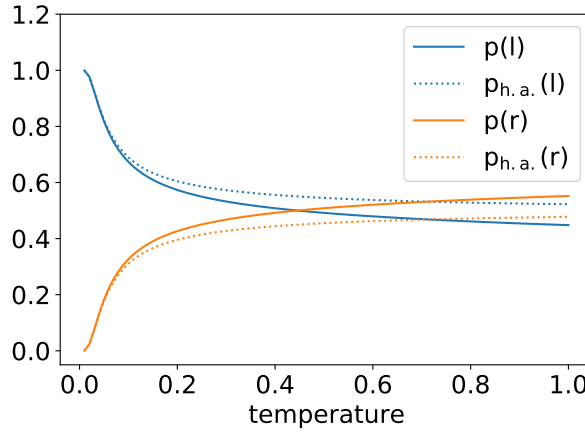


Figure 6.4: Probability of finding the example system on the left ($x < 0$) or right side ($x > 0$) of the barrier. Exact results ($p(l)$ and $p(r)$) as well as results obtained from the HSA ($P_{\text{h.a.}}(l)$ and $P_{\text{h.a.}}(r)$) are shown. The HSA fails to predict the slight preference for the right side at higher temperatures.

In Figure 6.4 the probability of finding the example system on the left side ($x < 0$) and right side ($x > 0$) of the barrier are shown. Again, at low temperatures the HSA is very close to the exact result. However, it is not able to correctly predict that the right side is preferred at higher temperatures. The HSA should therefore only be used at low temperatures. Up to which temperatures depends on the degree of anharmonicity of the local minima in the system. An application of the HSA to LJ clusters can be found in Reference [25]

6.2 ADVANCED MONTE CARLO TECHNIQUES

Since high energy barriers can be found in many systems, many approaches and methods have been developed that aim to overcome the problem of broken ergodicity in MC based simulations. Some methods, such as umbrella sampling [12–14] or metadynamics [15] use biasing potentials to overcome energy barriers. While in umbrella sampling, the potential is added in advance to the simulation, metadynamics adds biasing potentials dynamically during the simulation to avoid revisiting regions that are already well explored by the MC simulation. Both methods use collective variables to define the biasing potentials. Collective variables are parameters, derived from the atomic coordinates, that can be used to characterize the transition between the local minima that are considered in the simulation. Such collective variables, for example order parameters, describing a phase transition, have to be chosen manually and are very system specific. Finding a suitable collective variable can therefore be a challenge on its own.

Other approaches try to sample the inverse density of states to obtain a flat energy histogram. One such method is multicanonical sampling [16, 17], for which the density of states has to be known *a priori*. Wang–Landau sampling [18, 19] overcomes this problem by computing the density of states on the fly during the simulation. Despite its elegance and broad applicability, the Wang–Landau method can be difficult to apply to systems with continuous degrees of freedom and requires knowledge about the range of accessible energies. If multiple funnels with high barriers are present, the Wang–Landau method can fail to achieve adequate transition rates between the funnels as only local moves are used. In particular, the method was not able to converge to the correct result when applied to the 31 and 38 atom LJ clusters and satisfactory results were achieved only after an order parameter was used to construct a two-dimensional density of states [218]. In nested sampling [20–23], a random uniform sample from the full configuration space is generated in the first step. The sampled configuration space volume is then gradually reduced by replacing the highest energy sample with a new sample that is constrained to the sub-volume of configuration space which is lower in energy than the previous maximum energy. The difficulty of the method lies in the proposal of new, lower energy configurations. Due to the rapidly decreasing acceptable configuration space volume, rejection sampling becomes infeasible and more sophisticated methods have to be used [23]. In Boltzmann generators [219], invertible ANNs are trained to learn a coordinate transformation between a systems configuration and a latent

space, such that the Boltzmann distribution in the configuration space maps to a Gaussian distribution in the latent space. Once trained, the Boltzmann generator can then be used to generate one-shot samples from the Boltzmann distribution by applying the learnt transformation to Gaussian distributed samples in the latent space. Thermodynamic quantities can then be computed by reweighting the one-shot samples appropriately to account for errors in the learnt transformation.

Thermodynamic integration is a related technique, which does not aim to sample the whole PES in one simulation but instead allows for the computation of free energy differences, i.e., the ratio between partition functions for different parts of the PES. In thermodynamic integration, a parametrized path between two regions of interest has to be found along which the derivative of the free energy is numerically integrated to obtain the total free energy difference. Such a path can often be difficult to find. Therefore, paths to systems for which the free energy is known analytically, such as Einstein crystals or an ideal gas, can be used to obtain absolute free energies [220]. Since the free energy difference, is then an often relatively small difference between two large absolute free energies, special attention has to be paid to errors introduced during the integration. Furthermore, the method can still suffer from broken ergodicity when, for example, the free energy of a whole funnel is computed since the simulation still needs to cross the barriers between minima within the same funnel [221].

6.2.1 REPLICA EXCHANGE MONTE CARLO

Another very popular approach are replica exchange (RX) [222] methods. In RX simulations, configurations between parallel MC simulations that sample different distributions are exchanged. One might for example couple a MC simulation to another simulation on a PES, where barrier heights are artificially lowered. Another possibility is, to couple several simulations at different temperatures. This method, also called parallel tempering (PT) [223, 224], takes advantage of the fact that MC simulations at higher temperatures are able to cross barriers by exchanging configurations between simulations at different temperatures. If we consider an ensemble of N MC simulations at different temperatures T_i and potential energy functions E_i , as one global simulation, the probability of a state $\{\mathbf{R}_i\}$ is given by the product of the individual probabilities.

$$P_{\text{global}}(\{\mathbf{R}_i\}) = \prod_{i=1}^N P(\mathbf{R}_i) = \prod_{i=1}^N \exp\left(\frac{-E_i(\mathbf{R}_i)}{k_B T_i}\right) \quad (6.5)$$

We can now propose a MC move that exchanges the configuration between two replicas j and k . We then accept or reject the move according to the Metropolis–Hastings criterion.

$$\begin{aligned}
& \alpha(\mathbf{R}_1, \dots, \mathbf{R}_k, \dots, \mathbf{R}_j, \dots, \mathbf{R}_N | \mathbf{R}_1, \dots, \mathbf{R}_j, \dots, \mathbf{R}_k, \dots, \mathbf{R}_N) \\
&= \min \left(1, \frac{\exp\left(\frac{-E_1(\mathbf{R}_1)}{k_B T_1}\right) \dots \exp\left(\frac{-E_j(\mathbf{R}_k)}{k_B T_j}\right) \dots \exp\left(\frac{-E_k(\mathbf{R}_j)}{k_B T_k}\right) \dots \exp\left(\frac{-E_N(\mathbf{R}_N)}{k_B T_N}\right)}{\exp\left(\frac{-E_1(\mathbf{R}_1)}{k_B T_1}\right) \dots \exp\left(\frac{-E_j(\mathbf{R}_j)}{k_B T_j}\right) \dots \exp\left(\frac{-E_k(\mathbf{R}_k)}{k_B T_k}\right) \dots \exp\left(\frac{-E_N(\mathbf{R}_N)}{k_B T_N}\right)} \right) \\
&= \min \left(1, \exp \left(\frac{E_j(\mathbf{R}_j) - E_j(\mathbf{R}_k)}{k_B T_j} - \frac{E_k(\mathbf{R}_j) - E_k(\mathbf{R}_k)}{k_B T_k} \right) \right)
\end{aligned} \tag{6.6}$$

Since the move is performed according to the Metropolis–Hastings criterion, detailed balance is preserved and the method is exact. The temperatures at which the individual simulations are performed have to be chosen carefully. The lowest temperature is the lowest one for which simulation results are needed. The highest temperature in the ensemble has to be chosen such that the simulation is able to cross the highest barriers in the system. This barrier height is not easy to obtain and a good intuition or knowledge of the studied system is required.

Unfortunately it is in most cases not sufficient to only perform simulations at two temperatures. If the temperature difference between two simulations that exchange configurations is too high, the respective Boltzmann distributions have very little overlap and exchange moves are only very rarely accepted. Configurations taken from a high temperature simulation will have a very small Boltzmann probability at low temperatures. Therefore, usually a series of temperatures is simulated and exchanges are performed between neighboring temperatures. Using too many parallel simulations can also be disadvantageous. Not only does the computational cost of the simulations increase, but also the convergence of the simulation is impaired. The exchange of configurations between temperatures is similar to a diffusion process. If the temperatures are chosen too densely, the transfer of configurations from the higher temperatures, where barriers are crossed, to the lower temperatures is slowed down. The optimal temperature allocation is related to the entropy difference between temperatures but this quantity is typically not known before the simulation. A reasonable starting point can be obtained by assuming a system with constant heat capacity for which the optimal temperature allocation is a geometric series [225]. For real systems, where the heat capacity is not constant, a slightly different allocation might be better and algorithms that dynamically adapt the temperatures during

the simulation such that an optimal acceptance rate of 20 % is obtained, have been proposed [226]. In our simulations we found that a fixed allocation of temperatures in a geometric series performed reasonably well.

In many cases, the improved convergence of the PT simulation makes up for the additional cost of the extra simulations and often results for more than a single temperature are needed anyway. For example, in our studies we found, that even after 10^{10} iterations a standard MC simulation of the 38 atom Lennard-Jones cluster (LJ₃₈ cluster) was very far from convergence, while a PT simulation would converge after a tenth of the above-mentioned number of iterations. However, for many systems, PT still fails to converge. When very high barriers are present, PT can still fail to cross them efficiently, since configurations have to be passed between a larger number of simulations. Furthermore, the accessible configuration space becomes very large at high temperatures, making barrier crossings a very rare event. While PT is able to converge after 10^9 iterations for the LJ₃₈ cluster, we would not be able to afford this many energy and force evaluations for a system where DFT calculations need to be used.

6.2.2 SMART DARTING MONTE CARLO

We therefore developed a method called Funnel Hopping Monte Carlo (FHMC) [94], to overcome high energy barriers in MC simulations more efficiently. Our method was inspired by smart darting Monte Carlo [24], a method that introduces a new MC move, that is not local, but goes directly from one low energy region to another, bypassing the barrier in between entirely.

In advance to a smart darting simulation, local minima $\{\mathbf{M}_i\}$ are identified and so-called darting vectors are defined as the difference between two local minima.

$$\mathbf{D}_{ij} = \mathbf{M}_i - \mathbf{M}_j \quad (6.7)$$

Also a parameter ϵ has to be chosen, to define spherical darting regions around each local minimum. The parameter ϵ should be chosen small enough, that no two darting regions overlap. During the simulation, darting moves will be used in addition to standard MC moves with a certain probability. If a darting move is attempted, it is first determined, if the current MC walker is inside one of the darting regions, i.e., if $\|\mathbf{R} - \mathbf{M}_i\| < \epsilon$ for any i . If this is the case, a darting move is attempted by first picking a random darting vector \mathbf{D}_{ij} starting from the current darting region i

and going to region j . The proposed configuration is then generated by adding the darting vector to the current position of the walker.

$$\mathbf{R}' = \mathbf{R} + \mathbf{D}_{ij} \quad (6.8)$$

The move is then accepted or rejected according to the Metropolis–Hastings criterion. Despite its elegance, the method has several disadvantages. Since atomic systems are independent under rigid transformations, such as translation and rotation, the darting vectors are ill-defined and a rotation of the system during the simulation will prevent all later darting moves from ending up close to the desired local minimum. A similar problem occurs when two atoms of the same element exchange positions. We also found that local minima are in most cases not spherical like the darting regions but have very different hard and soft modes and should rather be considered very eccentric ellipsoids. Simply darting by addition of a darting vector as in Equation 6.8 will therefore only lead to very little overlap of the low energy regions and hence a low acceptance rate of darting moves. The problem is illustrated in Figure 6.5.

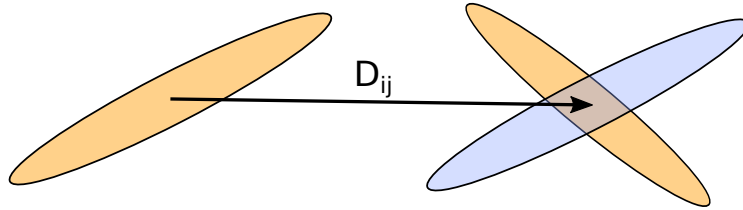


Figure 6.5: The two low energy regions shown in orange are connected by the darting vector D_{ij} . Every point from the left region is darted to the blue region on the right. Due to the eccentric shape of the region, the overlap, where darting moves would be accepted, is minimal. The problem is even more severe in higher dimensions.

Lattice switch MC [227–229] also uses a global move constructed according to Equation 6.8. In this method applicable to systems with periodic boundary conditions an artificial bias is added to the simulation to drive the MC walker towards the regions where the darting moves are more likely to be accepted.

6.3 THE FUNNEL HOPPING MONTE CARLO ALGORITHM

The above-mentioned challenges of a missing invariance under important symmetries and the low acceptance rate of global moves are overcome by FHMC with two important ingredients. Firstly, we developed a way to identify atomic configurations that is invariant under rotation, translation, as well as permutations of equivalent

atoms. The second ingredient is the use of Gaussian mixtures (GMs) instead of darting vectors to efficiently propose new configurations. This way high quality moves with a high chance of being accepted can be proposed and no artificial biasing is needed which would lead to unnecessary sampling.

6.3.1 IDENTIFYING EQUIVALENT CONFIGURATIONS USING ECKART SPACE AND THE RMSD

As already mentioned, atomic systems with free boundary conditions are invariant under rotation, translation and the permutation of equivalent atoms. To remove this ambiguity from a given configuration, we used the root mean squared deviation (RMSD). The RMSD is defined as follows.

$$\text{RMSD}(\mathbf{R}, \mathbf{R}^{\text{ref}}) = \sqrt{\frac{\sum_{i=1}^{N_{\text{at}}} \|\vec{R}_i - \vec{R}_i^{\text{ref}}\|^2}{N_{\text{at}}}} \quad (6.9)$$

Given a reference configuration \mathbf{R}_{ref} , we can fix the translation, rotation and permutation of the atoms, by finding the optimal translation rotation and permutation, that minimize $\text{RMSD}(\mathbf{R}, \mathbf{R}^{\text{ref}})$. The optimal translation can always be found by superimposing the centers of mass of the two configurations. We will therefore always assume, without loss of generality, that the centers of mass are set to the coordinate origin. It can be shown, that if the RMSD between two configurations is minimal, the so-called Eckart conditions [230] are met [231].

The Eckart conditions are the following.

$$\sum_{i=1}^N \vec{R}_i - \vec{R}_i^{\text{ref}} = \vec{0} \quad (6.10)$$

$$\sum_{i=1}^N \vec{R}_i \times \vec{R}_i^{\text{ref}} = \vec{0} \quad (6.11)$$

We now define the displacement \mathbf{d} as the difference between the aligned structure and the reference.

$$\vec{d}_i = \vec{R}_i - \vec{R}_i^{\text{ref}} \quad (6.12)$$

With these we can now write the Eckart conditions as follows.

$$\sum_{i=1}^N \vec{d}_i = \vec{0} \quad (6.13)$$

$$\sum_{i=1}^N \vec{d}_i \times \vec{R}_i = \vec{0} \quad (6.14)$$

From these six linear equations it follows that all displacement vectors \mathbf{d} , obtained from a minimal RMSD alignment, are orthogonal to the following six vectors.

$$\begin{aligned} \mathbf{V}^1 &= \begin{pmatrix} 1 \\ 0 \\ 0 \\ 1 \\ 0 \\ 0 \\ 1 \\ \vdots \end{pmatrix} \quad \mathbf{V}^2 = \begin{pmatrix} 0 \\ 1 \\ 0 \\ 0 \\ 1 \\ 0 \\ 0 \\ \vdots \end{pmatrix} \quad \mathbf{V}^3 = \begin{pmatrix} 0 \\ 0 \\ 1 \\ 0 \\ 0 \\ 1 \\ 0 \\ \vdots \end{pmatrix} \\ \mathbf{V}^4 &= \begin{pmatrix} 0 \\ \vec{R}_{1,z}^{\text{ref}} \\ -\vec{R}_{1,y}^{\text{ref}} \\ 0 \\ \vec{R}_{2,z}^{\text{ref}} \\ -\vec{R}_{2,y}^{\text{ref}} \\ 0 \\ \vdots \end{pmatrix} \quad \mathbf{V}^5 = \begin{pmatrix} -\vec{R}_{1,z}^{\text{ref}} \\ 0 \\ \vec{R}_{1,x}^{\text{ref}} \\ -\vec{R}_{2,z}^{\text{ref}} \\ 0 \\ \vec{R}_{2,x}^{\text{ref}} \\ \vec{R}_{3,z}^{\text{ref}} \\ \vdots \end{pmatrix} \quad \mathbf{V}^6 = \begin{pmatrix} \vec{R}_{1,y}^{\text{ref}} \\ -\vec{R}_{1,x}^{\text{ref}} \\ 0 \\ \vec{R}_{2,y}^{\text{ref}} \\ -\vec{R}_{2,x}^{\text{ref}} \\ 0 \\ \vec{R}_{3,y}^{\text{ref}} \\ \vdots \end{pmatrix} \end{aligned} \quad (6.15)$$

Here the vectors \mathbf{V}^1 , \mathbf{V}^2 and \mathbf{V}^3 are obtained from Equation 6.13 and \mathbf{V}^4 , \mathbf{V}^5 and \mathbf{V}^6 are obtained from Equation 6.14.

We now construct $3N - 6$ basis vectors \mathbf{B}^i which are orthogonal to each other as well as to the vectors \mathbf{V}^j .

$$\|\mathbf{B}^i\| = 1 \quad (6.16)$$

$$\mathbf{B}^i \cdot \mathbf{B}^j = 0 \quad \forall \quad i \neq j \quad (6.17)$$

$$\mathbf{B}^i \cdot \mathbf{V}^j = 0 \quad (6.18)$$

The \mathbf{B}^i can be obtained using an orthogonalization algorithm such as for example the stabilized Gram-Schmidt process.

Using the \mathbf{B}^i as a basis we can remove 6 coordinates from our displacement vectors \mathbf{d} . These six coordinates become redundant because we fixed the rotation and

translation of the configuration. This allows us to assign a unique set of $3N - 6$ coordinates to every configuration.

The $3N$ dimensional vector \mathbf{d} is transformed to the $3N - 6$ dimensional vector \mathbf{d}' , using the basis spanned by the \mathbf{B}^i , as follows.

$$d'_i = \mathbf{d} \cdot \mathbf{B}^i \quad | \quad i = 1 \dots 3N - 6 \quad (6.19)$$

Here d'_i denotes the i th component of vector \mathbf{d}' .

To obtain the original configuration \mathbf{R} , \mathbf{d}' is simply transformed back to the $3N$ dimensional space and added to the reference configuration \mathbf{R}^{ref} .

$$\mathbf{R} = \mathbf{R}^{\text{ref}} + \mathbf{d} = \mathbf{R}^{\text{ref}} + \sum_{i=1}^{3N-6} d'_i \mathbf{B}^i \quad (6.20)$$

The Eckart conditions were also previously used in a modified version of the smart darting algorithm [232]. Since the transformations to the Eckart space used Euler angles, the transformation was non-linear and a Jacobian matrix had to be computed. Results were only reported for the 7 atom LJ cluster.

MINIMIZATION OF THE RMSD

In systems of distinguishable atoms, the RMSD can be considered a function of the rotation of the system as the optimal translation can be found trivially by superimposing the mean atom positions of the two systems. In systems consisting of indistinguishable atoms however we are confronted with some kind of chicken and egg problem, as the optimal rotation depends on one hand on the permutation indicating which atoms from each system we pair together while on the other hand the optimal permutation depends on the rotation. Each problem by itself can be solved by known algorithms. To find the optimal rotation to a given permutation we can use an algorithm based on quaternions [233–235]. To determine the optimal permutation for a given rotation we can use the Hungarian algorithm [236] or the shortest augmenting path algorithm [237]. In our implementation we used the algorithm outlined in Section 4 of Reference [238], which we adapted to accept floating point numbers in the cost matrix. To solve the combined problems we use both algorithms in alternation until a converged solution is found. As each of the two algorithms will only decrease the RMSD, repeated application of them will lead to a local optimum of the RMSD. To find the globally optimal RMSD we initialized the local optimization with different initial rotations. These rotations were represented

by unit quaternions. Because quaternions with opposite sign represent the same rotation each rotation has to be represented by a pair of points on opposite sides of a four dimensional unit hypersphere. To distribute these rotations as uniformly as possible over the hypersphere of all rotations, we put a charge on each point and minimized the Coulomb energy using a simple gradient descent algorithm with the additional constraints that the points be on the unit sphere. An illustration of the results of this method, when applied to points on a 3D sphere is shown in Figure 6.6. These uniformly distributed rotations increase the chances of finding the globally minimal RMSD within a limited number of steps significantly.

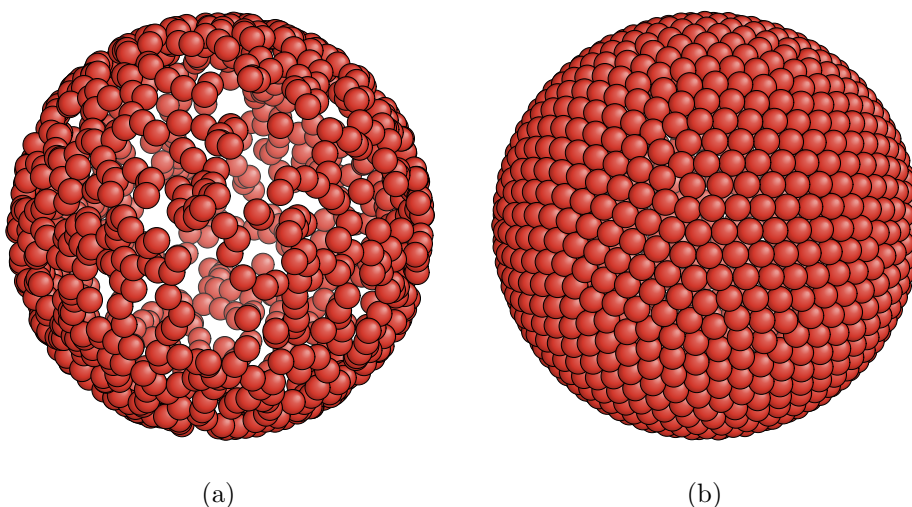


Figure 6.6: Two sets of 500 points, distributed on a 3D sphere are shown. It can be seen that a random distribution (a) leaves wide gaps, that are not covered by points while also putting some points very close together, resulting in redundant computation. These problems are avoided by using an even distribution of points as shown in (b).

To test our algorithm we generated random configurations with an RMSD of 0.1 to the local minimum of the 38 atom LJ cluster with the third-lowest energy. We chose this configuration because it is the lowest local minimum, that has no rotational symmetry. The RMSD of 0.1 was chosen because it is large enough such that the alignment is not trivial, but small enough to ensure no other permutation than the original one can result in a smaller RMSD. In our experiments we found that by using 400 evenly spread initial rotations the globally minimal RMSD solution was found in 100% of the 10000 test alignments performed. If we used random initial rotations instead, only 85% of the alignments succeeded. Even when using 600 random initial rotations, the minimal RMSD solution was only found in 95% of the attempts.

The code used for finding the minimal RMSD between two structures has been published online [239].

6.3.2 USING GAUSSIAN MIXTURES TO PROPOSE MONTE CARLO MOVES

Using the methods described in the previous section, we are able to uniquely map structures into a $3N - 6$ dimensional coordinate space. This capability is the foundation of our FHMC algorithm, as it allows us to generate Monte Carlo moves that directly target regions of low energy.

By using some metric, which may be the RMSD or fingerprints [240], we assign each point in configuration space to its nearest minimum. Thus, each minimum is assigned a part of the configuration space. In our implementation we used fingerprints because they are computationally cheaper. For each minimum \mathbf{R}_i we will then define a probability distribution $q_i(\mathbf{r})$ which will live in the $3N - 6$ dimensional fixed frame coordinate space, and sample the low energy region around this minimum. These q_i should cover the high probability regions as exhaustively as possible. This can be done for example by using the harmonic approximation which would result in an algorithm similar to the one proposed in Reference [241] or by a Gaussian mixture as we will propose in the following section. It is important to note here that these distributions do not carry any physical meaning. How well these resemble the Boltzmann distribution does not influence the accuracy of the final algorithm as detailed balance is always satisfied. The $q_i(\mathbf{r})$ s just allow the FHMC algorithm to propose better moves that are more likely to be accepted which results in a more efficient sampling.

To propose a FHMC move, we first determine the minimum \mathbf{R}_i that is closest to the current configuration. We then randomly choose one of the other minima and draw a configuration from the corresponding q_j . The choice of the target minimum can be done completely random or one can include a transition matrix T with T_{ij} being the probability to choose minimum j when the current configuration is closest to minimum i . Such a transition matrix can be used for example to avoid proposing moves to minima that are too different in energy. The proposed move is then accepted with probability α according to the Metropolis criterion.

$$\alpha(\mathbf{r} \rightarrow \mathbf{r}') = \min\left(1, \exp\left(-\frac{E(\mathbf{r}') - E(\mathbf{r})}{k_B T}\right) \frac{q_i(\mathbf{r})}{q_j(\mathbf{r}')} \frac{T_{ji}}{T_{ij}} \frac{h_{\alpha i}}{h_{\alpha j}}\right) \quad (6.21)$$

Here $h_{\alpha i}$ is the point group order, i.e., the number of symmetry operations that leave the geometry unchanged, of the i th minimum. If a minimum has a rotational

symmetry, $h_{\alpha i}$ alignments with the same RMSD exist. All these alignments will result in different coordinates if transformed to the basis vectors \mathbf{B}^i while they describe exactly the same configuration. It is therefore $h_{\alpha i}$ as likely to pick a configuration as $q_i(\mathbf{r})$ indicates, because $h_{\alpha i}$ points exist that correspond to that configuration and are equally likely.

The distributions q_i play two important roles. First we can see from the above equation that the acceptance probability is proportional to $q_i(\mathbf{r})$ which means that the better the q_i cover the high probability regions the higher is the expected acceptance rate. The other role of the q_i is that they are used to generate the proposed configurations. Again one can see that if the q_i cover the high probability regions well we will propose configurations with a low energy which will result in a high acceptance probability.

Although the Gaussian mixtures are usually quite localized they do in principle have infinite support. This means that it is possible that the proposed configuration \mathbf{r}' lies outside the part of configuration space that is assigned to the minimum j . This would result in a move where detailed balance is not satisfied, as the inverse move is not possible. Rejecting moves to configurations outside the region of configuration space assigned to minimum j ensures that the detailed balance condition is met and no errors are introduced.

GAUSSIAN MIXTURES

A rather straight forward approach to define the q_i is to use the harmonic approximation of the energy. As the harmonic approximation is a quadratic function, the Boltzmann distribution of this energy will be a Gaussian distribution of the following form.

$$q_i^{\text{h.a.}}(\mathbf{r}) = \frac{1}{\sqrt{(2\pi k_B T)^{3N-6} \text{Det}(H^{-1})}} \exp\left[-\frac{\mathbf{r}^\top H \mathbf{r}}{2k_B T}\right] \quad (6.22)$$

In this equation H represents the Hessian matrix of the energy, transformed to the basis spanned by the \mathbf{B}^i . It should be noted that at every local minimum of the energy the Hessian matrix will have 6 eigenvalues that are zero. These corresponding eigenvectors coincide with the \mathbf{V}^i defined in Equation 6.16. The Hessian matrix is therefore not singular in the basis spanned by the \mathbf{B}^i .

Although this approximation becomes exact in the limit of the temperature going to zero we found that at finite temperatures acceptance rates of our algorithm were very low using the harmonic approximation. For the 38 and 75 atom LJ

clusters the acceptance rates were around 0.2 % and 0.04 % respectively. Similar behaviour was also observed in the context of the auxiliary harmonic superposition system [25]. Using the harmonic approximation in FHMC results in an algorithm which is very similar to the auxiliary harmonic superposition system. We therefore include calculations using the harmonic approximation in the following sections for comparison.

To overcome the deficiencies of the harmonic approximation, we propose a different approach to find suitable q_i by using a mixture of Gaussians which is defined as

$$q_i^{\text{g.m.}}(\mathbf{r}) = \sum_{k=1}^m a_i^k \mathcal{N}_i^k(\mathbf{r}) \quad \left| \quad \sum_{k=1}^m a_i^k = 1 \text{ and } a_i^k \geq 0 \forall k \right. . \quad (6.23)$$

Here the \mathcal{N}_i^k represent normalized Gaussians defined by means $\boldsymbol{\mu}_i^k$ and covariance matrices Σ_i^k . Once the a_i^k and \mathcal{N}_i^k are determined we can generate samples from the Gaussian mixture by picking a random k with probability a_i^k and then drawing a random sample from \mathcal{N}_i^k . To generate samples from \mathcal{N}_i^k we first generate a set of random numbers drawn from a standard-normal distribution using the Box-Müller algorithm. We then use the Cholesky decomposition of Σ_i^k as well as $\boldsymbol{\mu}_i^k$ to transform the random numbers to the desired distribution [242].

The parameters a_i^k , $\boldsymbol{\mu}_i^k$ and Σ_i^k are determined by fitting the Gaussian mixture to samples drawn from the Boltzmann distribution using the Expectation-Maximization (EM) algorithm [243–245]. Our implementation of the EM algorithm has been published online [246]. The implementation was written in Fortran and is highly efficient due to its extensive use of the BLAS library [247].

Such a fit for the example energy function, consisting of three Gaussians, is shown in Figure 6.7.

For each of the local minima that are included, samples are generated and the Gaussian mixtures are fit individually. The samples are collected from a standard Monte Carlo run initialized at the local minimum \mathbf{R}_i after a short equilibration phase. During the Monte Carlo run we repeatedly check if the current configuration is still inside the region assigned to the local minimum \mathbf{R}_i . If the region was left the simulation is reinitialized at \mathbf{R}_i and some equilibration steps are performed. This ensures that the samples are all drawn from a single peak in the Boltzmann distribution that belongs to the corresponding minimum.

If only a single Gaussian is fit, the resulting method is equivalent to the principle mode analysis method [248]. Alternatively the self-consistent phonon method [249, 250] could also be used to fit a single Gaussian distribution [251]. As in our method

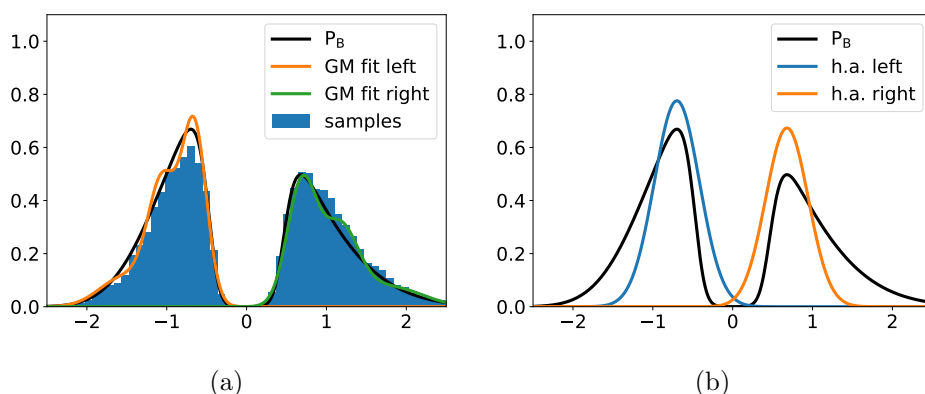


Figure 6.7: Boltzman probabilities for the example energy function shown in Figure 6.1a at $T = 0.25$, obtained from Gaussian mixtures of three Gaussian fit to 10'000 samples from each local minimum (a) and the harmonic approximation (b) are shown. The fitted Boltzmann probabilities are scaled according to the partition function of each side, such that they match the exact Boltzmann probability shown in black. Usually, these partition functions are not known and the scaling in this figure is only down to show the good agreement between the Gaussian mixture fit and the real Boltzmann distribution. It can be seen that the Gaussian mixture fit improves the overlap with the real Boltzmann distribution compared to the harmonic approximation.

the required number of energy and force evaluations was dominated by the Monte Carlo sampling and not by the construction of the Gaussian mixtures, an improved efficiency in this part would not be of great advantage. What matters is the improved acceptance rates that can be achieved with fits that use multiple Gaussians.

We also developed a modified version of the EM algorithm which takes advantage of the high symmetry present in many low energy configurations. By constraining the Gaussian mixture to have the same symmetry as the local minima the number of free parameters can be reduced which leads to a better quality of the fit. An outline of the modified algorithm is given in Section 6.3.2.

For our LJ clusters, we used a local geometry optimization to check if the Monte Carlo walker has left the catchment basin of the local minimum. In our experiments this required approximately 100 energy and force evaluations per sample that we collected. For the LJ clusters these energy and force evaluations are extremely cheap. If a more expensive method, such as for instance DFT, would be used one would have to resort to fingerprints or RMSD calculations to check if the catchment basin has been left. We therefore decided not to include these energy and force evaluations into the final results given in Section 6.4.

FITTING SYMMETRIC GAUSSIAN MIXTURES

Low energy configurations of clusters often exhibit a high degree of symmetry. This is especially the case for the 38 atom LJ cluster where the ground state has 24 rotational symmetries as well as a point reflection symmetry resulting in a total of 48 symmetries.

These symmetries will also be present in the Boltzmann distribution which we approximate using the Gaussian mixtures. By constraining the Gaussian mixtures to have the same symmetries as the local minima, the number of free parameters can be reduced, which results in an increased quality of fit with the same number of training samples used. We therefore developed the following variant of the EM algorithm.

In a first step we determine all rotation and point reflection symmetries of the configuration. For that the configuration is first rotated randomly, then the alignment algorithm described in Section 6.3.1 is used to align the rotated structure to the original configuration. All distinct assignments with an RMSD of zero correspond to a symmetry operation. The procedure is then repeated after a point reflection was applied to the structure such that all symmetries that include a point reflection can be found. Alternatively the symmetries can also be detected using a more efficient code, such as for example libmsym [252].

We then define a symmetric Gaussian mixture by replicating a normal Gaussian mixture for each of the symmetry operations.

$$q^{\text{sym}}(\mathbf{r}) = \sum_{j=1}^{N_{\text{sym}}} \sum_{k=1}^m a^k \mathcal{N}_j^k(\mathbf{r}) \quad (6.24)$$

Here N_{sym} is the number of symmetries, m is the number of Gaussians per symmetry and \mathcal{N}_j^k is the k th Gaussian under the j th symmetry transformation. Similar to the non symmetric Gaussian mixture the a_k s are weights for the individual Gaussians. Because each Gaussian is replicated N_{sym} times the a_k have to sum up to $1/N_{\text{sym}}$.

Each symmetry operation consists of a rotation represented by a rotation matrix R , a permutation represented by a permutation matrix P , and optionally a point reflection. To apply a symmetry transformation to the $3N - 6$ dimensional vectors we first have to transform them back to the $3N$ dimensional space. Then the rotation,

6.3 The Funnel Hopping Monte Carlo Algorithm

permutation and point reflection are applied before transforming back to the $3N - 6$ dimensional coordinates. Combining all of these operations yields the matrix M .

$$M = B^\top PQIB \quad (6.25)$$

With B being a $3N \times 3N - 6$ matrix with its columns consisting of the $3N - 6$ basis vectors \mathbf{B}^i , Q being a block diagonal matrix with the rotation matrix R repeated N times along its diagonal and I being the identity matrix $\mathbb{1}$, or $-\mathbb{1}$ if a point reflection is applied. The Gaussian \mathcal{N}_j^k is hence defined by the mean $\boldsymbol{\mu}_j^k = M_j \boldsymbol{\mu}^k$ and the covariance $\Sigma_j^k = M_j \Sigma^k M_j^\top$. The symmetric Gaussian mixture model is therefore parametrized by m weights a^k , m mean vectors, and m covariance matrices.

To fit this symmetric Gaussian mixture we modified the original EM algorithm in the following way. During the expectation part of each iteration we first construct the full symmetric Gaussian mixture as it is given by Equation 6.24. We then calculate the weights y_i^{jk} for each sample \mathbf{x}_i in the same way as in the original algorithm.

$$y_i^{jk} = \frac{a^k \mathcal{N}_j^k(\mathbf{x}_i)}{\sum_{j=1}^{N_{\text{sym}}} \sum_{k=1}^m a^k \mathcal{N}_j^k(\mathbf{x}_i)} \quad (6.26)$$

For the parameter estimation in the maximization step of the algorithm we apply the inverse symmetry transformations M_j^\top to the samples. The weight calculated for sample i with Gaussian k transformed with symmetry j is now used on the sample transformed with M_j^\top to estimate the parameters $\boldsymbol{\mu}^k$ and Σ^k

$$\boldsymbol{\mu}^k = \frac{\sum_{j=1}^{N_{\text{sym}}} \sum_{i=1}^N y_i^{jk} M_j^\top \mathbf{x}_i}{\sum_{ij} y_i^{jk}} \quad (6.27)$$

$$\Sigma^k = \frac{1}{\sum_{ij} y_i^{jk}} \sum_{j=1}^{N_{\text{sym}}} \sum_{i=1}^N y_i^{jk} (M_j^\top \mathbf{x}_i - \boldsymbol{\mu}^k)(M_j^\top \mathbf{x}_i - \boldsymbol{\mu}^k)^\top \quad (6.28)$$

As in the original version of the algorithm the expectation and maximization steps are repeated alternately until convergence is achieved.

With this modified version of the EM algorithm we were able to achieve significantly better fits and hence a higher performance in our FHMC simulations, whenever symmetries were present in any of the local minima used.

6.4 RESULTS

We tested our newly developed algorithm on clusters consisting of 38 and 75 atoms interacting with the pairwise LJ potential, as described in Equation 2.44.

To avoid evaporation events, where a single atom detaches from the cluster, we used a confining potential as proposed by Nigra, Freeman, and Doll [232], which is defined as follows:

$$V(\mathbf{r}) = \sum_{i=1}^N \epsilon \left(\frac{\|\vec{r}_i - \vec{r}_{\text{cm}}\|}{r_c} \right)^{20} \quad (6.29)$$

With \vec{r}_{cm} being the center of mass and r_c the radius of the confining potential. We experimentally found $r_c = 3.5\sigma$ to be a good choice for the LJ₃₈ cluster and $r_c = 4\sigma$ for the 75 atom Lennard-Jones cluster (LJ₇₅ cluster). The confining radii have to be chosen such that atoms are prevented from escaping without influencing the energy of the clusters too much. A soft potential was used because the derivatives/forces were needed for the Hamiltonian dynamics.

During each step of the simulation, Funnel Hopping moves were performed with a 10 % probability. All other moves were performed using Hamiltonian Monte Carlo (HMC) as described in Section 2.2.3 using 25 time steps.

The individual temperatures were selected using a geometric series, as proposed by Kofke [225]. This produced an acceptance rate of PT moves of 16 – 19 % for the LJ₃₈ cluster and 13 – 17 % for the LJ₇₅ cluster which is close to the optimal acceptance rate of 20 % as suggested by Rathore, Chopra, and Pablo [226]. Parallel tempering swaps were performed in an alternating manner between pairs of subsequent temperatures, e.g., after the first ten steps swaps were attempted between pairs 1–2, 3–4, 5–6, ... and then after ten more steps pairs 2–3, 4–5, 6–7, etc., were used.

The heat capacity was calculated using the following equation.

$$C_V(T) = \frac{3}{2} + \frac{1}{NT^2} \left(\langle E^2 \rangle_T - \langle E \rangle_T^2 \right) \quad (6.30)$$

With $\langle \cdot \rangle_T$ representing expectation values over the Boltzmann distribution at temperature T .

To obtain smooth plots of the heat capacity we used the re-weighting scheme proposed by Sharapov and Mandelshtam [25] to interpolate between the different temperatures.

6.4.1 38 ATOM LENNARD-JONES CLUSTER

The most studied LJ cluster is presumably the LJ_{38} cluster, which is known for its two funnel energy landscape that almost completely prevents ergodic sampling by conventional MC methods.

One funnel ends in the global minimum, which is a face-centered-cubic truncated octahedral structure. The other funnel ends in the second-lowest minimum, which is an incomplete Mackay icosahedron. These two funnels are separated by a high energy barrier with a transition state energy of 4.219ϵ above the ground state energy [89] which is almost impossible to overcome at low temperatures.

Gaussian mixtures were fit to the ten lowest local minima (stereoisomers were counted as one) using 2×10^5 samples. The acceptance rates of the FHMC moves achieved are shown in Figure 6.8. As one can see, increasing the number of Gaussians

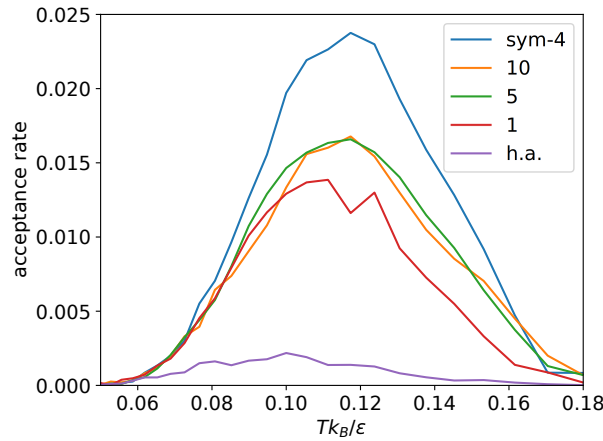


Figure 6.8: Acceptance rate of funnel hopping moves in LJ_{38} cluster plotted against temperature. The numbers represent the number of Gaussians used in the Gaussian Mixtures. For the line labelled h.a. the harmonic approximation was used and for the line labelled sym-4 an extended version of the EM algorithm was used to fit a symmetric Gaussian Mixture with 4 Gaussians per symmetry. (Figure reproduced with permission from Reference [94].)

from 5 to 10 did not increase the acceptance rate. We suspect that this is due to the number of samples not being sufficient for the high numbers of parameters that have to be fitted. In this case we have 5995 free parameters per Gaussian. $n(n+1)/2$ from the covariance matrix, n from the mean and one a_i^k with n being the dimensionality of the Gaussian which is $3 \times 38 - 6$ in this case. The use of the adapted EM algorithm presented in Section 6.3.2, that takes the symmetry of the local minima into account,

allows us to further increase the quality of the fit, and hence the acceptance rate, without using more samples. The acceptance rate for the Monte Carlo run using a symmetric Gaussian Mixture is labeled *sym-4* in Figure 6.8. The Gaussian Mixture for this fit consists of 4 Gaussians per symmetry of the local minima.

This fit was then used to calculate the heat capacity of the LJ₃₈ cluster using FHMC in combination with PT. The result is shown in Figure 6.9 where it is compared to a reference calculation using PT with 10^9 steps. The curve using both methods in combination was obtained after 10^7 steps. While this result is in agreement with the reference, the result obtained with PT alone using the same number of steps is clearly not converged.

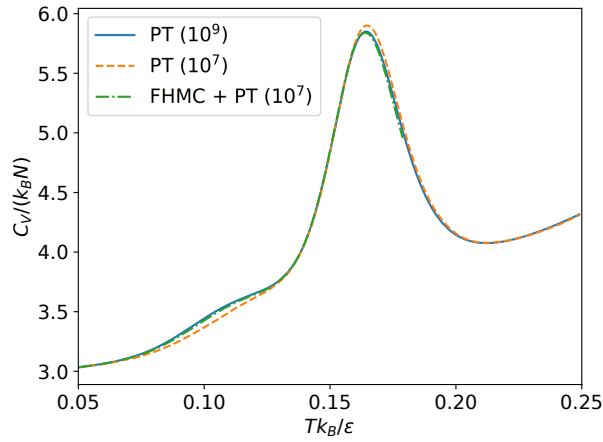


Figure 6.9: Heat capacity of LJ₃₈ calculated with our method compared to the result obtained using PT after different numbers of steps. (Figure reproduced with permission from Reference [94].)

To assess the convergence properties of our method we repeated the calculation of the heat capacity ten times with both methods individually and combined using 10^7 steps. We then calculated the RMSE with respect to the reference obtained with 10^9 PT steps. The resulting RMSEs are shown in Figure 6.10.

The results show that our method alone, outperforms PT at the lower temperature range up to $T = 0.11 \epsilon/k_B$. In this range the number of accessible minima is low, such that they are well included into the FHMC. In this special case FHMC can be used to perform ergodic sampling with only one simulation at a single temperature, reducing the computational effort by several orders of magnitude compared to PT simulations where a whole range of temperatures has to be simulated. We found that if we included only the lowest minimum in each funnel the FHMC calculation

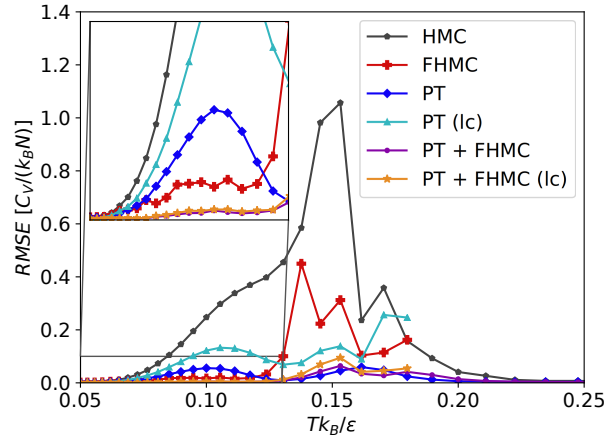


Figure 6.10: Root mean squared error of the heat capacity of the LJ₃₈ cluster calculated with Hamiltonian Monte Carlo (HMC), parallel tempering (PT), Funnel Hopping Monte Carlo (FHMC), PT and FHMC in combination with a regular or with a lower maximum temperature (lc). (Figure reproduced with permission from Reference [94].)

did not converge within 10^7 steps. If combined with PT however, the convergence was only slightly slower than with 10 minima.

At higher temperatures additional minima become relevant that are not included into the FHMC scheme and have to be reached by standard Monte Carlo moves which can slow down convergence.

One major drawback of PT is that a large range of temperatures has to be simulated with the maximum temperature being high enough such that the highest energy barriers can be crossed by the Monte Carlo simulation. In our experiments we chose a maximum temperature of $0.4 \epsilon / k_B$ for PT while the maximum temperature for the FHMC simulations can be chosen arbitrarily because each simulation is performed independently of the others. For our FHMC simulations we chose a maximum temperature of $0.18 \epsilon / k_B$. Parallel tempering simulations with this maximum temperature did not converge to the correct result. When we combined PT with our method however, convergence could be achieved. In this case the FHMC moves allow the simulation to cross the highest barriers while PT enables the crossing of the lower barriers between basins within a funnel that are not included into the FHMC scheme. Using both methods in combination allows therefore to use a significantly lower cutoff temperature than with standalone PT. It combines the best of both methods by using PT to skip barriers inside funnels and FHMC to move between different

funnels, leading to improved sampling capabilities across the whole temperature range which can also be seen in Figure 6.10.

6.4.2 75 ATOM LENNARD-JONES CLUSTER

As a final test we applied FHMC to an even more challenging system, namely the LJ₇₅ cluster. Similar to the LJ₃₈ cluster, its energy landscape also consists of two major funnels, one ending in the global minimum which has a decahedral structure and the other one ending in the second-lowest local minimum which has an icosahedral structure. These two minima are separated by a barrier that lies 8.69ϵ above the ground state energy. This barrier is over 3ϵ higher than any other barrier between the 250 lowest minima [88]. Unlike in the case of the LJ₃₈ cluster the peak in the heat capacity caused by the solid-solid transition is well separated from the melting peak.

The very high barrier between the two funnels makes ergodic sampling of this system particularly difficult. It seems that PT alone is not enough to obtain converged results for the LJ₇₅ cluster [25, 232]. Our own calculation using PT with HMC did not converge after 5×10^8 steps per temperature (5×10^{11} energy and force evaluations in total). Because of the high energy barrier between the two funnels transitions are limited to the very high temperature range of the PT simulation. At these temperatures the accessible configuration space is extremely large causing the transition between the funnels to be particularly rare.

By combining PT with FHMC, transitions between the two funnels become possible already at low temperature.

We used FHMC in combination with PT to calculate the heat capacity of the LJ₇₅ cluster. The two lowest minima were included into the FHMC scheme to facilitate the crossing of the high inter funnel barrier. We used our version of the EM algorithm to fit Gaussian mixtures of three Gaussians per symmetry using 2×10^5 samples per local minimum.

FHMC moves were included with a probability of 10% up to a temperature of $0.119\epsilon/k_B$ above which the acceptance rate of the moves decays to almost zero. A total of 40 PT replicas were used, which were run in parallel each on one CPU core. The lower 20 of the replicas included FHMC moves. Because we included two local minima into the FHMC scheme, 40 Gaussian mixtures were fit. The resulting acceptance rates are shown in Figure 6.11. The fitted Gaussian mixtures outperform the harmonic approximation in terms of the acceptance rate of the proposed moves by about a factor of 20.

PT swaps were again included after every 10 steps. Samples were collected after an equilibration period of 10^5 steps.

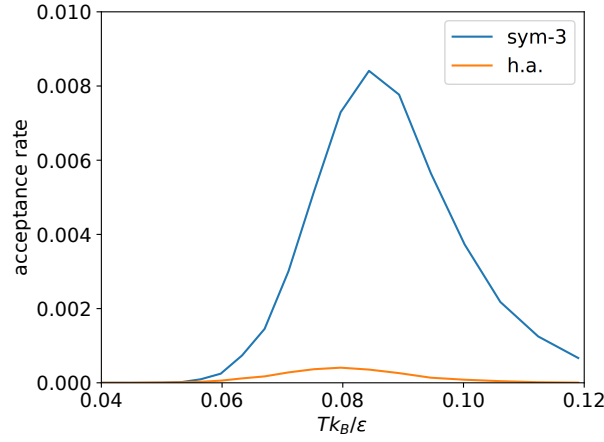


Figure 6.11: Acceptance rate of funnel hopping moves in the LJ_{75} cluster plotted against temperature. The result obtained using the Gaussian mixtures consisting of 3 Gaussians per symmetry, are labeled with *sym-3* while the result obtained using the harmonic approximation are labeled *h.a.*. (Figure reproduced with permission from Reference [94].)

The obtained heat capacity after 1.4×10^7 steps is shown in Figure 6.12. We identified the peak of the heat capacity corresponding to the solid-solid transition at a temperature of $0.085 \epsilon/k_B$. This is slightly higher than the result of $0.083 \epsilon/k_B$ reported by Sharapov and Mandelshtam [25]. To explain this minor discrepancy we ran several simulation, initialized with the second lowest instead of the lowest minimum, with a larger confining radius as well as with a longer equilibration period. However, the results of all these calculations gave the same numerical value for the peak.

In Figure 6.13 the peak corresponding to the low temperature solid-solid transition is shown again and compared to the results obtained with our method and with a run where the harmonic approximation was used instead of fitted Gaussians, both after 10^5 and 10^6 steps. After 10^6 steps the FHMC calculation is converged to the final result after 1.4×10^7 steps up to a very high precision while the result from the harmonic approximation is still significantly shifted towards the right. Even after only 10^5 steps the FHMC calculation is already converged to a result where the heat capacity peak is in good qualitative agreement with the converged result. These results clearly indicate that the rate at which the simulation jumps between the two funnels is the limiting factor for the convergence of the Monte Carlo simulation.

Hence, using FHMC we were able to obtain a converged result after only 10^6 steps (3.25×10^7 energy and force evaluations per temperature or 1.3×10^9 in total, including sample generation for the Gaussian mixtures as well as the equilibration part). This is almost 100 times less than the 3×10^9 energy evaluations per temperature reported by Sharapov, Meluzzi, and Mandelshtam [241] where an auxiliary harmonic superposition systems was used and more than 100 times less than the 4×10^{11} energy evaluations in total reported by Martiniani et al. [253] where the approximate SENS method was employed. The basin-sampling method [254] used 0.27×10^9 energy evaluations per replica resulting in a total of 8.64×10^9 energy evaluations for all 32 replicas combined not including the energy evaluations required for the minimizations in the final phase. This is significantly more than in the FHMC method.

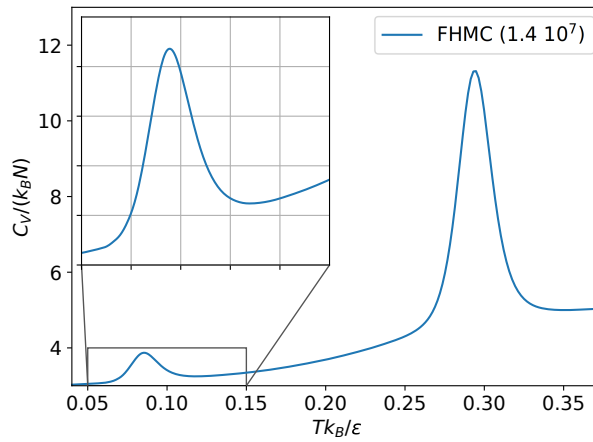


Figure 6.12: Heat capacity of LJ₇₅ calculated with FHMC. (Figure reproduced with permission from Reference [94].)

6.5 SUMMARY

With FHMC, we developed a new tool to overcome broken ergodicity by introducing knowledge about the energy landscape in the form of local minima into the Monte Carlo simulation. Our method generates an accurate approximation to the Boltzmann distribution even for anharmonic systems. This allows us to propose good moves between different funnels that have a high chance of being accepted by the Monte Carlo algorithm. Using Gaussian mixtures allows for a systematic improvement of the proposed moves by increasing the number of samples used for fitting and the number of Gaussians in the Gaussian mixture. With our newly developed variant of

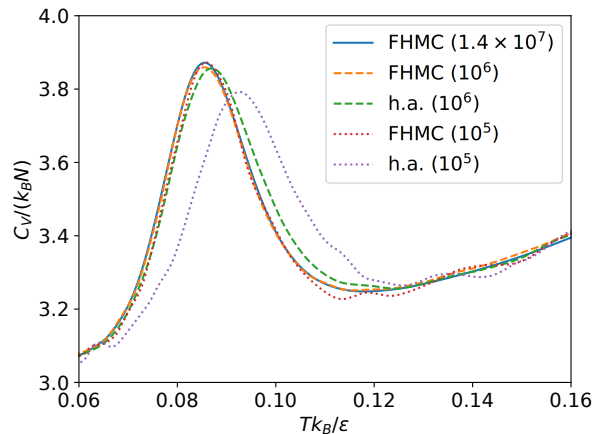


Figure 6.13: Low temperature heat capacity peak of the LJ₇₅ cluster calculated with our method using a Gaussian mixture and the harmonic approximation. The number given in the legend indicates the number of HMC steps during which samples were collected (1 step = 25 energy and force evaluations per temperature). (Figure reproduced with permission from Reference [94].)

the EM algorithm we are able to take advantage of the high symmetry present in many local minima which results in an even better fit of the Gaussian mixtures. With our fits we were able to achieve acceptance rates about twenty times higher than with the harmonic approximation. We observed that the convergence of the Monte Carlo simulation is limited by the rate at which the simulation is able to transition between the different funnels and therefore directly dependent on the acceptance rate of the inter-funnel moves.

If the temperature of interest is low enough such that only a limited number of basins are accessible and if it is possible to include all of them into the algorithm, FPMC can be performed at a single temperature whereas PT requires many auxiliary simulations at higher temperatures.

We also showed that the maximum simulation temperature of PT simulations, can be significantly reduced by combining our method with PT. This allows to reduce the number of parallel simulations that are needed resulting in a reduced computational cost. Also, the convergence of the simulation is sped up massively as the FPMC moves help the simulation to cross the highest barriers between different funnels very efficiently.

Using FPMC we were able to obtain the heat capacity of the LJ₇₅ cluster, a notoriously difficult system, known to suffer from a particularly strong broken ergodicity. Nevertheless, using a relatively small number of 1.3×10^9 energy and force

evaluations in total we could obtain converged results. This number of evaluations is significantly less than the number required by existing state-of-the-art methods. We also observed that the results were already in good qualitative agreement after only about 10^8 energy and force evaluations.

7 EXPERIMENTAL ABSENCE OF THE NON-PEROVSKITE GROUND STATE PHASES OF MAPbI_3 EXPLAINED BY A MLP BASED FHMC STUDY

7.1 INTRODUCTION

In recent years, perovskites have gathered a lot of attention due to their exceptional opto-electronic properties, which make them suitable for high performance devices, such as solar cells, lasers, photodetectors or light emitting diodes [255, 256]. The general structure of perovskites, given by the formula ABX_3 , consists of corner sharing BX_6 octahedra arranged in a cubic lattice, that form cuboctahedral cavities, in which the A species are found. Due to many possible choices for the A, B, and X components, perovskites form a large design space that can be explored to optimize material properties [257, 258].

Many perovskite materials undergo so-called tilting phase transitions, that are characterized by a cooperative tilting of the corner sharing octahedra that leaves the internal connectivity of the B and X atoms intact [260, 261]. Some materials, such as FaPbI_3 and CsPbI_3 can even undergo transitions to unwanted non-perovskite phases and there is ongoing research on stabilizing the perovskite phases [262, 263]. Due to the different properties of the phases, understanding and predicting the phase transition behaviour in perovskite materials is of great interest.

The presumably most widely used tools to study free energetic orderings in materials are the harmonic approximation (HA) [264] and quasi harmonic approximation (QHA) [265, 266]. Unfortunately, the applicability of these methods to perovskites is limited since the tilting motion of the octahedral structure was found

The content of this chapter was adapted from J. A. Finkler and S. Goedecker. “Experimental Absence of the Non-Perovskite Ground State Phases of MaPbI_3 Explained by a Funnel Hopping Monte Carlo Study Based on a Neural Network Potential”. *Materials Advances* 4, 2023, pp. 184–194.

to be highly anharmonic [267–269]. Many systems, such as CsSnI_3 [268], MaPbI_3 [270], or CsSnX_3 and CsPbX_3 [271] can also be found in a high symmetry cubic phase, that is only stable at high temperatures. The geometries associated with these cubic phases can be constructed in small unit cells but they are dynamically unstable under collective rotations of the octahedral cages as an analysis of their imaginary frequency phonon modes reveals [267, 272–274]. The existence of these phases can therefore only be explained by entropic contributions to the free energy at higher temperatures. Carignano et al. [269] found that the cubic symmetry of MaPbI_3 is almost always broken locally and that the cubic symmetry found in experiments can be interpreted as averaging of distorted geometries. The HA and QHA are hence not directly applicable to these phases.

An alternative way to study phase transitions is a direct simulation of the atomistic dynamics through *ab-initio* molecular dynamics (MD). Unfortunately, due to the high computational cost of *ab-initio* methods, the affordable time-scales are limited. Classical force fields on the other hand would provide the required performance but their accuracy is limited by the simple functional form of the interaction potentials. Recently, this gap between performance and accuracy has been filled by MLPs. Once trained on high accuracy *ab-initio* data, MLPs can predict energies and forces with almost *ab-initio* accuracy at a fraction of the computational cost [275, 276].

We therefore developed a MLP to study phase transitions in methylammonium lead iodide (MaPbI_3), where the B and X sites are formed by lead and iodine atoms and the A sites are occupied by the organic molecule methylammonium (CH_3NH_3) (Ma).

Depending on the temperature, MaPbI_3 can be found in three different phases in experiment. At low temperatures, MaPbI_3 adapts an orthorhombic phase with Pnma symmetry. Upon heating above 160 K, MaPbI_3 undergoes a first order phase transition to a tetragonal phase with I4/mcm symmetry. Under a further increase of the temperature above 330 K, the material was observed to undergo a second order phase transition to a cubic phase with Pm-3m symmetry [277]. A recent theoretical structure search [26], based on the minima hopping method [81, 82], discovered two additional non-perovskite polymorphs of MaPbI_3 , that, according to DFT calculations based on the strongly constrained and appropriately normed (SCAN) [40] density functional, appear to be significantly lower in energy than the experimentally observed phases. The energetically lowest polymorph is the double-delta structure, which has a unit cell containing 48 atoms and consists of edge-sharing octahedra forming pillars that are surrounded by Ma molecules. The reported delta polymorph consists of a unit cell containing 24 atoms, where face-sharing octahedra form pillars, arranged in

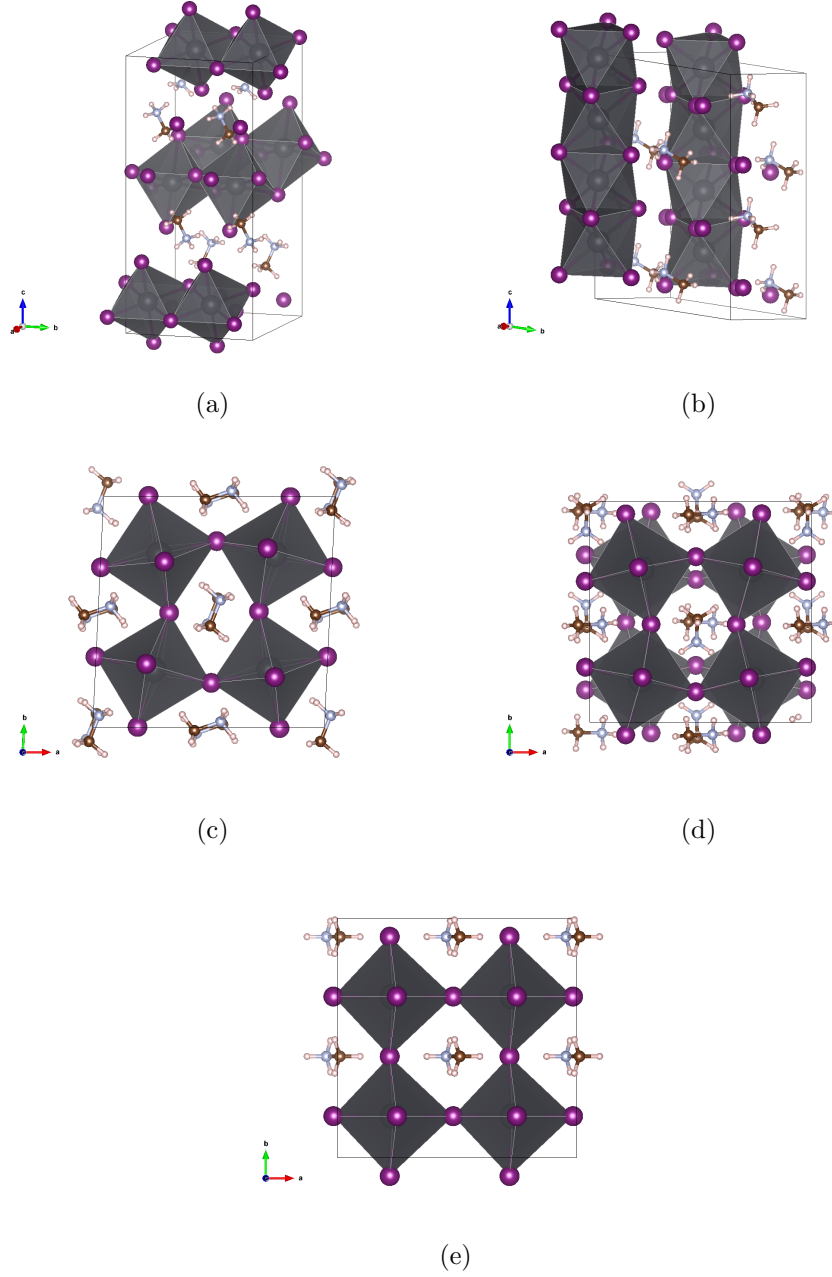


Figure 7.1: Geometry of the double-delta (a), delta (b), orthorhombic (c), tetragonal (d) and cubic (e) phases of MaPbI_3 .

a hexagonal pattern, that are uniformly surrounded by Ma molecules. The double-delta phase resembles the δ phase observed in CsPbI_3 [278], while the delta phase is similar to the δ phase of FaPbI_3 [262, 279]. The geometries of all MaPbI_3 phases are visualized in Figure 7.1. Results based on the random phase approximation (RPA)

support, that the double-delta phase is lower in energy than the perovskite phases [280, 281].

The hexagonal delta phase has also previously been investigated by Thind et al. [282]. In both CsPbI_3 and FaPbI_3 , a transition to the non-perovskite δ phases can be observed. The stability of the perovskite phases of MaPbI_3 is therefore rather surprising, given that the newly discovered delta phases should be energetically preferred. Understanding this unexpected behaviour using our MLP is unfortunately not straight forward. The large structural difference between the delta and the perovskite phases, suggests a complex reaction pathway, that would require unfeasibly long simulation times to explore using MD. Similarities can be found in the structurally similar phase transition between the hexagonal delta and cubic phases of FaPbI_3 . This transformation shows a complex reaction pathway with high barriers, that result in a large hysteresis of the transition with respect to temperature [283].

To circumvent the problem of high barriers, we extended our Funnel Hopping Monte Carlo (FHMC) method [94], which was presented in Chapter 6, to periodic systems and applied it to MaPbI_3 using our newly developed MLP. Similarly to a MD simulation, FHMC samples the Boltzmann distribution at a given temperature. However, it is not limited to a physical trajectory and carefully designed FHMC moves allow the MC walker to jump between different phases, that are separated by high free energy barriers, without violating the detailed balance condition. Sampling of the true PES allows us to obtain phase transition temperatures without using any approximate expansion of the PES like in the HA and QHA. Additionally, the FHMC method is particularly well suited for applications with MLPs. Due to the global moves, the high energy transition states are not visited and do not need to be included in the training data.

7.2 MODIFICATION OF THE FHMC METHOD FOR MAPbI_3

The FHMC method was originally developed for systems with free boundary conditions, such as atomic cluster. The methods performance was demonstrated on the 38 and 75 atom LJ clusters, which are known for their double funnel PES. The 75 atom LJ cluster is a particularly difficult system to treat with MC simulations, since not even parallel tempering (PT) [222, 223] simulations converge [25, 232].

In this work, we set out to extend the FHMC method to periodic systems and apply it to MaPbI_3 . This requires several adjustments of the FHMC algorithm that will be explained in the following sections. Some changes were required because the

initial method was proposed for atomic clusters with free boundary conditions and hence the method needed to be adopted to periodic boundary conditions. Other changes were necessary to adopt the method to MaPbI_3 in specific.

7.2.1 EXTENSION TO PERIODIC BOUNDARY CONDITIONS

FHMC uses Gaussian mixtures (GMs) to approximate the Boltzmann distribution around local minima. Since atomic systems with free boundary conditions are invariant under rotation, translation and permutation of atoms of the same species, the RMSD is used to align the current configuration of the MC walker with the reference configuration. This alignment allows for a basis transformation of the atomic displacements that projects out the 6 degrees of freedom associated with translation and rotation.

In systems with periodic boundary conditions, only a finite number of symmetry operations, that preserve the periodic lattice of the unit cell, have to be considered. Since the maximum temperature of 400 K used in our FHMC simulations is below the melting temperature, permutations of atoms do not occur. We therefore only have to consider a fixed number of symmetry operation, that can be computed for the reference configurations obtained from minima hopping using spglib [284]. For each operation that we have to consider, we first apply it to the current configuration of the MC walker. We then find the translation that minimizes the mass weighted RMSD by superimposing the centers of mass of the current configuration \mathbf{r} and the reference \mathbf{R} .

$$\sum_i^{N_{\text{at}}} \frac{m_i \vec{r}_i}{m_{\text{tot}}} = \sum_i^{N_{\text{at}}} \frac{m_i \vec{R}_i}{m_{\text{tot}}} \quad (7.1)$$

The atomic displacement vectors $\mathbf{D} = \mathbf{r} - \mathbf{R}$, are then projected onto the basis vectors \mathbf{B}_j to obtain a vector representation \mathbf{V} of the current configuration. Here, the vectors \mathbf{r} and \mathbf{R} contain all $3N_{\text{at}}$ atomic coordinates of the current and the reference configuration respectively ($\mathbf{r} = (r_{1x}, r_{1y}, r_{1z}, r_{2x}, \dots, r_{N_{\text{at}}z})^\top$). The $3N_{\text{at}} - 3$ basis

vectors \mathbf{B}_j are chosen such that they are orthogonal to the three vectors \mathbf{T}_1 , \mathbf{T}_2 and \mathbf{T}_3 which are given below.

$$\mathbf{T}_1 = \begin{pmatrix} m_1/m_{\text{tot}} \\ 0 \\ 0 \\ m_2/m_{\text{tot}} \\ 0 \\ 0 \\ m_3/m_{\text{tot}} \\ \vdots \end{pmatrix} \quad \mathbf{T}_2 = \begin{pmatrix} 0 \\ m_1/m_{\text{tot}} \\ 0 \\ 0 \\ m_2/m_{\text{tot}} \\ 0 \\ 0 \\ \vdots \end{pmatrix} \quad \mathbf{T}_3 = \begin{pmatrix} 0 \\ 0 \\ m_1/m_{\text{tot}} \\ 0 \\ 0 \\ m_2/m_{\text{tot}} \\ 0 \\ \vdots \end{pmatrix} \quad (7.2)$$

To obtain the \mathbf{B}_j , which are also orthonormal to each other, the stabilized Gram-Schmidt process is used. Since the translation of the configuration has been fixed, the projection of the displacement vector \mathbf{D} onto the \mathbf{T}_i will always be zero because of Equation 7.1. Our GMs, which are formed by a sum of Gaussian functions \mathcal{N}_i , each with their own mean and covariance matrix, weighted by factors a_i , live in the space spanned by the basis vectors \mathbf{B}_j . The total probability of the current configuration can then be evaluated as the mean over all N_{sym} applicable symmetry operations.

$$P_{\text{GM}}(\mathbf{V}) = \frac{1}{N_{\text{sym}}} \sum_i^{N_{\text{sym}}} \sum_j^{N_{\text{GM}}} a_j \mathcal{N}_j(\mathbf{V}_i) \gamma \quad (7.3)$$

Here \mathbf{V}_i is the vector representation that is obtained after applying the i th symmetry operation onto the atomic positions and γ is the degeneracy of the unit cell choice. In our FHMC simulations, we only include one reference for each phase. However, due to symmetry, some phases have a degeneracy related to the choice of the unit cell. For example, when the cubic phase undergoes a transition to the tetragonal phase, three equivalent possibilities exist in which the symmetry can be broken. We therefore use the ratio between the numbers of symmetries of the highest symmetry cubic lattice and the number of symmetries of each phase for γ .

To propose a FHMC move, the process outlined above is reversed. First a random phase j is select and then a sample \mathbf{V}' is drawn from the respective GM. The sample is then transformed into an atomic displacement by applying the transformation from the coordinate system spanned by the basis vectors \mathbf{B} to Cartesian coordinates.

To obtain the new configuration, the displacement is added onto the reference configuration. The new configuration \mathbf{r}' is then accepted with the probability $\alpha_{\mathbf{r} \rightarrow \mathbf{r}'}^{\text{FHMC}}$.

$$\alpha_{\mathbf{r} \rightarrow \mathbf{r}'}^{\text{FHMC}} = \min \left[1, \exp \left(\frac{E(\mathbf{r}) - E(\mathbf{r}'(\mathbf{V}'))}{k_{\text{B}}T} \right) \frac{P_i(\mathbf{V}(\mathbf{r}))}{P_j(\mathbf{V}')} \right] \quad (7.4)$$

Here $E(\mathbf{r})$ and $E(\mathbf{r}')$ are the energies of the old and new configurations, T is the temperature and k_{B} the Boltzmann constant. Unlike in standard MC simulations, where the trial distribution is symmetric, the probability $P_j(\mathbf{V}')$ of proposing the new configuration and the probability $P_i(\mathbf{V})$ of proposing the inverse move have to be included into the acceptance/rejection step of Equation 7.4.

7.2.2 CHANGES IN VOLUME

To allow for thermal expansion, we included the volume of the unit cell into the vector representation. Changes in the shape of the unit cell were not included, since FHMC moves between the different phases allow already for the simulation to access differently shaped unit cells. When a structure is transformed to its vector representation, it is first scaled to match the size of the reference unit cell, before the displacement vector is computed. During the sampling of a new configuration, the structure is first constructed, as described above, and then rescaled, to match the volume that is sampled from the GM.

7.2.3 SPECIAL TREATMENT OF THE METHYLAMMONIUM MOLECULES

Even at lower temperatures, where the MaPbI_3 is in a crystalline phase, the Ma cations can rotate almost freely within the cavities formed around them by the lead-iodine lattice. This rotational motion would be extremely difficult to capture even with a large number of Gaussians included in the GMs. We therefore decided to only include the center of mass of each Ma molecule into the GM, like any other atomic position. When a FHMC move is performed, the Ma molecule is cut out from its original environment and placed to the position of the new center of mass sampled from the GM. Since this process is reversible, detailed balance is preserved.

7.2.4 REPLICA EXCHANGE

Even with the special treatment of the Ma molecules included into the method, acceptance rates of the FHMC moves are vanishingly low and only few moves are accepted during long simulations. This behaviour is due to the fact that the special

treatment of the Ma molecules removes the ability of the GMs to capture any correlation between the Ma orientation and its internal configuration as well as the surrounding lead and iodine atoms positions. This results in a small overlap between the true Boltzmann distribution and the approximation of the GMs.

We therefore decided to couple the method with Hamiltonian replica exchange (RX) MC [285, 286]. We defined an artificial potential energy surface (APES) using the GMs, such that our FHMC moves are trivially accepted on the APES. The intermediate replicas will then allow for an exchange of configurations between the well sampled APES and the PES.

The GMs approximate the Boltzmann distribution as

$$P_B(\mathbf{r}) = \frac{1}{Z} \exp\left(\frac{-E(\mathbf{r})}{k_B T}\right) \approx P_{\text{GM}}(\mathbf{r}) \quad (7.5)$$

We can reverse this equation to obtain an approximation of the PES E_{GM} from the GM.

$$E_{\text{GM}}(\mathbf{r}) = -\ln(P_{\text{GM}}(\mathbf{V}(\mathbf{r})))k_B T \quad (7.6)$$

As only the center of mass of the Ma molecules enters the GM, an additional internal energy term E_{Ma} is added for each Ma molecule to obtain the total energy E_{APES} .

$$E_{\text{APES}}(\mathbf{r}) = -\ln(P_{\text{GM}}(\mathbf{V}(\mathbf{r})))k_B T + \sum_j^{N_{\text{Ma}}} E_{\text{Ma}_j}(\mathbf{r}) \quad . \quad (7.7)$$

The energy E_{Ma} is obtained from a neural network potential (NNP) trained to reproduce the energy of a single Ma molecule in vacuum. Forces can be obtained by differentiating E_{APES} with respect to the atomic coordinates. It should be noted, that partial derivatives from $\frac{d\mathbf{V}(\mathbf{r})}{d\mathbf{r}}$ have to be included because the center of mass of the structures is fixed. This results in invariance of E_{APES} under translation.

As we can see from Equation 7.4, FHMC moves will always be accepted on the APES, since the Boltzmann probability of E_{APES} is identical to the trial probability of the FHMC moves. The energy contributions $E_{\text{Ma}_j}(\mathbf{r})$ also cancel out in the FHMC moves, since the internal geometry of the Ma molecules is left unchanged by the FHMC moves and hence, the internal energy remains constant. Therefore, performing an FHMC simulation on the APES will converge extremely fast, since with every FHMC move, a new structure is generated which is, up to the internal geometry of the Ma molecules, completely uncorrelated to the previous geometry.

The MC simulation on the physical PES is then coupled to the APES using RX MC. A series of intermediate PESs are defined using a parameter λ that varies from 0, at the physical PES, to 1 at the APES.

$$E_\lambda(\mathbf{r}) = (1 - \lambda)E(\mathbf{r}) + \lambda E_{\text{APES}}(\mathbf{r}) \quad (7.8)$$

We also included replicas at different temperatures, that are arranged in a geometric series. RX moves are therefore performed on a 2 dimensional grid in the final simulations.

Configurations between neighboring simulations are then exchanged at regular intervals according to the Metropolis–Hastings criterion. The acceptance probability α^{RX} for RX moves between two replicas a and b with configurations \mathbf{r}_a and \mathbf{r}_b and energy expressions E_a and E_b at temperatures T_a and T_b are given as

$$\alpha^{\text{RX}} = \min \left[1, \exp \left(\frac{E_a(\mathbf{r}_a) - E_a(\mathbf{r}_b)}{T_a k_B} - \frac{E_b(\mathbf{r}_a) - E_b(\mathbf{r}_b)}{T_b k_B} \right) \right] . \quad (7.9)$$

7.2.5 OTHER SIMULATION DETAILS

We used Hamiltonian Monte Carlo (HMC) [68, 287] (see Section 2.2.3) with 20 MD time steps of 0.8 fs each for the local MC moves. To avoid large differences in timescale between the vibrations of the light hydrogen and heavy lead atoms, we set all masses to the mass of a hydrogen atom. MC moves changing the volume were included with a probability of 20%. The GMs were fit to 10^5 samples using our symmetry adapted version of the EM algorithm [94] (see Section 6.3.2) with 1 Gaussian per symmetry. FHMC moves were attempted with a probability of 10%. We used a 2D grid of replicas with 24 different temperatures from $T_{\text{min}} = 40$ K to $T_{\text{max}} = 400$ K arranged in a geometric series and 10 different values of λ , which results in a total of 240 replicas. RX moves were performed between neighboring replicas in an alternating fashion every 5 MC iterations. We collected samples from our FHMC simulations during 200'000 iterations after an equilibration period that lasted for 150'000 iterations. We used unit cells containing 8 functional units for each phase. Details on the choice of unit cells can be found in Appendix B.2.1.

In Figure 7.2, acceptance rates plotted against temperature and the parameter λ are shown. Since a 2D grid of replicas was used, the shown acceptance rates were averaged over all replicas at the same temperature or λ values. The acceptance rate of the HMC moves are almost independent of the temperature and λ . The acceptance

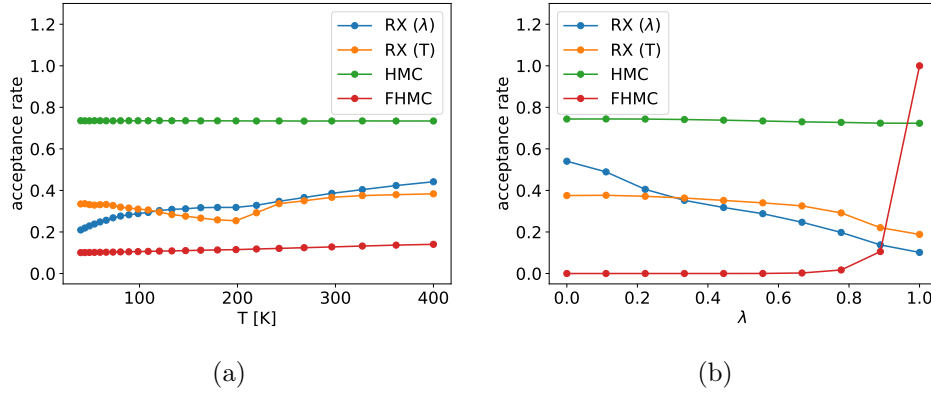


Figure 7.2: Acceptance rate of the Hamiltonian MC Monte Carlo (HMC), funnel hopping Monte Carlo (FHMC) and replica exchange moves between replicas with different λ values (RX (λ)) and temperatures (RX (T)) plotted against temperature (a) and λ (b). The values shown in (a) are averages over all replicas with the same value of λ and the values shown in (b) are averages over all replicas with the same temperature. (Figure adapted with permission from Reference [259].)

rate of the FHMC moves is, as expected, exactly 1 at $\lambda = 1$ and decays very rapidly for decreasing λ .

7.3 NEURAL NETWORK POTENTIAL

To obtain predictive power, a faithful representation of the PES is needed. It was previously shown, that DFT using the SCAN density functional is in good agreement with RPA [281] and experimental results [288] for MaPbI_3 . Unfortunately, performing FHMC simulations on a SCAN-DFT PES is not feasible due to the high computational cost and the large number of energy and force calculations that are required. We therefore decided to train a HDNNP [9] using SCAN-DFT training data. A 2G-HDNNP was used, since we found that a 4G-HDNNP only resulted in a marginal improvement of the fitting errors, that would not justify the additional computational cost. All DFT calculations were performed with the VASP [29, 289–292] code using the SCAN functional meta-GGA [40]. A plane-wave basis set with a cutoff energy of 800 eV was used within the projector augmented wave (PAW) formalism. The basis set was constructed with Pb d-shell (14), I (7), N (5), C (4), H (1) electrons as valence states in the PAW potentials. The reciprocal space was sampled using Γ -centered k-grid meshes with spacings of 0.2 \AA^{-1} and all calculations were not spin polarized.

Unlike previously published machine learned potentials for MaPbI_3 [141, 293], we also included the two non-perovskite phases in our training data. The HDNNP was trained by the RuNNer software [150, 172] using energies and forces. For the prediction of energies and forces, we employed our own code [294] in the FHMC simulations and n2p2 [139] in the MD simulations. ACSFs [10] were employed as atomic environment descriptors. A detailed list of the parameters of the ACSF can be found in Appendix B.2.2. Neural networks consisting of two hidden layers with 10 nodes each were used for each element, resulting in 3545 free parameters that were optimized during training. As activation function, the hyperbolic tangent and a linear function were used for the hidden and output layers respectively.

To generate the training dataset, we took an active learning approach. We first trained a set of HDNNPs on a small set of structures that were sampled from a MC simulation driven by a classical force field [295] and then recomputed with DFT. We then performed MC simulations for all 5 crystalline phases on the HDNNP-PES. The standard deviation between the energies predicted by the different HDNNPs, trained on the same data but with different initializations of the weights and biases, was applied to estimate the accuracy of the HDNNP’s prediction for a given structure. The structures with the lowest accuracy were then recomputed using DFT and added to the dataset. This process was repeated until a satisfying accuracy was reached. The final dataset consists of 34’400 structures. We randomly selected 10 % of the structures as a test set and used the remaining structures to train the HDNNPs. The resulting HDNNPs are highly accurate and can run stable MD simulations at up to 400 K. However, we found that in some rare cases, during our FHMC simulations, structures were generated by the FHMC moves, that would be extremely high in energy due to unphysically short bond lengths. As the training data for our HDNNPs was sampled from the Boltzmann distribution, such high energy structures are not present and the HDNNP prediction will be wrong. In some cases the HDNNPs would severely underestimate the energy which would lead to the acceptance of a highly unphysical configuration. To counteract this problem, we used the average over the predictions of five HDNNPs that were trained with a different weight initialization. A small positive energy bias was then added to configuration for which the prediction accuracy was low.

$$E = \bar{E} + \alpha\sigma^2 \quad (7.10)$$

Here \bar{E} is the mean of the five energy predictions and σ the standard deviation. The parameter α was set to 2.0 Ha^{-1} . This energy bias comes at little cost, since the

7 Experimental Absence of the Non-perovskite Ground State Phases of MaPbI_3 Explained by a MLP Based FHMC Study

computationally most expensive part of the HDNNP evaluation, the computation of the ACSFs, has to be performed only once. During a typical FHMC simulation, the average value of σ at the simulation on the true PES ($\lambda = 0$) is around 14.9 meV (0.15 meV/atom). The maximum value was found at 63.3 meV (0.66 meV/atom), which results in an energy bias of 0.29 meV (0.003 meV/atom). Only at replicas with $\lambda > 0$ a significant influence of the energy biasing is present. The total energy and force RMSD of our fit is 0.885 meV/atom and 118.4 meV/Å on the training set and 1.032 meV/atom and 120.0 meV/Å on the test set. Correlation plots for the energies and forces are shown in Figure 7.3.

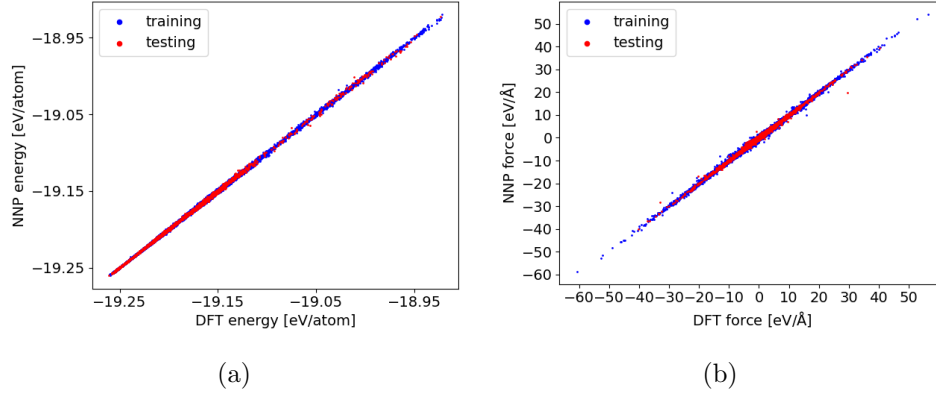


Figure 7.3: Correlation plot of the energy per atom (a) and force components (b) predicted by the NNP versus the reference energies for the training and test datasets. (Figure adapted with permission from Reference [259].)

Table 7.1: Energies (meV/f.u.) of the phases, computed with DFT and the HDNNP. Energies are given relative to the DFT energy of the double-delta phase.

phase	SCAN	HDNNP	HDNNP relaxed
double-delta	0.0	1.5	-2.2
delta	12.3	20.6	11.1
orthorhombic	26.3	28.7	26.1
tetragonal	46.4	59.2	49.6
cubic	130.2	138.3	124.7

Table 7.1 shows the energy of the local minimum configuration for all five phases. Energies per functional unit are given for DFT optimized geometries, the energy predicted by the HDNNP for the same geometry and the HDNNP energy after the lattice and atom positions were further relaxed on the HDNNP PES. The values

for the cubic phase were obtained using a small unit cell containing only a single functional unit. When expanded to a $2 \times 2 \times 2$ super cell, the cubic geometry is not a minimum anymore, but a saddle point.

The lattice parameters of the orthorhombic phase predicted by the MLP are in close agreement with the values obtained from DFT and experimental results [277] at 10 K as shown in Table 7.2.

Table 7.2: Lattice parameters (a, b and c) (\AA) and volume (\AA^3) of the orthorhombic phase obtained from DFT, the NNP and experiment [277] at 10 K.

	a	b	c	volume
SCAN	8.99073	12.71980	8.62164	985.973
NNP	9.00764	12.69012	8.59005	981.912
experiment	8.81155(6)	12.58714(9)	8.55975(6)	949.38(1)

We used a radial cutoff of 12 Bohr for our ACSFs. This distance is roughly equal to the distance between neighboring PbI octahedra in the perovskite phases. It is important to note, that the HDNNP is able to describe interactions with a range of up to twice the maximum cutoff distance of the ACSFs, as atoms that are present in between the interacting atoms include both atoms inside their cutoff radius. To confirm, that the interaction between neighbouring Ma cations is well described by our HDNNPs, we placed two Ma molecules inside neighboring PbI cages. The lead and iodine atoms were placed at their high symmetry positions from the cubic phase. This way, the local environment of the PbI cage, as seen by the Ma cation, is completely symmetric and invariant when a point symmetry operation is applied to the Ma cation through the cage center. We then compared the energies of the two cases, where both Ma cations were in parallel and antiparallel configurations with DFT references. Due to the symmetry, the only difference in the environments of the Ma molecules is the Ma molecule in the neighboring cage. This allows us to test if the interaction between neighbouring Ma molecules is adequately described, by eliminating the interaction between the Ma molecules and the surrounding cage. The HDNNPs predict that on average, the parallel configuration is preferred by 61.3 meV which agrees well with the DFT result of 71.6 meV.

7.4 RESULTS

7.4.1 FHMC STUDY OF THE EXPERIMENTALLY KNOWN PHASES

In a first step we ran FHMC simulation that only included the three experimentally known phases of MaPbI₃. We also performed MD simulations using lammmps [296] and the HDNNP code n2p2 [139] to validate our FHMC results. As we used variable cell shape MD, the determination of the phase from the lattice parameters is difficult. The variability of the lattice during the MD is close in magnitude to the variability between the different phases. This problem is not present in the FHMC simulations, since there the ratio between the lattice parameters is kept fixed to the value of the optimized unit cell and only the volume is allowed to change. However, an identification of a given phase using the lattice parameters is also not always possible. We observed, that sometimes geometries in one lattice are present, that show a tilting of the PbI octahedra that is typical for another phase. This effect is especially pronounced for the tetragonal and cubic phases that have very similar lattice constants. We therefore used an order parameter, to determine the phase transition temperatures between the orthorhombic, tetragonal and cubic phases. This order parameter is given by the mean absolute value of the normalized dot product between vectors that span the three diagonals of neighboring PbI octahedra pointing along the same axis. We hence obtain three order parameter values (one per diagonal of the octahedra) for each configuration, that indicate the tilting between neighboring PbI octahedra.

To compute our order parameter, we first identify all PbI octahedra that are present. We then define three vectors $\vec{v}_{i\alpha}$ for each octahedron i , that connect two opposing iodine atoms (index α). We then compute three order parameter values O_α by taking the mean of the absolute value of the dot product between nearest neighbor $\vec{v}_{i\alpha}$ pointing in the same direction α . Pairs of vectors pointing in two of the three directions are shown in Figure 7.4.

$$O_\alpha = \frac{1}{6N} \sum_i \sum_j \frac{|\vec{v}_{i\alpha} \cdot \vec{v}_{j\alpha}|}{\|\vec{v}_{i\alpha}\| \|\vec{v}_{j\alpha}\|} \quad (7.11)$$

Here the sum over i includes all N octahedra, while the sum over j only includes the nearest neighbor octahedra to i .

In Figure 7.5, histograms of the order parameter for different temperatures are shown. The MD simulations were performed at temperatures ranging from 25 K to 400 K with a spacing of 25 K. The order parameters were computed for a duration of

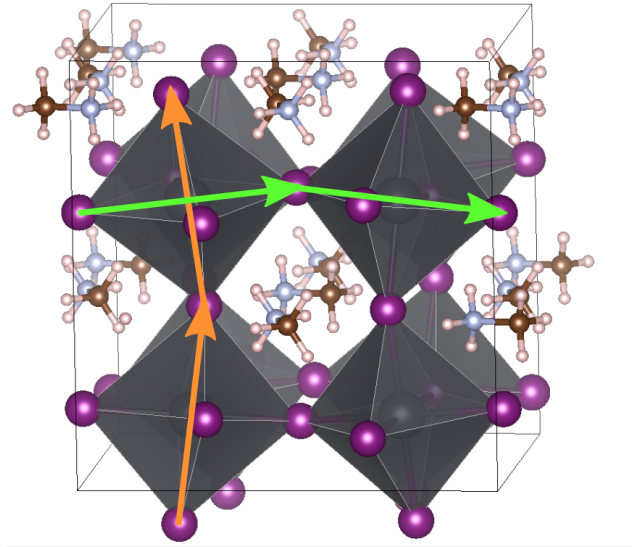


Figure 7.4: Pairs of vectors used for computing the order parameters. Two pairs, pointing into the two directions parallel to the image plane are shown in green and orange.

25'000 ps after an equilibration period that lasted for the same duration. MD simulations that were initialized with a tetragonal or cubic geometry would only extremely rarely undergo a phase transition to the orthorhombic phase at temperatures close to the phase transition temperature, while the reverse transition was readily observed. We therefore initialized our simulation with the orthorhombic ground state geometry. Our FHMC simulations however, converge to the same relative probability of the different phases, independent of the phase that was used during initialization, since the FHMC moves allow for direct transitions between phases and are not hindered by energetic or dynamics barriers.

The phase transition from the orthorhombic to the tetragonal phase can clearly be identified in both, the FHMC and the MD results, around 130 K by the disappearance of order parameter values around 0.95. The transition between the tetragonal and cubic phase is less clearly identifiable and occurs around 300 K in the MD simulation, where the two peaks in the order parameter histogram merge into a single peak. The FHMC results appear to show a slightly lower tetragonal cubic transition temperature. This is because of the high sensitivity of the transition to the lattice parameters [288]. With increasing temperature, the ratio between the two lattice parameters of the tetragonal phase will get closer to one. Since this ratio is kept fixed to the ratio of the ground state geometry in our FHMC simulations, the tetragonal phase will necessarily

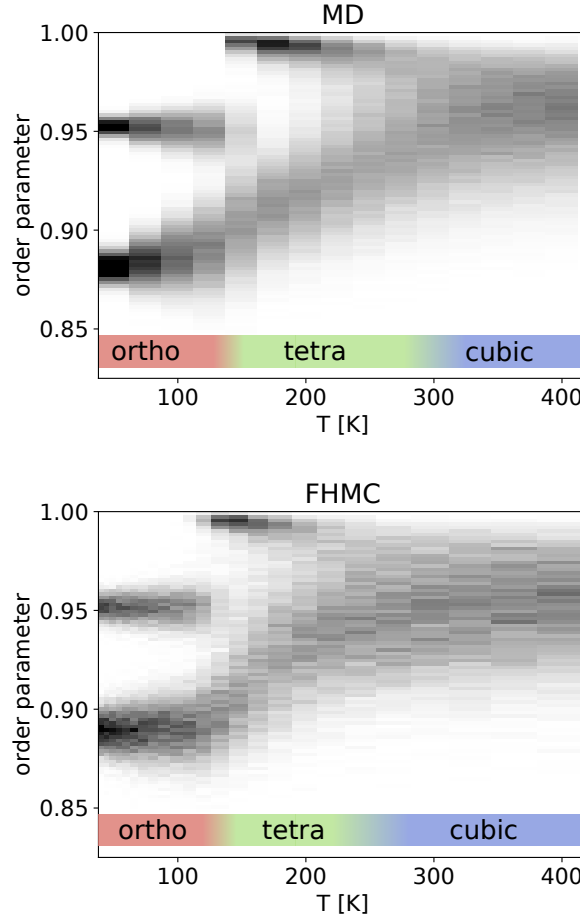


Figure 7.5: Histogram of the order parameter versus temperature obtained from MD and FHMC simulation. The orthorhombic phase can be identified by the presence of an order parameter value around 0.95. In the tetragonal phase this order parameter value disappears and values close to 1 are present. At higher temperatures the two distinct peaks in the order parameter merge into a single peak which marks the transition to the cubic phase. (Figure adapted with permission from Reference [259].)

be slightly strained at higher temperatures. Using the average lattice parameters of the tetragonal phase at 250 K obtained from variable cell shape MD in our FHMC simulations, we obtain a higher transition temperature that agrees extremely well with the MD results. The order parameter histogram of this simulation is shown in Figure 7.6. To keep our simulations consistent and to not introduce any bias by picking lattice parameters from different temperatures, we decided to use lattice parameters from ground state geometries.

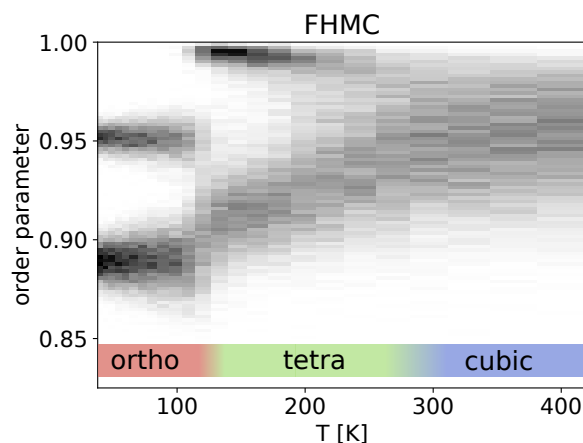


Figure 7.6: Histogram of the order parameter versus temperature obtained from a FHMC simulation where the tetragonal lattice was slightly adjusted. (Figure adapted with permission from Reference [259].)

7.4.2 FHMC STUDY INCLUDING THE TWO DELTA PHASES

After confirming that FHMC is able to reproduce results obtained from MD simulations for the three experimental perovskite phases, we continue our investigation by performing FHMC simulations that include the two delta phases in addition to the three perovskite phases. Phase transitions involving the delta phases cannot be simulated using classical MD simulations. Both delta phases appear to be stable at our maximum simulation temperature of 400 K. We would therefore need to go to even higher temperatures or longer timescales to access the transition states, that connect the delta phases with the perovskite phases. Due to the large structural difference between the phases, complex transition states, that are not included in the training data of our HDNNPs are expected, rendering our HDNNPs inaccurate. Furthermore, we expect that the timescales needed for such transitions would be prohibitively large. This is supported by the fact, that even transitions between the structurally very similar orthorhombic and tetragonal phases are hard to observe in our MD simulations. Chen et al. [283] experimentally investigated the structurally similar transition between the delta and cubic phases of FaPbI_3 and found a large energetic barrier and reported complete kinetic trapping of the material in the higher energy cubic phase after cooling the material from 400 K to 200 K within 80 minutes. Clearly, such timescales are not accessible by any form of MD simulation. A large hysteresis of the transition between heating and cooling further supports the high free energy barrier and complex transition pathway.

FHMC simulations can avoid this problem of high barriers and allow us to determine phase transition temperatures involving the delta phases without the need to also explore the large configuration space of transition states while still taking anharmonic effects into account without any approximation.

Unlike for the experimental phases, no transition from a delta phase to any other phase within the same lattice configuration was ever observed in our FHMC and MD simulations. We can therefore directly use the lattice configuration as an indicator of the delta phases. A plot showing the probability of finding the system in the

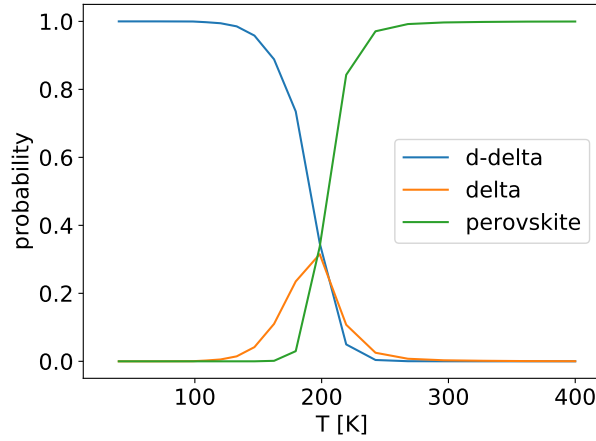


Figure 7.7: Probability of finding the FHMC walker in of the delta phases or a perovskite phase. (Figure reproduced with permission from Reference [259].)

double-delta phase, the delta phase, or a perovskite phase versus temperatures is shown in Figure 7.7. At low temperatures, the double-delta phase is dominant. The delta phase has only for a small temperature window a significantly non-zero probability. At higher temperatures above 200 K, the system is most likely to be found in a perovskite phase.

We also computed free energies using the HA and QHA for all phases, except the cubic phase using the phonopy code [297] and our HDNNP. We excluded the cubic phase, since it does not relate to a minimum on the PES. Both, the HA and QHA free energies are in qualitative agreement, indicating that effects of thermal expansion are not the main reason of the anharmonicity of the system. The relative free energies as well as plots of the phonon density of state for all phases are included in Appendix B.2.3.

We found, that even for the non-cubic phases, extremely tight settings, such as tight geometry optimization thresholds and small displacements for the calculation

of the force constants through finite differences were necessary to avoid imaginary frequency modes. Similar findings were also reported by Marrognier et al. [298]. Compared to a DFT PES, where noise is present, smaller displacements are not problematic on our HDNNP PES, since it is an analytical function, that can be evaluated with almost machine precision. Geometry optimizations were performed using the vc-SQNM algorithm [299].

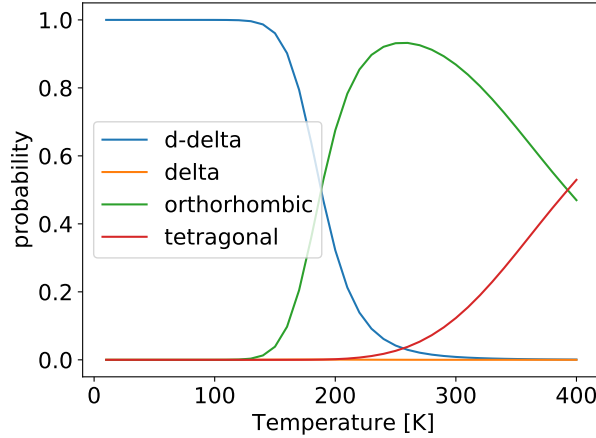


Figure 7.8: Probability of finding the system in a given phase, computed using the quasi-harmonic approximation.

We then used the free energies computed within the QHA to calculate probabilities of finding the system in a given phase for the same unit cells that were used for the FHMC and MD simulations. The results are shown in Figure 7.8.

At low temperatures, the double-delta phase is most stable. Above 180 K the orthorhombic phase is predicted by the QHA to be thermodynamically more stable.

This is surprisingly close to our FHMC results, that predict that the double-delta phase is only preferred up to a temperature of 200 K. However, the HA and QHA further predict, that the orthorhombic phase is preferred over the tetragonal phase up to a temperature of 380 K, which is inconsistent with experimental results as well as our FHMC and MD results. The correct prediction of the disappearing of the double delta phase above 200 K by the QHA, is therefore most likely an accidental result caused by error cancellation.

We also devised an additional test to further investigate the anharmonicity of the vibrational modes found by the HA. For this, we made an estimate ω_{fit} of each vibrational frequency, that is not based on the second derivative of the potential energy at the local minimum but instead uses a quadratic fit of the potential energy

through points placed further away from the minimum along the vibrational mode. These points were chosen such that they represent a realistic displacement from the local minimum as it could be observed during a finite temperature simulation. We first used the harmonic approximation to estimate the magnitude of the displacements, at which an energy of $\frac{1}{2}k_B T$ above the local minimum energy should be expected. This procedure was then repeated multiple times using the fitted curvature of the potential energy instead of the HA, such that a consistent fit was obtained. The converged fits were then used to estimate the vibrational frequencies ω_{fit} . The ration between the ω_{fit} calculated for a temperature of 300 K and the harmonic frequencies ω_{HA} serves as a rough measure of the anharmonicity of each vibrational mode and are shown in Figure 7.9. The results show the presence of anharmonic modes in all

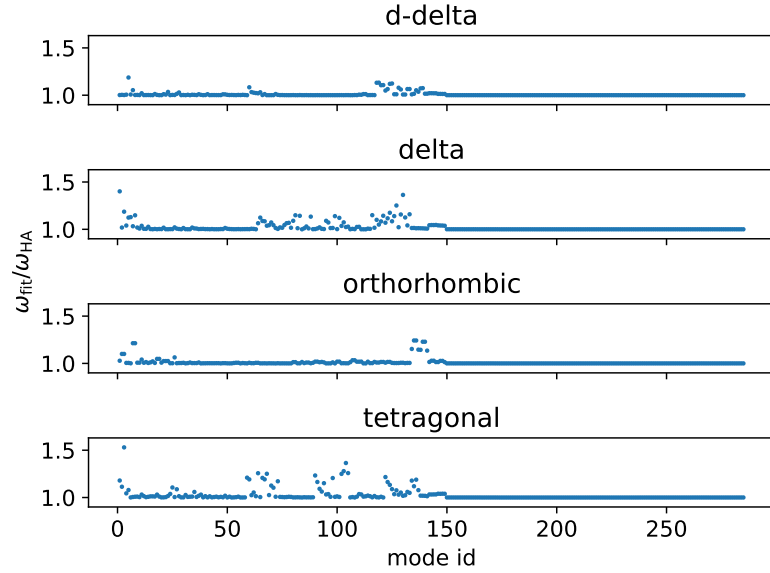


Figure 7.9: Ratio between the vibrational frequencies ω_{fit} and ω_{HA} . Unlike the HA, which is based on the second derivatives of the potential energy at the local minimum, the fitted frequencies are obtained from fitting a quadratic approximation of the potential energy using larger displacements along vibrational modes. (Figure adapted with permission from Reference [259].)

four phases. Interestingly, there seem to be fewer anharmonic modes in the double delta and the orthorhombic phase than in the delta and tetragonal phase. This might be an indication as to why the HA performs better for these two phases.

In general, however, it is not known, up to which temperatures the HA can be trusted and how strong the influence of the anharmonicity is in the final results.

For example, Thind et al. [282] also calculated free energies using the QHA for the delta and cubic phases of MaPbI_3 and found a transition temperature of 750 K. This again is inconsistent with our FHMC results, which suggest a much lower transition temperature. Furthermore, it was also reported that the HA and QHA fail to assign the lowest free energy to the experimentally found tetragonal phase of the structurally similar system of CsSnI_3 [300].

These results underline the high anharmonicity of the PES of perovskite materials and show, that methods beyond the HA and QHA are needed to obtain reliable phase transition temperatures.

7.5 SUMMARY

We developed a highly accurate and reliable MLP for MaPbI_3 , that is trained on data including all three experimentally observed perovskite phases as well as the two theoretically predicted non-perovskite polymorphs. We studied phase transitions in MaPbI_3 using MD, as well as FHMC, which we extended to periodic systems. The complicated nature of the PES required further modifications of the method, such as a special treatment of the Ma molecules and coupling FHMC with RX. The final version of our FHMC method constructs an artificial potential energy surface (APES), based on Gaussian mixtures, on which all FHMC moves are accepted. These global MC moves, that directly jump from one phase to another, without violating detailed balance, allow for an extremely efficient sampling of the APES. We then couple a simulation on the proper machine learned PES to this APES through RX. The efficiency of the method is further increased by including RX moves between different temperatures. FHMC directly circumvents the high energy barriers. This makes it particularly well suited for applications based on machine learned potentials, since the complicated transition states do not need to be included in the training dataset.

We validated the method by simulating the phase transitions between the three perovskite phases and comparing our results to long timescale MD simulations. An order parameter, that measures the tilting between neighboring PbI_3 octahedra allows us to clearly identify the transition temperature between the orthorhombic and tetragonal phase at 130 K.

FHMC simulations including the delta and double-delta phases, which have a lower potential energy than the perovskite phases, reveal, that above 200 K, the perovskite phases are thermodynamically favoured. This could explain the elusiveness of the delta phases in experiments. At room temperature MaPbI_3 will readily form

the perovskite phases and the low transition temperature combined with the high free energy barriers to the delta phases lead to kinetic trapping when the material is cooled down. A synthesis of the delta phases can therefore be expected to be very challenging and might only be possible under special conditions, such as high pressures as suggested by Flores-Livas et al. [26] and very slow cooling rates.

A comparison with the QHA supports previous reports of the high anharmonicity of perovskite materials. While the QHA's prediction agrees with our FHMC results, in that the delta phase is only favoured by the free energy at low temperatures, it fails to give a reasonable prediction for the orthorhombic to tetragonal phase transition temperature. This suggests, that the QHA's prediction of the delta to orthorhombic phase transition temperature is caused by accidental error cancellation. Furthermore, the QHA cannot directly be applied to the cubic phase, which does not correspond to a local minimum in the PES. An accurate prediction of transition temperatures, therefore requires the use of methods beyond the harmonic approximation, such as our FHMC method.

Due to the rotational degree of freedom of the Ma molecules, MaPbI_3 turned out to be a particularly challenging system for the application of FHMC. This rare feature of MaPbI_3 required an additional adaption of the FHMC method, which is a special treatment of the Ma molecules during FHMC moves. For most materials, such a special adaptation should not be necessary. We therefore expect that the method is directly applicable to a large range of strongly anharmonic systems, such as other perovskite materials, silicates [301] or superionic conductors [302].

8 CONCLUSION AND OUTLOOK

Due to the continuously increasing speed of computers and the development of simulation techniques and algorithms computer simulations have become an important cornerstone to physics, materials science and chemistry. More recently, methods based on machine learning techniques have also been gaining a lot of attention and have seen a rapid adoption by the community. While impressive progress has been made in the last decade, it is clear, that many open questions remain and further research is needed to take full advantage of machine learning techniques in materials sciences simulations.

In this thesis, we tried to address two important issues, namely, how long range interactions caused by charge transfer can be integrated into machine learned potentials (MLPs) and how materials that suffer from broken ergodicity due to high energetic barriers can be simulated efficiently.

To understand why the proper inclusion of charge transfer effects in MLPs is important, we first need to take a step back and have a look at the history of MLPs. For this we classified MLPs into four generations [109, 132]. The first generation of MLPs directly used atomic coordinates as inputs to artificial neural networks (ANNs). This allows for a complete description of the whole system, which also includes effects due to charge transfer and electrostatics. However, these first generation potentials have a major disadvantage in that they are very system specific and cannot extrapolate to different system sizes. Additionally, important symmetries, such as the invariance of the energy under rotation or translation of the whole system and permutations of equivalent atoms are not preserved. These problems were overcome by the introduction of the high dimensional neural network potential (HDNNP) by Behler and Parrinello [9], which is the first example of a second generation MLP. In the HDNNP, the total energy is expressed as a sum of atomic energies, each of which depend on the local atomic environment, encoded by atom centered symmetry functions (ACSFs) that ensure the preservation of the required symmetries. While this enables simulations of large systems based on training data from smaller systems, it also imposes a new limitation due to the assumption of local atomic interactions.

Important long range interactions, such as electrostatics are therefore necessarily truncated at the cutoff radius of the ACSFs. This was quickly realized and led to the development of third generation methods which include explicit electrostatics through environment dependent atomic charges. However, more recently it became clear, that effects due to charge transfer caused by remote structural changes, outside the local atomic environment or changes in the total system charge, are still missing. Such effects can be found in many important systems, including organic reactions involving protonation or deprotonation of molecules, in the doping of semiconductor materials or in cases, where the total charge of a system changes through ionization. These findings inspired us to develop the fourth generation high-dimensional neural network potential (4G-HDNNP) [107] presented in this thesis.

The 4G-HDNNP uses a charge equilibration scheme, based on environment dependent electronegativities, to predict accurate atomic charges that depend on the geometry of the full system. The charge equilibration scheme is similar to the one employed in the charge equilibration via neural network technique (CENT) but uses a different training procedure. Instead of optimizing the electronegativity predicting ANNs, such that the total system energy is reproduced, reference atomic charges, obtained from density functional theory (DFT) calculations are targeted. These charges are then used to calculate the Coulomb interactions. In addition to the ANNs predicting the electronegativities, a second set of ANNs is employed that, just like in the HDNNP, predicts atomic energies to capture the remaining short ranged interactions. However, there is one important difference. The atomic energy predicting ANNs do not only depend on the local atomic environment through the use of ACSFs but also the atomic charge obtained from the charge equilibration process is used as input. This way, changes in local reactivity and bonding caused by charge transfer due to far away configuration changes can be accounted for. This capability was demonstrated on several test systems, taken from different fields to demonstrate the 4G-HDNNP’s applicability for different scenarios.

While these results are extremely promising, research on improvements and extensions of the 4G-HDNNP is still ongoing. Currently, an implementation of the 4G-HDNNP is under development which employs an iterative solver to overcome the currently cubic scaling of the computation cost with respect to system size.

Other extensions to the 4G-HDNNP, that do not address the computational efficiency but instead aim to improve the transferability of the potential to structures outside the training data set have been introduced in the electrostatically embedded fourth generation high-dimensional neural network potential (ee4G-HDNNP) [199]. In

the ee4G-HDNNP, additional pairwise potentials, fitted to binding curves, are added to the potential. Due to their physical form, these additional two body contribution ensure a reasonable behaviour of the potential in cases where training data is missing. This way, so-called holes in the potential energy surface (PES), where unphysically low energies are predicted, due to a lack of appropriate training data, can be avoided. Additionally, a new type of environment descriptor, that also captures information about the atomic charges of neighboring atoms, is introduced. This improves the accuracy of the potential for cases where similar atomic environments are present for which the charge on the central environment is the same, but the charge on neighboring atoms differs.

We hope that the 4G-HDNNP will enable qualitatively and quantitatively accurate simulations of large systems that include long ranged charge transfer effects. Such systems might be large conjugated organic molecules, ionized clusters or clusters deposited on doped substrates as already illustrated in the examples presented in this thesis. We expect that the 4G-HDNNP will be particularly useful for modelling chemistry in solution where charge transfer effects commonly occur due to protonation reactions or changing oxidation states. Investigating such systems is the goal of a current project in collaboration with the group of Jörg Behler where we will first assess the accuracy of different reference methods including DFT for describing charge transfer. Later on, we will investigate if the current version of the charge equilibration process is sufficient for describing chemistry in solution or if additional modifications will be needed to ,for example, prevent unphysical charge transfer between different molecules.

A critical component to many MLPs, including our 4G-HDNNP, are atomic environment descriptors (AEDs). We saw in this thesis, that many AEDs, including the ACSF only provide an incomplete description of the atomic environment. Our results based on an n-body decomposition of a methane molecule’s energy highlight this problem by demonstrating that the ACSFs are not able to capture the four-body interactions. While the overlap matrix (OM) fingerprint is able to capture the four-body energy contribution, it suffers from discontinuities in its first derivative due to the sorting of the eigenvalues of the OM matrix. Although this can be advantageous in rare cases, where the discontinuities coincide with conical intersections, it is in most cases undesirable, since it leads to discontinuous forces in the final MLP. We presented a method that resolves this problem by projecting the OM eigenvalues onto basis functions represented by ANNs. Different training procedures are proposed to fit the basis functions, such that either pairwise fingerprint distances are targeted or

the original OM fingerprint is reproduced as closely as possible. The final results are promising and show that the smoothed version of the OM fingerprint is able to capture the four-body interactions of the methane test system. Unfortunately, the OM fingerprint seems to be suboptimal for the description of important two-body energies. A combined descriptor, which is constructed by concatenating the OM fingerprint with ACSFs helps to improve the description of two-body terms but this is not a very elegant solution and leads to an increased length of the final descriptor. Therefore, further research is still needed to improve the description of two-body terms in the OM fingerprint. In the future we will also need to investigate applications of a smoothed OM fingerprint, where it is used in a HDNNP, i.e., where the AED of every atom is used instead of a single atom only as in our methane test system.

Due to their high accuracy and the favourable scaling of the computational cost with respect to system size, MLPs bridge the gap between fast but inaccurate classical force fields and more accurate but computationally demanding *ab-initio* methods. They enable simulations at unprecedented time and length scales and even real-size simulations of microscopic devices are becoming possible [303]. However, in many systems, high energy barriers are present which make transitions between metastable states incredibly rare events. A simulation of such reactions by standard molecular dynamics (MD) or Monte Carlo (MC) procedures would therefore require prohibitively long simulation times that, even with the steady increase in computation power, will not be possible in the near future.

The Funnel Hopping Monte Carlo (FHMC) method [94] presented in this thesis solves this problem by introducing a global MC move that directly circumvents the high energy barriers. In the FHMC method, a reference frame for each minimum is constructed to capture the displacements of the atoms from the minimum geometry. The root mean squared deviation (RMSD) is used to align the current configuration to the reference frame, such that atom permutations, rotations and translations can be accounted for. The Boltzmann distribution around each local minimum is approximated by Gaussian mixtures fit to MC samples from preliminary MC simulations which are constrained to the regions around the local minima. Global MC moves can then be constructed by sampling trial geometries from the Gaussian mixtures.

In a first test, we applied the FHMC method to the 38 and 75 atom Lennard-Jones (LJ) clusters. These are particularly challenging test systems, due to their double funnel PESs. Our results show, that FHMC is able achieve a converged

sampling of the PES at lower temperatures requiring orders of magnitude less MC samples than comparable methods. At higher temperatures, the performance of the method deteriorates, since many more local minima, which are not included in the FHMC scheme, become accessible. This problem can be solved by combining FHMC with parallel tempering (PT). The PT helps the simulation to overcome the low barriers to the additional, higher energy, local minima while the FHMC help the simulation to overcome the high, inter-funnel barriers. The final results on the LJ test systems show, that FHMC is much more efficient than comparable methods and requires less energy and force computations until convergence.

Inspired by these positive results, we decided to apply the FHMC method to study a real system, for which we found the perovskite material methylammonium lead iodide (MaPbI_3) to be a particularly interesting (although in hindsight also particularly challenging) candidate. MaPbI_3 is a widely studied material, due to its special opto-electronic properties which make it a promising candidate for highly efficient solar cells. In a recent structure search study [26], based on the minima hopping method, two new non-perovskite polymorphs of MaPbI_3 were discovered, which are lower in energy than the experimentally known ground state. Furthermore, the highly anharmonic nature of the material makes the use of methods beyond the harmonic approximation (HA), such as our FHMC necessary. The fact that the methylammonium (CH_3NH_3) (Ma) molecules can rotate almost freely in the PbI cavities around them, made an application of FHMC particularly challenging and required several extensions of the method, such as a special treatment of the Ma molecules during FHMC moves and the introduction of Hamiltonian replica exchange (RX). With these additional extensions, we were able to run FHMC simulations that include the experimentally observed perovskite phases as well as the theoretically predicted ground state phases. These simulations were based on a HDNNP, which we trained to reference data obtained from DFT calculations using the strongly constrained and appropriately normed (SCAN) exchange correlation functional.

Our results show, that the newly found ground state phases are only thermodynamically preferred up to a temperature of 200 K. This rather low transition temperature may explain the elusiveness of the theoretically predicted non-perovskite phases from experimental studies. During synthesis at room temperature, the perovskite phases will readily form. When the material is cooled down below the transition temperature, the low thermal energy is insufficient to cross the high barrier to the non-perovskite phases and the material will remain in the meta-stable perovskite

phase. A synthesis of the non-perovskite phases might therefore only be possible under special conditions, such as high pressures as suggested by Flores-Livas et al. [26] and very slow annealing rates.

Being able to successfully apply FHMC to the particularly challenging case of MaPbI_3 suggests that the method should be applicable to a wide range of materials. In many materials, such as the perovskite material studied in this thesis or for example alanites [304], polymorphs are found by theoretical studies which are absent from experiments. This shows, that simple energetics are often not sufficient to assess the synthesizability of a material. Since high anharmonicity is present in many materials methods that go beyond simple energetics or the HA such as our FHMC method are needed.

Examples of highly anharmonic materials include thermoelectric materials [305–307] where so-called rattling atoms lead to a high anharmonicity that scatters phonons that are responsible for heat transport [308]. Similarly to perovskites, borates [309] also exhibit a high anharmonicity due to the presence rigid groups which rotate as a unit relative to other groups [310]. High anharmonicity and a complex phase diagram can also be found in silicates which make up large portions of the earths mantle [311].

We therefore hope, that FHMC will be useful in the future to calculate phase transition temperatures with an accuracy beyond the HA and assess the synthesizability of highly anharmonic materials without expensive experimentation.

ACRONYMS

2G-HDNNP	Second generation high-dimensional neural network potential
3G-HDNNP	Third generation high-dimensional neural network potential
4G-HDNNP	Fourth generation high-dimensional neural network potential
ACSF	Atom centered symmetry function
AED	Atomic environment descriptor
ANN	Artificial neural network
APES	Artificial potential energy surface
CENT	Charge equilibration via neural network technique
CI	Configuration interaction
DFT	Density functional theory
ee4G-HDNNP	Electrostatically embedded fourth generation high-dimensional neural network potential
EM	Expectation-maximization
FFT	Fast Fourier transform
FHMC	Funnel Hopping Monte Carlo
GGA	Generalized gradient approximation
GM	Gaussian mixture
GPU	Graphics processing unit
HA	Harmonic approximation
HDNNP	High-dimensional neural network potential
HEG	Homogeneous electron gas
HF	Hartree-Fock
HMC	Hamiltonian Monte Carlo
HSA	Harmonic superposition approximation
LCAO	Linear combination of atomic orbitals
LDA	Local density approximation
LJ	Lennard-Jones
LJ ₃₈ cluster	38 atom Lennard-Jones cluster
LJ ₇₅ cluster	75 atom Lennard-Jones cluster

Acronyms

Ma	Methylammonium (CH_3NH_3)
MC	Monte Carlo
MD	Molecular dynamics
MLP	Machine learned potential
MPNN	Message passing neural network
NNP	Neural network potential
OM	Overlap matrix
PBE	Perdew Burke and Ernzerhof
PES	Potential energy surface
PT	Parallel tempering
QHA	Quasi harmonic approximation
QM/MM	Quantum mechanics / molecular mechanics
RMSD	Root mean squared deviation
RMSE	Root mean squared error
RPA	Random phase approximation
RX	Replica exchange
SCAN	Strongly constrained and appropriately normed
SOAP	Smooth overlap of atomic positions

BIBLIOGRAPHY

1. J. R. Partington. *A short history of chemistry*. Courier Corporation, 1989.
2. N. Metropolis, A. W. Rosenbluth, M. N. Rosenbluth, A. H. Teller, and E. Teller. “Equation of state calculations by fast computing machines”. *The journal of chemical physics* 21:6, 1953, pp. 1087–1092.
3. B. J. Alder and T. E. Wainwright. “Phase transition for a hard sphere system”. *The Journal of chemical physics* 27:5, 1957, pp. 1208–1209.
4. A. Rahman. “Correlations in the motion of atoms in liquid argon”. *Physical review* 136:2A, 1964, A405.
5. A. Rahman and F. H. Stillinger. “Molecular dynamics study of liquid water”. *The Journal of Chemical Physics* 55:7, 1971, pp. 3336–3359.
6. G. Battimelli, G. Battimelli, G. Ciccotti, P. Greco, and Scalone. *Computer Meets Theoretical Physics*. Springer, 2020.
7. R. Car and M. Parrinello. “Unified approach for molecular dynamics and density-functional theory”. *Physical review letters* 55:22, 1985, p. 2471.
8. T. B. Blank, S. D. Brown, A. W. Calhoun, and D. J. Doren. “Neural network models of potential energy surfaces”. *The Journal of chemical physics* 103:10, 1995, pp. 4129–4137.
9. J. Behler and M. Parrinello. “Generalized neural-network representation of high-dimensional potential-energy surfaces”. *Physical review letters* 98:14, 2007, p. 146401.
10. J. Behler. “Atom-centered symmetry functions for constructing high-dimensional neural network potentials”. *The Journal of chemical physics* 134:7, 2011, p. 074106.
11. N. Artrith, T. Morawietz, and J. Behler. “High-dimensional neural-network potentials for multicomponent systems: Applications to zinc oxide”. *Physical Review B* 83:15, 2011, p. 153101.

12. G.M. Torrie and J.P. Valleau. “Monte Carlo free energy estimates using non-Boltzmann sampling: Application to the sub-critical Lennard-Jones fluid”. *Chemical Physics Letters* 28:4, 1974, pp. 578–581.
13. G.M. Torrie and J.P. Valleau. “Nonphysical sampling distributions in Monte Carlo free-energy estimation: Umbrella sampling”. *Journal of Computational Physics* 23:2, 1977, pp. 187–199.
14. J. Kästner. “Umbrella sampling”. *Wiley Interdisciplinary Reviews: Computational Molecular Science* 1:6, 2011, pp. 932–942.
15. A. Laio and M. Parrinello. “Escaping free-energy minima”. *Proceedings of the National Academy of Sciences* 99:20, 2002, pp. 12562–12566.
16. B.A. Berg and T. Neuhaus. “Multicanonical algorithms for first order phase transitions”. *Physics Letters B* 267:2, 1991, pp. 249–253.
17. B.A. Berg and T. Neuhaus. “Multicanonical ensemble: A new approach to simulate first-order phase transitions”. *Physical Review Letters* 68:1, 1992, p. 9.
18. F. Wang and D. Landau. “Determining the density of states for classical statistical models: A random walk algorithm to produce a flat histogram”. *Physical Review E* 64:5, 2001, p. 056101.
19. F. Wang and D.P. Landau. “Efficient, multiple-range random walk algorithm to calculate the density of states”. *Physical review letters* 86:10, 2001, p. 2050.
20. J. Skilling. “Nested sampling”. In: *Aip conference proceedings*. Vol. 735. 1. American Institute of Physics. 2004, pp. 395–405.
21. J. Skilling. “Nested sampling for general Bayesian computation”. *Bayesian analysis* 1:4, 2006, pp. 833–859.
22. J. Skilling. “Nested sampling’s convergence”. In: *AIP Conference Proceedings*. Vol. 1193. 1. American Institute of Physics. 2009, pp. 277–291.
23. L.B. Pártay, G. Csányi, and N. Bernstein. “Nested sampling for materials”. *The European Physical Journal B* 94:8, 2021, pp. 1–18.
24. I. Andricioaei, J.E. Straub, and A.F. Voter. “Smart darting monte carlo”. *The Journal of Chemical Physics* 114:16, 2001, pp. 6994–7000.

25. V. A. Sharapov and V. A. Mandelshtam. “Solid-solid structural transformations in Lennard-Jones clusters: Accurate simulations versus the harmonic superposition approximation”. *The Journal of Physical Chemistry A* 111:41, 2007, pp. 10284–10291.
26. J. A. Flores-Livas, D. Tomerini, M. Amsler, A. Boziki, U. Rothlisberger, and S. Goedecker. “Emergence of hidden phases of methylammonium lead iodide (CH₃NH₃PbI₃) upon compression”. *Physical Review Materials* 2:8, 2018, p. 085201.
27. M. Born and R. Oppenheimer. “Zur Quantentheorie der Molekeln *Annalen der Physik*, v. 84”, 1927.
28. R. P. Feynman. “Forces in molecules”. *Physical review* 56:4, 1939, p. 340.
29. G. Kresse and J. Furthmüller. “Efficiency of ab-initio total energy calculations for metals and semiconductors using a plane-wave basis set”. *Computational materials science* 6:1, 1996, pp. 15–50.
30. L. E. Ratcliff, W. Dawson, G. Fisicaro, D. Caliste, S. Mohr, A. Degomme, B. Videau, V. Cristiglio, M. Stella, M. D’Alessandro, et al. “Flexibilities of wavelets as a computational basis set for large-scale electronic structure calculations”. *The Journal of chemical physics* 152:19, 2020, p. 194110.
31. W. J. Hehre, R. F. Stewart, and J. A. Pople. “self-consistent molecular-orbital methods. i. use of gaussian expansions of Slater-type atomic orbitals”. *The Journal of Chemical Physics* 51:6, 1969, pp. 2657–2664.
32. V. Blum, R. Gehrke, F. Hanke, P. Havu, V. Havu, X. Ren, K. Reuter, and M. Scheffler. “Ab initio molecular simulations with numeric atom-centered orbitals”. *Computer Physics Communications* 180:11, 2009, pp. 2175–2196.
33. D. L. Strout and G. E. Scuseria. “A quantitative study of the scaling properties of the Hartree–Fock method”. *The Journal of chemical physics* 102:21, 1995, pp. 8448–8452.
34. P. Hohenberg and W. Kohn. “Inhomogeneous electron gas”. *Physical review* 136:3B, 1964, B864.
35. T. Van Mourik, M. Bühl, and M.-P. Gaigeot. *Density functional theory across chemistry, physics and biology*. 2014.
36. F. Giustino. *Materials modelling using density functional theory: properties and predictions*. Oxford University Press, 2014.

37. W. Kohn and L. J. Sham. “Self-consistent equations including exchange and correlation effects”. *Physical review* 140:4A, 1965, A1133.
38. D. M. Ceperley and B. J. Alder. “Ground state of the electron gas by a stochastic method”. *Physical review letters* 45:7, 1980, p. 566.
39. J. P. Perdew, K. Burke, and M. Ernzerhof. “Generalized gradient approximation made simple”. *Physical review letters* 77:18, 1996, p. 3865.
40. J. Sun, A. Ruzsinszky, and J. P. Perdew. “Strongly constrained and appropriately normed semilocal density functional”. *Physical review letters* 115:3, 2015, p. 036402.
41. J. P. Perdew, M. Ernzerhof, and K. Burke. “Rationale for mixing exact exchange with density functional approximations”. *The Journal of chemical physics* 105:22, 1996, pp. 9982–9985.
42. P. J. Stephens, F. J. Devlin, C. F. Chabalowski, and M. J. Frisch. “Ab initio calculation of vibrational absorption and circular dichroism spectra using density functional force fields”. *The Journal of physical chemistry* 98:45, 1994, pp. 11623–11627.
43. S. Goedecker. “Linear scaling electronic structure methods”. *Reviews of Modern Physics* 71:4, 1999, p. 1085.
44. S. Mohr, L. E. Ratcliff, P. Boulanger, L. Genovese, D. Caliste, T. Deutsch, and S. Goedecker. “Daubechies wavelets for linear scaling density functional theory”. *The Journal of chemical physics* 140:20, 2014, p. 204110.
45. R. S. Mulliken. “Electronic population analysis on LCAO–MO molecular wave functions. I”. *The Journal of Chemical Physics* 23:10, 1955, pp. 1833–1840.
46. P.-O. Löwdin. “On the non-orthogonality problem connected with the use of atomic wave functions in the theory of molecules and crystals”. *The Journal of Chemical Physics* 18:3, 1950, pp. 365–375.
47. R. F. Bader. “Atoms in molecules”. *Accounts of Chemical Research* 18:1, 1985, pp. 9–15.
48. F. L. Hirshfeld. “Bonded-atom fragments for describing molecular charge densities”. *Theoretica chimica acta* 44:2, 1977, pp. 129–138.
49. A. D. Becke. “A multicenter numerical integration scheme for polyatomic molecules”. *The Journal of chemical physics* 88:4, 1988, pp. 2547–2553.

50. B. Parsaeifard, D. S. De, J. A. Finkler, and S. Goedecker. "Fingerprint-Based Detection of Non-Local Effects in the Electronic Structure of a Simple Single Component Covalent System". *Condensed Matter* 6:1, 2021, p. 9.
51. A. E. Sifain, N. Lubbers, B. T. Nebgen, J. S. Smith, A. Y. Lokhov, O. Isayev, A. E. Roitberg, K. Barros, and S. Tretiak. "Discovering a transferable charge assignment model using machine learning". *The journal of physical chemistry letters* 9:16, 2018, pp. 4495–4501.
52. K. B. Wiberg and P. R. Rablen. "Comparison of atomic charges derived via different procedures". *Journal of Computational Chemistry* 14:12, 1993, pp. 1504–1518.
53. B. H. Besler, K. M. Merz Jr, and P. A. Kollman. "Atomic charges derived from semiempirical methods". *Journal of computational chemistry* 11:4, 1990, pp. 431–439.
54. C. M. Breneman and K. B. Wiberg. "Determining atom-centered monopoles from molecular electrostatic potentials. The need for high sampling density in formamide conformational analysis". *Journal of Computational Chemistry* 11:3, 1990, pp. 361–373.
55. Y. Mei, A. C. Simmonett, F. C. Pickard IV, R. A. DiStasio Jr, B. R. Brooks, and Y. Shao. "Numerical study on the partitioning of the molecular polarizability into fluctuating charge and induced atomic dipole contributions". *The Journal of Physical Chemistry A* 119:22, 2015, pp. 5865–5882.
56. O. T. Unke and M. Meuwly. "PhysNet: A neural network for predicting energies, forces, dipole moments, and partial charges". *Journal of chemical theory and computation* 15:6, 2019, pp. 3678–3693.
57. E. R. Khajepasha, J. A. Finkler, T. D. Kühne, and S. A. Ghasemi. "CENT2: Improved charge equilibration via neural network technique". *Physical Review B* 105:14, 2022, p. 144106.
58. C. G. Staacke, S. Wengert, C. Kunkel, G. Csányi, K. Reuter, and J. T. Margraf. "Kernel charge equilibration: efficient and accurate prediction of molecular dipole moments with a machine-learning enhanced electron density model". *Machine Learning: Science and Technology* 3:1, 2022, p. 015032.
59. L. Verlet. "Computer" experiments" on classical fluids. I. Thermodynamical properties of Lennard-Jones molecules". *Physical review* 159:1, 1967, p. 98.

60. S. Nosé. “A unified formulation of the constant temperature molecular dynamics methods”. *The Journal of chemical physics* 81:1, 1984, pp. 511–519.
61. W. G. Hoover. “Canonical dynamics: Equilibrium phase-space distributions”. *Physical review A* 31:3, 1985, p. 1695.
62. W. G. Hoover, A. J. Ladd, and B. Moran. “High-strain-rate plastic flow studied via nonequilibrium molecular dynamics”. *Physical Review Letters* 48:26, 1982, p. 1818.
63. H. C. Andersen. “Molecular dynamics simulations at constant pressure and/or temperature”. *The Journal of chemical physics* 72:4, 1980, pp. 2384–2393.
64. W. K. Hastings. “Monte Carlo sampling methods using Markov chains and their applications”, 1970.
65. A. Gelman, W. R. Gilks, and G. O. Roberts. “Weak convergence and optimal scaling of random walk Metropolis algorithms”. *The annals of applied probability* 7:1, 1997, pp. 110–120.
66. M. Betancourt. “A conceptual introduction to Hamiltonian Monte Carlo”. *arXiv preprint arXiv:1701.02434*, 2017.
67. E. Meeds, R. Leenders, and M. Welling. “Hamiltonian abc”. *arXiv preprint arXiv:1503.01916*, 2015.
68. S. Duane, A. D. Kennedy, B. J. Pendleton, and D. Roweth. “Hybrid monte carlo”. *Physics letters B* 195:2, 1987, pp. 216–222.
69. G. E. Box. “A note on the generation of random normal deviates”. *Ann. Math. Statist.* 29, 1958, pp. 610–611.
70. R. E. A. C. Paley and N. Wiener. *Fourier transforms in the complex domain*. Vol. 19. American Mathematical Soc., 1934.
71. O. M. Becker and M. Karplus. “The topology of multidimensional potential energy surfaces: Theory and application to peptide structure and kinetics”. *The Journal of chemical physics* 106:4, 1997, pp. 1495–1517.
72. D. J. Wales. “Energy landscapes: some new horizons”. *Current opinion in structural biology* 20:1, 2010, pp. 3–10.
73. C. Levinthal. “Mossbauer spectroscopy in biological systems”. In: *Proceedings of a meeting held at Allerton House. P. Debrunner, JCM Tsibris, and E. Munck, editors. University of Illinois Press, Urbana, IL*. 1969.

74. D. S. De, B. Schaefer, B. von Issendorff, and S. Goedecker. "Nonexistence of the decahedral Si₂₀H₂₀ cage: Levinthal's paradox revisited". *Physical Review B* 101:21, 2020, p. 214303.
75. P. Salamon, P. Sibani, and R. Frost. *Facts, conjectures, and improvements for simulated annealing*. SIAM, 2002.
76. D. J. Wales and J. P. Doye. "Global optimization by basin-hopping and the lowest energy structures of Lennard-Jones clusters containing up to 110 atoms". *The Journal of Physical Chemistry A* 101:28, 1997, pp. 5111–5116.
77. D. E. Golberg. "Genetic algorithms in search, optimization, and machine learning". *Addison Wesley* 1989:102, 1989, p. 36.
78. T. Bush, C. R. A. Catlow, and P. Battle. "Evolutionary programming techniques for predicting inorganic crystal structures". *Journal of Materials Chemistry* 5:8, 1995, pp. 1269–1272.
79. A. R. Oganov and C. W. Glass. "Evolutionary crystal structure prediction as a tool in materials design". *Journal of Physics: Condensed Matter* 20:6, 2008, p. 064210.
80. R. Martoňák, A. Laio, and M. Parrinello. "Predicting crystal structures: the Parrinello-Rahman method revisited". *Physical review letters* 90:7, 2003, p. 075503.
81. S. Goedecker. "Minima hopping: An efficient search method for the global minimum of the potential energy surface of complex molecular systems". *The Journal of chemical physics* 120:21, 2004, pp. 9911–9917.
82. M. Amsler and S. Goedecker. "Crystal structure prediction using the minima hopping method". *The Journal of chemical physics* 133:22, 2010, p. 224104.
83. F. Jensen. *Introduction to computational chemistry*. John Wiley & Sons, 2017.
84. D. S. De, M. Krummenacher, B. Schaefer, and S. Goedecker. "Finding reaction pathways with optimal atomic index mappings". *Physical Review Letters* 123:20, 2019, p. 206102.
85. H. Huber, M. Sommer, M. Gubler, and S. Goedecker. "Targeting high symmetry in structure predictions by biasing the potential energy surface". *arXiv preprint arXiv:2209.05342*, 2022.

86. J. E. Jones. “On the determination of molecular fields. –I. From the variation of the viscosity of a gas with temperature”. *Proceedings of the Royal Society of London. Series A, Containing Papers of a Mathematical and Physical Character* 106:738, 1924, pp. 441–462.
87. J. E. Jones. “On the determination of molecular fields. –II. From the equation of state of a gas”. *Proceedings of the Royal Society of London. Series A, Containing Papers of a Mathematical and Physical Character* 106:738, 1924, pp. 463–477.
88. J. P. Doye, M. A. Miller, and D. J. Wales. “Evolution of the potential energy surface with size for Lennard-Jones clusters”. *The Journal of Chemical Physics* 111:18, 1999, pp. 8417–8428.
89. J. P. Doye, M. A. Miller, and D. J. Wales. “The double-funnel energy landscape of the 38-atom Lennard-Jones cluster”. *The Journal of Chemical Physics* 110:14, 1999, pp. 6896–6906.
90. D. Daven, N. Tit, J. Morris, and K. Ho. “Structural optimization of Lennard-Jones clusters by a genetic algorithm”. *Chemical physics letters* 256:1-2, 1996, pp. 195–200.
91. V. A. Mandelshtam, P. A. Frantsuzov, and F. Calvo. “Structural transitions and melting in LJ74-78 Lennard-Jones clusters from adaptive exchange Monte Carlo simulations”. *The Journal of Physical Chemistry A* 110:16, 2006, pp. 5326–5332.
92. F. Calvo, J. Neirotti, D. L. Freeman, and J. Doll. “Phase changes in 38-atom Lennard-Jones clusters. II. A parallel tempering study of equilibrium and dynamic properties in the molecular dynamics and microcanonical ensembles”. *The Journal of Chemical Physics* 112:23, 2000, pp. 10350–10357.
93. J. Neirotti, F. Calvo, D. L. Freeman, and J. Doll. “Phase changes in 38-atom Lennard-Jones clusters. I. A parallel tempering study in the canonical ensemble”. *The Journal of Chemical Physics* 112:23, 2000, pp. 10340–10349.
94. J. A. Finkler and S. Goedecker. “Funnel hopping Monte Carlo: An efficient method to overcome broken ergodicity”. *The Journal of chemical physics* 152:16, 2020, p. 164106.
95. J. Barnes and P. Hut. “A hierarchical $O(N \log N)$ force-calculation algorithm”. *nature* 324:6096, 1986, pp. 446–449.

96. V. Rokhlin. "Rapid solution of integral equations of classical potential theory". *Journal of computational physics* 60:2, 1985, pp. 187–207.
97. L. Genovese, T. Deutsch, and S. Goedecker. "Efficient and accurate three-dimensional Poisson solver for surface problems". *The Journal of chemical physics* 127:5, 2007, p. 054704.
98. L. Genovese, T. Deutsch, A. Neelov, S. Goedecker, and G. Beylkin. "Efficient solution of Poisson's equation with free boundary conditions". *The Journal of chemical physics* 125:7, 2006, p. 074105.
99. P. P. Ewald. "Die Berechnung optischer und elektrostatischer Gitterpotentiale". *Annalen der physik* 369:3, 1921, pp. 253–287.
100. T. Darden, D. York, and L. Pedersen. "Particle mesh Ewald: An $N \cdot \log(N)$ method for Ewald sums in large systems". *The Journal of chemical physics* 98:12, 1993, pp. 10089–10092.
101. A. C. Van Duin, S. Dasgupta, F. Lorant, and W. A. Goddard. "ReaxFF: a reactive force field for hydrocarbons". *The Journal of Physical Chemistry A* 105:41, 2001, pp. 9396–9409.
102. J. D. Gale. "Empirical potential derivation for ionic materials". *Philosophical Magazine B* 73:1, 1996, pp. 3–19.
103. B. R. Brooks, R. E. Bruccoleri, B. D. Olafson, D. J. States, S. a. Swaminathan, and M. Karplus. "CHARMM: a program for macromolecular energy, minimization, and dynamics calculations". *Journal of computational chemistry* 4:2, 1983, pp. 187–217.
104. J. C. Phillips, R. Braun, W. Wang, J. Gumbart, E. Tajkhorshid, E. Villa, C. Chipot, R. D. Skeel, L. Kale, and K. Schulten. "Scalable molecular dynamics with NAMD". *Journal of computational chemistry* 26:16, 2005, pp. 1781–1802.
105. A. K. Rappé, C. J. Casewit, K. Colwell, W. A. Goddard III, and W. M. Skiff. "UFF, a full periodic table force field for molecular mechanics and molecular dynamics simulations". *Journal of the American chemical society* 114:25, 1992, pp. 10024–10035.
106. J. A. Harrison, J. D. Schall, S. Maskey, P. T. Mikulski, M. T. Knippenberg, and B. H. Morrow. "Review of force fields and intermolecular potentials used in atomistic computational materials research". *Applied Physics Reviews* 5:3, 2018, p. 031104.

107. T. W. Ko, J. A. Finkler, S. Goedecker, and J. Behler. “A fourth-generation high-dimensional neural network potential with accurate electrostatics including non-local charge transfer”. *Nature communications* 12:398, 2021.
108. *Creative Commons Attribution 4.0 International*. URL: <https://creativecommons.org/licenses/by/4.0/>.
109. T. W. Ko, J. A. Finkler, S. Goedecker, and J. Behler. “General-Purpose Machine Learning Potentials Capturing Nonlocal Charge Transfer”. *Accounts of Chemical Research* 54:4, 2021, pp. 808–817.
110. J. S. Smith, B. T. Nebgen, R. Zubatyuk, N. Lubbers, C. Devereux, K. Barros, S. Tretiak, O. Isayev, and A. E. Roitberg. “Approaching coupled cluster accuracy with a general-purpose neural network potential through transfer learning”. *Nature communications* 10:1, 2019, pp. 1–8.
111. K. T. Schütt, H. E. Sauceda, P.-J. Kindermans, A. Tkatchenko, and K.-R. Müller. “SchNet—a deep learning architecture for molecules and materials”. *The Journal of Chemical Physics* 148:24, 2018, p. 241722.
112. J. S. Smith, O. Isayev, and A. E. Roitberg. “ANI-1: an extensible neural network potential with DFT accuracy at force field computational cost”. *Chemical science* 8:4, 2017, pp. 3192–3203.
113. A. P. Bartók, M. C. Payne, R. Kondor, and G. Csányi. “Gaussian approximation potentials: The accuracy of quantum mechanics, without the electrons”. *Physical review letters* 104:13, 2010, p. 136403.
114. A. V. Shapeev. “Moment tensor potentials: A class of systematically improvable interatomic potentials”. *Multiscale Modeling & Simulation* 14:3, 2016, pp. 1153–1173.
115. A. P. Thompson, L. P. Swiler, C. R. Trott, S. M. Foiles, and G. J. Tucker. “Spectral neighbor analysis method for automated generation of quantum-accurate interatomic potentials”. *Journal of Computational Physics* 285, 2015, pp. 316–330.
116. R. Drautz. “Atomic cluster expansion for accurate and transferable interatomic potentials”. *Physical Review B* 99:1, 2019, p. 014104.
117. R. M. Balabin and E. I. Lomakina. “Support vector machine regression (LS-SVM)—an alternative to artificial neural networks (ANNs) for the analysis of quantum chemistry data?” *Physical Chemistry Chemical Physics* 13:24, 2011, pp. 11710–11718.

118. Y. LeCun, B. Boser, J.S. Denker, D. Henderson, R.E. Howard, W. Hubbard, and L.D. Jackel. “Backpropagation applied to handwritten zip code recognition”. *Neural computation* 1:4, 1989, pp. 541–551.
119. A. Vaswani, N. Shazeer, N. Parmar, J. Uszkoreit, L. Jones, A.N. Gomez, L. Kaiser, and I. Polosukhin. “Attention is all you need”. In: *Advances in neural information processing systems*. 2017, pp. 5998–6008.
120. M. Abadi, A. Agarwal, P. Barham, E. Brevdo, Z. Chen, C. Citro, G.S. Corrado, A. Davis, J. Dean, M. Devin, S. Ghemawat, I. Goodfellow, A. Harp, G. Irving, M. Isard, J. Yangqing, R. Jozefowicz, L. Kaiser, M. Kudlur, J. Levenberg, D. Man’e, R. Monga, S. Moore, D. Murray, C. Olah, M. Schuster, J. Shlens, B. Steiner, I. Sutskever, K. Talwar, P. Tucker, V. Vanhoucke, V. Vasudevan, F. Vi’egas, O. Vinyals, P. Warden, M. Wattenberg, M. Wicke, Y. Yu, and X. Zheng. *TensorFlow: Large-Scale Machine Learning on Heterogeneous Systems*. Software available from tensorflow.org. 2015. URL: <https://www.tensorflow.org/>.
121. A. Paszke, S. Gross, S. Chintala, G. Chanan, E. Yang, Z. DeVito, Z. Lin, A. Desmaison, L. Antiga, and A. Lerer. “Automatic differentiation in PyTorch”, 2017.
122. D.P. Kingma and J. Ba. “Adam: A method for stochastic optimization”. *arXiv preprint arXiv:1412.6980*, 2014.
123. S. Smith, E. Elsen, and S. De. “On the generalization benefit of noise in stochastic gradient descent”. In: *International Conference on Machine Learning*. PMLR. 2020, pp. 9058–9067.
124. N. Yang, C. Tang, and Y. Tu. “Stochastic gradient descent introduces an effective landscape-dependent regularization favoring flat solutions”. *arXiv preprint arXiv:2206.01246*, 2022.
125. A. Singraber, T. Morawietz, J. Behler, and C. Dellago. “Parallel multistream training of high-dimensional neural network potentials”. *Journal of chemical theory and computation* 15:5, 2019, pp. 3075–3092.
126. S. Santurkar, D. Tsipras, A. Ilyas, and A. Madry. “How does batch normalization help optimization?” *Advances in neural information processing systems* 31, 2018.
127. Y. Wu and K. He. “Group normalization”. In: *Proceedings of the European conference on computer vision (ECCV)*. 2018, pp. 3–19.

128. N. Srivastava, G. Hinton, A. Krizhevsky, I. Sutskever, and R. Salakhutdinov. “Dropout: a simple way to prevent neural networks from overfitting”. *The journal of machine learning research* 15:1, 2014, pp. 1929–1958.
129. M. Belkin, D. Hsu, S. Ma, and S. Mandal. “Reconciling modern machine-learning practice and the classical bias–variance trade-off”. *Proceedings of the National Academy of Sciences* 116:32, 2019, pp. 15849–15854.
130. C. Zhang, S. Bengio, M. Hardt, B. Recht, and O. Vinyals. “Understanding deep learning (still) requires rethinking generalization”. *Communications of the ACM* 64:3, 2021, pp. 107–115.
131. E. Kocer, T.W. Ko, and J. Behler. “Neural network potentials: A concise overview of methods”. *Annual review of physical chemistry* 73, 2022, pp. 163–186.
132. J. Behler. “Four generations of high-dimensional neural network potentials”. *Chemical Reviews* 121:16, 2021, pp. 10037–10072.
133. G. Imbalzano, A. Anelli, D. Giofr , S. Klees, J. Behler, and M. Ceriotti. “Automatic selection of atomic fingerprints and reference configurations for machine-learning potentials”. *The Journal of chemical physics* 148:24, 2018, p. 241730.
134. F. A. Faber, A. S. Christensen, B. Huang, and O. A. Von Lilienfeld. “Alchemical and structural distribution based representation for universal quantum machine learning”. *The Journal of chemical physics* 148:24, 2018, p. 241717.
135. A. P. Bart k, R. Kondor, and G. Cs nyi. “On representing chemical environments”. *Physical Review B* 87:18, 2013, p. 184115.
136. L. Zhu, M. Amsler, T. Fuhrer, B. Schaefer, S. Faraji, S. Rostami, S. A. Ghasemi, A. Sadeghi, M. Grauzinyte, C. Wolverton, et al. “A fingerprint based metric for measuring similarities of crystalline structures”. *The Journal of chemical physics* 144:3, 2016, p. 034203.
137. B. Parsaeifard, D. S. De, A. S. Christensen, F. A. Faber, E. Kocer, S. De, J. Behler, O. A. von Lilienfeld, and S. Goedecker. “An assessment of the structural resolution of various fingerprints commonly used in machine learning”. *Machine Learning: Science and Technology* 2:1, 2021, p. 015018.
138. S. N. Pozdnyakov, M. J. Willatt, A. P. Bart k, C. Ortner, G. Cs nyi, and M. Ceriotti. “Incompleteness of atomic structure representations”. *Physical Review Letters* 125:16, 2020, p. 166001.

139. A. Singraber, J. Behler, and C. Dellago. “Library-based LAMMPS implementation of high-dimensional neural network potentials”. *Journal of chemical theory and computation* 15:3, 2019, pp. 1827–1840.
140. P. Rowe, G. Csányi, D. Alfè, and A. Michaelides. “Development of a machine learning potential for graphene”. *Physical Review B* 97:5, 2018, p. 054303.
141. H.-A. Chen and C.-W. Pao. “Fast and accurate artificial neural network potential model for MAPbI₃ perovskite materials”. *ACS omega* 4:6, 2019, pp. 10950–10959.
142. R. Jinnouchi, K. Miwa, F. Karsai, G. Kresse, and R. Asahi. “On-the-fly active learning of interatomic potentials for large-scale atomistic simulations”. *The Journal of Physical Chemistry Letters* 11:17, 2020, pp. 6946–6955.
143. S. Wille, H. Jiang, O. Bünermann, A. M. Wodtke, J. Behler, and A. Kandratenka. “An experimentally validated neural-network potential energy surface for H-atom on free-standing graphene in full dimensionality”. *Physical Chemistry Chemical Physics* 22:45, 2020, pp. 26113–26120.
144. N. Artrith, B. Hiller, and J. Behler. “Neural network potentials for metals and oxides—First applications to copper clusters at zinc oxide”. *physica status solidi (b)* 250:6, 2013, pp. 1191–1203.
145. V. L. Deringer and G. Csányi. “Machine learning based interatomic potential for amorphous carbon”. *Physical Review B* 95:9, 2017, p. 094203.
146. M. Herbold and J. Behler. “A Hessian-based assessment of atomic forces for training machine learning interatomic potentials”. *The Journal of Chemical Physics* 156:11, 2022, p. 114106.
147. Z. Deng, C. Chen, X.-G. Li, and S. P. Ong. “An electrostatic spectral neighbor analysis potential for lithium nitride”. *npj Computational Materials* 5:1, 2019, pp. 1–8.
148. J. Wang, R. M. Wolf, J. W. Caldwell, P. A. Kollman, and D. A. Case. “Development and testing of a general amber force field”. *Journal of computational chemistry* 25:9, 2004, pp. 1157–1174.
149. T. Morawietz, V. Sharma, and J. Behler. “A neural network potential-energy surface for the water dimer based on environment-dependent atomic energies and charges”. *The Journal of chemical physics* 136:6, 2012, p. 064103.

150. J. Behler. “Constructing high-dimensional neural network potentials: a tutorial review”. *International Journal of Quantum Chemistry* 115:16, 2015, pp. 1032–1050.
151. J. Behler. “Representing potential energy surfaces by high-dimensional neural network potentials”. *Journal of Physics: Condensed Matter* 26:18, 2014, p. 183001.
152. J. Behler. “First principles neural network potentials for reactive simulations of large molecular and condensed systems”. *Angewandte Chemie International Edition* 56:42, 2017, pp. 12828–12840.
153. A. Grisafi and M. Ceriotti. “Incorporating long-range physics in atomic-scale machine learning”. *The Journal of chemical physics* 151:20, 2019, p. 204105.
154. A. Grisafi, J. Nigam, and M. Ceriotti. “Multi-scale approach for the prediction of atomic scale properties”. *Chemical science* 12:6, 2021, pp. 2078–2090.
155. A. K. Rappe and W. A. Goddard III. “Charge equilibration for molecular dynamics simulations”. *The Journal of Physical Chemistry* 95:8, 1991, pp. 3358–3363.
156. X. W. Zhou and H. N. Wadley. “A charge transfer ionic-embedded atom method potential for the O–Al–Ni–Co–Fe system”. *Journal of Physics: Condensed Matter* 17:23, 2005, p. 3619.
157. J. Gasteiger and M. Marsili. “Iterative partial equalization of orbital electronegativity—a rapid access to atomic charges”. *Tetrahedron* 36:22, 1980, pp. 3219–3228.
158. S. A. Ghasemi, A. Hofstetter, S. Saha, and S. Goedecker. “Interatomic potentials for ionic systems with density functional accuracy based on charge densities obtained by a neural network”. *Physical Review B* 92:4, 2015, p. 045131.
159. S. Faraji, S. A. Ghasemi, S. Rostami, R. Rasoulkhani, B. Schaefer, S. Goedecker, and M. Amsler. “High accuracy and transferability of a neural network potential through charge equilibration for calcium fluoride”. *Physical Review B* 95:10, 2017, p. 104105.
160. M. Amsler, S. Rostami, H. Tahmasbi, E. R. Khajepasha, S. Faraji, R. Rasoulkhani, and S. A. Ghasemi. “FLAME: A library of atomistic modeling environments”. *Computer Physics Communications* 256, 2020, p. 107415.
161. R. Hafizi, S. A. Ghasemi, S. J. Hashemifar, and H. Akbarzadeh. “A neural-network potential through charge equilibration for WS₂: From clusters to sheets”. *The Journal of Chemical Physics* 147:23, 2017, p. 234306.

162. S. Faraji, S. A. Ghasemi, B. Parsaeifard, and S. Goedecker. "Surface reconstructions and premelting of the (100) CaF₂ surface". *Physical Chemistry Chemical Physics* 21:29, 2019, pp. 16270–16281.
163. R. Rasoulkhani, H. Tahmasbi, S. A. Ghasemi, S. Faraji, S. Rostami, and M. Amsler. "Energy landscape of ZnO clusters and low-density polymorphs". *Physical Review B* 96:6, 2017, p. 064108.
164. X. Xie, K. A. Persson, and D. W. Small. "Incorporating electronic information into machine learning potential energy surfaces via approaching the ground-state electronic energy as a function of atom-based electronic populations". *Journal of chemical theory and computation* 16:7, 2020, pp. 4256–4270.
165. R. Zubatyuk, J. S. Smith, B. T. Nebgen, S. Tretiak, and O. Isayev. "Teaching a neural network to attach and detach electrons from molecules". *Nature communications* 12:1, 2021, pp. 1–11.
166. P. P. Poier, L. Lagardère, J.-P. Piquemal, and F. Jensen. "Molecular dynamics using nonvariational polarizable force fields: Theory, periodic boundary conditions implementation, and application to the bond capacity model". *Journal of Chemical Theory and Computation* 15:11, 2019, pp. 6213–6224.
167. T. R. Gingrich and M. Wilson. "On the Ewald summation of Gaussian charges for the simulation of metallic surfaces". *Chem. Phys. Lett.* 500:1-3, 2010, pp. 178–183.
168. P. T. Kiss, M. Sega, and A. Baranyai. "Efficient handling of Gaussian charge distributions: An application to polarizable molecular models". *J. Chem. Theory Comput.* 10:12, 2014, pp. 5513–5519.
169. H. Lee and W. Cai. "Ewald summation for Coulomb interactions in a periodic supercell". *Lecture Notes, Stanford University*, 2009.
170. R. Jackson and C. Catlow. "Computer simulation studies of zeolite structure". *Molecular Simulation* 1:4, 1988, pp. 207–224.
171. J. A. Finkler. *ewald-summation*. 2020. URL: <https://github.com/Jonas-Finkler/ewald-summation>.
172. J. Behler. *RuNNer – A program for constructing high-dimensional neural network potentials*, Universität Göttingen. 2020.
173. Y. Ma, G. K. Lockwood, and S. H. Garofalini. "Development of a transferable variable charge potential for the study of energy conversion materials FeF₂ and FeF₃". *The Journal of Physical Chemistry C* 115:49, 2011, pp. 24198–24205.

174. Q. Fan and G. V. Pfeiffer. "Theoretical study of linear C_n ($n= 6- 10$) and HC_nH ($n= 2- 10$) molecules". *Chemical physics letters* 162:6, 1989, pp. 472–478.
175. L. Horný, N. D. Petraco, and H. F. Schaefer. "Odd Carbon Long Linear Chains HC_2n+1H ($n= 4- 11$): Properties of the Neutrals and Radical Anions". *Journal of the American Chemical Society* 124:49, 2002, pp. 14716–14720.
176. L. Pan, B. Rao, A. Gupta, G. Das, and P. Ayyub. "H-substituted anionic carbon clusters C_nH ($n \leq 10$): Density functional studies and experimental observations". *The Journal of chemical physics* 119:15, 2003, pp. 7705–7713.
177. K. Duanmu, O. Roberto-Neto, F. B. Machado, J. A. Hansen, J. Shen, P. Piecuch, and D. G. Truhlar. "Geometries, binding energies, ionization potentials, and electron affinities of metal clusters: Mg_n $0, \pm 1$, $n= 1-7$ ". *The Journal of Physical Chemistry C* 120:24, 2016, pp. 13275–13286.
178. N. Goel, S. Gautam, and K. Dharamvir. "Density functional studies of LiN and LiN^+ ($N= 2-30$) clusters: Structure, binding and charge distribution". *International Journal of Quantum Chemistry* 112:2, 2012, pp. 575–586.
179. R. Fournier. "Trends in energies and geometric structures of neutral and charged aluminum clusters". *Journal of Chemical Theory and computation* 3:3, 2007, pp. 921–929.
180. S. De, S. A. Ghasemi, A. Willand, L. Genovese, D. Kanhere, and S. Goedecker. "The effect of ionization on the global minima of small and medium sized silicon and magnesium clusters". *The Journal of chemical physics* 134:12, 2011, p. 124302.
181. M. Haruta and M. Daté. "Advances in the catalysis of Au nanoparticles". *Applied Catalysis A: General* 222:1-2, 2001, pp. 427–437.
182. N. Mammen, S. Narasimhan, and S. de Gironcoli. "Tuning the morphology of gold clusters by substrate doping". *Journal of the American Chemical Society* 133:9, 2011, pp. 2801–2803.
183. N. Mammen and S. Narasimhan. "Inducing wetting morphologies and increased reactivities of small Au clusters on doped oxide supports". *The Journal of Chemical Physics* 149:17, 2018, p. 174701.
184. X. Shao, S. Prada, L. Giordano, G. Pacchioni, N. Nilius, and H.-J. Freund. "Tailoring the shape of metal Ad-particles by doping the oxide support". *Angewandte Chemie International Edition* 50:48, 2011, pp. 11525–11527.

185. J. S. Elias, N. Artrith, M. Bugnet, L. Giordano, G. A. Botton, A. M. Kolpak, and Y. Shao-Horn. "Elucidating the nature of the active phase in copper/ceria catalysts for CO oxidation". *ACS Catalysis* 6:3, 2016, pp. 1675–1679.
186. M. L. Paleico and J. Behler. "Global optimization of copper clusters at the ZnO (10 $\bar{1}$ 0) surface using a DFT-based neural network potential and genetic algorithms". *The Journal of Chemical Physics* 153:5, 2020, p. 054704.
187. B. Kaduk, T. Kowalczyk, and T. Van Voorhis. "Constrained density functional theory". *Chemical reviews* 112:1, 2012, pp. 321–370.
188. L. D. Jacobson, J. M. Stevenson, F. Ramezanghorbani, D. Ghoreishi, K. Leswing, E. D. Harder, and R. Abel. "Transferable Neural Network Potential Energy Surfaces for Closed-Shell Organic Molecules: Extension to Ions". *Journal of Chemical Theory and Computation* 18:4, 2022, pp. 2354–2366.
189. J. Gilmer, S. S. Schoenholz, P. F. Riley, O. Vinyals, and G. E. Dahl. "Neural message passing for quantum chemistry". In: *International conference on machine learning*. PMLR. 2017, pp. 1263–1272.
190. K. T. Schütt, F. Arbabzadah, S. Chmiela, K. R. Müller, and A. Tkatchenko. "Quantum-chemical insights from deep tensor neural networks". *Nature communications* 8:1, 2017, pp. 1–8.
191. R. Zubatyuk, J. S. Smith, J. Leszczynski, and O. Isayev. "Accurate and transferable multitask prediction of chemical properties with an atoms-in-molecules neural network". *Science advances* 5:8, 2019, eaav6490.
192. D. P. Metcalf, A. Jiang, S. A. Spronk, D. L. Cheney, and C. D. Sherrill. "Electron-passing neural networks for atomic charge prediction in systems with arbitrary molecular charge". *Journal of Chemical Information and Modeling* 61:1, 2020, pp. 115–122.
193. N. Lubbers, J. S. Smith, and K. Barros. "Hierarchical modeling of molecular energies using a deep neural network". *The Journal of chemical physics* 148:24, 2018, p. 241715.
194. S. Batzner, A. Musaelian, L. Sun, M. Geiger, J. P. Mailoa, M. Kornbluth, N. Molinari, T. E. Smidt, and B. Kozinsky. "E (3)-equivariant graph neural networks for data-efficient and accurate interatomic potentials". *Nature communications* 13:1, 2022, pp. 1–11.

195. O. T. Unke, S. Chmiela, M. Gastegger, K. T. Schütt, H. E. Saucedo, and K.-R. Müller. “SpookyNet: Learning force fields with electronic degrees of freedom and nonlocal effects”. *Nature communications* 12:1, 2021, pp. 1–14.
196. K. Schütt, O. Unke, and M. Gastegger. “Equivariant message passing for the prediction of tensorial properties and molecular spectra”. In: *International Conference on Machine Learning*. PMLR. 2021, pp. 9377–9388.
197. M. Haghighatlari, J. Li, X. Guan, O. Zhang, A. Das, C. J. Stein, F. Heidar-Zadeh, M. Liu, M. Head-Gordon, L. Bertels, et al. “Newtonnet: A newtonian message passing network for deep learning of interatomic potentials and forces”. *Digital Discovery*, 2022.
198. A. Musaelian, S. Batzner, A. Johansson, L. Sun, C. J. Owen, M. Kornbluth, and B. Kozinsky. “Learning Local Equivariant Representations for Large-Scale Atomistic Dynamics”. *arXiv preprint arXiv:2204.05249*, 2022.
199. T. W. Ko, J. A. Finkler, S. Goedecker, and J. Behler. “Accurate Fourth-Generation Machine Learning Potentials by Electrostatic Embedding”. in preparation.
200. O. T. Unke, S. Chmiela, H. E. Saucedo, M. Gastegger, I. Poltavsky, K. T. Schütt, A. Tkatchenko, and K.-R. Müller. “Machine learning force fields”. *Chemical Reviews* 121:16, 2021, pp. 10142–10186.
201. J. T. Frank, O. T. Unke, and K.-R. Müller. “So3krates–Self-attention for higher-order geometric interactions on arbitrary length-scales”. *arXiv preprint arXiv:2205.14276*, 2022.
202. Y. Shao, M. Head-Gordon, and A. I. Krylov. “The spin–flip approach within time-dependent density functional theory: Theory and applications to diradicals”. *The Journal of chemical physics* 118:11, 2003, pp. 4807–4818.
203. M. S. Schuurman and A. Stolow. “Dynamics at conical intersections”. *Annual review of physical chemistry* 69, 2018, pp. 427–450.
204. J. Westermayr, M. Gastegger, M. F. Menger, S. Mai, L. González, and P. Marquetand. “Machine learning enables long time scale molecular photodynamics simulations”. *Chemical science* 10:35, 2019, pp. 8100–8107.
205. S. Chmiela, A. Tkatchenko, H. E. Saucedo, I. Poltavsky, K. T. Schütt, and K.-R. Müller. “Machine learning of accurate energy-conserving molecular force fields”. *Science advances* 3:5, 2017, e1603015.

206. O. A. Von Lilienfeld. "Quantum machine learning in chemical compound space". *Angewandte Chemie International Edition* 57:16, 2018, pp. 4164–4169.
207. M. J. Willatt, F. Musil, and M. Ceriotti. "Atom-density representations for machine learning". *The Journal of chemical physics* 150:15, 2019, p. 154110.
208. A. Sadeghi, S. A. Ghasemi, B. Schaefer, S. Mohr, M. A. Lill, and S. Goedecker. "Metrics for measuring distances in configuration spaces". *The Journal of chemical physics* 139:18, 2013, p. 184118.
209. A. Glielmo, C. Zeni, and A. De Vita. "Efficient nonparametric n-body force fields from machine learning". *Physical Review B* 97:18, 2018, p. 184307.
210. O. A. Von Lilienfeld, R. Ramakrishnan, M. Rupp, and A. Knoll. "Fourier series of atomic radial distribution functions: A molecular fingerprint for machine learning models of quantum chemical properties". *International Journal of Quantum Chemistry* 115:16, 2015, pp. 1084–1093.
211. E. Kocer, J. K. Mason, and H. Erturk. "Continuous and optimally complete description of chemical environments using Spherical Bessel descriptors". *AIP Advances* 10:1, 2020, p. 015021.
212. B. Parsaeifard and S. Goedecker. "Manifolds of quasi-constant SOAP and ACSF fingerprints and the resulting failure to machine learn four-body interactions". *The Journal of Chemical Physics* 156:3, 2022, p. 034302.
213. S. N. Pozdnyakov, L. Zhang, C. Ortner, G. Csányi, and M. Ceriotti. "Local invertibility and sensitivity of atomic structure-feature mappings". *Open Research Europe* 1:126, 2021, p. 126.
214. M. Zaheer, S. Kottur, S. Ravanbakhsh, B. Poczos, R. R. Salakhutdinov, and A. J. Smola. "Deep sets". *Advances in neural information processing systems* 30, 2017.
215. F. H. Stillinger. "Exponential multiplicity of inherent structures". *Physical Review E* 59:1, 1999, p. 48.
216. F. Calvo, J. Doye, and D. Wales. "Equilibrium properties of clusters in the harmonic superposition approximation". *Chemical physics letters* 366:1-2, 2002, pp. 176–183.
217. F. H. Stillinger and T. A. Weber. "Hidden structure in liquids". *Physical Review A* 25:2, 1982, p. 978.

218. P. Poulain, F. Calvo, R. Antoine, M. Broyer, and P. Dugourd. “Performances of Wang-Landau algorithms for continuous systems”. *Physical Review E* 73:5, 2006, p. 056704.
219. F. Noé, S. Olsson, J. Köhler, and H. Wu. “Boltzmann generators: Sampling equilibrium states of many-body systems with deep learning”. *Science* 365:6457, 2019, eaaw1147.
220. D. Frenkel and A. J. Ladd. “New Monte Carlo method to compute the free energy of arbitrary solids. Application to the fcc and hcp phases of hard spheres”. *The Journal of chemical physics* 81:7, 1984, pp. 3188–3193.
221. T. Straatsma and J. McCammon. “Multiconfiguration thermodynamic integration”. *The Journal of chemical physics* 95:2, 1991, pp. 1175–1188.
222. R. H. Swendsen and J.-S. Wang. “Replica Monte Carlo simulation of spin-glasses”. *Physical review letters* 57:21, 1986, p. 2607.
223. D. J. Earl and M. W. Deem. “Parallel tempering: Theory, applications, and new perspectives”. *Physical Chemistry Chemical Physics* 7:23, 2005, pp. 3910–3916.
224. E. Marinari and G. Parisi. “Simulated tempering: a new Monte Carlo scheme”. *EPL (Europhysics Letters)* 19:6, 1992, p. 451.
225. D. A. Kofke. “On the acceptance probability of replica-exchange Monte Carlo trials”. *The Journal of chemical physics* 117:15, 2002, pp. 6911–6914.
226. N. Rathore, M. Chopra, and J. J. de Pablo. “Optimal allocation of replicas in parallel tempering simulations”. *The Journal of chemical physics* 122:2, 2005, p. 024111.
227. A. Jackson and G. Ackland. “Lattice-switch Monte Carlo simulation for binary hard-sphere crystals”. *Physical Review E* 76:6, 2007, p. 066703.
228. A. Jackson, A. Bruce, and G. Ackland. “Lattice-switch Monte Carlo method: Application to soft potentials”. *Physical Review E* 65:3, 2002, p. 036710.
229. A. Bruce, N. Wilding, and G. Ackland. “Free energy of crystalline solids: a lattice-switch Monte Carlo method”. *Physical review letters* 79:16, 1997, p. 3002.
230. C. Eckart. “Some studies concerning rotating axes and polyatomic molecules”. *Physical Review* 47:7, 1935, p. 552.

231. K. N. Kudin and A. Y. Dymarsky. “Eckart axis conditions and the minimization of the root-mean-square deviation: Two closely related problems”. *The Journal of chemical physics* 122:22, 2005, p. 224105.
232. P. Nigra, D. L. Freeman, and J. Doll. “Combining smart darting with parallel tempering using Eckart space: Application to Lennard–Jones clusters”. *The Journal of chemical physics* 122:11, 2005, p. 114113.
233. S. K. Kearsley. “On the orthogonal transformation used for structural comparisons”. *Acta Crystallographica Section A: Foundations of Crystallography* 45:2, 1989, pp. 208–210.
234. E. A. Coutsiyas, C. Seok, and K. A. Dill. “Using quaternions to calculate RMSD”. *Journal of computational chemistry* 25:15, 2004, pp. 1849–1857.
235. S. V. Krasnoshchekov, E. V. Isayeva, and N. F. Stepanov. “Determination of the Eckart molecule-fixed frame by use of the apparatus of quaternion algebra”. *The Journal of Chemical Physics* 140:15, 2014, p. 154104.
236. H. W. Kuhn. “The Hungarian method for the assignment problem”. *Naval research logistics quarterly* 2:1-2, 1955, pp. 83–97.
237. R. Jonker and A. Volgenant. “A shortest augmenting path algorithm for dense and sparse linear assignment problems”. *Computing* 38:4, 1987, pp. 325–340.
238. G. Carpaneto, S. Martello, and P. Toth. “Algorithms and codes for the assignment problem”. *Annals of operations research* 13:1, 1988, pp. 191–223.
239. J. A. Finkler. *RMSD-finder*. 2021. URL: <https://github.com/Jonas-Finkler/RMSD-finder>.
240. B. Schaefer and S. Goedecker. “Computationally efficient characterization of potential energy surfaces based on fingerprint distances”. *The Journal of chemical physics* 145:3, 2016, p. 034101.
241. V. A. Sharapov, D. Meluzzi, and V. A. Mandelshtam. “Low-temperature structural transitions: Circumventing the broken-ergodicity problem”. *Physical review letters* 98:10, 2007, p. 105701.
242. J. E. Gentle. *Computational statistics*. Vol. 308. Springer, 2009, pp. 315–316. ISBN: 978-0-387-98143-7.
243. A. P. Dempster, N. M. Laird, and D. B. Rubin. “Maximum likelihood from incomplete data via the EM algorithm”. *Journal of the Royal Statistical Society: Series B (Methodological)* 39:1, 1977, pp. 1–22.

244. J. A. Bilmes et al. “A gentle tutorial of the EM algorithm and its application to parameter estimation for Gaussian mixture and hidden Markov models”. *International Computer Science Institute* 4:510, 1998, p. 126.
245. M. R. Gupta and Y. Chen. *Theory and use of the EM algorithm*. Now Publishers Inc, 2011.
246. J. A. Finkler. *fortran-gmm-EM*. 2020. URL: <https://github.com/Jonas-Finkler/fortran-gmm-EM>.
247. L. S. Blackford, A. Petitet, R. Pozo, K. Remington, R. C. Whaley, J. Demmel, J. Dongarra, I. Duff, S. Hammarling, G. Henry, et al. “An updated set of basic linear algebra subprograms (BLAS)”. *ACM Transactions on Mathematical Software* 28:2, 2002, pp. 135–151.
248. B. R. Brooks, D. Janežič, and M. Karplus. “Harmonic analysis of large systems. I. Methodology”. *Journal of computational chemistry* 16:12, 1995, pp. 1522–1542.
249. T. R. Koehler. “Theory of the self-consistent harmonic approximation with application to solid neon”. *Physical Review Letters* 17:2, 1966, p. 89.
250. N. Gillis, N. Werthamer, and T. Koehler. “Properties of crystalline argon and neon in the self-consistent phonon approximation”. *Physical Review* 165:3, 1968, p. 951.
251. I. Georgescu and V. A. Mandelshtam. “Self-consistent phonons revisited. I. The role of thermal versus quantum fluctuations on structural transitions in large Lennard-Jones clusters”. *The Journal of chemical physics* 137:14, 2012, p. 144106.
252. M. Johansson and V. Veryazov. “Automatic procedure for generating symmetry adapted wavefunctions”. *Journal of cheminformatics* 9:1, 2017, pp. 1–8.
253. S. Martiniani, J. D. Stevenson, D. J. Wales, and D. Frenkel. “Superposition enhanced nested sampling”. *Physical Review X* 4:3, 2014, p. 031034.
254. D. J. Wales. “Surveying a complex potential energy landscape: Overcoming broken ergodicity using basin-sampling”. *Chemical Physics Letters* 584, 2013, pp. 1–9.
255. J. M. Buriak, P. V. Kamat, K. S. Schanze, A. P. Alivisatos, C. J. Murphy, G. C. Schatz, G. D. Scholes, P. J. Stang, and P. S. Weiss. *Virtual Issue on Metal-Halide Perovskite Nanocrystals - A Bright Future for Optoelectronics*. 2017.

256. M. A. Green, A. Ho-Baillie, and H. J. Snaith. “The emergence of perovskite solar cells”. *Nature photonics* 8:7, 2014, pp. 506–514.
257. A. A. Emery and C. Wolverton. “High-throughput DFT calculations of formation energy, stability and oxygen vacancy formation energy of ABO₃ perovskites”. *Scientific data* 4:1, 2017, pp. 1–10.
258. A. Jain, O. Voznyy, and E. H. Sargent. “High-throughput screening of lead-free perovskite-like materials for optoelectronic applications”. *The Journal of Physical Chemistry C* 121:13, 2017, pp. 7183–7187.
259. J. A. Finkler and S. Goedecker. “Experimental Absence of the Non-Perovskite Ground State Phases of MaPbI₃ Explained by a Funnel Hopping Monte Carlo Study Based on a Neural Network Potential”. *Materials Advances* 4, 2023, pp. 184–194.
260. A. M. Glazer. “The classification of tilted octahedra in perovskites”. *Acta Crystallographica Section B: Structural Crystallography and Crystal Chemistry* 28:11, 1972, pp. 3384–3392.
261. A. Glazer. “Simple ways of determining perovskite structures”. *Acta Crystallographica Section A: Crystal Physics, Diffraction, Theoretical and General Crystallography* 31:6, 1975, pp. 756–762.
262. Z. Li, M. Yang, J.-S. Park, S.-H. Wei, J. J. Berry, and K. Zhu. “Stabilizing perovskite structures by tuning tolerance factor: formation of formamidinium and cesium lead iodide solid-state alloys”. *Chemistry of Materials* 28:1, 2016, pp. 284–292.
263. I. Deretzis, C. Bongiorno, G. Mannino, E. Smecca, S. Sanzaro, S. Valastro, G. Fiscaro, A. La Magna, and A. Alberti. “Exploring the structural competition between the black and the yellow phase of cspbi₃”. *Nanomaterials* 11:5, 2021, p. 1282.
264. K. Parlinski, Z. Li, and Y. Kawazoe. “First-principles determination of the soft mode in cubic ZrO₂”. *Physical Review Letters* 78:21, 1997, p. 4063.
265. P. Pavone, K. Karch, O. Schütt, D. Strauch, W. Windl, P. Giannozzi, and S. Baroni. “Ab initio lattice dynamics of diamond”. *Physical Review B* 48:5, 1993, p. 3156.
266. A. Togo, L. Chaput, I. Tanaka, and G. Hug. “First-principles phonon calculations of thermal expansion in Ti₃SiC₂, Ti₃AlC₂, and Ti₃GeC₂”. *Physical Review B* 81:17, 2010, p. 174301.

267. F. Brivio, J. M. Frost, J. M. Skelton, A. J. Jackson, O. J. Weber, M. T. Weller, A. R. Goni, A. M. Leguy, P. R. Barnes, and A. Walsh. “Lattice dynamics and vibrational spectra of the orthorhombic, tetragonal, and cubic phases of methylammonium lead iodide”. *Physical Review B* 92:14, 2015, p. 144308.
268. C. E. Patrick, K. W. Jacobsen, and K. S. Thygesen. “Anharmonic stabilization and band gap renormalization in the perovskite CsSnI₃”. *Physical Review B* 92:20, 2015, p. 201205.
269. M. A. Carignano, S. A. Aravindh, I. S. Roqan, J. Even, and C. Katan. “Critical fluctuations and anharmonicity in lead iodide perovskites from molecular dynamics supercell simulations”. *The Journal of Physical Chemistry C* 121:38, 2017, pp. 20729–20738.
270. A. N. Beecher, O. E. Semonin, J. M. Skelton, J. M. Frost, M. W. Terban, H. Zhai, A. Alatas, J. S. Owen, A. Walsh, and S. J. Billinge. “Direct observation of dynamic symmetry breaking above room temperature in methylammonium lead iodide perovskite”. *ACS energy Letters* 1:4, 2016, pp. 880–887.
271. R. X. Yang, J. M. Skelton, E. L. Da Silva, J. M. Frost, and A. Walsh. “Spontaneous octahedral tilting in the cubic inorganic cesium halide perovskites CsSnX₃ and CsPbX₃ (X= F, Cl, Br, I)”. *The journal of physical chemistry letters* 8:19, 2017, pp. 4720–4726.
272. C.-J. Yu. “Advances in modelling and simulation of halide perovskites for solar cell applications”. *Journal of Physics: Energy* 1:2, 2019, p. 022001.
273. N. A. Benedek and C. J. Fennie. “Why are there so few perovskite ferroelectrics?” *The Journal of Physical Chemistry C* 117:26, 2013, pp. 13339–13349.
274. L. D. Whalley, J. M. Skelton, J. M. Frost, and A. Walsh. “Phonon anharmonicity, lifetimes, and thermal transport in CH₃NH₃PbI₃ from many-body perturbation theory”. *Physical Review B* 94:22, 2016, p. 220301.
275. J. Behler. “Perspective: Machine learning potentials for atomistic simulations”. *The Journal of chemical physics* 145:17, 2016, p. 170901.
276. Y. Zuo, C. Chen, X. Li, Z. Deng, Y. Chen, J. Behler, G. Csányi, A. V. Shapeev, A. P. Thompson, M. A. Wood, et al. “Performance and cost assessment of machine learning interatomic potentials”. *The Journal of Physical Chemistry A* 124:4, 2020, pp. 731–745.

277. P. Whitfield, N. Herron, W. Guise, K. Page, Y. Cheng, I. Milas, and M. Crawford. “Structures, phase transitions and tricritical behavior of the hybrid perovskite methyl ammonium lead iodide”. *Scientific reports* 6:1, 2016, pp. 1–16.
278. W. Ke, I. Spanopoulos, C. C. Stoumpos, and M. G. Kanatzidis. “Myths and reality of HPbI₃ in halide perovskite solar cells”. *Nature communications* 9:1, 2018, pp. 1–9.
279. L. Gu, D. Zhang, M. Kam, Q. Zhang, S. Poddar, Y. Fu, X. Mo, and Z. Fan. “Significantly improved black phase stability of FAPbI₃ nanowires via spatially confined vapor phase growth in nanoporous templates”. *Nanoscale* 10:32, 2018, pp. 15164–15172.
280. M. Bokdam and G. Kresse. personal communication. 2022.
281. M. Bokdam, J. Lahnsteiner, B. Ramberger, T. Schäfer, and G. Kresse. “Assessing density functionals using many body theory for hybrid perovskites”. *Physical review letters* 119:14, 2017, p. 145501.
282. A. S. Thind, X. Huang, J. Sun, and R. Mishra. “First-principles prediction of a stable hexagonal phase of CH₃NH₃PbI₃”. *Chemistry of Materials* 29:14, 2017, pp. 6003–6011.
283. T. Chen, B. J. Foley, C. Park, C. M. Brown, L. W. Harriger, J. Lee, J. Ruff, M. Yoon, J. J. Choi, and S.-H. Lee. “Entropy-driven structural transition and kinetic trapping in formamidinium lead iodide perovskite”. *Science advances* 2:10, 2016, e1601650.
284. A. Togo and I. Tanaka. “Spglib: a software library for crystal symmetry search”. *arXiv preprint arXiv:1808.01590*, 2018.
285. Y. Sugita, A. Kitao, and Y. Okamoto. “Multidimensional replica-exchange method for free-energy calculations”. *The Journal of Chemical Physics* 113:15, 2000, pp. 6042–6051.
286. H. Fukunishi, O. Watanabe, and S. Takada. “On the Hamiltonian replica exchange method for efficient sampling of biomolecular systems: Application to protein structure prediction”. *The Journal of chemical physics* 116:20, 2002, pp. 9058–9067.
287. R. M. Neal et al. “MCMC using Hamiltonian dynamics”. *Handbook of markov chain monte carlo* 2:11, 2011, p. 2.

288. J. Lahnsteiner, G. Kresse, J. Heinen, and M. Bokdam. “Finite-temperature structure of the MAPbI₃ perovskite: Comparing density functional approximations and force fields to experiment”. *Physical Review Materials* 2:7, 2018, p. 073604.
289. G. Kresse and J. Hafner. “Ab initio molecular dynamics for liquid metals”. *Physical review B* 47:1, 1993, p. 558.
290. G. Kresse and J. Furthmüller. “Efficient iterative schemes for ab initio total-energy calculations using a plane-wave basis set”. *Physical review B* 54:16, 1996, p. 11169.
291. G. Kresse and J. Hafner. “Norm-conserving and ultrasoft pseudopotentials for first-row and transition elements”. *Journal of Physics: Condensed Matter* 6:40, 1994, p. 8245.
292. G. Kresse and D. Joubert. “From ultrasoft pseudopotentials to the projector augmented-wave method”. *Physical review B* 59:3, 1999, p. 1758.
293. R. Jinnouchi, J. Lahnsteiner, F. Karsai, G. Kresse, and M. Bokdam. “Phase transitions of hybrid perovskites simulated by machine-learning force fields trained on the fly with Bayesian inference”. *Physical review letters* 122:22, 2019, p. 225701.
294. J. A. Finkler. *High-Dimensional-Neural-Network-Potential*. 2022. URL: <https://github.com/Jonas-Finkler/High-Dimensional-Neural-Network-Potential>.
295. C. Handley and C. Freeman. “A new potential for methylammonium lead iodide”. *Physical Chemistry Chemical Physics* 19:3, 2017, pp. 2313–2321.
296. A. P. Thompson, H. M. Aktulga, R. Berger, D. S. Bolintineanu, W. M. Brown, P. S. Crozier, P. J. in’t Veld, A. Kohlmeyer, S. G. Moore, T. D. Nguyen, et al. “LAMMPS-a flexible simulation tool for particle-based materials modeling at the atomic, meso, and continuum scales”. *Computer Physics Communications* 271, 2022, p. 108171.
297. A. Togo and I. Tanaka. “First principles phonon calculations in materials science”. *Scripta Materialia* 108, 2015, pp. 1–5.
298. A. Marrognier, H. Lee, B. Geffroy, J. Even, Y. Bonnassieux, and G. Roma. “Structural instabilities related to highly anharmonic phonons in halide perovskites”. *The journal of physical chemistry letters* 8:12, 2017, pp. 2659–2665.

299. M. Gubler, M. Krummenacher, H. Huber, and S. Goedecker. “Efficient variable cell shape geometry optimization”. *arXiv preprint arXiv:2206.07339*, 2022.
300. E. L. Da Silva, J. M. Skelton, S. C. Parker, and A. Walsh. “Phase stability and transformations in the halide perovskite CsSnI₃”. *Physical Review B* 91:14, 2015, p. 144107.
301. S. Taraskin and S. Elliott. “Anharmonicity and localization of atomic vibrations in vitreous silica”. *Physical Review B* 59:13, 1999, p. 8572.
302. M.K. Gupta, J. Ding, D. Bansal, D.L. Abernathy, G. Ehlers, N.C. Osti, W.G. Zeier, and O. Delaire. “Strongly Anharmonic Phonons and Their Role in Superionic Diffusion and Ultralow Thermal Conductivity of Cu₇PSe₆”. *Advanced Energy Materials*, 2022, p. 2200596.
303. Y. Zhou, W. Zhang, E. Ma, and V.L. Deringer. “Unlocking device-scale atomistic modelling of phase-change memory materials”. *arXiv preprint arXiv:2207.14228*, 2022.
304. T.D. Huan, M. Amsler, M. A. Marques, S. Botti, A. Willand, and S. Goedecker. “Low-energy polymeric phases of aluminates”. *Physical review letters* 110:13, 2013, p. 135502.
305. J. Ding, T. Lanigan-Atkins, M. Calderón-Cueva, A. Banerjee, D.L. Abernathy, A. Said, A. Zevalkin, and O. Delaire. “Soft anharmonic phonons and ultralow thermal conductivity in Mg₃ (Sb, Bi)₂ thermoelectrics”. *Science advances* 7:21, 2021, eabg1449.
306. W. Lai, Y. Wang, D.T. Morelli, and X. Lu. “From bonding asymmetry to anharmonic rattling in Cu₁₂Sb₄S₁₃ tetrahedrites: When lone-pair electrons are not so lonely”. *Advanced Functional Materials* 25:24, 2015, pp. 3648–3657.
307. O. Delaire, J. Ma, K. Marty, A.F. May, M. A. McGuire, M.-H. Du, D. J. Singh, A. Podlesnyak, G. Ehlers, M. Lumsden, et al. “Giant anharmonic phonon scattering in PbTe”. *Nature materials* 10:8, 2011, pp. 614–619.
308. G. A. Slack and V.G. Tsoukala. “Some properties of semiconducting IrSb₃”. *Journal of Applied Physics* 76:3, 1994, pp. 1665–1671.
309. R. Bubnova, S. Volkov, B. Albert, and S. Filatov. “Borates—crystal structures of prospective nonlinear optical materials: high anisotropy of the thermal expansion caused by anharmonic atomic vibrations”. *Crystals* 7:3, 2017, p. 93.

Bibliography

- 310. S.K. Filatov and R.S. Bubnova. “Atomic nature of the high anisotropy of borate thermal expansion”. *Physics and Chemistry of Glasses-European Journal of Glass Science and Technology Part B* 56:1, 2015, pp. 24–35.
- 311. A.R. Oganov, J.P. Brodholt, and G.D. Price. “The elastic constants of MgSiO₃ perovskite at pressures and temperatures of the Earth’s mantle”. *Nature* 411:6840, 2001, pp. 934–937.

APPENDIX

A.1 DETAILS FOR THE 4GHDNNP TEST SYSTEMS

A.1.1 $\text{C}_{10}\text{H}_2/\text{C}_{10}\text{H}_3^+$

Table A.1.1: Root mean squared error (RMSE) of charges (me), energies (meV/atom) and forces (meV/Å) for the three different HDNNP generations for the $\text{C}_{10}\text{H}_2/\text{C}_{10}\text{H}_3^+$ data set with 9035 and 984 structures for training and testing points respectively.

		charges	energy	forces
2G	train	—	1.583	130.7
	test	—	1.619	129.5
3G (unscaled)	train	27.36	3.192	652.5
	test	27.35	3.197	658.3
3G (scaled)	train	19.98	2.017	229.9
	test	20.08	2.045	231.0
4G	train	5.783	1.148	77.65
	test	6.577	1.194	78.00

Table A.1.2: Symmetry functions for $\text{C}_{10}\text{H}_2/\text{C}_{10}\text{H}_3^+$

no.	type	at. i	at. j	at. k	$\eta(1/\text{Bohr}^2)$	λ	ζ	$R_c(\text{Bohr})$	$R_s(\text{Bohr})$
1	G^2	H	H		0.0			8.0	0.0
2	G^2	H	H		0.006			8.0	0.0
3	G^2	H	H		0.011			8.0	0.0

The content of this section was adapted from the supplementary information of T. W. Ko, J. A. Finkler, S. Goedecker, and J. Behler. “A fourth-generation high-dimensional neural network potential with accurate electrostatics including non-local charge transfer”. *Nature communications* 12:398, 2021 (CC BY 4.0 [108]).

Appendix

no.	type	at. i	at. j	at. k	$\eta(1/\text{Bohr}^2)$	λ	ζ	$R_c(\text{Bohr})$	$R_s(\text{Bohr})$
4	G^2	H	H		0.018			8.0	0.0
5	G^2	H	H		0.026			8.0	0.0
6	G^2	H	H		0.035			8.0	0.0
7	G^2	C	H		0.0			8.0	0.0
8	G^2	C	H		0.013			8.0	0.0
9	G^2	C	H		0.029			8.0	0.0
10	G^2	C	H		0.054			8.0	0.0
11	G^2	C	H		0.093			8.0	0.0
12	G^2	C	H		0.161			8.0	0.0
13	G^2	H	C		0.0			8.0	0.0
14	G^2	H	C		0.013			8.0	0.0
15	G^2	H	C		0.029			8.0	0.0
16	G^2	H	C		0.054			8.0	0.0
17	G^2	H	C		0.093			8.0	0.0
18	G^2	H	C		0.161			8.0	0.0
19	G^2	C	C		0.0			8.0	0.0
20	G^2	C	C		0.01			8.0	0.0
21	G^2	C	C		0.023			8.0	0.0
22	G^2	C	C		0.041			8.0	0.0
23	G^2	C	C		0.065			8.0	0.0
24	G^2	C	C		0.103			8.0	0.0
25	G^4	C	C	C	0.0	1.0	1.0	8.0	
26	G^4	C	C	C	0.0	1.0	2.0	8.0	
27	G^4	C	C	C	0.0	1.0	4.0	8.0	
28	G^4	C	C	C	0.0	1.0	8.0	8.0	
29	G^4	C	C	C	0.0	-1.0	1.0	8.0	
30	G^4	C	C	C	0.0	-1.0	2.0	8.0	
31	G^4	C	C	C	0.0	-1.0	4.0	8.0	
32	G^4	C	C	C	0.0	-1.0	8.0	8.0	
33	G^4	C	H	H	0.0	1.0	1.0	8.0	
34	G^4	C	H	H	0.0	1.0	2.0	8.0	
35	G^4	C	H	H	0.0	1.0	4.0	8.0	
36	G^4	C	H	H	0.0	1.0	8.0	8.0	
37	G^4	C	H	H	0.0	-1.0	1.0	8.0	
38	G^4	C	H	H	0.0	-1.0	2.0	8.0	

A.1 Details for the 4GHDNNP Test Systems

no.	type	at. i	at. j	at. k	$\eta(1/\text{Bohr}^2)$	λ	ζ	$R_c(\text{Bohr})$	$R_s(\text{Bohr})$
39	G^4	C	H	H	0.0	-1.0	4.0	8.0	
40	G^4	C	H	H	0.0	-1.0	8.0	8.0	
41	G^4	C	C	H	0.0	1.0	1.0	8.0	
42	G^4	C	C	H	0.0	1.0	2.0	8.0	
43	G^4	C	C	H	0.0	1.0	4.0	8.0	
44	G^4	C	C	H	0.0	1.0	8.0	8.0	
45	G^4	C	C	H	0.0	-1.0	1.0	8.0	
46	G^4	C	C	H	0.0	-1.0	2.0	8.0	
47	G^4	C	C	H	0.0	-1.0	4.0	8.0	
48	G^4	C	C	H	0.0	-1.0	8.0	8.0	
49	G^4	H	C	C	0.0	1.0	1.0	8.0	
50	G^4	H	C	C	0.0	1.0	2.0	8.0	
51	G^4	H	C	C	0.0	1.0	4.0	8.0	
52	G^4	H	C	C	0.0	1.0	8.0	8.0	
53	G^4	H	C	C	0.0	-1.0	1.0	8.0	
54	G^4	H	C	C	0.0	-1.0	2.0	8.0	
55	G^4	H	H	C	0.0	1.0	1.0	8.0	
56	G^4	H	H	C	0.0	1.0	2.0	8.0	
57	G^4	H	H	C	0.0	1.0	4.0	8.0	
58	G^4	H	H	C	0.0	1.0	8.0	8.0	
59	G^4	H	H	C	0.0	-1.0	1.0	8.0	
60	G^4	H	H	C	0.0	-1.0	2.0	8.0	

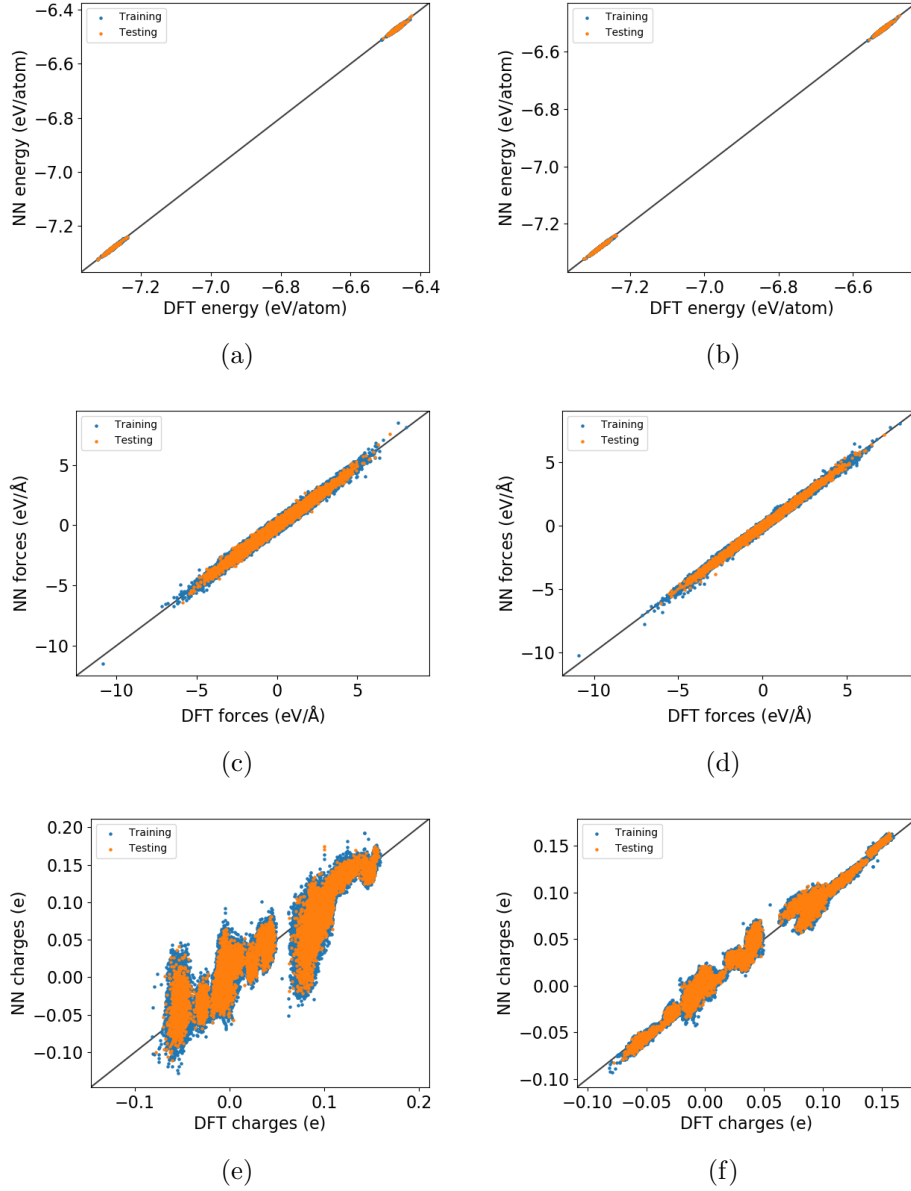


Figure A.1.1: Correlation plots of energies obtained from a 2G-HDNNP (a) and a 4G-HDNNP (b), forces from a 2G-HDNNP (c) and a 4G-HDNNP (d) and charges from a scaled 3G-HDNNP (e) and a 4G-HDNNP (f) for $C_{10}H_2/C_{10}H_3^+$

A.1 Details for the 4GHDNNP Test Systems

Table A.1.3: DFT-optimized structure of C_{10}H_2 in XYZ format (distance unit in Å)
12 atoms

C	0.621 587 11	0.000 000 00	0.000 000 00
C	−0.621 587 10	0.000 000 00	0.000 000 00
C	1.952 478 40	0.000 000 00	0.000 000 00
C	−1.952 478 47	0.000 000 00	0.000 000 00
C	3.192 145 71	0.000 000 00	0.000 000 00
C	−3.192 145 71	0.000 000 00	0.000 000 00
C	4.535 930 62	0.000 000 00	0.000 000 00
C	−4.535 930 61	0.000 000 00	0.000 000 00
C	5.761 179 51	0.000 000 00	0.000 000 00
C	−5.761 179 49	0.000 000 00	0.000 000 00
H	6.831 800 63	0.000 000 00	0.000 000 00
H	−6.831 800 59	0.000 000 00	0.000 000 00

Table A.1.4: DFT-optimized structure of $\text{C}_{10}\text{H}_3^+$ in XYZ format (distance unit in Å)
13 atoms

C	0.629 569 25	0.000 007 77	0.000 008 66
C	−0.630 171 87	0.000 006 61	0.000 007 49
C	1.927 800 72	0.000 005 14	0.000 005 65
C	−1.939 451 25	0.000 003 66	0.000 004 44
C	3.196 698 75	−0.000 004 40	−0.000 004 75
C	−3.188 248 16	0.000 001 20	0.000 001 93
C	4.485 686 49	−0.000 026 21	−0.000 028 65
C	−4.518 203 60	−0.000 000 93	−0.000 000 22
C	5.792 415 11	−0.000 049 55	−0.000 059 76
C	−5.745 974 58	−0.000 002 54	−0.000 001 78
H	6.356 582 33	0.664 760 64	−0.662 349 90
H	−6.821 318 48	−0.000 003 46	−0.000 002 64
H	6.356 596 39	−0.664 669 86	0.662 408 63

Appendix

A.1.2 $\text{Ag}_3^{+/-}$ CLUSTERS

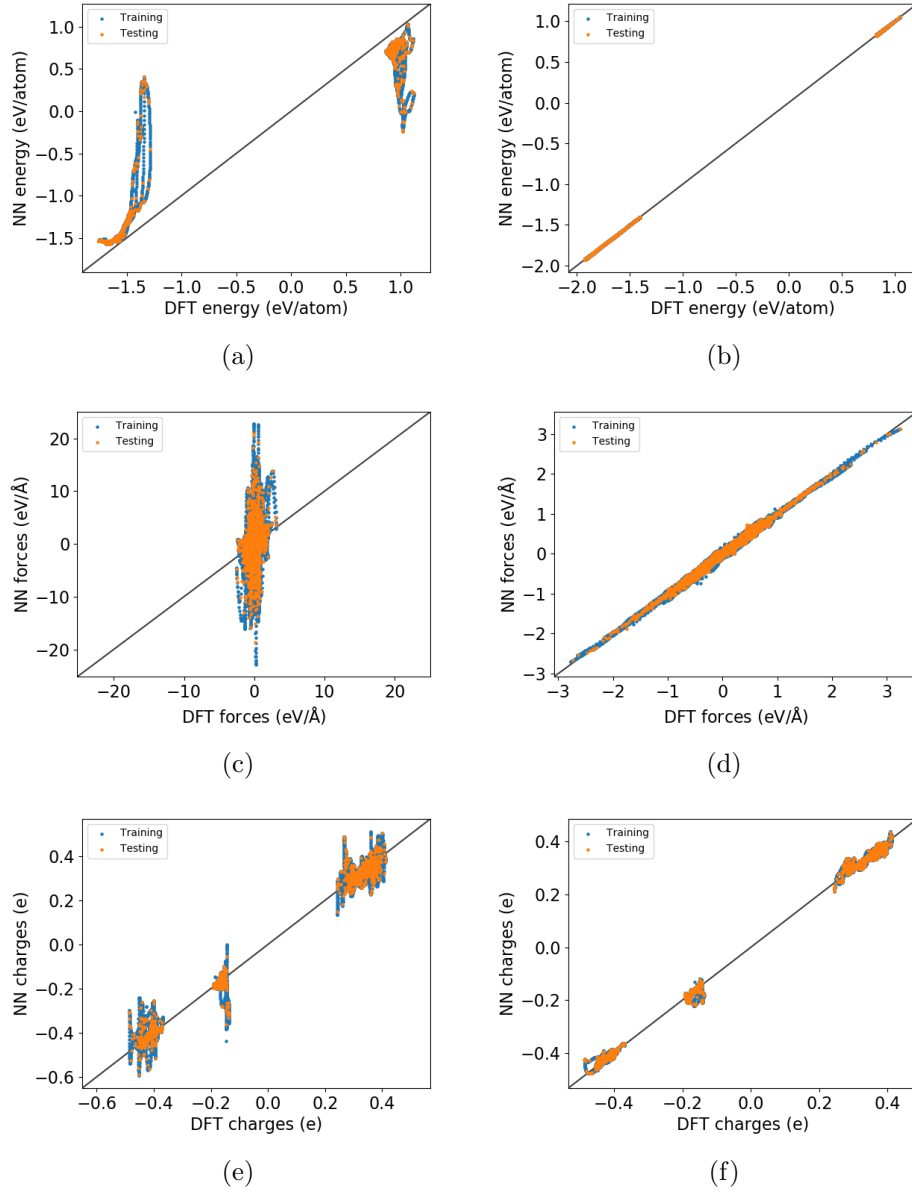


Figure A.1.2: Correlation plots of energies obtained from a 2G-HDNNP (a) and a 4G-HDNNP (b) forces from a 2G-HDNNP (c) and a 4G-HDNNP (d) and charges from a scaled 3G-HDNNP (e) and a 4G-HDNNP (f) for $\text{Ag}_3^{+/-}$

A.1 Details for the 4GHDNNP Test Systems

Table A.1.5: Root mean square errors (RMSE) of charges (me), energies (meV/atom) and forces (meV/Å) for the three different HDNNP generations for the $\text{Ag}_3^{+/-}$ data set with 9930 and 1083 structures for training and testing points respectively.

		charges	energy	forces
2G	train	—	355.0	1812
	test	—	352.0	1803
3G (unscaled)	train	75.50	345.0	1909
	test	77.55	340.0	1963
3G (scaled)	train	26.24	321.1	1912
	test	26.48	320.2	1913
4G	train	10.61	1.293	32.12
	test	9.976	1.323	31.69

Table A.1.6: Symmetry functions for $\text{Ag}^{+/-}$ clusters

no.	type	at. i	at. j	at. k	$\eta(1/\text{Bohr}^2)$	λ	ζ	$R_c(\text{Bohr})$	$R_s(\text{Bohr})$
1	G^2	Ag	Ag		0.0			10.0	0.0
2	G^2	Ag	Ag		0.007			10.0	0.0
3	G^2	Ag	Ag		0.014			10.0	0.0
4	G^2	Ag	Ag		0.025			10.0	0.0
5	G^2	Ag	Ag		0.04			10.0	0.0
6	G^2	Ag	Ag		0.062			10.0	0.0
7	G^4	Ag	Ag	Ag	0.0	1.0	1.0	10.0	
8	G^4	Ag	Ag	Ag	0.0	1.0	2.0	10.0	
9	G^4	Ag	Ag	Ag	0.0	1.0	4.0	10.0	
10	G^4	Ag	Ag	Ag	0.0	1.0	8.0	10.0	
11	G^4	Ag	Ag	Ag	0.0	−1.0	1.0	10.0	
12	G^4	Ag	Ag	Ag	0.0	−1.0	2.0	10.0	

Appendix

Table A.1.7: DFT-optimized structure of Ag_3^+ in XYZ format (distance unit in Å)
3 atoms

Ag	0.000 000 00	0.000 644 41	1.556 755 15
Ag	0.000 000 00	1.347 626 41	−0.779 404 15
Ag	0.000 000 00	−1.348 270 81	−0.777 351 99

Table A.1.8: DFT-optimized structure of Ag_3^- in XYZ format (distance unit in Å)
3 atoms

Ag	0.000 000 00	−1.326 870 06	2.317 857 81
Ag	0.000 000 00	1.340 265 98	−2.309 774 04
Ag	0.000 000 00	−0.013 395 92	−0.008 084 77

A.1.3 $\text{Na}_{8/9}\text{Cl}_8^+$ CLUSTERS

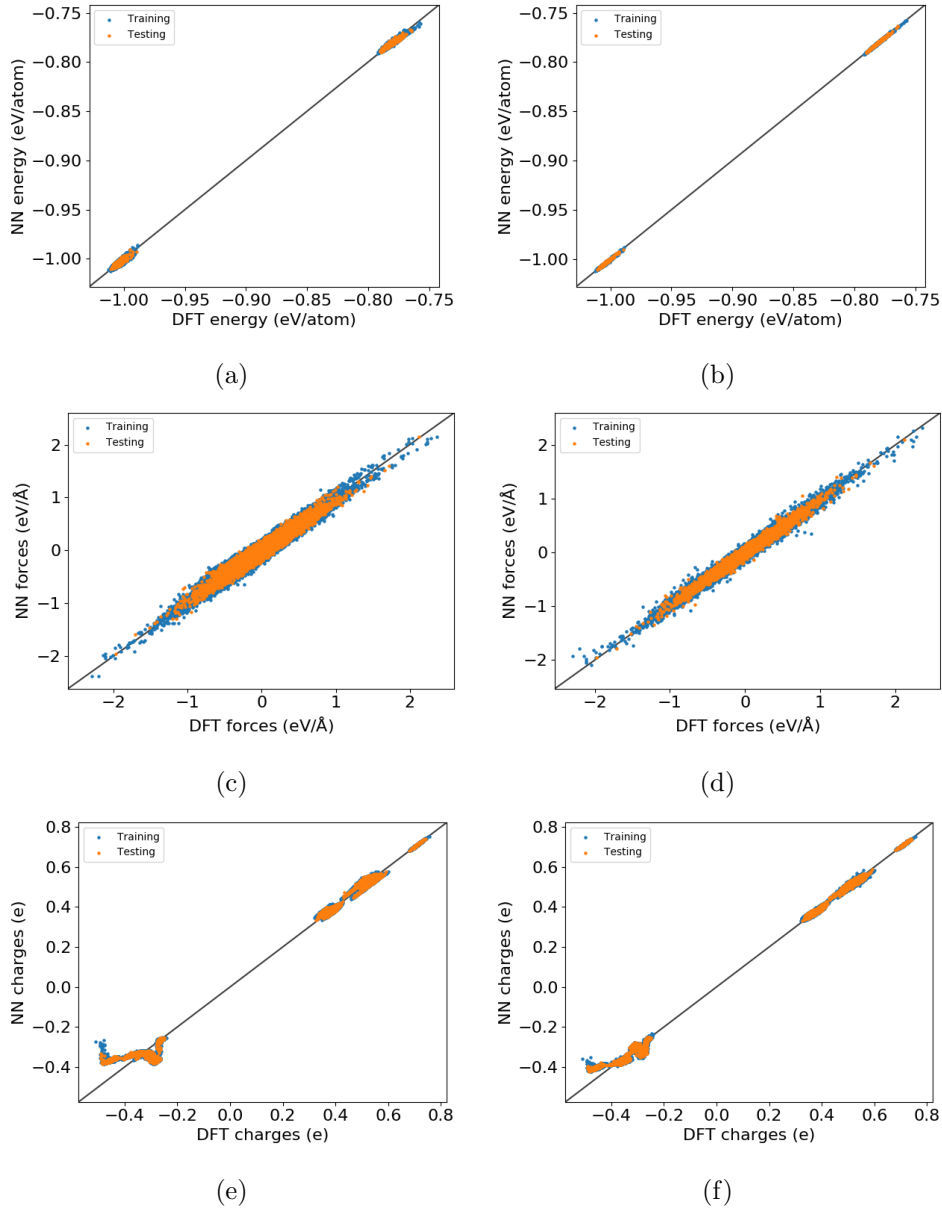


Figure A.1.3: Correlation plots of energies obtained from a 2G-HDNNP (a) and a 4G-HDNNP (b) forces from a 2G-HDNNP (c) and a 4G-HDNNP (d) and charges from an unscaled 3G-HDNNP (e) and a 4G-HDNNP (f) for $\text{Na}_{8/9}\text{Cl}_8^+$

Table A.1.9: Root mean square errors (RMSE) of charges (me), energies (meV/atom) and forces (meV/Å) for the three different HDNNP generations for the $\text{Na}_{8/9}\text{Cl}_8^+$ data set with 4493 and 507 structures for training and testing points respectively.

		charges	energy	forces
2G	train	—	1.690	57.54
	test	—	1.692	57.39
3G (unscaled)	train	28.28	1.426	57.69
	test	28.52	1.470	59.49
3G (scaled)	train	20.75	2.058	73.47
	test	20.80	2.042	76.67
4G	train	15.87	0.474	32.45
	test	15.83	0.481	32.78

Table A.1.10: Symmetry functions for $\text{Na}_{8/9}\text{Cl}_8^+$ clusters

no.	type	at. i	at. j	at. k	$\eta(1/\text{Bohr}^2)$	λ	ζ	$R_c(\text{Bohr})$	$R_s(\text{Bohr})$
1	G^2	Na	Na		0.0			10.0	0.0
2	G^2	Na	Na		0.001			10.0	0.0
3	G^2	Na	Na		0.002			10.0	0.0
4	G^2	Na	Na		0.003			10.0	0.0
5	G^2	Na	Na		0.004			10.0	0.0
6	G^2	Na	Na		0.005			10.0	0.0
7	G^2	Na	Cl		0.0			10.0	0.0
8	G^2	Na	Cl		0.003			10.0	0.0
9	G^2	Na	Cl		0.005			10.0	0.0
10	G^2	Na	Cl		0.007			10.0	0.0
11	G^2	Na	Cl		0.01			10.0	0.0
12	G^2	Na	Cl		0.013			10.0	0.0
13	G^2	Cl	Na		0.0			10.0	0.0
14	G^2	Cl	Na		0.003			10.0	0.0
15	G^2	Cl	Na		0.005			10.0	0.0
16	G^2	Cl	Na		0.007			10.0	0.0
17	G^2	Cl	Na		0.01			10.0	0.0
18	G^2	Cl	Na		0.013			10.0	0.0
19	G^2	Cl	Cl		0.0			10.0	0.0
20	G^2	Cl	Cl		0.001			10.0	0.0

A.1 Details for the 4GHDNNP Test Systems

no.	type	at. i	at. j	at. k	$\eta(1/\text{Bohr}^2)$	λ	ζ	$R_c(\text{Bohr})$	$R_s(\text{Bohr})$
21	G^2	Cl	Cl		0.002			10.0	0.0
22	G^2	Cl	Cl		0.003			10.0	0.0
23	G^2	Cl	Cl		0.004			10.0	0.0
24	G^2	Cl	Cl		0.005			10.0	0.0
25	G^4	Na	Na	Cl	0.0	1.0	1.0	10.0	
26	G^4	Na	Na	Cl	0.0	1.0	2.0	10.0	
27	G^4	Na	Na	Cl	0.0	1.0	4.0	10.0	
28	G^4	Na	Na	Cl	0.0	1.0	8.0	10.0	
29	G^4	Na	Na	Cl	0.0	-1.0	1.0	10.0	
30	G^4	Na	Na	Cl	0.0	-1.0	2.0	10.0	
31	G^4	Na	Cl	Cl	0.0	1.0	1.0	10.0	
32	G^4	Na	Cl	Cl	0.0	1.0	2.0	10.0	
33	G^4	Na	Cl	Cl	0.0	-1.0	1.0	10.0	
34	G^4	Na	Cl	Cl	0.0	-1.0	2.0	10.0	
35	G^4	Na	Cl	Cl	0.0	-1.0	4.0	10.0	
36	G^4	Cl	Cl	Na	0.0	1.0	1.0	10.0	
37	G^4	Cl	Cl	Na	0.0	1.0	2.0	10.0	
38	G^4	Cl	Cl	Na	0.0	1.0	4.0	10.0	
39	G^4	Cl	Cl	Na	0.0	1.0	8.0	10.0	
40	G^4	Cl	Cl	Na	0.0	-1.0	1.0	10.0	
41	G^4	Cl	Na	Na	0.0	1.0	1.0	10.0	
42	G^4	Cl	Na	Na	0.0	1.0	2.0	10.0	
43	G^4	Cl	Na	Na	0.0	1.0	4.0	10.0	
44	G^4	Cl	Na	Na	0.0	-1.0	1.0	10.0	
45	G^4	Cl	Na	Na	0.0	-1.0	2.0	10.0	

Appendix

Table A.1.11: DFT-optimized structure of Na_9Cl_8^+ in XYZ format (distance unit in Å)
17 atoms

Na	−4.672 483 91	1.744 323 61	0.066 917 32
Cl	−4.674 131 38	−0.763 117 13	−0.005 394 92
Cl	−2.156 850 54	2.353 451 40	0.126 851 59
Na	−2.120 583 99	−0.453 759 70	0.037 785 66
Na	0.430 089 05	2.067 507 92	0.061 237 48
Cl	0.514 739 28	−0.620 487 80	0.003 580 16
Cl	3.054 771 88	2.435 379 02	0.005 454 56
Na	3.081 187 44	−0.275 178 18	−0.020 881 71
Na	5.635 084 96	2.195 983 30	−0.008 956 06
Cl	5.728 609 48	−0.495 161 62	−0.005 581 27
Cl	8.304 179 09	2.518 938 87	0.008 721 19
Na	15.163 008 08	4.522 166 97	−0.019 004 50
Na	10.847 244 50	2.274 841 80	−0.037 879 82
Cl	10.992 739 88	−0.383 182 02	−0.002 413 13
Cl	13.644 077 08	2.525 223 09	0.039 396 59
Na	13.502 039 57	−0.152 682 89	0.114 915 06
Na	8.284 823 01	−0.197 007 56	0.036 113 70

A.1.4 Au₂–MgO

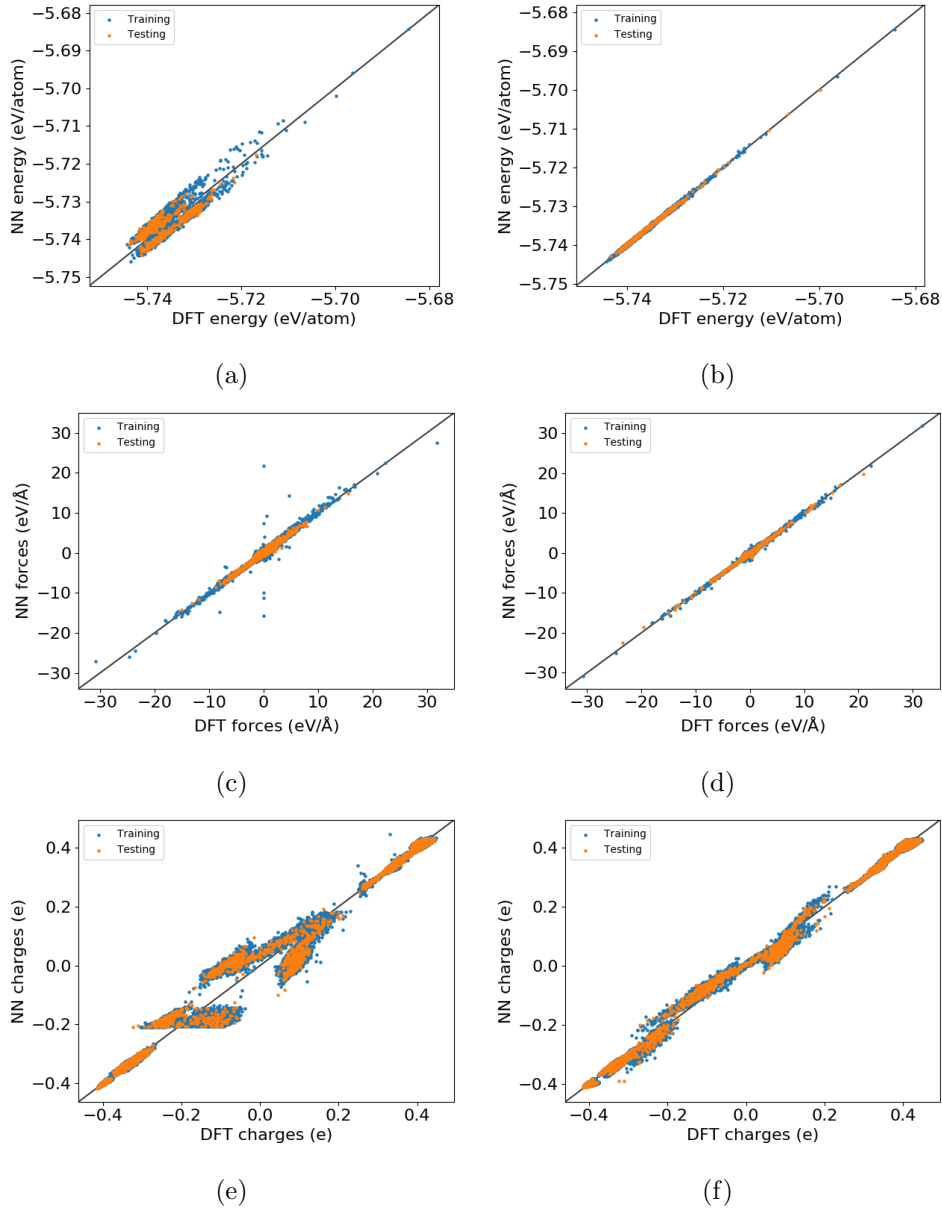


Figure A.1.4: Correlation plots of energies obtained from a 2G-HDNNP (a) and a 4G-HDNNP (b) forces from a 2G-HDNNP (c) and a 4G-HDNNP (d) and charges from a scaled 3G-HDNNP (e) and a 4G-HDNNP (f) for Au₂–MgO

Appendix

Table A.1.12: Root mean square errors (RMSE) of charges (me), energies (meV/atom) and forces (meV/Å) for the Au₂-MgO data set with 4468 and 532 structures for training and testing points respectively.

		charges	energy	forces
2G	train	—	2.299	155.4
	test	—	2.287	153.1
4G	train	5.663	0.209	81.05
	test	5.698	0.219	66.00

Table A.1.13: Symmetry functions for Au₂-MgO slabs

no.	type	at. i	at. j	at. k	$\eta(1/\text{Bohr}^2)$	λ	ζ	$R_c(\text{Bohr})$	$R_s(\text{Bohr})$
1	G^2	Mg	Mg		0.0			8.0	0.0
2	G^2	Mg	Mg		0.001			8.0	0.0
3	G^2	Mg	Mg		0.002			8.0	0.0
4	G^2	Mg	Mg		0.003			8.0	0.0
5	G^2	Mg	Mg		0.004			8.0	0.0
6	G^2	Mg	Mg		0.005			8.0	0.0
7	G^2	O	Mg		0.0			8.0	0.0
8	G^2	O	Mg		0.004			8.0	0.0
9	G^2	O	Mg		0.007			8.0	0.0
10	G^2	O	Mg		0.01			8.0	0.0
11	G^2	O	Mg		0.014			8.0	0.0
12	G^2	O	Mg		0.018			8.0	0.0
13	G^2	Mg	O		0.0			8.0	0.0
14	G^2	Mg	O		0.004			8.0	0.0
15	G^2	Mg	O		0.007			8.0	0.0
16	G^2	Mg	O		0.01			8.0	0.0
17	G^2	Mg	O		0.014			8.0	0.0
18	G^2	Mg	O		0.018			8.0	0.0
19	G^2	O	O		0.0			8.0	0.0
20	G^2	O	O		0.001			8.0	0.0
21	G^2	O	O		0.002			8.0	0.0
22	G^2	O	O		0.003			8.0	0.0
23	G^2	O	O		0.004			8.0	0.0

A.1 Details for the 4GHDNNP Test Systems

no.	type	at. i	at. j	at. k	$\eta(1/\text{Bohr}^2)$	λ	ζ	$R_c(\text{Bohr})$	$R_s(\text{Bohr})$
24	G^2	O	O		0.005			8.0	0.0
25	G^2	Mg	Au		0.0			8.0	0.0
26	G^2	Mg	Au		0.001			8.0	0.0
27	G^2	Mg	Au		0.002			8.0	0.0
28	G^2	Mg	Au		0.003			8.0	0.0
29	G^2	Mg	Au		0.004			8.0	0.0
30	G^2	Mg	Au		0.005			8.0	0.0
31	G^2	Au	Mg		0.0			8.0	0.0
32	G^2	Au	Mg		0.001			8.0	0.0
33	G^2	Au	Mg		0.002			8.0	0.0
34	G^2	Au	Mg		0.003			8.0	0.0
35	G^2	Au	Mg		0.004			8.0	0.0
36	G^2	Au	Mg		0.005			8.0	0.0
37	G^2	Au	O		0.0			8.0	0.0
38	G^2	Au	O		0.004			8.0	0.0
39	G^2	Au	O		0.008			8.0	0.0
40	G^2	Au	O		0.013			8.0	0.0
41	G^2	Au	O		0.018			8.0	0.0
42	G^2	Au	O		0.024			8.0	0.0
43	G^2	O	Au		0.0			8.0	0.0
44	G^2	O	Au		0.004			8.0	0.0
45	G^2	O	Au		0.008			8.0	0.0
46	G^2	O	Au		0.013			8.0	0.0
47	G^2	O	Au		0.018			8.0	0.0
48	G^2	O	Au		0.024			8.0	0.0
49	G^2	Au	Au		0.0			8.0	0.0
50	G^2	Au	Au		0.004			8.0	0.0
51	G^2	Au	Au		0.008			8.0	0.0
52	G^2	Au	Au		0.012			8.0	0.0
53	G^2	Au	Au		0.017			8.0	0.0
54	G^2	Au	Au		0.022			8.0	0.0
55	G^2	O	Al		0.0			8.0	0.0
56	G^2	O	Al		0.003			8.0	0.0
57	G^2	O	Al		0.005			8.0	0.0
58	G^2	O	Al		0.008			8.0	0.0

Appendix

no.	type	at. i	at. j	at. k	$\eta(1/\text{Bohr}^2)$	λ	ζ	$R_c(\text{Bohr})$	$R_s(\text{Bohr})$
59	G^2	O	Al		0.011			8.0	0.0
60	G^2	O	Al		0.014			8.0	0.0
61	G^2	Al	O		0.0			8.0	0.0
62	G^2	Al	O		0.003			8.0	0.0
63	G^2	Al	O		0.005			8.0	0.0
64	G^2	Al	O		0.008			8.0	0.0
65	G^2	Al	O		0.011			8.0	0.0
66	G^2	Al	O		0.014			8.0	0.0
67	G^2	Al	Mg		0.0			8.0	0.0
68	G^2	Al	Mg		0.001			8.0	0.0
69	G^2	Al	Mg		0.002			8.0	0.0
70	G^2	Al	Mg		0.003			8.0	0.0
71	G^2	Al	Mg		0.004			8.0	0.0
72	G^2	Al	Mg		0.005			8.0	0.0
73	G^2	Mg	Al		0.0			8.0	0.0
74	G^2	Mg	Al		0.001			8.0	0.0
75	G^2	Mg	Al		0.002			8.0	0.0
76	G^2	Mg	Al		0.003			8.0	0.0
77	G^2	Mg	Al		0.004			8.0	0.0
78	G^2	Mg	Al		0.005			8.0	0.0
79	G^4	Mg	Mg	Mg	0.0	1.0	1.0	8.0	
80	G^4	Mg	Mg	Mg	0.0	1.0	2.0	8.0	
81	G^4	Mg	Mg	Mg	0.0	1.0	4.0	8.0	
82	G^4	Mg	Mg	Mg	0.0	-1.0	1.0	8.0	
83	G^4	Mg	Mg	O	0.0	1.0	1.0	8.0	
84	G^4	Mg	Mg	O	0.0	1.0	2.0	8.0	
85	G^4	Mg	Mg	O	0.0	1.0	4.0	8.0	
86	G^4	Mg	Mg	O	0.0	1.0	8.0	8.0	
87	G^4	Mg	Mg	O	0.0	-1.0	1.0	8.0	
88	G^4	Mg	Mg	O	0.0	-1.0	2.0	8.0	
89	G^4	Mg	O	O	0.0	1.0	1.0	8.0	
90	G^4	Mg	O	O	0.0	1.0	2.0	8.0	
91	G^4	Mg	O	O	0.0	1.0	4.0	8.0	
92	G^4	Mg	O	O	0.0	-1.0	1.0	8.0	
93	G^4	Mg	O	O	0.0	-1.0	2.0	8.0	

A.1 Details for the 4GHDNNP Test Systems

no.	type	at. i	at. j	at. k	$\eta(1/\text{Bohr}^2)$	λ	ζ	$R_c(\text{Bohr})$	$R_s(\text{Bohr})$
94	G^4	Mg	O	O	0.0	-1.0	4.0	8.0	
95	G^4	Mg	O	Al	0.0	1.0	1.0	8.0	
96	G^4	Mg	O	Al	0.0	1.0	2.0	8.0	
97	G^4	Mg	O	Al	0.0	1.0	4.0	8.0	
98	G^4	Mg	O	Al	0.0	1.0	8.0	8.0	
99	G^4	Mg	O	Al	0.0	-1.0	1.0	8.0	
100	G^4	Mg	O	Au	0.0	1.0	1.0	8.0	
101	G^4	Mg	O	Au	0.0	1.0	2.0	8.0	
102	G^4	Mg	O	Au	0.0	1.0	4.0	8.0	
103	G^4	Mg	O	Au	0.0	1.0	8.0	8.0	
104	G^4	Mg	O	Au	0.0	-1.0	1.0	8.0	
105	G^4	Mg	O	Au	0.0	-1.0	2.0	8.0	
106	G^4	O	Mg	Mg	0.0	1.0	1.0	8.0	
107	G^4	O	Mg	Mg	0.0	1.0	2.0	8.0	
108	G^4	O	Mg	Mg	0.0	1.0	4.0	8.0	
109	G^4	O	Mg	Mg	0.0	-1.0	1.0	8.0	
110	G^4	O	Mg	Mg	0.0	-1.0	2.0	8.0	
111	G^4	O	Mg	Mg	0.0	-1.0	4.0	8.0	
112	G^4	O	Mg	O	0.0	1.0	1.0	8.0	
113	G^4	O	Mg	O	0.0	1.0	2.0	8.0	
114	G^4	O	Mg	O	0.0	1.0	4.0	8.0	
115	G^4	O	Mg	O	0.0	1.0	8.0	8.0	
116	G^4	O	Mg	O	0.0	-1.0	1.0	8.0	
117	G^4	O	Mg	O	0.0	-1.0	2.0	8.0	
118	G^4	O	Mg	Al	0.0	1.0	1.0	8.0	
119	G^4	O	Mg	Al	0.0	1.0	2.0	8.0	
120	G^4	O	Mg	Al	0.0	1.0	4.0	8.0	
121	G^4	O	Mg	Al	0.0	-1.0	1.0	8.0	
122	G^4	O	Mg	Al	0.0	-1.0	2.0	8.0	
123	G^4	O	Mg	Al	0.0	-1.0	4.0	8.0	
124	G^4	O	Mg	Au	0.0	1.0	1.0	8.0	
125	G^4	O	Mg	Au	0.0	1.0	2.0	8.0	
126	G^4	O	Mg	Au	0.0	-1.0	1.0	8.0	
127	G^4	O	Mg	Au	0.0	-1.0	2.0	8.0	
128	G^4	O	O	O	0.0	1.0	1.0	8.0	

Appendix

no.	type	at. i	at. j	at. k	$\eta(1/\text{Bohr}^2)$	λ	ζ	$R_c(\text{Bohr})$	$R_s(\text{Bohr})$
129	G^4	O	O	O	0.0	1.0	2.0	8.0	
130	G^4	O	O	O	0.0	-1.0	1.0	8.0	
131	G^4	O	O	Al	0.0	1.0	1.0	8.0	
132	G^4	O	O	Al	0.0	1.0	2.0	8.0	
133	G^4	O	O	Al	0.0	-1.0	1.0	8.0	
134	G^4	O	O	Al	0.0	-1.0	2.0	8.0	
135	G^4	Al	Mg	Mg	0.0	1.0	1.0	8.0	
136	G^4	Al	Mg	O	0.0	1.0	1.0	8.0	
137	G^4	Al	Mg	O	0.0	1.0	2.0	8.0	
138	G^4	Al	Mg	O	0.0	-1.0	1.0	8.0	
139	G^4	Al	O	O	0.0	1.0	1.0	8.0	
140	G^4	Al	O	O	0.0	1.0	2.0	8.0	
141	G^4	Al	O	O	0.0	-1.0	1.0	8.0	
142	G^4	Al	O	O	0.0	-1.0	2.0	8.0	
143	G^4	Au	Mg	Mg	0.0	1.0	1.0	8.0	
144	G^4	Au	Mg	Mg	0.0	1.0	2.0	8.0	
145	G^4	Au	Mg	O	0.0	1.0	1.0	8.0	
146	G^4	Au	Mg	O	0.0	1.0	2.0	8.0	
147	G^4	Au	Mg	O	0.0	-1.0	1.0	8.0	
148	G^4	Au	Mg	O	0.0	-1.0	2.0	8.0	
149	G^4	Au	O	O	0.0	1.0	1.0	8.0	
150	G^4	Au	O	Au	0.0	1.0	-1.0	8.0	
151	G^4	Au	O	Au	0.0	1.0	-2.0	8.0	

B.2 DETAILS FOR THE MAPbI_3 FHMC SIMULATIONS

B.2.1 SUPERCELLS

We used the same supercells for all FHMC, MD and phonon calculations. Pictures of the supercells for each phase are shown in the figures below.

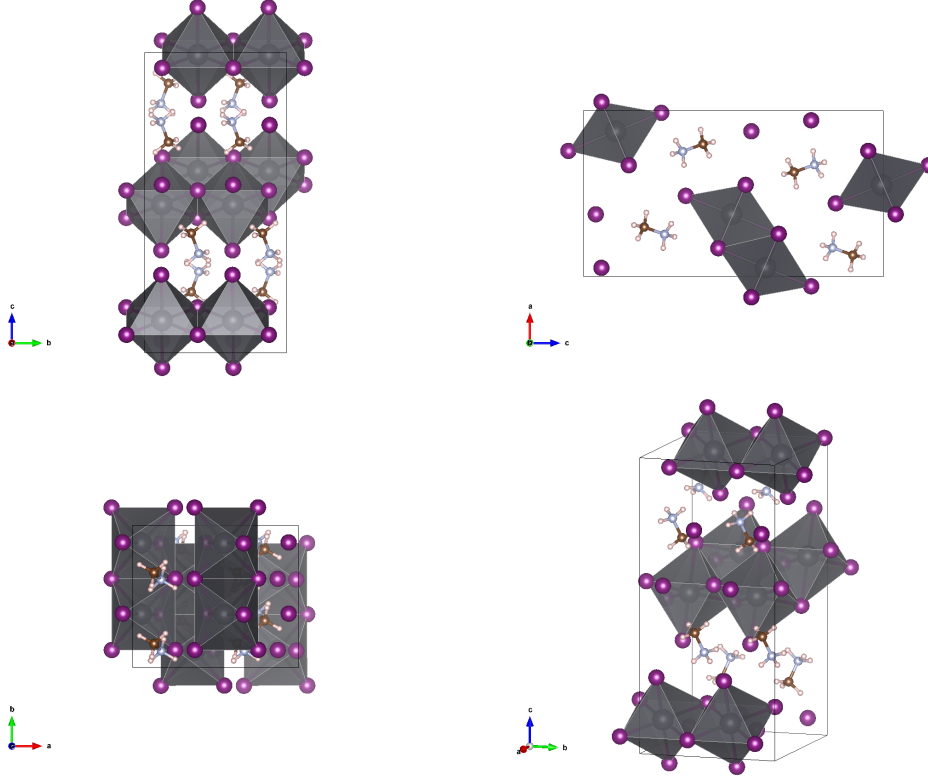


Figure B.2.5: Geometry of the supercell used for the double delta phase.

The content of this section was adapted from J. A. Finkler and S. Goedecker. “Experimental Absence of the Non-Perovskite Ground State Phases of MaPbI_3 Explained by a Funnel Hopping Monte Carlo Study Based on a Neural Network Potential”. *Materials Advances* 4, 2023, pp. 184–194 and its supplemental information.

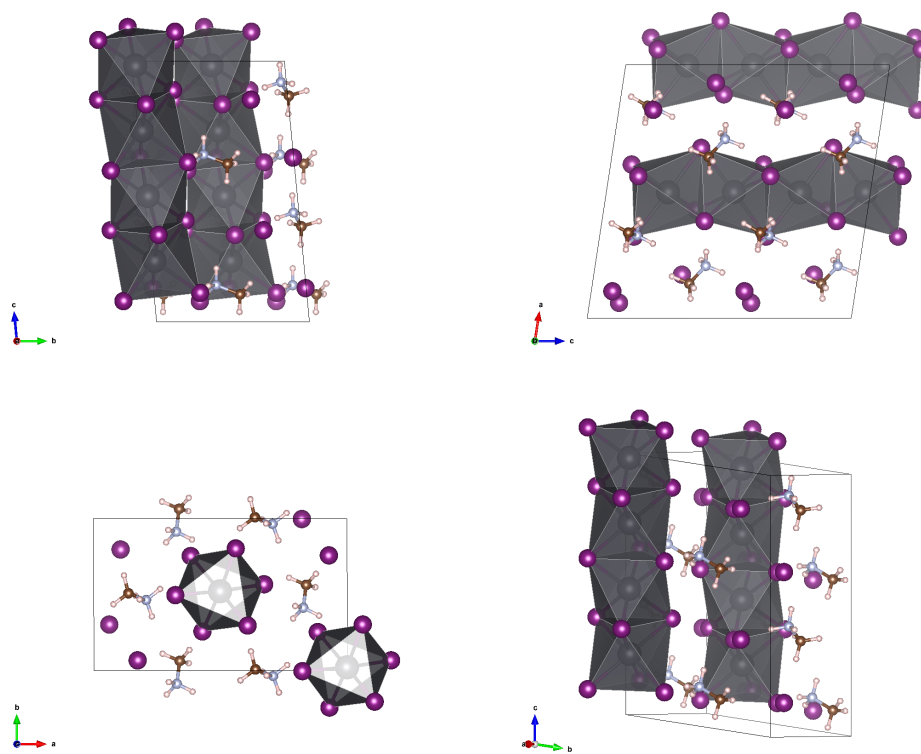


Figure B.2.6: Geometry of the supercell used for the delta phase.

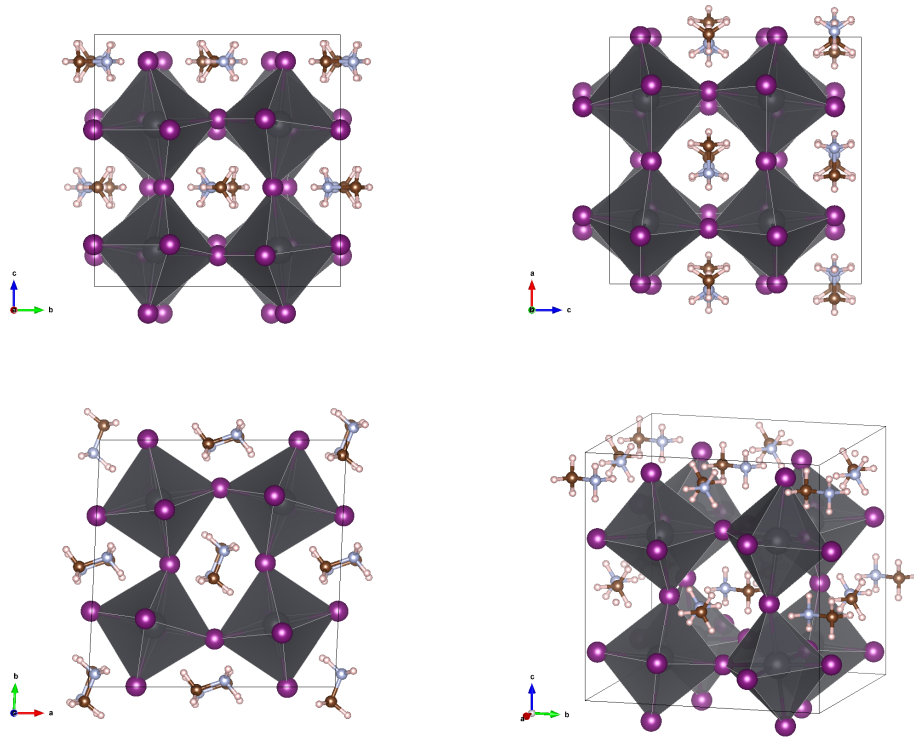


Figure B.2.7: Geometry of the supercell used for the orthorhombic phase.

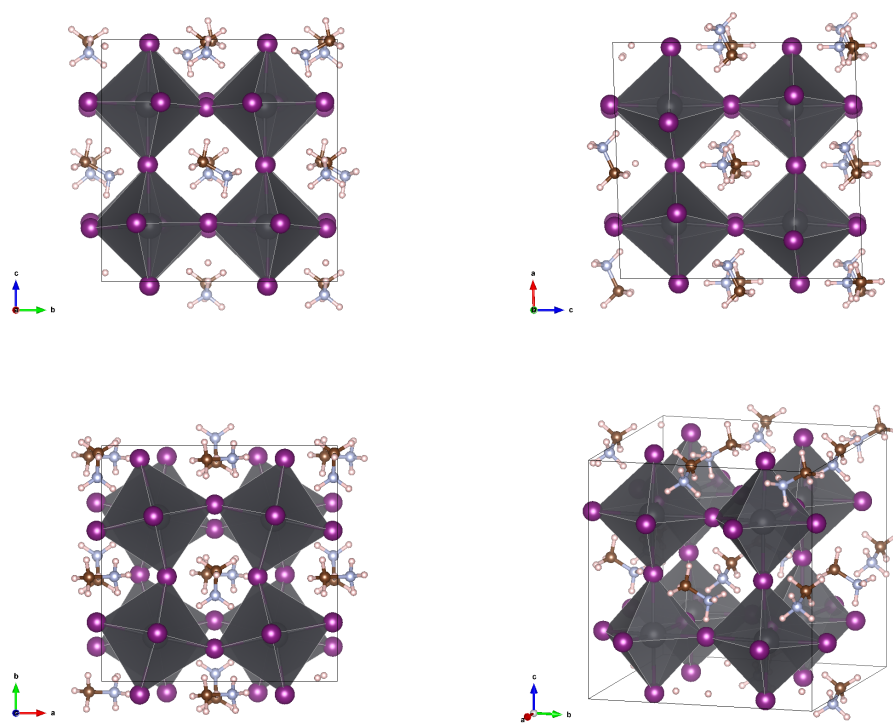


Figure B.2.8: Geometry of the supercell used for the tetragonal phase.

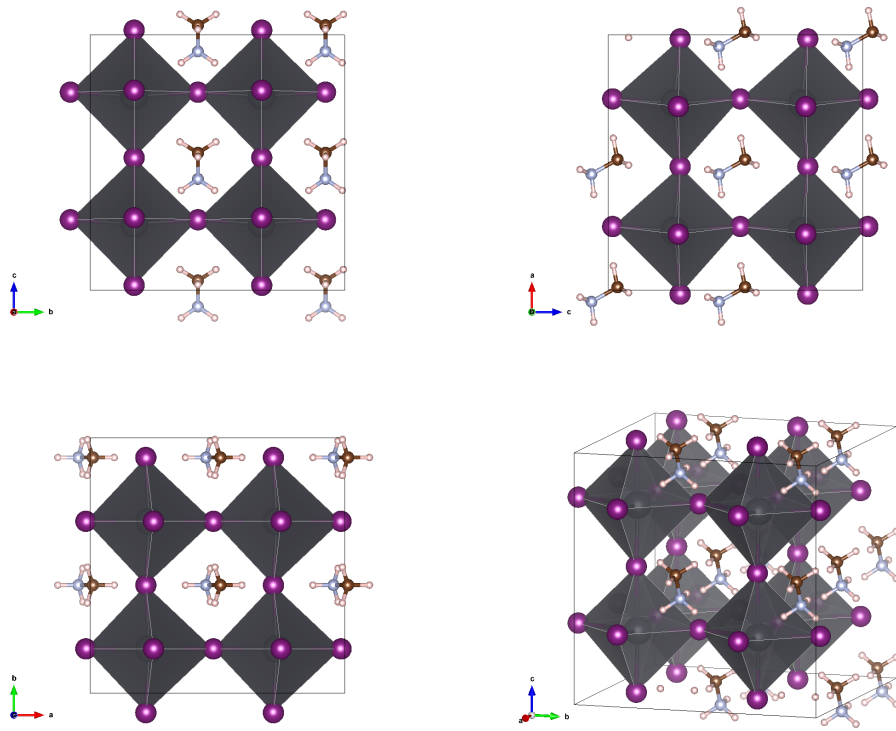


Figure B.2.9: Geometry of the supercell used for the cubic phase.

B.2.2 SYMMETRY FUNCTIONS USED FOR THE MAPBI₃ HDNNP

We used 2- (G^2) and 3-body (G^4) atom centered symmetry functions [10] as atomic environment descriptors for our neural network potential.

$$G_i^2 = \sum_j e^{-\eta(R_{ij}-R_s)^2} \cdot f_c(R_{ij}) \quad (1)$$

$$G_i^4 = 2^{1-\zeta} \sum_{j,k \neq i} (1 + \lambda \cos(\theta_{ijk}))^\zeta \cdot e^{-\eta(R_{ij}^2 + R_{ik}^2 + R_{jk}^2)} \cdot f_c(R_{ij}) \cdot f_c(R_{ik}) \cdot f_c(R_{jk}) \quad (2)$$

$$f_c(r) = \tanh(1 - r/R_c)^3 \quad (3)$$

Table B.2.14: Symmetry functions used for the neural network potential

no.	type	at. i	at. j	at. k	$\eta(1/\text{Bohr}^2)$	λ	ζ	$R_c(\text{Bohr})$	$R_s(\text{Bohr})$
1	G^2	H	H		0.004			12.0	0.0
2	G^2	H	H		0.028			12.0	0.0
3	G^2	H	H		0.139			12.0	0.0
4	G^2	H	H		0.556			12.0	0.0
5	G^2	H	H		1.000			12.0	0.0
6	G^2	H	C		0.004			12.0	0.0
7	G^2	H	C		0.028			12.0	0.0
8	G^2	H	C		0.139			12.0	0.0
9	G^2	H	C		0.556			12.0	0.0
10	G^2	H	C		1.000			12.0	0.0
11	G^2	H	N		0.004			12.0	0.0
12	G^2	H	N		0.028			12.0	0.0
13	G^2	H	N		0.139			12.0	0.0
14	G^2	H	N		0.556			12.0	0.0
15	G^2	H	N		1.000			12.0	0.0
16	G^2	H	I		0.004			12.0	0.0
17	G^2	H	I		0.028			12.0	0.0
18	G^2	H	I		0.139			12.0	0.0
19	G^2	H	Pb		0.004			12.0	0.0
20	G^2	H	Pb		0.028			12.0	0.0
21	G^2	H	Pb		0.139			12.0	0.0
22	G^4	H	H	H	0.005	-1.0	1.0	12.0	
23	G^4	H	H	H	0.005	-1.0	4.0	12.0	

B.2 Details for the MaPbI₃ FHMC Simulations

no.	type	at. i	at. j	at. k	$\eta(1/\text{Bohr}^2)$	λ	ζ	$R_c(\text{Bohr})$	$R_s(\text{Bohr})$
24	G^4	H	H	H	0.005	1.0	1.0	12.0	
25	G^4	H	H	H	0.005	1.0	4.0	12.0	
26	G^4	H	H	C	0.005	-1.0	1.0	12.0	
27	G^4	H	H	C	0.005	-1.0	4.0	12.0	
28	G^4	H	H	C	0.005	1.0	1.0	12.0	
29	G^4	H	H	C	0.005	1.0	4.0	12.0	
30	G^4	H	H	N	0.005	-1.0	1.0	12.0	
31	G^4	H	H	N	0.005	-1.0	4.0	12.0	
32	G^4	H	H	N	0.005	1.0	1.0	12.0	
33	G^4	H	H	N	0.005	1.0	4.0	12.0	
34	G^4	H	H	I	0.005	-1.0	1.0	12.0	
35	G^4	H	H	I	0.005	-1.0	4.0	12.0	
36	G^4	H	H	I	0.005	1.0	1.0	12.0	
37	G^4	H	H	I	0.005	1.0	4.0	12.0	
38	G^4	H	H	Pb	0.005	-1.0	1.0	12.0	
39	G^4	H	H	Pb	0.005	-1.0	4.0	12.0	
40	G^4	H	H	Pb	0.005	1.0	1.0	12.0	
41	G^4	H	H	Pb	0.005	1.0	4.0	12.0	
42	G^4	H	C	C	0.005	-1.0	1.0	12.0	
43	G^4	H	C	C	0.005	-1.0	4.0	12.0	
44	G^4	H	C	C	0.005	1.0	1.0	12.0	
45	G^4	H	C	C	0.005	1.0	4.0	12.0	
46	G^4	H	C	N	0.005	-1.0	1.0	12.0	
47	G^4	H	C	N	0.005	-1.0	4.0	12.0	
48	G^4	H	C	N	0.005	1.0	1.0	12.0	
49	G^4	H	C	N	0.005	1.0	4.0	12.0	
50	G^4	H	C	I	0.005	-1.0	1.0	12.0	
51	G^4	H	C	I	0.005	-1.0	4.0	12.0	
52	G^4	H	C	I	0.005	1.0	1.0	12.0	
53	G^4	H	C	I	0.005	1.0	4.0	12.0	
54	G^4	H	C	Pb	0.005	-1.0	1.0	12.0	
55	G^4	H	C	Pb	0.005	-1.0	4.0	12.0	
56	G^4	H	C	Pb	0.005	1.0	1.0	12.0	
57	G^4	H	C	Pb	0.005	1.0	4.0	12.0	
58	G^4	H	N	N	0.005	-1.0	1.0	12.0	

Appendix

no.	type	at. i	at. j	at. k	$\eta(1/\text{Bohr}^2)$	λ	ζ	$R_c(\text{Bohr})$	$R_s(\text{Bohr})$
59	G^4	H	N	N	0.005	-1.0	4.0	12.0	
60	G^4	H	N	N	0.005	1.0	1.0	12.0	
61	G^4	H	N	I	0.005	-1.0	1.0	12.0	
62	G^4	H	N	I	0.005	-1.0	4.0	12.0	
63	G^4	H	N	I	0.005	1.0	1.0	12.0	
64	G^4	H	N	I	0.005	1.0	4.0	12.0	
65	G^4	H	N	Pb	0.005	-1.0	1.0	12.0	
66	G^4	H	N	Pb	0.005	-1.0	4.0	12.0	
67	G^4	H	N	Pb	0.005	1.0	1.0	12.0	
68	G^4	H	I	I	0.005	-1.0	1.0	12.0	
69	G^4	H	I	I	0.005	-1.0	4.0	12.0	
70	G^4	H	I	I	0.005	1.0	1.0	12.0	
71	G^4	H	I	I	0.005	1.0	4.0	12.0	
72	G^4	H	I	Pb	0.005	-1.0	1.0	12.0	
73	G^4	H	I	Pb	0.005	1.0	1.0	12.0	
74	G^4	H	I	Pb	0.005	1.0	4.0	12.0	
75	G^2	C	H		0.004			12.0	0.0
76	G^2	C	H		0.028			12.0	0.0
77	G^2	C	H		0.139			12.0	0.0
78	G^2	C	H		0.556			12.0	0.0
79	G^2	C	H		1.000			12.0	0.0
80	G^2	C	C		0.004			12.0	0.0
81	G^2	C	C		0.028			12.0	0.0
82	G^2	C	C		0.139			12.0	0.0
83	G^2	C	N		0.004			12.0	0.0
84	G^2	C	N		0.028			12.0	0.0
85	G^2	C	N		0.139			12.0	0.0
86	G^2	C	N		0.556			12.0	0.0
87	G^2	C	N		1.000			12.0	0.0
88	G^2	C	I		0.004			12.0	0.0
89	G^2	C	I		0.028			12.0	0.0
90	G^2	C	I		0.139			12.0	0.0
91	G^2	C	Pb		0.004			12.0	0.0
92	G^2	C	Pb		0.028			12.0	0.0
93	G^2	C	Pb		0.139			12.0	0.0

B.2 Details for the MaPbI₃ FHMC Simulations

no.	type	at. i	at. j	at. k	$\eta(1/\text{Bohr}^2)$	λ	ζ	$R_c(\text{Bohr})$	$R_s(\text{Bohr})$
94	G^4	C	H	H	0.005	-1.0	1.0	12.0	
95	G^4	C	H	H	0.005	-1.0	4.0	12.0	
96	G^4	C	H	H	0.005	1.0	1.0	12.0	
97	G^4	C	H	H	0.005	1.0	4.0	12.0	
98	G^4	C	H	C	0.005	-1.0	1.0	12.0	
99	G^4	C	H	C	0.005	-1.0	4.0	12.0	
100	G^4	C	H	C	0.005	1.0	1.0	12.0	
101	G^4	C	H	C	0.005	1.0	4.0	12.0	
102	G^4	C	H	N	0.005	-1.0	1.0	12.0	
103	G^4	C	H	N	0.005	-1.0	4.0	12.0	
104	G^4	C	H	N	0.005	1.0	1.0	12.0	
105	G^4	C	H	N	0.005	1.0	4.0	12.0	
106	G^4	C	H	I	0.005	-1.0	1.0	12.0	
107	G^4	C	H	I	0.005	-1.0	4.0	12.0	
108	G^4	C	H	I	0.005	1.0	1.0	12.0	
109	G^4	C	H	I	0.005	1.0	4.0	12.0	
110	G^4	C	H	Pb	0.005	-1.0	1.0	12.0	
111	G^4	C	H	Pb	0.005	-1.0	4.0	12.0	
112	G^4	C	H	Pb	0.005	1.0	1.0	12.0	
113	G^4	C	H	Pb	0.005	1.0	4.0	12.0	
114	G^4	C	C	N	0.005	-1.0	1.0	12.0	
115	G^4	C	C	N	0.005	-1.0	4.0	12.0	
116	G^4	C	C	N	0.005	1.0	1.0	12.0	
117	G^4	C	C	N	0.005	1.0	4.0	12.0	
118	G^4	C	C	I	0.005	-1.0	1.0	12.0	
119	G^4	C	C	I	0.005	1.0	1.0	12.0	
120	G^4	C	C	I	0.005	1.0	4.0	12.0	
121	G^4	C	N	N	0.005	-1.0	1.0	12.0	
122	G^4	C	N	N	0.005	-1.0	4.0	12.0	
123	G^4	C	N	N	0.005	1.0	1.0	12.0	
124	G^4	C	N	I	0.005	-1.0	1.0	12.0	
125	G^4	C	N	I	0.005	-1.0	4.0	12.0	
126	G^4	C	N	I	0.005	1.0	1.0	12.0	
127	G^4	C	N	I	0.005	1.0	4.0	12.0	
128	G^4	C	N	Pb	0.005	-1.0	1.0	12.0	

Appendix

no.	type	at. i	at. j	at. k	$\eta(1/\text{Bohr}^2)$	λ	ζ	$R_c(\text{Bohr})$	$R_s(\text{Bohr})$
129	G^4	C	N	Pb	0.005	-1.0	4.0	12.0	
130	G^4	C	N	Pb	0.005	1.0	1.0	12.0	
131	G^4	C	I	I	0.005	-1.0	1.0	12.0	
132	G^4	C	I	I	0.005	1.0	1.0	12.0	
133	G^4	C	I	I	0.005	1.0	4.0	12.0	
134	G^4	C	I	Pb	0.005	-1.0	1.0	12.0	
135	G^4	C	I	Pb	0.005	1.0	1.0	12.0	
136	G^4	C	I	Pb	0.005	1.0	4.0	12.0	
137	G^2	N	H		0.004			12.0	0.0
138	G^2	N	H		0.028			12.0	0.0
139	G^2	N	H		0.139			12.0	0.0
140	G^2	N	H		0.556			12.0	0.0
141	G^2	N	H		1.000			12.0	0.0
142	G^2	N	C		0.004			12.0	0.0
143	G^2	N	C		0.028			12.0	0.0
144	G^2	N	C		0.139			12.0	0.0
145	G^2	N	C		0.556			12.0	0.0
146	G^2	N	C		1.000			12.0	0.0
147	G^2	N	N		0.004			12.0	0.0
148	G^2	N	N		0.028			12.0	0.0
149	G^2	N	I		0.004			12.0	0.0
150	G^2	N	I		0.028			12.0	0.0
151	G^2	N	I		0.139			12.0	0.0
152	G^2	N	Pb		0.004			12.0	0.0
153	G^2	N	Pb		0.028			12.0	0.0
154	G^4	N	H	H	0.005	-1.0	1.0	12.0	
155	G^4	N	H	H	0.005	-1.0	4.0	12.0	
156	G^4	N	H	H	0.005	1.0	1.0	12.0	
157	G^4	N	H	H	0.005	1.0	4.0	12.0	
158	G^4	N	H	C	0.005	-1.0	1.0	12.0	
159	G^4	N	H	C	0.005	-1.0	4.0	12.0	
160	G^4	N	H	C	0.005	1.0	1.0	12.0	
161	G^4	N	H	C	0.005	1.0	4.0	12.0	
162	G^4	N	H	N	0.005	-1.0	1.0	12.0	
163	G^4	N	H	N	0.005	1.0	1.0	12.0	

B.2 Details for the MaPbI_3 FHMC Simulations

no.	type	at. i	at. j	at. k	$\eta(1/\text{Bohr}^2)$	λ	ζ	$R_c(\text{Bohr})$	$R_s(\text{Bohr})$
164	G^4	N	H	N	0.005	1.0	4.0	12.0	
165	G^4	N	H	I	0.005	-1.0	1.0	12.0	
166	G^4	N	H	I	0.005	-1.0	4.0	12.0	
167	G^4	N	H	I	0.005	1.0	1.0	12.0	
168	G^4	N	H	I	0.005	1.0	4.0	12.0	
169	G^4	N	H	Pb	0.005	-1.0	1.0	12.0	
170	G^4	N	H	Pb	0.005	1.0	1.0	12.0	
171	G^4	N	H	Pb	0.005	1.0	4.0	12.0	
172	G^4	N	C	C	0.005	-1.0	1.0	12.0	
173	G^4	N	C	C	0.005	-1.0	4.0	12.0	
174	G^4	N	C	C	0.005	1.0	1.0	12.0	
175	G^4	N	C	C	0.005	1.0	4.0	12.0	
176	G^4	N	C	N	0.005	1.0	1.0	12.0	
177	G^4	N	C	N	0.005	1.0	4.0	12.0	
178	G^4	N	C	I	0.005	-1.0	1.0	12.0	
179	G^4	N	C	I	0.005	-1.0	4.0	12.0	
180	G^4	N	C	I	0.005	1.0	1.0	12.0	
181	G^4	N	C	I	0.005	1.0	4.0	12.0	
182	G^4	N	C	Pb	0.005	-1.0	1.0	12.0	
183	G^4	N	C	Pb	0.005	1.0	1.0	12.0	
184	G^4	N	C	Pb	0.005	1.0	4.0	12.0	
185	G^4	N	N	I	0.005	1.0	1.0	12.0	
186	G^4	N	N	I	0.005	1.0	4.0	12.0	
187	G^4	N	I	I	0.005	-1.0	1.0	12.0	
188	G^4	N	I	I	0.005	1.0	1.0	12.0	
189	G^4	N	I	I	0.005	1.0	4.0	12.0	
190	G^4	N	I	Pb	0.005	-1.0	1.0	12.0	
191	G^4	N	I	Pb	0.005	1.0	1.0	12.0	
192	G^4	N	I	Pb	0.005	1.0	4.0	12.0	
193	G^2	I	H		0.004			12.0	0.0
194	G^2	I	H		0.028			12.0	0.0
195	G^2	I	H		0.139			12.0	0.0
196	G^2	I	C		0.004			12.0	0.0
197	G^2	I	C		0.028			12.0	0.0
198	G^2	I	C		0.139			12.0	0.0

Appendix

no.	type	at. i	at. j	at. k	$\eta(1/\text{Bohr}^2)$	λ	ζ	$R_c(\text{Bohr})$	$R_s(\text{Bohr})$
199	G^2	I	N		0.004			12.0	0.0
200	G^2	I	N		0.028			12.0	0.0
201	G^2	I	N		0.139			12.0	0.0
202	G^2	I	I		0.004			12.0	0.0
203	G^2	I	I		0.028			12.0	0.0
204	G^2	I	Pb		0.004			12.0	0.0
205	G^2	I	Pb		0.028			12.0	0.0
206	G^2	I	Pb		0.139			12.0	0.0
207	G^4	I	H	H	0.005	-1.0	1.0	12.0	
208	G^4	I	H	H	0.005	-1.0	4.0	12.0	
209	G^4	I	H	H	0.005	1.0	1.0	12.0	
210	G^4	I	H	H	0.005	1.0	4.0	12.0	
211	G^4	I	H	C	0.005	-1.0	1.0	12.0	
212	G^4	I	H	C	0.005	-1.0	4.0	12.0	
213	G^4	I	H	C	0.005	1.0	1.0	12.0	
214	G^4	I	H	C	0.005	1.0	4.0	12.0	
215	G^4	I	H	N	0.005	-1.0	1.0	12.0	
216	G^4	I	H	N	0.005	-1.0	4.0	12.0	
217	G^4	I	H	N	0.005	1.0	1.0	12.0	
218	G^4	I	H	N	0.005	1.0	4.0	12.0	
219	G^4	I	H	I	0.005	-1.0	1.0	12.0	
220	G^4	I	H	I	0.005	1.0	1.0	12.0	
221	G^4	I	H	I	0.005	1.0	4.0	12.0	
222	G^4	I	H	Pb	0.005	-1.0	1.0	12.0	
223	G^4	I	H	Pb	0.005	-1.0	4.0	12.0	
224	G^4	I	H	Pb	0.005	1.0	1.0	12.0	
225	G^4	I	H	Pb	0.005	1.0	4.0	12.0	
226	G^4	I	C	C	0.005	-1.0	1.0	12.0	
227	G^4	I	C	C	0.005	1.0	1.0	12.0	
228	G^4	I	C	C	0.005	1.0	4.0	12.0	
229	G^4	I	C	N	0.005	-1.0	1.0	12.0	
230	G^4	I	C	N	0.005	1.0	1.0	12.0	
231	G^4	I	C	N	0.005	1.0	4.0	12.0	
232	G^4	I	C	I	0.005	-1.0	1.0	12.0	
233	G^4	I	C	I	0.005	1.0	1.0	12.0	

B.2 Details for the MaPbI_3 FHMC Simulations

no.	type	at. i	at. j	at. k	$\eta(1/\text{Bohr}^2)$	λ	ζ	$R_c(\text{Bohr})$	$R_s(\text{Bohr})$
234	G^4	I	C	I	0.005	1.0	4.0	12.0	
235	G^4	I	C	Pb	0.005	-1.0	1.0	12.0	
236	G^4	I	C	Pb	0.005	1.0	1.0	12.0	
237	G^4	I	C	Pb	0.005	1.0	4.0	12.0	
238	G^4	I	N	N	0.005	-1.0	1.0	12.0	
239	G^4	I	N	N	0.005	1.0	1.0	12.0	
240	G^4	I	N	I	0.005	-1.0	1.0	12.0	
241	G^4	I	N	I	0.005	1.0	1.0	12.0	
242	G^4	I	N	I	0.005	1.0	4.0	12.0	
243	G^4	I	N	Pb	0.005	-1.0	1.0	12.0	
244	G^4	I	N	Pb	0.005	1.0	1.0	12.0	
245	G^4	I	I	I	0.005	1.0	1.0	12.0	
246	G^4	I	I	Pb	0.005	-1.0	1.0	12.0	
247	G^4	I	I	Pb	0.005	1.0	1.0	12.0	
248	G^4	I	I	Pb	0.005	1.0	4.0	12.0	
249	G^4	I	Pb	Pb	0.005	-1.0	1.0	12.0	
250	G^4	I	Pb	Pb	0.005	1.0	1.0	12.0	
251	G^2	Pb	H		0.004			12.0	0.0
252	G^2	Pb	H		0.028			12.0	0.0
253	G^2	Pb	H		0.139			12.0	0.0
254	G^2	Pb	C		0.004			12.0	0.0
255	G^2	Pb	C		0.028			12.0	0.0
256	G^2	Pb	C		0.139			12.0	0.0
257	G^2	Pb	N		0.004			12.0	0.0
258	G^2	Pb	N		0.028			12.0	0.0
259	G^2	Pb	I		0.004			12.0	0.0
260	G^2	Pb	I		0.028			12.0	0.0
261	G^2	Pb	I		0.139			12.0	0.0
262	G^2	Pb	Pb		0.004			12.0	0.0
263	G^2	Pb	Pb		0.028			12.0	0.0
264	G^4	Pb	H	H	0.005	-1.0	1.0	12.0	
265	G^4	Pb	H	H	0.005	1.0	1.0	12.0	
266	G^4	Pb	H	H	0.005	1.0	4.0	12.0	
267	G^4	Pb	H	C	0.005	-1.0	1.0	12.0	
268	G^4	Pb	H	C	0.005	1.0	1.0	12.0	

no.	type	at. i	at. j	at. k	$\eta(1/\text{Bohr}^2)$	λ	ζ	$R_c(\text{Bohr})$	$R_s(\text{Bohr})$
269	G^4	Pb	H	C	0.005	1.0	4.0	12.0	
270	G^4	Pb	H	N	0.005	1.0	1.0	12.0	
271	G^4	Pb	H	N	0.005	1.0	4.0	12.0	
272	G^4	Pb	H	I	0.005	-1.0	1.0	12.0	
273	G^4	Pb	H	I	0.005	1.0	1.0	12.0	
274	G^4	Pb	H	I	0.005	1.0	4.0	12.0	
275	G^4	Pb	C	N	0.005	1.0	1.0	12.0	
276	G^4	Pb	C	N	0.005	1.0	4.0	12.0	
277	G^4	Pb	C	I	0.005	-1.0	1.0	12.0	
278	G^4	Pb	C	I	0.005	1.0	1.0	12.0	
279	G^4	Pb	C	I	0.005	1.0	4.0	12.0	
280	G^4	Pb	N	I	0.005	-1.0	1.0	12.0	
281	G^4	Pb	N	I	0.005	1.0	1.0	12.0	
282	G^4	Pb	N	I	0.005	1.0	4.0	12.0	
283	G^4	Pb	I	I	0.005	-1.0	1.0	12.0	
284	G^4	Pb	I	I	0.005	-1.0	4.0	12.0	
285	G^4	Pb	I	I	0.005	1.0	1.0	12.0	
286	G^4	Pb	I	I	0.005	1.0	4.0	12.0	
287	G^4	Pb	I	Pb	0.005	-1.0	1.0	12.0	
288	G^4	Pb	I	Pb	0.005	1.0	1.0	12.0	
289	G^4	Pb	I	Pb	0.005	1.0	4.0	12.0	

B.2.3 QUASI HARMONIC APPROXIMATION

We used phonopy [297] to compute free energy of the different MaPbI_3 phases in the harmonic approximation (HA) and quasi harmonic approximation (QHA). The free energies were calculated using the same HDNNP based PES that was also used for our FHMC simulations. Due to the strong anharmonicity and large difference between the softest and hardest modes, computing the HA and QHA was challenging. The local minima were optimized using the vc-SQNM algorithm [299] to a maximum force value of 10^{-8} Ha/Bohr. Force constants were computed through finite differences with an extremely small displacements of 10^{-5} Å as larger displacements would result in imaginary phonon frequencies. Such small displacements are only possible because the NNP PES is a smooth function, that can be computed with almost machine precision. On a DFT PES, larger displacements would have to be used. For all

phases, super cells consisting of 8 formula units, as shown in Appendix B.2.1, were used. The relative free energies are shown in Figure B.2.10 and the phonon densities of state are shown in Figure B.2.11.

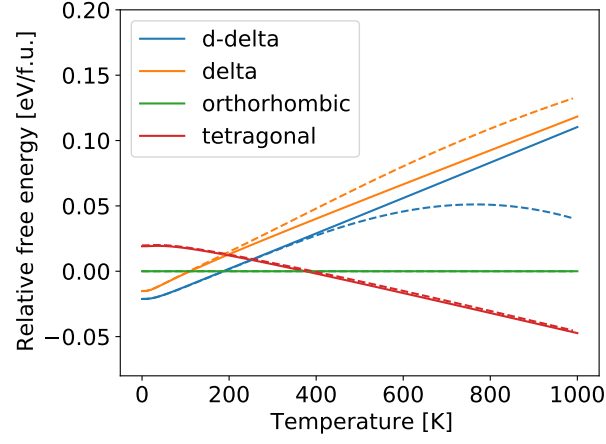


Figure B.2.10: Relative free energies computed with the HA (solid lines) and QHA (dashed lines) with respect to the orthorhombic phase.

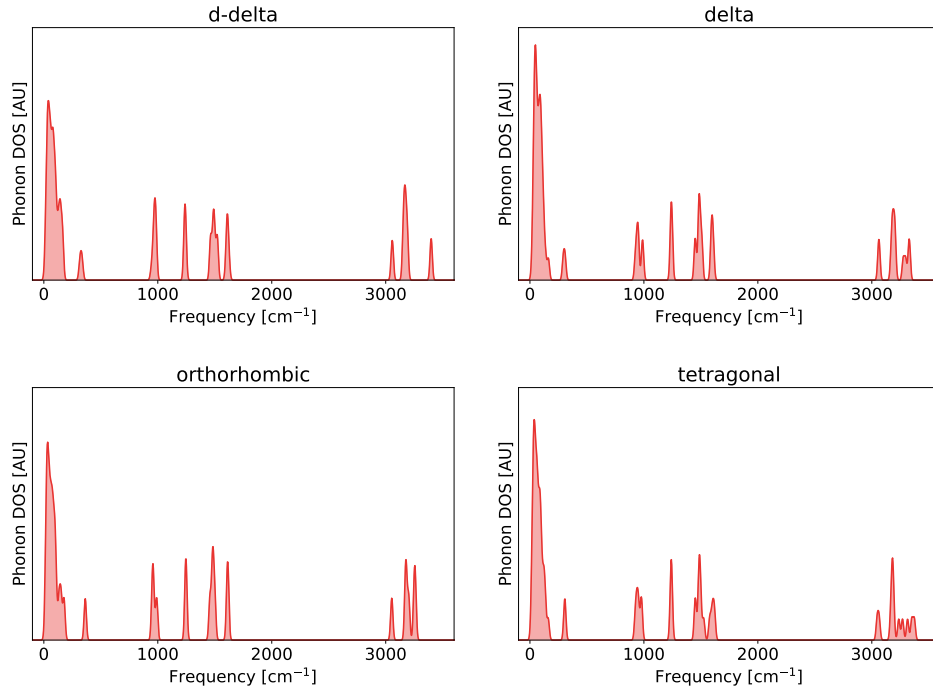


Figure B.2.11: Phonon density of states computed using the HDNNP and phonopy for all MaPbI_3 phases except the cubic phase. A convolution with a Gaussian function with a standard deviation of 10 cm^{-1} was used to obtain a smooth density of states.